The Redox Potentials of *n*-type Colloidal Semiconductor Nanocrystals

Gerard Michael Carroll

A dissertation

submitted in partial fulfillment of the

requirements for the degree of

Doctor of Philosophy

University of Washington

2016

Reading Committee:

Daniel Gamelin, Chair

D. Michael Heinekey

Brandi Cossairt

Program Authorized to Offer Degree:

Chemistry

University of Washington

Abstract

The Redox Potentials of *n*-Type Colloidal Semiconductor Nanocrystals

Gerard Carroll

Chair of the Supervisory Committee:
Professor Daniel Gamelin
Chemistry

This thesis presents investigations for two related fields of semiconductor electrochemistry: redox potential determination of colloidal semiconductor nanocrystals, and mechanistic analysis of photoelectrochemical water oxidation with electrocatalyst modified mesostructured hematite photoanodes.

Adapting electrochemical techniques to colloidal semiconductor nanocrystals (SC NC) is a long-standing challenge for this class of materials. Subject to a variety of complications, standard voltammetric techniques are not as straight forward for SC NCs as they are for small molecules. As a result, researchers have developed creative ways to side step these complications by coupling electrochemistry with NC spectroscopy. Chapter 1 discusses the fundamental electronic and spectroscopic properties of SC NCs at different redox states. We present a brief

review of some of the notable studies employing SC NC spectroelectrochemistry that provide the theoretical and experimental context for the following chapters. Chapter 2 presents an investigation on NC redox potentials of photochemically reduced colloidal ZnO NCs using a solvated redox-indicator method. In the one electron limit, conduction band electrons show evidence of quantum confinement, but at higher electron concentrations, the NC Fermi-level becomes dependent on the electron density across all NC sizes. Chapter 3 outlines a poteniometric method for monitoring the NC redox potentials *in situ*. NC redox potentials for ZnO and CdSe are measured, and as predicted from these measurements, spontaneous electron transfer from CdSe to ZnO is demonstrated. Chapter 4 details the impact of the surface of CdSe NCs on the NC redox potentials. We find that the ratio of Cd^{2+}:Se^{2-} on the surface of CdSe NCs changes both the NC band edge potentials, as well as the maximum electron density achievable by photochemical reduction. These changes are proposed to arise from interfacial dipoles when CdSe has a Se^{2-}-rich surface.

Chapters 5 and 6 examine the mechanistic pathways of solar water oxidation on Co-Pi modified α-Fe_2O_3 photoanodes. A rate constant analysis of water oxidation and electron-hole recombination paired with the identification of surface-morphology-dependent current-voltage characteristics reveal new insights into the role of the semiconductor/electrocatalyst interface on the overall solar water oxidation efficiency. These findings reconcile disparate observations from previous studies.

Table of Contents

List of Figures

List of Tables

Acknowledgements

I would like to express my deepest gratitude to Prof. Daniel Gamelin. As a mentor, scientist, and friend, Daniel has shaped both my graduate career and my perspective on scientific research in an extremely positive manner. Providing strong leadership while still respecting the opinions of his group members, Daniel has cultivated an environment that promotes breakthrough research while pushing both professional and personal growth for all of the members of his group. His patience and guidance provide the members of his group, myself included, with the tools to become successful independent scientists in future endeavors. I hold Prof. Gamelin in the highest regard, and I am sure that his impact on my life will continue well beyond graduate school.

I would also like to thank the members of the Gamelin group. Throughout the nearly six years of my time at UW, I have had the pleasure of working with many talented individuals. Diane Zhong introduced me to the nature of graduate research. Instructing me not only on the electrochemistry of semiconductors, Diane described the subtleties of scientific writing and inquiry. Diane was a great mentor for a first-year graduate student. Following the first two years of graduate school, the Molecular Engineering and Sciences building opened and the Gamelin group was provided lab space on the first floor. Working in renewable energy technologies, Katherine Bryant and myself were stationed in this building. In an office composed of chemical engineers, materials scientist, and chemists, Katherine quickly became my friend and confidant. Together, we navigated the transition from CHB to MolES. I must thank Katherine as she shouldered much of the responsibility of transitioning lab spaces. When I switched focus from semiconductor thin films to colloidal ZnO nanocrystals, I had the opportunity to work with Alina Schimpf. Paired with her expertise and encouragement, we spearheaded a novel method for nanocrystal Fermi-level detection that I am particularly proud of. I am very grateful to Alina for her help and positive outlook. In my final years at UW, Emily Tsui, Kimberly Hartstein, Carl Brozek and myself worked closely together. Emily, Carl, and Kim are all extremely talented chemists with a keen eye. Challenged by their fortitude, they pushed me to a level that I likely wouldn't have reached otherwise. I would like to thank them for their thoughtfulness and time. I would also like to thank the rest of the Gamelin lab for your friendship and support. Relaxing over a beer after group meeting and discussing non-science related subjects could sometimes prove to be just as productive as working in the lab.

I cannot, in good conscience, forget to thank my friends outside of my lab for fun times and good talks. Whether we're playing softball in the intermural leagues, playing golf on a weekend, or just drinking beers at someone's house, these moments had a significant effect on my overall happiness and were integral to my success in graduate school. I would especially like to thank Dustin Kramer, Adam Colbert, Hester Dang, Jenni Smith, Joan Bleeker, Patrick Whitham, Miles Braten, Joelle Rolfs, and Bejan Hakimi. You guys are great friends and I will cherish the memories we have together.

I would like to thank a few individuals who, whether they know it or not, had a particularly significant influence on the direction of my like. My high school chemistry teacher, Laura Guida, introduced me to the subject which I would direct my attention for the foreseeable

future. Chemistry is not an exceptionally popular subject in high school, and as a high school junior going into chemistry class for the first time; I didn't imagine it would be of any interest to me. However, Laura presented chemistry in a way that both captivated my imagination and inspired me to continue to learn about the chemical sciences. Sharing her passion transformed my perspective, and I want her to know that I am extremely grateful to her for her hard work and dedication.

At Fort Lewis College, Monte Helm and Ted Bartlett cemented my interest in chemistry. As an undergraduate, Monte Helm took me on as a summer researcher where I had my first experience into scientific inquiry. This summer proved to be a deciding factor in my pursuit of a Ph.D. Montes mentorship meant a lot to me and I am very grateful for the opportunities he gave to me, both as a mentor and as a friend. Ted Bartlett was not only my instructor for undergraduate organic chemistry but also an inspiration to pursue a career in chemistry research. His encouragement had a sizeable impact on my professional trajectory, and I am very grateful to him.

Finally, I would like to thank my mother and father- you have enabled me to become the man that I am today. I cannot fully express my gratitude in the text, but I will forever be grateful for your selflessness and support. I hope that I can continue to make you proud.

Chapter 1. A Review on the Spectroelectrochemistry of Semiconductor Nanocrystals

1.1 Introduction

Since the development of simple solution-based syntheses of nearly monodisperse semiconductor nanocrystals (SC NCs),[1-3] these materials have gained popularity in both fundamental and applied research fields. The size tunable optical and electronic properties of SC NCs as well as their ease of synthesis and device integration offer advantages for large-scale manufacturing in applications such as photocatalysis,[4-6] photovoltaic solar energy conversion,[7-10] photoelectrochemical cells,[11] battery materials,[12] photo-detection, and LED technology[13] that is unmatched by their bulk SC counterparts. Research into this promising class of materials has made tremendous strides elucidating the parameters that affect the SC NC physical properties, but simple and effective means for quantifying NC redox potentials remains a challenge. Before the unique electronic properties of these materials can be utilized on a large scale, they must be better defined.

Characterizing the redox chemistry of SC NCs is one of the most challenging aspects of colloidal SC NC research.[14] *Ex situ* characterization such as scanning tunneling microscopy,[15] atomic force microscopy, and photoelectron spectroscopy,[9,16,17] has been carried out to define the electronic energy levels in SC NCs. While these methods provide insight into the absolute energies of isolated SC NCs, the NCs must be taken from their native solution environment and placed in air or under high vacuum. As a result, critical information is lost on the solution chemistry of SC NCs such as surface reconstruction, ion adsorption/desorption processes, equilibrium processes, and solvation energies. Further investigations into the redox properties of suspended colloidal SC NCs are thus warranted.

Traditional solution based electrochemical methods have proven difficult to adapt to SC NCs. Cyclic voltammetry (CV), for example, is a widely used electrochemical technique to quantify the redox potentials of solvated small molecules. Applied to SC NCs, CV can provide fair agreement between the electrochemical bandgap potentials and the optical gap, but complications arising from irreversible redox chemistry, redox active surface states, low signal to

noise ratios, NC solubility, and NC colloidal instability under applied bias all hinder the use of CV for colloidal NCs.[14,18,19] Additionally, variations in the SC NC band edge potentials for a single material as large as 1V have been reported leading to the general conclusion that CV is not as straightforward on NCs as it is for small molecules. Alternatively, differential pulse voltammetry (DPV) improves signal-to-noise ratios, and has made progress on narrowing the uncertainty in the assignment of band edge potentials.[20,21] However, DPV suffers from problems similar to CV as the NC colloids are often unstable under bias, and the voltammogram can be convoluted with redox active NC surface states. Thus, classical voltammetric methods may not be stand-alone techniques for measuring SC NC redox potentials *in situ*.

An important and useful feature of SC NCs is their predicable spectroscopic changes upon introduction of band-like charge carriers: an absorption bleach of excitonic transitions and a simultaneous growth of comparably intense NIR-IR absorption features. Photoluminescence and electron-paramagnetic resonances also change upon carrier injection. These spectroscopic characteristics present the opportunity to discern between injection of band-like carriers and all other redox processes, and when coupled with solution-based electrochemistry, provide the level of precision required to accurately describe SC NC redox properties. The remainder of this chapter will focus on recent accounts of using spectroelectrochemistry as a tool to study electronic and optical properties of SC NCs.

1.2 The Electronic Properties of Excess Charge Carriers in Semiconductor Nanocrystals.

It is instructive to first discuss the electronic properties and definitions of reduced and oxidized SC NCs. The Fermi-level (E_F) is a measure of the chemical potential of the frontier-orbital electron density in semiconductors.[22,23] Defined as the energy at which the normalized probability of finding an electron at 0 K is 0.5, E_F is the common formalism used to discuss the energetic state of a system relative to a static reference point. Figure 1.1 schematically illustrates E_F of SC NCs at different redox states.

Intrinsic SC NCs are pure, stoichiometric materials with a non-zero energetic separation between the fully occupied valence band (VB) and the electron vacant conduction band (CB). At 0 K, E_F of intrinsic SC NCs ($E_{F,\,i}$) is positioned exactly half way between the two bands. If an electron is added to the SC NC, it must occupy the lowest energy unoccupied orbital, in this case,

the CB minimum. As a result, the SC NC is now considered *n*-type degenerately doped, and E_F now resides within the CB ($E_{F,n}$). The opposite is true for extracting an electron from the VB and forming *p*-type NCs ($E_{F,\,p}$). In either *n*- or *p*-type SC NCs, the excess charge carriers occupy delocalized electronic bands and not localized surface states. This is an important distinguishing characteristic for spectroelectrochemical measurements; SC NCs often contain localized redox-active surface states that chemically change based on the material, exposed crystal facet, and the ligation shell. These states can alter E_F, but are practically invisible to electronic absorption spectroscopy, indicating that there is no carrier exchange between surface states and the delocalized bands (*vida infra*). Therefore, SC NCs are defined explicitly as *n*- or *p*-type when charge carriers occupy delocalized, spectroscopically active SC bands.

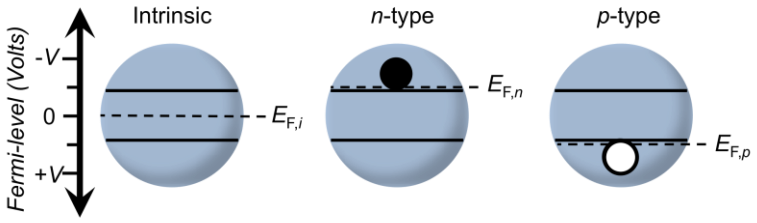

Figure 1.1. Schematic illustrations of intrinsic, *n*-type, and *p*-type colloidal nanocrystals.

1.3 The Spectroscopic Properties of Charge Carriers in Semiconductor Nanocrystals.

The spectroscopic characteristics of delocalized charge carriers present a useful handle for quantifying changes in the SC NC redox state. Figure 1.2a plots the absorption spectrum of colloidal CdSe NCs being gradually 'reduced' by populating the conduction band with electrons.[24-26] Upon electron injection into the conduction band (CB), the first excitonic (*inter*-band) absorption feature bleaches due to Pauli-blocking. Also known as the Moss-Burstein effect, the degree of the excitonic absorption bleach is a product of both the electronic degeneracy of the SC band edge, and the number of additional charge carriers occupying that band. For example, the conduction band minimum of CdSe NCs have two-fold degeneracy ($1S_e$) such that when the average number of conduction band electrons (<*n*>) is 1, the first excitonic

transition bleaches by 50%.[27] This bleach scales linearly with the number of excess carriers. If two electrons reside in the SC NC CB, the first excitonic transition is fully bleached. Further NC reduction then populates the next lowest energy ($1P_e$) orbital and, spectroscopically, presents as a bleach in higher energy transitions.[28] In most quantum-confined SC NCs, the SC band edges are composed of discrete states that can be energetically resolved by absorption spectroscopy. This property is useful for quantifying $\langle n \rangle$.

While *inter*-band transitions are blocked and the excitonic absorption is bleached with carrier introduction, *intra*-band electronic transitions become available. For example, the same $1S_e$ CB electron in reduced CdSe NCs may be photoexcited to $1P_e$. The spectroscopic manifestation of these transitions is a NIR/IR absorption feature that gains intensity as the NCs become increasingly *n* or *p*-type as shown by the increasing low energy absorption feature in figure 1.2a. These NIR/IR transitions too can be used to quantify the number of excess carriers.

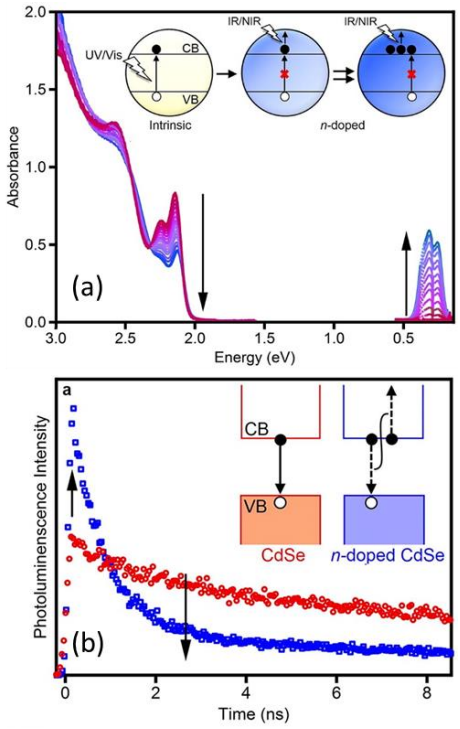

Figure 1.2. Spectroscopic signatures of band-like carriers in semiconductor nanocrystals.

(a) The addition of CB electrons to CdSe nanocrystals bleaches band-edge absorption and introduces new IR intraband absorption. Visible and IR absorption as a function of photodoping level. The arrows show increased electron accumulation up to an average of two electrons NC^{-1}. These data were adapted from ref. 24 and 25. **(b)** Photoluminescent decay trace for intrinsic CdSe NCs (red) and *n*-type CdSe NCs (blue). The inset scheme shows the negative trion Auger process with accelerates the non-radiative excitonic relaxation. These data were adapted from ref. 24 and 26.

In addition to the electronic absorption changes, the photoluminescence (PL) recombination dynamics change as well.[24,29,30] Excess delocalized carriers in SC NC bands promote trion Auger recombination; the excitonic energy is transferred to the excess delocalized carrier resulting in non-radiative excitonic recombination and promotion of the excess carrier to a 'hot' state. Macroscopically, this phenomenon dramatically decreases photoluminescence quantum yield (PLQY) relative to the NC's intrinsic state. Although the change in PLQY qualitatively indicates injection of excess charge carriers, other factors that alter PLQY with changes in E_F, such as mid-gap surface-state passivation,[31,32] complicate the quantitative

analysis. Therefore, electronic absorption spectroscopy is the primary spectroscopic tool used to analyze the redox state of SC NCs.

The faithful spectroscopic signatures of *n*- or *p*-type SC NCs are integral to studying NC redox properties, as well as utilization for applications involving NC chromatics.

1.4 Spectroelectrochemistry of Semiconductor Nanocrystals

Spectroelectrochemistry of SC NCs simultaneously employs both spectroscopy and electrochemistry to analyze either the electrochemical potential or spectroscopic changes of SC NCs both under equilibrium and non-equilibrium conditions. A schematic illustration of a typical spectroelectrochemical cell is shown in figure 1.3. The electrochemical portion of this experiment uses a three-electrode configuration comprising a working, counter, and reference electrode, which are submerged in an organic electrolyte medium with the NCs. The working electrode can range in material from transparent conducting oxides (TCOs) to a simple platinum wire. The important criterion of the working electrode is that the electrochemical potential of the electrode/electrolyte junction under potentiostatic bias is equal to the input bias of the potentiostat relative to the reference electrode (*i.e.* the electrode must be an electrical conductor), and the NC surface must be able to sample this electrified interface. The reference electrode can range in material as well. Because SC NC spectroelectrochemical experiments are often carried out in organic electrolyte media, the typical reference electrode of choice is a silver wire *pseudo*-reference, but Ag/AgCl leakless electrodes, and $Ag/AgNO_3$ electrodes can be used as well. Silver wire *pseudo*-reference electrodes are generally preferred as problems arising from junction potential build-up and electrolyte-leakage are alleviated. As the name implies however, *pseudo*-reference electrodes do not have a well-defined redox potential, and are subject to change in different electrolytes based on the $Ag|Ag^+$ equilibrium in the particular medium. Thus internal standards, such as ferrocinium/ferrocene, are added to the solution as an internal reference. The counter electrode is, in most cases, a platinum wire that provides a conductive channel for a continuous circuit. Figure 1.3 schematically illustrates a typical spectroelectrochemical setup. In this configuration, the electrodes may be used to perturb the SC NCs while light is passed through the sample as a probe, or vice versa. Several configurations of SC NC spectroelectrochemistry have been carried out, and a few are discussed below.

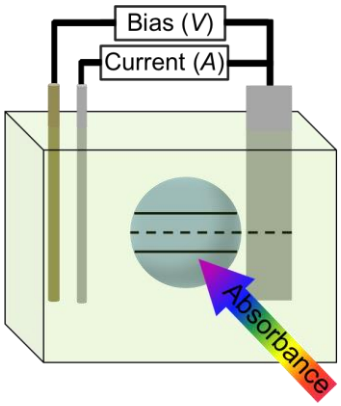

Figure 1.3. Schematic illustration of a typical spectroelectrochemical apparatus.

The first comprehensive and unambiguous spectroelectrochemical investigation of colloidal SC NCs came from Guyot-Sionnest and coworkers in 2001.[33] E_F of colloidal CdSe and CdSe/ZnS core/shell NCs were voltammetrically controlled while electronic reflectance spectra were recorded. Figure 1.4 shows the UV/vis/NIR electronic reflectance spectra of colloidal CdSe NCs at open-circuit and under negative bias. At open circuit, the NCs are approximately intrinsic SCs, but upon application of a negative bias, the first excitonic transition bleaches, and growth of the NIR absorption feature becomes apparent. Both spectral phenomena are fully reversible when the electrochemical cell is brought back to open circuit, indicating reversible CB electron injection into the colloidal NCs.

To test the effects of quantum confinement on electron injection, the authors measured the electrochemical potential of the integrated NIR absorbance for different CdSe NC sizes. These data are shown in figure 1.4b. Consistent with predictions from Brus,[34] the authors found that the necessary electrochemical potential for CB electron injection was dependent on the NC size. The normalized NIR/IR absorption plotted as a function of the applied potential shows similar sigmoidal shapes for all NC sizes, but the NIR/IR onset shifts cathodically (negative) as the size of the CdSe NC decreases. Modeling these data, the authors show that the negative shift is in good agreement with the predicted CB energy shifts from quantum confinement, as shown in the inset in figure 1.4b.

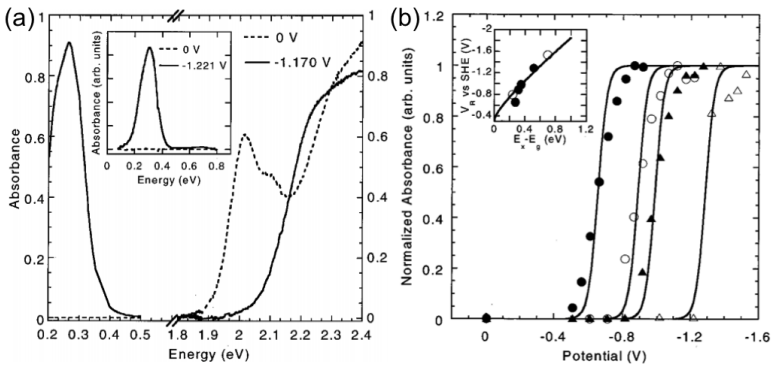

Figure 1.4. Absorption spectra of colloidal CdSe NCs under voltammetric bias

(a) Electronic absorption spectra of 5.8 nm diameter CdSe nanocrystal film at 0 V (dashed line) and -1.7 V (solid line). The inset shows IR spectra of 5.0 nm CdSe NC film at 0 and -1.221 V. **(b)** Potential dependence of IR absorption of 4.2 nm (open triangles), 5.4 nm (solid triangles), 5.8 nm (open circles), and 6.8 nm (solid circles) diameter CdSe nanocrystal films. The lines are least-squares fits from quasi-equilibrium approximations. The inset shows the dependence of the reduction potentials of nanocrystals on the confinement energy, (E_x-E_g). E_x is the first exciton transition energy measured from the optical absorption spectrum. E_g is the room temperature bulk band gap. V_R is with respect to Standard Hydrogen Electrode. Solid and open circles are results from the measurement of nanocrystal films and solutions. These data were adapted from refs. 33 and 35.

The third spectroscopic signature of electron injection, photoluminescence, was also investigated. Figure 1.5 plots the PL of core/shell CdSe/ZnS NCs at different NC redox states. Upon application of a negative bias, the PLQY nearly instantaneously drops by ~60 %. When the electrochemical cell is brought back to open circuit, the PL slowly recovers over the period of ~60min. This process was repeated several times and is shown to reach nearly the same level of PL quench and recovery for each cycle, indicating the reversibility of electron injection. The authors did note, however, that the PL was not as quantitatively reproducible as the absorption spectroscopy experiments, and that the PLQY did gradually decrease over multiple cycles. These changes were attributed to the formation of mid-gap surface-trap states (which are well known to alter the PLQYs of semiconductor nanocrystals) upon electrochemical cycling. Nevertheless, the combination of excitonic, and intra-band absorption, paired with the PL changes of NC size

dependent electron injection unambiguously demonstrate the electrochromism of CdSe NCs, and the utility of spectroelectrochemistry for SC NC materials.

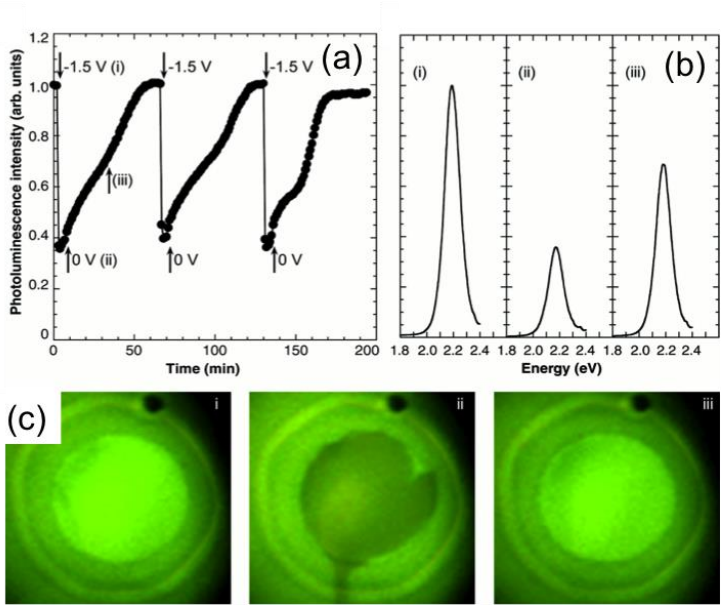

Figure 1.5. Photoluminescence of colloidal CdSe NCs under voltammetric bias

(**a**) Integrated photoluminescence intensity of CdSe/ZnS core/shell nanocrystals (core diameter 4 nm) at different potentials. The photoluminescence is quenched at −1.5 V and recovers at 0 V. The photoluminescence may be quenched further at longer duration of applied potential or at higher potentials. (**b**) Photoluminescence spectra at 0 V (i), at 3 min after setting the potential to −1.5 V (ii), and at 25 min after resetting the potential to 0 V (iii). (**c**) Photographs of the sample cell illuminated by a handheld UV lamp at 0 V (i), 3 min after applying a potential of −1.5 V (ii), and 25 min after resetting the potential to 0 V (iii). The exposure time is the same in all three images. These data were adapted from ref. 33.

Since this pioneering investigation many subsequent reports have employed spectroelectrochemistry to elucidate the physical properties of SC NCs. In the following sections we compare different spectroelectrochemical configurations of SC NCs, namely NC thin films versus NC colloids, and discuss the experimental detection of different NC properties.

1.5 Thin films.

SC NC thin films are ubiquitous in nano-materials research.[12,13,36-44] As a colloidal suspension, SC NCs can be directly deposited onto conductive surfaces and still retain their spectroscopic and electronic properties, making them solution-processable building blocks for higher order electronic and optoelectronic architectures.[36,45] The ability of SC NCs to maintain their unique physical properties when transformed from colloidal suspensions to solid-state devices is one of the most important aspects of this class of materials for many of their proposed applications. In the following section, we present a brief summary of the methodological development of SC NC spectroelectrochemistry for oxide and chalcogenide NC thin films, and discuss some of the significant findings.

1.5.1 *Oxides*

Some of the earliest accounts of spectroelectrochemical analysis of SC NCs employed ZnO NCs deposited onto transparent conducting oxide electrodes. Originally, these experiments sought to clarify the origin of a blue shift in the excitonic absorbance when colloidal NCs were mixed with organic free radicals.[46] In 1995 Hoyer and Weller studied the electrochromism of sol-gel derived nanocrystalline ZnO thin films.[47] They observed a reversible blue shift in the excitonic absorbance spectrum and electrochemical capacitive charging upon application of negative potential to the ZnO NC thin film. However, due to large size dispersion of the ZnO NCs, the authors could not conclude definitively whether electrons were deposited in the ZnO CB, or localized surface trap states. Nevertheless, Hoyer and Weller first demonstrated that the spectroscopic properties of ZnO NCs could be controlled electrochemically in a thin film configuration.

Meulenkamp, Vanmaekelbergh and coworkers later confirmed that CB electrons could indeed be electrochemically injected into the ZnO NC CB.[48-53] Adapted from ref. 51, figure 1.6a plots the differential capacitance ($\Delta Q(\mu_e)$) of ZnO NC thin films in an electrochemical field effect transistor device (also known as electrochemical gating[54]) from these experiments. Here, $\Delta Q(\mu_e)$ coincides with a bleach in the ZnO NC excitonic transition, indicating an increasing CB electron population. Fit to an orbital-filling model (S-P-D) of quantum confined ZnO NCs, $\Delta Q(\mu_e)$ was deconvoluted into individual atomic-like orbitals (shown by the dashed and dotted

lines in fig. 1.6a). The energetic contributions of orbital filling, electron-electron repulsion ($E_{e\text{-}e}$), and NC dielectric polarization from electron injection (E_{pol}) could then be ascertained. The S-P-D orbital filling energies were concluded to be size dependent, as expected, and were in fair agreement with those obtained from IR spectroscopy.[50]

In addition to the capacitive charging, the authors also measured changes in film conductivity (R^{-1}) and electron mobility (μ_e) as a function of NC electron injection (figure 1.6b). From these data, R^{-1} increases with an increasing number of conduction band electrons (<*n*>), and μ_e exhibits several maxima when the ZnO films are charged to different degrees. Plotting μ_e as a function of <*n*>, μ_e maximizes when the ZnO NC CB orbitals ($1S_e$, $1P_e$) are partially filled. The highest electronic mobility in an otherwise insulating material exists when no thermal, or electronic barrier blocks the electron-transport mechanism. In the case of these ZnO NCs, that criterion is met when the CB orbitals are partially filled.[49] Thus R^{-1} and μ_e show the expected pattern of conduction for these quantum confined ZnO NCs. Despite some controversy,[55,56] the correlation between the spectroscopic and electrochemical signatures as well as the electron mobility changes associated with charge injection allowed the authors to firmly conclude that electrons were in fact injected in the ZnO NC CB upon an electrochemical bias. Similar results were obtained for CdSe NC thin films.[57]

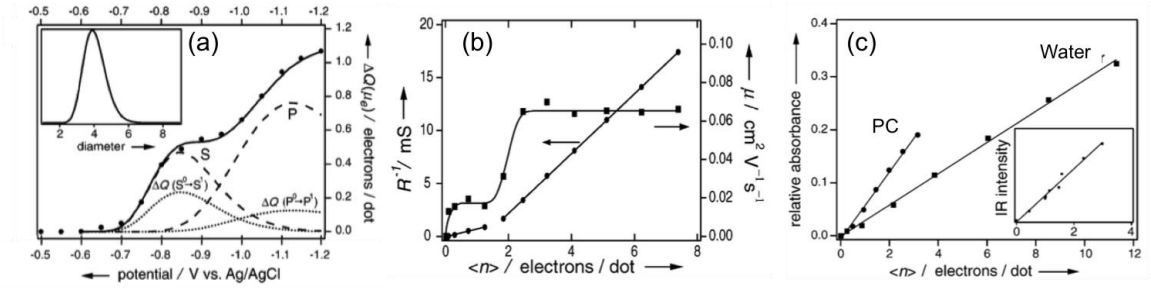

Figure 1.6. Electron injection into ZnO NC thin films

(a) Differential capacitance measurements (closed circles) $\Delta Q(\mu_e)$, expressed in electrons per dot of d = 3.9 nm ZnO NC thin films permeated with water with a phosphate buffer. The solid lines give the best fit obtained with the sum of single-electron addition functions (example $\Delta Q(S^0 \rightarrow S^1)$) calculated from quantum confined shell filling model. **(b)** The source/drain conductance (R^{-1}) and the corresponding electron mobility (μ) as a function of <*n*> of d =3.9 nm ZnO in aqueous phosphate electrolyte. **(c)** The relative absorbance as a function of the average number of electrons for the water and PC

systems. The relative absorbance is defined as the quenching of the absorbance between 3.3 and 4.0 eV divided by the total absorbance between 3.3 and 4.0 eV at 0 V. The IR absorbance is shown in the inset as a function of $<n>$. These data were adapted from ref. 51.

Interestingly, the electrolyte in these experiments strongly influenced the electrochemical properties of the ZnO NCs; the electron injection potential into the 1S orbital of ZnO varied by several hundred mV for water versus propylene carbonate (PC). Additionally, the maximum number of conduction band electrons $<n_{max}>$ was shown to nearly double in water vs PC. The authors rationalized these observations by considering $E_{e\text{-}e}$ to change in the different electrolyte media. From the modeled differential capacitance data in aqueous/phosphate vs PC/$[Bu_4N][ClO_4]$ solutions, the authors found that $E_{e\text{-}e} < kT$ (kT ~25 meV) in water, whereas $E_{e\text{-}e}$ = 200 meV in PC. The authors propose that protons in water adsorb to the surfaces of ZnO NCs and reduce $E_{e\text{-}e}$ within the bulk of the NCs. Conduction band electron charge compensation later became a topic of great interest in *n*-type ZnO NCs.[24,58-61] The conclusion that conduction band electrons in ZnO NCs could be controlled by means of electrochemistry provided a strong foundation for future spectroelectrochemical investigations on oxide NCs, and experimentally verified the theoretical framework for electronic conduction in NC thin films.

While these earlier studies of oxide NCs relied on spectroscopy of the excitonic absorption bleach to characterize CB electrons, recent investigations have switched focus to the NIR/IR intra-band absorption feature, also described as localized surface plasmon resonances (LSPR).[42,62] The broad and intense NIR/IR absorption band that grows in with increasing carrier density can be exploited for both fundamental and applied objectives. Indeed one of the most promising aspects of doped oxide NC assemblies is the possibility of utilizing their electrochromic properties for smart window applications.[13,37,42] With the ability to accommodate carrier densities on the order of 10^{21} cm^{-3}, manipulation of the NIR/IR absorption band of oxide NCs can be achieved through synthetic, post-synthetic, and electrochemical means.[42] An example of both synthetic and electrochemical modulation of the NIR/IR absorption band is plotted in Figure 1.7 from the Milliron group.

Figure 1.7a plots the optical density of d = 4.1 nm tin doped indium oxide (ITO) nanocrystals deposited onto a glass substrate in $LiClO_4$/PC electrolyte at various applied potentials. Here, CB electron charge compensation is afforded internally through aliovalent Sn^{4+}

dopants within the In^{3+} lattice, and conduction band electrons are therefore present at open circuit giving rise to the broad and intense NIR/IR absorption. As either anodic (positive) or cathodic (negative) bias is applied to the NC thin film, modulation of the NC CB electron density is observed via a change in the peak position and intensity of the NIR/IR absorption band. This modulation is described by a modified form of the Drude equation.[62] At the most oxidizing potential measured, 4.0V vs Li^+/Li, the NIR/IR absorption feature is nearly eliminated indicating a near complete extraction of majority charge carriers relative to the equilibrium electron concentration. Due to the extraction of electrons upon positive bias and the static arrangement of the Sn^{4+} dopants within the NC, the authors propose that ITO NCs develop a depletion region near the surface of the NCs under positive bias. While typically reserved for bulk SCs, this hypothesis predicts that, given a constant donor density, the size of the ITO NC dictates the amount of charge extracted at a given potential, which is reflected in the NIR/IR absorption.[63,64] To test this, the authors performed spectroelectrochemical measurements on three different sizes of identically doped ITO NCs. The results are presented in figure 1.7b.

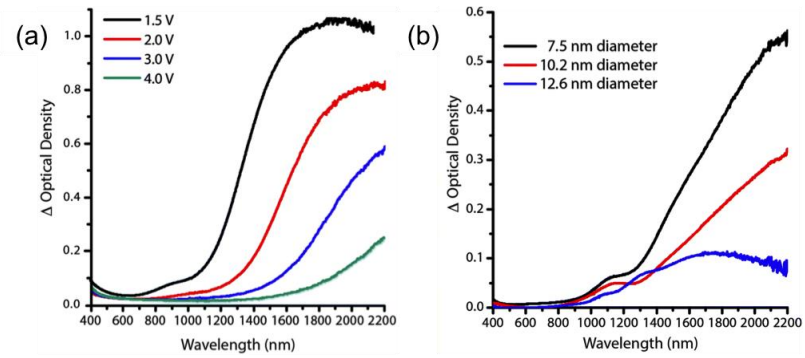

Figure 1.7. LSPR modulation of ITO NC thin films

(a) Optical density at different applied voltages of an ITO nanocrystal network film with 4.1 nm diameter, 16.8% Sn nanocrystals. **(b)** Change in optical density between 1.5 V and 4 V (*vs.* Li/Li^+) for various nanocrystal sizes, each with 4.65 ± 0.25% Sn. The ITO films were prepared from formic acid capped ITO NCs spin cast onto a glass slide and were measured in a $LiClO_4$ propylene carbonate electrolyte. These data were adapted from ref. 42 and 65.

Figure 1.7b plots the change in the optical density between 1.5 V and 4 V for the three different sizes of ITO NCs of the same tin content. In accord with their proposed depletion

region hypothesis, the change in the OD between 1.5 and 4V decreases as the size of the NC increases. The dielectric screening from a depletion region within ITO NCs limits the effective potential of the electrochemical bias to a finite distance within the NC. As the size of the NC increases, the depletion region becomes smaller than the radius of the NC and the donor density near the center of the NC is decoupled from the applied bias resulting in a decreased modulation of the NIR/IR absorption band. Depletion region effects have also been proposed to account for non-ideal NIR/IR absorbance modulation in antimony doped tin oxide (ATO).[66]

LSPR modulation with doped SC NC oxides has garnered increasing attention for applications in smart window technology. Including ITO, nanocrystal materials such as aluminum doped zinc oxide (AZO),[67] antimony doped tin oxide (ATO),[66] cesium doped tungsten oxide ($Cs:WO_3$),[68] and niobium doped titanium oxide ($Nb:TiO_2$)[69] show promising electrochromic properties for such applications. Indeed tuning the spectroscopic properties of doped SC NC oxide thin films under electrochemical bias is a scientifically rich field that will likely see increasing attention as NC thin-film technology matures.

1.5.2 *Chalcogenides*

Since the initial report by Guyot-Sionnest and coworkers on the electrochromic properties of CdSe NCs, several experimental bottlenecks have been identified with using voltammetry on colloidal NCs for NC spectroelectrochemistry. In particular, the NC charge/discharge time is diffusion-limited when the NCs are suspended in solution, where tens of minutes are required for full reduction and recovery of NCs suspended in a 300 μM thick electrochemical cell.[33,70] Practical optoelectronic devices require charge/discharge times to be nearly instantaneous to the human eye (ms), and thermodynamic measurements of NC electronic properties require limited kinetic interference from processes such as diffusion. Therefore, NC chalcogenide thin films became of great interest for research into these materials.

Deposited as thin-films without post-treatment surface modification, the spectroelectrochemical charge/discharge response of CdSe NC redox processes was improved to the single minute timescale,[35] however still lacking the desired functionality. Further improvements came with post-synthetic interparticle cross-linking treatments.[57,71] NCs treated with diamine or dithiol terminated linear hydrocarbons of various lengths tether the SC NCs both to the conductive substrate, and to one another, resulting in a *semi*-ordered NC super lattice that

is conductive and permeable to charge-balancing counter-ions. Through cross-linking, the charge/discharge times improved to the ms timescale, film conductivity improved by ~3 orders of magnitude (depending on the degree of NC reduction and the specific cross-linking ligand), and the NC film assembly could be electrochemically cycled more than 10,000 times with minimal signs of degradation.[71] Cross-linking is now instrumental for NC based solar cell, field-effect transistor, and photoconductive technologies.[13,37]

In the years since the advent of NC cross-linking, various chalcogenide NC materials have been measured in this configuration including CdSe,[57,72-76] CdTe,[77,78] PbS,[79] PbSe,[80-83] as well as inter-particle electron-transfer studies of heterogeneous cross-linked NC thin films.[80,84] Indeed, modifying the electronic structure of the cross-linking ligands themselves to manipulate the NC thin film characteristics is a field in and of itself.[85] As NC cross-linking is still relatively new, however, the properties of these structures are still under investigation. One such property, the inter-particle void volume, was investigated by Houtepen and coworkers in 2013 for electrochemically reduced CdSe NCs.[73]

Figure 1.8a shows the excitonic absorption spectrum of d = 8nm CdSe NCs cross-linked with 1,8-octanediamine (8DA) in an anhydrous solution of deaerated acetonitrile with $LiClO_4$ as the electrolyte. At open circuit the NC film is nearly intrinsic, but upon step-wise application of a negative bias, the excitonic feature bleaches, and a capacitive current is recorded, both observations indicative of CB electron injection. NC CB electron injection was found to be reversible when the negative bias was removed. To quantify $\langle n \rangle$ (V), the authors modeled the excitonic absorbance spectrum (accounting for CB state-filling) at each potential step and calculated the differential relative bleach. Comparing several NC sizes in these thin films, the authors found a strong correlation between the NC size and $\langle n_{max} \rangle$. The authors hypothesized that the size dependent $\langle n_{max} \rangle$ is not intrinsic to the CdSe NCs, but instead is a result of the geometric dimensions of the inter-particle void volume within the NC thin film that limits the intercalation of CB electron charge-compensating ions. To test this hypothesis, the authors examined the effects of extrinsic factors on CdSe NC reduction, such as the size of the charge-balancing counter-ion, and the length of the cross-linking ligand. Their results are plotted in figure 1.8b and c.

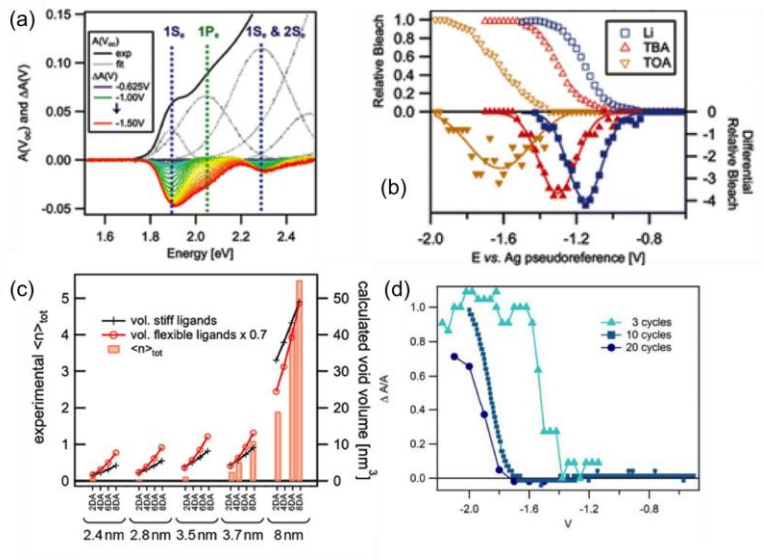

Figure 1.8. Spectroelectrochemistry of cross-linked CdSe NCs

(a) The absorption spectrum of 1,8-octanediamine-cross-linked (8DA) d = 8 nm CdSe NC (black continuous line) thin film fitted by multiple Gaussians (black dashed lines). The colored spectra show the differential absorbance upon application of an increasingly negative bias. The CB electron orbitals are indicated by vertical dashed lines. The supporting electrolyte is 0.1 M $LiClO_4$ in anhydrous acetonitrile. **(b)** Bleaching of an 8DA-linked d = 8nm CdSe NC film in acetonitrile electrolytes using cations of increasing size: from lithium (Li^+, squares) to tetrabutylammonium (TBA, upward triangles) to tetraoctylammonium (TOA, downward triangles). **(c)** Experimentally determined $<n_{max}>$ (bars) and calculated void volume assuming stiff ligands (line with crosses) and flexible ligands (line with open circles), respectively. The films are categorized by their diameter and their ligand length, the latter ranging from two (2DA) to eight (8DA) CH- units. **(d)** Potential dependent relative absorption bleach for NC films of d = 8 nm CdSe NCs with 8DA ligands, grown for three (triangles), ten (squares) and twenty (circles) layer-by-layer cycles, respectively. These data were adapted from ref. 73.

From figure 1.8b, as the size of the electron charge-compensating counter-ion increases from lithium (Li^+) to tetra-octylammonium (TOA), the onset potential for CB electron injection is shifted cathodically (negative) and the differential relative bleach profile broadens. This shift and broadening with increasing counter-ion size is consistent with a counter-ion diffusion barrier within the NC film as a result of finite void volumes. Figure 1.8c plots the dependence of $<n_{max}>$

on the ligand length for four sizes of CdSe NCs. Decreasing the length of the cross-linking chain was found to decrease $<n_{max}>$ and cathodically shift the onset potential for CB electron injection, again consistent with void-volume-limitations. In the absence of effective coulombic charge stabilization for CB electrons from solution-based cations, the CdSe NC reduction potential shifts cathodically and $<n_{max}>$ decreases. Such an effect is observed here as $<n_{max}>$ and E_F change by tuning the inter-NC-void-to-cation-size ratio. The implications of such an observation are important for understanding the spectroelectrochemical properties of NC thin films; the electron injection potential for cross-linked NC films are not strictly NC dependent, but are conflated with properties of the NC film, such as void volume. The consequences of such a conclusion are nicely illustrated by the NC film thickness dependence, plotted in figure 1.8d.

From figure 1.8d, the onset potential for CB electron injection in an otherwise identical CdSe NC thin film is shifted cathodically by ~400 mV as the film thickness increases from 3 to 20 deposition cycles (1 cycle = 1 NC monolayer addition). Changes in the slopes are also observed, where, the thinnest NC film (3 cycles) shows the steepest slope and the thickest (20 cycles) shows the flattest slope, thus altering the differential relative bleach. Conflating thin-film effects, such as inter-NC void volume, thus hinders the interpretation of electrochemical values for NC reduction in a thin film configuration.

One possible way to circumvent thin-film-induced effects such as inter-particle void volume, and isolate the electrochemical properties of the NCs themselves, is to measure NC redox potentials in the limit of one NC monolayer. Due to the small absorption cross-section of SC NCs, however, perpendicular optical transmission experiments are difficult to conduct in this limit. Instead, utilizing the electro-active substrate as an optical waveguide through attenuated total internal reflectance spectroscopy (ATR) can sidestep this limitation by providing a larger optical cross-section for a single monolayer of SC NCs. Saavedra and coworkers applied this technique to sub-monolayer thick CdSe NCs and nanorods tethered to an ITO coated ATR substrate.[86,87] Figure 1.9 shows a schematic illustration of potential modulated attenuated reflectance spectroscopy (PM-ATR) of CdSe NCs.

In this configuration, the CdSe NCs are tethered to the surface of an ITO electrode by a thiolate-terminated olifatic acid, which is pre-deposited onto an optical waveguide. Prismatic direction of the absorbance probe beam through the waveguide induces total internal reflection along the length of the substrate, and the NC absorbance is sampled several times. When the

probe beam reaches the end of the waveguide, the remaining light is detected with a photomultiplier tube, and converted into absorbance. Connected to an external potentiostat, the ITO-ATR substrate provides a conductive medium to apply an electrochemical bias to the NCs. In this particular study, the authors modulate the potential through a range of frequencies to quantify the sample impedance and consequently the electron transfer rate constants to and from the CdSe NCs.

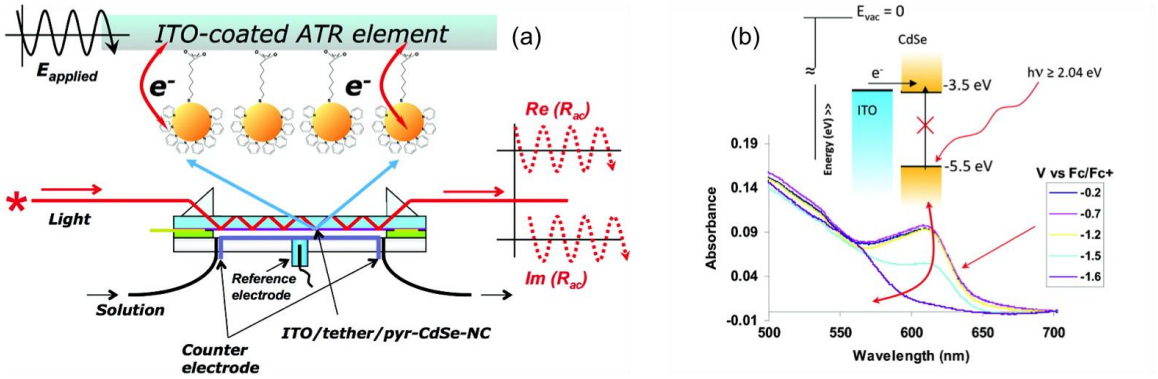

Figure 1.9. PM-ATR of monolayer thick CdSe NCs

(a) Schematic view of PM-ATR spectroelectrochemistry for monolayer-tethered NCs. Light is prism-coupled into and out of an ITO-coated waveguide, with CdSe NCs chemisorbed at the electrode/solution interface. The ITO electrode potential is modulated ±50 mV about −1.47 V vs Fc/Fc^+, which is the midpoint potential ($E_{applied}$) for reversible electron injection into the tethered NCs. The real (*Re*) and imaginary (*Im*) components of the ac portion of the electroreflectance response (R_{ac}) are monitored as a function of the modulation frequency, which is varied from 0.1 Hz to 1 kHz. **(b)** Representative ATR spectra obtained for a submonolayer film of d = 5 nm CdSe NCs adsorbed on 3-mercaptopropionic acid-modified ITO, immersed in 0.1M $TBAClO_4$/acetonitrile electrolyte, as a function of applied potential. The first excitonic transition is reversibly bleached at a midpoint potential of −1.47 V vs Fc/Fc^+ (−1.1 V vs normal hydrogen electrode (NHE)). Above the spectra is a schematic view of estimated frontier orbital energies of these 5.0 nm NCs with respect to vacuum. These data were adapted from ref. 86.

Figure 1.9b shows the absorption spectra of increasingly negatively biased CdSe NCs. At open circuit, the NC film is nearly intrinsic, but as the ITO is biased negatively, a bleach of the first excitonic absorbance becomes apparent. The authors report the value of the one electron reduction in these CdSe NCs as -1.47 V vs Fc^{+}/Fc. Importantly, this reduction potential is independent of the length of the molecular tether indicating that the measured redox potential is indeed a property of the SC NC and not the thin film architecture. Such a configuration, while complex and delicate, provides architecture-independent redox potential measurements that thicker films cannot attain.

SC NC thin film spectroelectrochemistry is indeed a powerful tool for investigating the physical properties of these materials. While not discussed in detail here, the photoluminescent properties of SC NC thin films have also been explored using spectroelectrochemistry. Electrochemical control of SC NCs immobilized onto films has enabled researchers to investigate the effects of redox active surface-states, and the non-radiative relaxation pathways both in ensemble,[32,77,78,88,89] and single particle measurements.[29,90-92] Coupling electrochemistry to PL spectroscopy has shed light onto the photophysical processes of non-equilibrium SC NCs that would otherwise be extremely difficult to probe.

Spectroelectrochemistry of SC NC thin films is an increasingly popular method of quantifying the redox potentials of NC optical and electronic properties. The fast voltammetric response coupled with the ease of measurement and device fabrication makes these configurations a popular choice for NC interrogation. However, information on the interaction of NCs with their native solution environment is lost. Questions pertaining to NC equilibria, surface reconstruction, and solvent interactions require SC NCs to remain suspended during experiment. In the following section we discuss a few examples of NC redox potential measurement of solvated NCs.

1.6 Spectroelectrochemistry of Nanocrystal Colloids.

Investigating the physical properties of SC NCs without introducing effects related to cross-linking or film deposition has proven difficult. However, several groups have devised creative methods for interrogating such properties. For example, Bard and coworkers exploited SC NC luminescence to measure their redox properties through electrochemiluminesce (ECL).[93-96] ECL relies on radiative inter-particle electron-transfer reactions between electrochemically generated reduced and oxidized NCs. Probing the NC luminescence during voltammetric sweeps thus provides a spectroscopic indication of electron injection or extraction from NCs. An example of this work is shown in figure 1.10.

Figure 1.10a plots the CV curve of colloidal CdSe NCs overlaid with the ECL curve. From the CV, no clear redox features are evident in the measured potential range as is common for colloidal SC NC CV. The ECL curve, however, shows a sharp onset in both the cathodic and anodic sweep directions. The voltage difference in the onset for ECL between the anodic and cathodic sweeps is in close agreement with the NC optical band gap, and the observation that the both anodic and cathodic voltage sweeps generate luminescence suggests that both the CB and VB are voltammetrically reduced and oxidized. From uni-directional sweeps (only generating one charged NC species) however, ECL is still generated. Because only one NC redox state (either reduced or oxidized) is generated from a uni-directional sweep, the authors speculate that under their circumstances, the annihilation mechanism that generates luminescence may arise from NCs with band-like carriers interacting with solution impurities and/or other NCs with mid-gap redox active surface states.

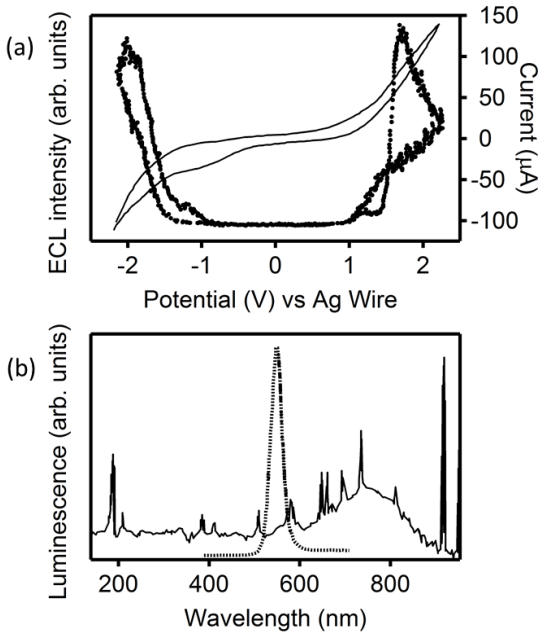

Figure 1.10. Electrochemiluminescence of collidal CdSe NCs

(a) Cyclic voltammogram (scan rate 1V/s, solid line) and ECL curve (dotted line) of CdSe NCs in 0.1M TBAP CH_2Cl_2 electrolyte. **(b)** Photoluminescence (dashed) and ECL (solid) spectra of CdSe NCs at +2.3 and – 2.3V. These data were adapted from ref. 93.

To investigate the origin of the annihilation mechanism in more detail, the authors compare the ECL spectrum with the PL spectrum, plotted in figure 1.10b. Comparing these two spectra, there is a clear red-shift in the ECL spectrum relative to the PL spectrum, leading to the conclusion that the ECL of these CdSe NCs arises from band-like carriers interacting with NC surface-states or solution impurities rather than other band-like carriers. In a follow-up study, the ECL spectrum of surface-passivated core/shell CdSe/ZnS colloidal NCs was investigated.[95] The authors found that the core/shell ECL spectrum matches closely with the excitonic PL spectrum, ruling out the possibility of solution-impurity-based annihilation mechanisms, and revealing that the bare CdSe NC ECL annihilation mechanism arises from the interaction of band-like carriers with NC surface states. Between the ECL studies on CdSe and CdSe/ZnS NCs, the authors show that the ECL signal is sensitive to the NC surface and can be used to probe the electrochemical potential of surface states as well as the electrochemical band gap. ECL studies were also carried out on colloidal CdTe[96] and Si[94] NCs, and has been found to be valuable in biological sensing applications.[97] Although ECL methods have realized some success for measuring NC redox

properties in solution, complications similar to those experienced with CV measurements arise, thus requiring alternative methods to quantify NC redox potentials.

The robust charge-transfer characteristics of semiconductor surfaces coupled with SC NCs' ability to accommodate several excess charge carriers per NC make them ideal candidates for direct chemical reduction, otherwise known as remote chemical doping.[24] Indeed some of the earliest accounts of carrier introduction into SC NCs involved chemical reduction.[46,98] When molecular species with a well-defined redox couple and colloidal NCs are mixed together, a redox-equilibrium is established. This equilibrium can be described by the Nernst equation to ascertain the electrochemical potential of band-like carriers in colloidal SC NCs. Though this method lacks the convenience of a potentiostat, it supplants the need for making NC/electrode contact thus bypassing several difficulties associated with NC voltammetry. An example of this technique from the Klimov group is shown in figure 1.11 where PbSe and PbS NCs are chemically reduced using solvated cobaltocene (Cp_2Co).[99]

Figure 1.11a shows absorption spectra for a size-series of colloidal PbSe NCs with and without Cp_2Co. Without Cp_2Co, the absorbance of the NCs indicates that all of the PbSe NCs are nearly intrinsic, but when Cp_2Co is added to the solution, a bleach of the excitonic transition becomes apparent, indicative of electron injection. For a given Cp_2Co/NC ratio, the magnitude of this bleach is proportional to NC size. A full bleach of the 8-fold degenerate $1S_e$ state is apparent for the largest PbSe NC sample (d = 7.9 nm), and no bleach is observed for the smallest PbSe NCs (d = 2.7nm). The authors invoke quantum confinement as the limiting factor for electron accumulation in PbSe of different sizes. Figure 1.11b plots the experimentally determined conduction band-edge potential as a function of NC size,[16] as well as the redox potential of Cp_2Co. Plotted in this manner, the data in figure 1.11a follow the expected trend for size-limited equilibrium charge injection into PbSe NCs.

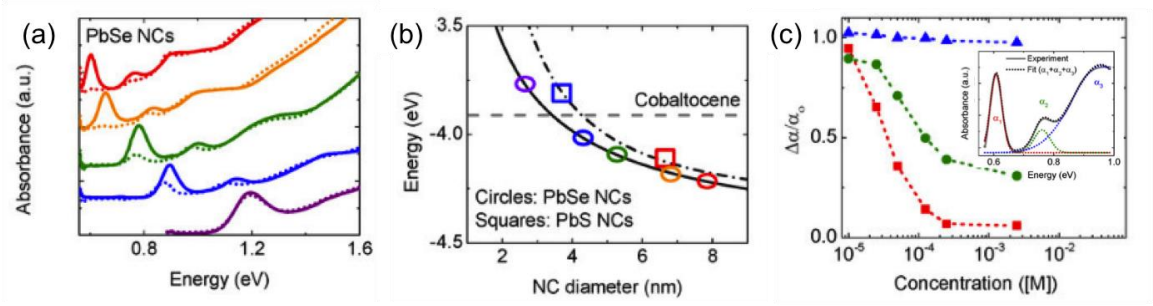

Figure 1.11. Equilibrium charge injection into PbSe NCs

(a) PbSe NC-size dependent electronic absorption spectra before (solid lines) and after (dashed lines) treatment with cobaltocene; color-coding matches that in panel b. **(b)** The redox potential of cobaltocene (dashed gray line) in comparison to the conduction band states in PbSe (solid black line) and PbS (dashed-dotted black line) NCs. The colored ovals correspond to the samples from panel a. **(c)** Normalized absorption intensity $\Delta\alpha_i/\alpha_i$ (i = 1, 2, 3) in each transition (α_1: red squares; α_2: green circles; α_3: blue triangles) for PbSe NCs as a function of the cobaltocene concentration. Inset: PbSe NC absorbance spectrum deconvoluted into individual NC transitions (α_1, α_2, and α_3). These data were adapted from ref. 99.

To gain deeper insight into the effects of equilibrium charge injection, the authors carried out an analysis of the Cp_2Co/NC concentration dependence. Figure 1.11c plots the spectrally deconvoluted PbSe NC excitonic bleach fraction for the three lowest energy transitions ($\Delta\alpha_n/\alpha_0$ n = transition number 1,2,3) as a function of the Cp_2Co concentration. From figure 1.11c $\Delta\alpha_1/\alpha_0$ shows a strong dependence on the Cp_2Co concentration between 10 μM and 100 μM where this transition is near completely bleached at 100 μM. $\Delta\alpha_2/\alpha_0$ follows the same trajectory as $\Delta\alpha_1/\alpha_0$, but saturates at $\Delta\alpha_2/\alpha_0 = 0.5$. The authors argue that $\Delta\alpha_2/\alpha_0$ derives a portion of its absorption intensity from the $1P_h \rightarrow 1S_e$ transition, thus electrons occupying the $1S_e$ orbital partially block the α_2 transition. The highest order optical transition measured, $\Delta\alpha_3/\alpha_0$, shows little or no dependence on the Cp_2Co concentration indicating that the $1P_e$ orbitals are indeed electron vacant. Thus all CB electrons reside in the $1S_e$ states, lending credence to the argument that the α_2 spectral feature is composed of more than one electronic transition.

While the authors do not carry out a detailed analysis on the change in E_F as a function of increasing $\langle n \rangle$, E_F may be estimated from their data. For the d = 7.9nm PbSe NCs, $\langle n_{max} \rangle$

occurs at a Cp_2Co/Cp_2Co^+ ratio of ~100:1. Using the Nernst equation ($E_F = E^0 - 0.0257* \ln [Cp_2Co/Cp_2Co^+]$ and E^0 = -1.33V vs Fc^+/Fc[100]) we estimate that E_F ~ -1.31V vs Fc^+/Fc when $\langle n \rangle = 8$, whereas E_F = -1.28 V at $\langle n \rangle = 1$, resulting in an observed change of 30 mV between $\langle n \rangle = 1$ and $\langle n \rangle = 8$. Indeed, a 30mV range for a full $1S_e$ bleach is much less then that observed on NC cross-linked films,[81,82] but this difference may be related to film-induced void-size limitations as discussed above. Similar discrepancies in the potential of sequential electron injection have been observed in ZnO NCs between colloids[60,101] and thin films.[49,52] Comparison of NC redox potentials between colloids and thin films thus requires further exploration to reconcile these observations.

Spectroelectrochemical measurements of colloidal NCs are still a relatively unexplored field, and may offer an alternative to the thin film configuration for investigating the redox properties of SC NCs. For developing fields such as NC solar photocatalysis, colloidal NC redox potentials are of great interest. A portion of this thesis is dedicated to the spectroelectrochemical investigation of colloidal SC NCs.

1.7 Conclusions

Spectroelectrochemistry of semiconductor nanocrystals is a powerful technique for elucidating the physical properties of this class of materials. With comparative instrumental ease, spectroelectrochemical measurements offer information similar to vacuum ionization measurements, but in a more flexible manner. The ability to perturb E_F through an external bias while monitoring the spectroscopic properties of the SC NCs provides researchers the ability to probe these materials under many different experimental conditions. Currently, however, it is unclear if the measured properties of NCs immobilized onto thin films translate to those suspended in solution. This thesis will examine the electrochemical properties of *n*-type SC NCs suspended in solution, as well as introduce new methods for the perturbation and detection of NC E_F without the use of an external electrochemical bias.

1.8 References

(1) Murray, C. B.; Norris, D. J.; Bawendi, M. G. Synthesis and characterization of nearly monodisperse CdE (E = sulfur, selenium, tellurium) semiconductor nanocrystallites. *J. Am. Chem. Soc.* **1993**, *115*, 8706-8715.

(2) Hines, M. A.; Guyot-Sionnest, P. Synthesis and Characterization of Strongly Luminescing ZnS-Capped CdSe Nanocrystals. *J. Phys. Chem.* **1996**, *100*, 468-471.

(3) Peng, Z. A.; Peng, X. Formation of High-Quality CdTe, CdSe, and CdS Nanocrystals Using CdO as Precursor. *J. Am. Chem. Soc.* **2001**, *123*, 183-184.

(4) Han, Z.; Qiu, F.; Eisenberg, R.; Holland, P. L.; Krauss, T. D. Robust Photogeneration of H2 in Water Using Semiconductor Nanocrystals and a Nickel Catalyst. *Science* **2012**, *338*, 1321-1324.

(5) Han, Z.; Eisenberg, R. Fuel from Water: The Photochemical Generation of Hydrogen from Water. *Accounts of Chemical Research* **2014**, *47*, 2537-2544.

(6) Brown, K. A.; Harris, D. F.; Wilker, M. B.; Rasmussen, A.; Khadka, N.; Hamby, H.; Keable, S.; Dukovic, G.; Peters, J. W.; Seefeldt, L. C.; King, P. W. Light-driven dinitrogen reduction catalyzed by a CdS:nitrogenase MoFe protein biohybrid. *Science* **2016**, *352*, 448-450.

(7) Boles, M. A.; Ling, D.; Hyeon, T.; Talapin, D. V. The surface science of nanocrystals. *Nat Mater* **2016**, *15*, 141-153.

(8) Ning, Z.; Voznyy, O.; Pan, J.; Hoogland, S.; Adinolfi, V.; Xu, J.; Li, M.; Kirmani, A. R.; Sun, J.-P.; Minor, J.; Kemp, K. W.; Dong, H.; Rollny, L.; Labelle, A.; Carey, G.; Sutherland, B.; Hill, I.; Amassian, A.; Liu, H.; Tang, J.; Bakr, O. M.; Sargent, E. H. Air-stable n-type colloidal quantum dot solids. *Nat Mater* **2014**, *13*, 822-828.

(9) Brown, P. R.; Kim, D.; Lunt, R. R.; Zhao, N.; Bawendi, M. G.; Grossman, J. C.; Bulović, V. Energy Level Modification in Lead Sulfide Quantum Dot Thin Films through Ligand Exchange. *ACS Nano* **2014**, *8*, 5863-5872.

(10) Carey, G. H.; Abdelhady, A. L.; Ning, Z.; Thon, S. M.; Bakr, O. M.; Sargent, E. H. Colloidal Quantum Dot Solar Cells. *Chemical Reviews* **2015**, *115*, 12732-12763.

(11) Kamat, P. V.; Tvrdy, K.; Baker, D. R.; Radich, J. G. Beyond Photovoltaics: Semiconductor Nanoarchitectures for Liquid-Junction Solar Cells. *Chem. Rev.* **2010**, *110*, 6664-6688.

(12) Oszajca, M. F.; Bodnarchuk, M. I.; Kovalenko, M. V. Precisely Engineered Colloidal Nanoparticles and Nanocrystals for Li-Ion and Na-Ion Batteries: Model Systems or Practical Solutions? *Chemistry of Materials* **2014**, *26*, 5422-5432.

(13) Talapin, D. V.; Lee, J.-S.; Kovalenko, M. V.; Shevchenko, E. V. Prospects of Colloidal Nanocrystals for Electronic and Optoelectronic Applications. *Chemical Reviews* **2010**, *110*, 389-458.

(14) Amelia, M.; Lincheneau, C.; Silvi, S.; Credi, A. Electrochemical properties of CdSe and CdTe quantum dots. *Chemical Society Reviews* **2012**, *41*, 5728-5743.

(15) Swart, I.; Liljeroth, P.; Vanmaekelbergh, D. Scanning probe microscopy and spectroscopy of colloidal semiconductor nanocrystals and assembled structures. *Chemical Reviews* **2016**.

(16) Jasieniak, J.; Califano, M.; Watkins, S. E. Size-Dependent Valence and Conduction Band-Edge Energies of Semiconductor Nanocrystals. *ACS Nano* **2011**, *5*, 5888-5902.

(17) Munro, A. M.; Zacher, B.; Graham, A.; Armstrong, N. R. Photoemission Spectroscopy of Tethered CdSe Nanocrystals: Shifts in Ionization Potential and Local Vacuum Level As a Function of Nanocrystal Capping Ligand. *ACS Applied Materials & Interfaces* **2010**, *2*, 863-869.

(18) Kucur, E.; Riegler, J.; Urban, G. A.; Nann, T. Determination of quantum confinement in CdSe nanocrystals by cyclic voltammetry. *The Journal of Chemical Physics* **2003**, *119*, 2333-2337.

(19) Inamdar, S. N.; Ingole, P. P.; Haram, S. K. Determination of Band Structure Parameters and the Quasi-Particle Gap of CdSe Quantum Dots by Cyclic Voltammetry. *ChemPhysChem* **2008**, *9*, 2574-2579.

(20) Amelia, M.; Impellizzeri, S.; Monaco, S.; Yildiz, I.; Silvi, S.; Raymo, F. M.; Credi, A. Structural and Size Effects on the Spectroscopic and Redox Properties of CdSe Nanocrystals in Solution: The Role of Defect States. *ChemPhysChem* **2011**, *12*, 2280-2288.

(21) Impellizzeri, S.; Monaco, S.; Yildiz, I.; Amelia, M.; Credi, A.; Raymo, F. M. Structural Implications on the Electrochemical and Spectroscopic Signature of CdSe-ZnS Core−Shell Quantum Dots. *The Journal of Physical Chemistry C* **2010**, *114*, 7007-7013.

(22) Reiss, H. The Fermi level and the redox potential. *J. Phys. Chem.* **1985**, *89*, 3783-3791.

(23) Khan, S. U. M.; Kainthla, R. C.; Bockris, J. O. M. The redox potential and the Fermi level in solution. *J. Phys. Chem.* **1987**, *91*, 5974-5977.

(24) Schimpf, A. M.; Knowles, K. E.; Carroll, G. M.; Gamelin, D. R. Electronic Doping and Redox-Potential Tuning in Colloidal Semiconductor Nanocrystals. *Accounts of Chemical Research* **2015**, *48*, 1929-1937.

(25) Rinehart, J. D.; Schimpf, A. M.; Weaver, A. L.; Cohn, A. W.; Gamelin, D. R. Photochemical Electronic Doping of Colloidal CdSe Nanocrystals. *Journal of the American Chemical Society* **2013**, *135*, 18782-18785.

(26) Cohn, A. W.; Rinehart, J. D.; Schimpf, A. M.; Weaver, A. L.; Gamelin, D. R. Size Dependence of Negative Trion Auger Recombination in Photodoped CdSe Nanocrystals. *Nano Letters* **2014**, *14*, 353-358.

(27) Ekimov, A. I.; Hache, F.; Schanne-Klein, M. C.; Ricard, D.; Flytzanis, C.; Kudryavtsev, I. A.; Yazeva, T. V.; Rodina, A. V.; Efros, A. L. Absorption and intensity-dependent photoluminescence measurements on CdSe quantum dots: assignment of the first electronic transitions. *J. Opt. Soc. Am. B* **1993**, *10*, 100-107.

(28) Shim, M.; Wang, C.; Guyot-Sionnest, P. Charge-Tunable Optical Properties in Colloidal Semiconductor Nanocrystals. *J. Phys. Chem. B* **2001**, *105*, 2369-2373.

(29) Jha, P. P.; Guyot-Sionnest, P. Trion Decay in Colloidal Quantum Dots. *ACS Nano* **2009**, *3*, 1011-1015.

(30) Klimov, V. I.; Mikhailovsky, A. A.; McBranch, D. W.; Leatherdale, C. A.; Bawendi, M. G. Quantization of Multiparticle Auger Rates in Semiconductor Quantum Dots. *Science* **2000**, *287*, 1011-1013.

(31) Rinehart, J. D.; Weaver, A. L.; Gamelin, D. R. Redox Brightening of Colloidal Semiconductor Nanocrystals Using Molecular Reductants. *Journal of the American Chemical Society* **2012**, *134*, 16175-16177.

(32) Weaver, A. L.; Gamelin, D. R. Photoluminescence Brightening via Electrochemical Trap Passivation in ZnSe and Mn2+-Doped ZnSe Quantum Dots. *Journal of the American Chemical Society* **2012**, *134*, 6819-6825.

(33) Wang, C.; Shim, M.; Guyot-Sionnest, P. Electrochromic Nanocrystal Quantum Dots. *Science* **2001**, *291*, 2390-2392.

(34) Brus, L. E. A simple model for the ionization potential, electron affinity, and aqueous redox potentials of small semiconductor crystallites. *The Journal of Chemical Physics* **1983**, *79*, 5566-5571.

(35) Wang, C.; Shim, M.; Guyot-Sionnest, P. Electrochromic semiconductor nanocrystal films. *Applied Physics Letters* **2002**, *80*, 4-6.

(36) Vanmaekelbergh, D. Self-assembly of colloidal nanocrystals as route to novel classes of nanostructured materials. *Nano Today* **2011**, *6*, 419-437.

(37) Kovalenko, M. V.; Manna, L.; Cabot, A.; Hens, Z.; Talapin, D. V.; Kagan, C. R.; Klimov, V. I.; Rogach, A. L.; Reiss, P.; Milliron, D. J.; Guyot-Sionnnest, P.; Konstantatos, G.; Parak, W. J.; Hyeon, T.; Korgel, B. A.; Murray, C. B.; Heiss, W. Prospects of Nanoscience with Nanocrystals. *ACS Nano* **2015**, *9*, 1012-1057.

(38) Kamat, P. V. Quantum Dot Solar Cells. Semiconductor Nanocrystals as Light Harvesters. *The Journal of Physical Chemistry C* **2008**, *112*, 18737-18753.

(39) Hillhouse, H. W.; Beard, M. C. Solar cells from colloidal nanocrystals: Fundamentals, materials, devices, and economics. *Current Opinion in Colloid & Interface Science* **2009**, *14*, 245-259.

(40) Snyder, G. J.; Toberer, E. S. Complex thermoelectric materials. *Nat Mater* **2008**, *7*, 105-114.

(41) Emin, S.; Singh, S. P.; Han, L.; Satoh, N.; Islam, A. Colloidal quantum dot solar cells. *Solar Energy* **2011**, *85*, 1264-1282.

(42) Runnerstrom, E. L.; Llordes, A.; Lounis, S. D.; Milliron, D. J. Nanostructured electrochromic smart windows: traditional materials and NIR-selective plasmonic nanocrystals. *Chemical Communications* **2014**, *50*, 10555-10572.

(43) Shirasaki, Y.; Supran, G. J.; Bawendi, M. G.; Bulovic, V. Emergence of colloidal quantum-dot light-emitting technologies. *Nat Photon* **2013**, *7*, 13-23.

(44) Hetsch, F.; Zhao, N.; Kershaw, S. V.; Rogach, A. L. Quantum dot field effect transistors. *Materials Today* **2013**, *16*, 312-325.

(45) Murray, C. B.; Kagan, C. R.; Bawendi, M. G. Self-Organization of CdSe Nanocrystallites into Three-Dimensional Quantum Dot Superlattices. *Science* **1995**, *270*, 1335-1338.

(46) Henglein, A. Small-particle research: physicochemical properties of extremely small colloidal metal and semiconductor particles. *Chemical Reviews* **1989**, *89*, 1861-1873.

(47) Hoyer, P.; Weller, H. Potential-Dependent Electron Injection in Nanoporous Colloidal ZnO Films. *The Journal of Physical Chemistry* **1995**, *99*, 14096-14100.

(48) Vanmaekelbergh, D.; Liljeroth, P. Electron-conducting quantum dot solids: novel materials based on colloidal semiconductor nanocrystals. *Chemical Society Reviews* **2005**, *34*, 299-312.

(49) Roest, A. L.; Kelly, J. J.; Vanmaekelbergh, D.; Meulenkamp, E. A. Staircase in the Electron Mobility of a ZnO Quantum Dot Assembly due to Shell Filling. *Physical Review Letters* **2002**, *89*, 036801.

(50) Germeau, A.; Roest, A. L.; Vanmaekelbergh, D.; Allan, G.; Delerue, C.; Meulenkamp, E. A. Optical Transitions in Artificial Few-Electron Atoms Strongly Confined inside ZnO Nanocrystals. *Physical Review Letters* **2003**, *90*, 097401.

(51) Roest, A. L.; Germeau, A.; Kelly, J. J.; Vanmaekelbergh, D.; Allan, G.; Meulenkamp, E. A. Long-Range Transport in an Assembly of ZnO Quantum Dots: The Effects of Quantum Confinement, Coulomb Repulsion and Structural Disorder. *ChemPhysChem* **2003**, *4*, 959-966.

(52) Roest, A. L.; Kelly, J. J.; Vanmaekelbergh, D. Coulomb blockade of electron transport in a ZnO quantum-dot solid. *Applied Physics Letters* **2003**, *83*, 5530-5532.

(53) Roest, A. L.; Houtepen, A. J.; Kelly, J. J.; Vanmaekelbergh, D. Electron-conducting quantum-dot solids with ionic charge compensation. *Faraday Discussions* **2004**, *125*, 55-62.

(54) Vanmaekelbergh, D.; Houtepen, A. J.; Kelly, J. J. Electrochemical gating: A method to tune and monitor the (opto)electronic properties of functional materials. *Electrochimica Acta* **2007**, *53*, 1140-1149.

(55) Shim, M.; Guyot-Sionnest, P. Comment on ``Staircase in the Electron Mobility of a ZnO Quantum Dot Assembly due to Shell Filling'' and ``Optical Transitions in Artificial Few-Electron Atoms Strongly Confined inside ZnO Nanocrystals''. *Physical Review Letters* **2003**, *91*, 169703.

(56) Vanmaekelbergh, D.; Roest, A. L.; Germeau, A.; Kelly, J. J.; Meulenkamp, E. A.; Allan, G.; Delerue, C. Vanmaekelbergh \textit{et al.} Reply. *Physical Review Letters* **2003**, *91*, 169704.

(57) Yu, D.; Wang, C.; Guyot-Sionnest, P. n-Type Conducting CdSe Nanocrystal Solids. *Science* **2003**, *300*, 1277-1280.

(58) Valdez, C. N.; Braten, M.; Soria, A.; Gamelin, D. R.; Mayer, J. M. Effect of Protons on the Redox Chemistry of Colloidal Zinc Oxide Nanocrystals. *Journal of the American Chemical Society* **2013**, *135*, 8492-8495.

(59) Schimpf, A. M.; Gunthardt, C. E.; Rinehart, J. D.; Mayer, J. M.; Gamelin, D. R. Controlling Carrier Densities in Photochemically Reduced Colloidal ZnO Nanocrystals: Size Dependence and Role of the Hole Quencher. *Journal of the American Chemical Society* **2013**, *135*, 16569-16577.

(60) Carroll, G. M.; Schimpf, A. M.; Tsui, E. Y.; Gamelin, D. R. Redox Potentials of Colloidal n-Type ZnO Nanocrystals: Effects of Confinement, Electron Density, and Fermi-Level Pinning by Aldehyde Hydrogenation. *Journal of the American Chemical Society* **2015**, *137*, 11163-11169.

(61) Schrauben, J. N.; Hayoun, R.; Valdez, C. N.; Braten, M.; Fridley, L.; Mayer, J. M. Titanium and Zinc Oxide Nanoparticles Are Proton-Coupled Electron Transfer Agents. *Science* **2012**, *336*, 1298-1301.

(62) Schimpf, A. M.; Thakkar, N.; Gunthardt, C. E.; Masiello, D. J.; Gamelin, D. R. Charge-Tunable Quantum Plasmons in Colloidal Semiconductor Nanocrystals. *ACS Nano* **2014**, *8*, 1065-1072.

(63) Krishnan, R.: Fundamentals of Semiconductor Electrochemistry and Photoelectrochemistry. In *Encyclopedia of Electrochemistry*; Wiley-VCH Verlag GmbH & Co. KGaA, 2007.

(64) Peter, L. M. Dye-sensitized nanocrystalline solar cells. *Physical Chemistry Chemical Physics* **2007**, *9*, 2630-2642.

(65) Garcia, G.; Buonsanti, R.; Runnerstrom, E. L.; Mendelsberg, R. J.; Llordes, A.; Anders, A.; Richardson, T. J.; Milliron, D. J. Dynamically Modulating the Surface Plasmon Resonance of Doped Semiconductor Nanocrystals. *Nano Letters* **2011**, *11*, 4415-4420.

(66) zum Felde, U.; Haase, M.; Weller, H. Electrochromism of Highly Doped Nanocrystalline SnO2:Sb. *The Journal of Physical Chemistry B* **2000**, *104*, 9388-9395.

(67) Garcia, G.; Buonsanti, R.; Llordes, A.; Runnerstrom, E. L.; Bergerud, A.; Milliron, D. J. Near-Infrared Spectrally Selective Plasmonic Electrochromic Thin Films. *Advanced Optical Materials* **2013**, *1*, 215-220.

(68) Mattox, T. M.; Bergerud, A.; Agrawal, A.; Milliron, D. J. Influence of Shape on the Surface Plasmon Resonance of Tungsten Bronze Nanocrystals. *Chem. Mater.* **2014**, *26*, 1779-1784.

(69) De Trizio, L.; Buonsanti, R.; Schimpf, A. M.; Llordes, A.; Gamelin, D. R.; Simonutti, R.; Milliron, D. J. Nb-Doped Colloidal TiO2 Nanocrystals with Tunable Infrared Absorption. *Chem. Mater.* **2013**, *25*, 3383-3390.

(70) Guyot-Sionnest, P. Charging colloidal quantum dots by electrochemistry. *Microchimica Acta* **2008**, *160*, 309-314.

(71) Guyot-Sionnest, P.; Wang, C. Fast Voltammetric and Electrochromic Response of Semiconductor Nanocrystal Thin Films. *The Journal of Physical Chemistry B* **2003**, *107*, 7355-7359.

(72) Jarosz, M. V.; Porter, V. J.; Fisher, B. R.; Kastner, M. A.; Bawendi, M. G. Photoconductivity studies of treated CdSe quantum dot films exhibiting increased exciton ionization efficiency. *Physical Review B* **2004**, *70*, 195327.

(73) Boehme, S. C.; Wang, H.; Siebbeles, L. D. A.; Vanmaekelbergh, D.; Houtepen, A. J. Electrochemical Charging of CdSe Quantum Dot Films: Dependence on Void Size and Counterion Proximity. *ACS Nano* **2013**, *7*, 2500-2508.

(74) Talgorn, E.; Moysidou, E.; Abellon, R. D.; Savenije, T. J.; Goossens, A.; Houtepen, A. J.; Siebbeles, L. D. A. Highly Photoconductive CdSe Quantum-Dot Films: Influence of Capping Molecules and Film Preparation Procedure. *The Journal of Physical Chemistry C* **2010**, *114*, 3441-3447.

(75) Houtepen, A. J.; Vanmaekelbergh, D. Orbital Occupation in Electron-Charged CdSe Quantum-Dot Solids. *The Journal of Physical Chemistry B* **2005**, *109*, 19634-19642.

(76) Querner, C.; Reiss, P.; Sadki, S.; Zagorska, M.; Pron, A. Size and ligand effects on the electrochemical and spectroelectrochemical responses of CdSe nanocrystals. *Physical Chemistry Chemical Physics* **2005**, *7*, 3204-3209.

(77) Boehme, S. C.; Azpiroz, J. M.; Aulin, Y. V.; Grozema, F. C.; Vanmaekelbergh, D.; Siebbeles, L. D. A.; Infante, I.; Houtepen, A. J. Density of Trap States and Auger-mediated Electron Trapping in CdTe Quantum-Dot Solids. *Nano Letters* **2015**, *15*, 3056-3066.

(78) Jin, L.; Shang, L.; Zhai, J.; Li, J.; Dong, S. Fluorescence Spectroelectrochemistry of Multilayer Film Assembled CdTe Quantum Dots Controlled by Applied Potential in Aqueous Solution. *The Journal of Physical Chemistry C* **2010**, *114*, 803-807.

(79) André, A.; Zherebetskyy, D.; Hanifi, D.; He, B.; Samadi Khoshkhoo, M.; Jankowski, M.; Chassé, T.; Wang, L.-W.; Schreiber, F.; Salleo, A.; Liu, Y.; Scheele, M. Toward Conductive Mesocrystalline Assemblies: PbS Nanocrystals Cross-Linked with Tetrathiafulvalene Dicarboxylate. *Chem. Mater.* **2015**, *27*, 8105-8115.

(80) Boehme, S. C.; Vanmaekelbergh, D.; Evers, W. H.; Siebbeles, L. D. A.; Houtepen, A. J. In Situ Spectroelectrochemical Determination of Energy Levels and Energy Level

Offsets in Quantum-Dot Heterojunctions. *The Journal of Physical Chemistry C* **2016**, *120*, 5164-5173.

(81) Wehrenberg, B. L.; Guyot-Sionnest, P. Electron and Hole Injection in PbSe Quantum Dot Films. *Journal of the American Chemical Society* **2003**, *125*, 7806-7807.

(82) Wehrenberg, B. L.; Yu, D.; Ma, J.; Guyot-Sionnest, P. Conduction in Charged PbSe Nanocrystal Films. *The Journal of Physical Chemistry B* **2005**, *109*, 20192-20199.

(83) Luther, J. M.; Law, M.; Song, Q.; Perkins, C. L.; Beard, M. C.; Nozik, A. J. Structural, optical, and electrical properties of self-assembled films of PbSe nanocrystals treated with 1, 2-ethanedithiol. *ACS nano* **2008**, *2*, 271-280.

(84) Boehme, S. C.; Walvis, T. A.; Infante, I.; Grozema, F. C.; Vanmaekelbergh, D.; Siebbeles, L. D. A.; Houtepen, A. J. Electrochemical Control over Photoinduced Electron Transfer and Trapping in CdSe-CdTe Quantum-Dot Solids. *ACS Nano* **2014**, *8*, 7067-7077.

(85) Scheele, M.; Brutting, W.; Schreiber, F. Coupled organic-inorganic nanostructures (COIN). *Phys. Chem. Chem. Phys.* **2015**, *17*, 97-111.

(86) Araci, Z. O.; Shallcross, C. R.; Armstrong, N. R.; Saavedra, S. S. Potential-Modulated Attenuated Total Reflectance Characterization of Charge Injection Processes in Monolayer-Tethered CdSe Nanocrystals. *The Journal of Physical Chemistry Letters* **2010**, *1*, 1900-1905.

(87) Ehamparam, R.; Pavlopoulos, N. G.; Liao, M. W.; Hill, L. J.; Armstrong, N. R.; Pyun, J.; Saavedra, S. S. Band Edge Energetics of Heterostructured Nanorods: Photoemission Spectroscopy and Waveguide Spectroelectrochemistry of Au-Tipped CdSe Nanorod Monolayers. *ACS Nano* **2015**, *9*, 8786-8800.

(88) Gooding, A. K.; Gómez, D. E.; Mulvaney, P. The Effects of Electron and Hole Injection on the Photoluminescence of CdSe/CdS/ZnS Nanocrystal Monolayers. *ACS Nano* **2008**, *2*, 669-676.

(89) Brovelli, S.; Galland, C.; Viswanatha, R.; Klimov, V. I. Tuning Radiative Recombination in Cu-Doped Nanocrystals via Electrochemical Control of Surface Trapping. *Nano Letters* **2012**, *12*, 4372-4379.

(90) Galland, C.; Ghosh, Y.; Steinbruck, A.; Sykora, M.; Hollingsworth, J. A.; Klimov, V. I.; Htoon, H. Two types of luminescence blinking revealed by spectroelectrochemistry of single quantum dots. *Nature* **2011**, *479*, 203-207.

(91) Qin, W.; Liu, H.; Guyot-Sionnest, P. Small Bright Charged Colloidal Quantum Dots. *ACS Nano* **2014**, *8*, 283-291.

(92) Jha, P. P.; Guyot-Sionnest, P. Electrochemical Switching of the Photoluminescence of Single Quantum Dots. *The Journal of Physical Chemistry C* **2010**, *114*, 21138-21141.

(93) Myung, N.; Ding, Z.; Bard, A. J. Electrogenerated Chemiluminescence of CdSe Nanocrystals. *Nano Letters* **2002**, *2*, 1315-1319.

(94) Ding, Z.; Quinn, B. M.; Haram, S. K.; Pell, L. E.; Korgel, B. A.; Bard, A. J. Electrochemistry and Electrogenerated Chemiluminescence from Silicon Nanocrystal Quantum Dots. *Science* **2002**, *296*, 1293-1297.

(95) Myung, N.; Bae, Y.; Bard, A. J. Effect of Surface Passivation on the Electrogenerated Chemiluminescence of CdSe/ZnSe Nanocrystals. *Nano Letters* **2003**, *3*, 1053-1055.

(96) Bae, Y.; Myung, N.; Bard, A. J. Electrochemistry and Electrogenerated Chemiluminescence of CdTe Nanoparticles. *Nano Letters* **2004**, *4*, 1153-1161.

(97) Zhao, W.-W.; Wang, J.; Zhu, Y.-C.; Xu, J.-J.; Chen, H.-Y. Quantum Dots: Electrochemiluminescent and Photoelectrochemical Bioanalysis. *Analytical Chemistry* **2015**, *87*, 9520-9531.

(98) Shim, M.; Guyot-Sionnest, P. n-type colloidal semiconductor nanocrystals. *Nature* **2000**, *407*, 981-983.

(99) Koh, W.-k.; Koposov, A. Y.; Stewart, J. T.; Pal, B. N.; Robel, I.; Pietryga, J. M.; Klimov, V. I. Heavily doped n-type PbSe and PbS nanocrystals using ground-state charge transfer from cobaltocene. *Scientific Reports* **2013**, *3*, 2004.

(100) Connelly, N. G.; Geiger, W. E. Chemical Redox Agents for Organometallic Chemistry. *Chemical Reviews* **1996**, *96*, 877-910.

(101) Valdez, C. N.; Schimpf, A. M.; Gamelin, D. R.; Mayer, J. M. Proton-Controlled Reduction of ZnO Nanocrystals: Effects of Molecular Reductants, Cations, and Thermodynamic Limitations. *Journal of the American Chemical Society* **2016**, *138*, 1377-1385.

Chapter 2. Redox Potentials of Colloidal *n*-Type ZnO Nanocrystals: Effects of Confinement, Electron Density, and Fermi-Level Pinning by Aldehyde Hydrogenation

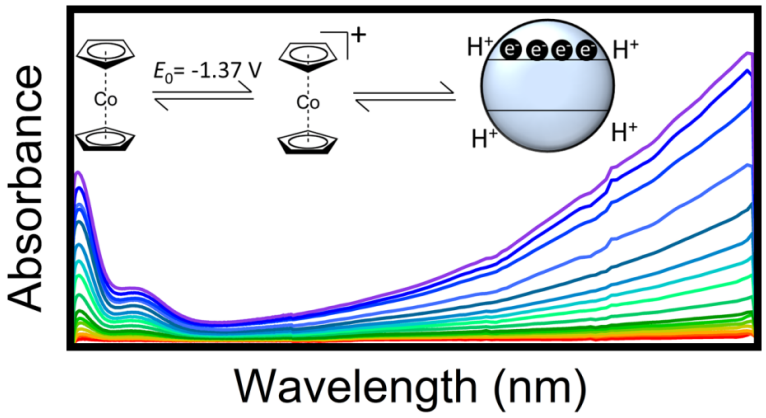

Adapted from: Carroll, G. M.; Schimpf, A. M.; Tsui, E. Y.; Gamelin, D. R. *J. Am. Chem. Soc.* **2015**, *137*, 11163.

2.1 Overview

Electronically doped colloidal semiconductor nanocrystals offer valuable opportunities to probe the new physical and chemical properties imparted by their excess charge carriers. Photodoping is a powerful approach to introducing and controlling free carrier densities within free-standing colloidal semiconductor nanocrystals. Photoreduced (*n*-type) colloidal ZnO nanocrystals possessing delocalized conduction-band (CB) electrons can be formed by photochemical oxidation of EtOH. Previous studies of this chemistry have demonstrated photochemical electron accumulation, in some cases reaching as many as >100 electrons per ZnO nanocrystal, but in every case examined to date this chemistry maximizes at a well-defined average electron density of $\langle N_{max} \rangle$ = ~1.4 ± 0.4 × 10^{20} cm^{-3}. The origins of this maximum have never been identified. Here, we use a solvated redox indicator for *in situ* determination of reduced ZnO nanocrystal redox potentials. The Fermi levels of various photodoped ZnO nanocrystals possessing on average just one excess CB electron show quantum-confinement effects, as expected, but are >600 meV lower than those of the same ZnO nanocrystals reduced

chemically using Cp^*_2Co, reflecting important differences between their charge-compensating cations. Upon photochemical electron accumulation, the Fermi levels become independent of nanocrystal volume at $\langle N \rangle$ above ~2×10^{19} cm^{-3}, and maximize at $\langle N_{max} \rangle$ = ~$1.6 \pm 0.3 \times 10^{20}$ cm^{-3}. This maximum is proposed to arise from Fermi-level pinning by the two-electron two-proton hydrogenation of acetaldehyde, which reverses the EtOH photooxidation reaction.

2.2 Introduction

Photodoping offers a convenient method for tuning carrier densities in colloidal semiconductor nanocrystals. Photochemical *n*-doping to yield excess delocalized band-like electrons has been studied for a variety of colloidal nanocrystals including ZnO,[1-6] In_2O_3,[7] and CdE (E = S, Se, Te),[8] and with a variety of hole quenchers.[6] The most thoroughly investigated system has been colloidal ZnO nanocrystals reduced using ethanol (EtOH) as the hole quencher.[1,3-6] Upon nanocrystal photoexcitation, an electron is excited from the valence band (VB) to the conduction band (CB). The photogenerated hole is then quenched within picoseconds,[9] leaving the electron in the ZnO CB. EtOH oxidation liberates protons (H^+) that compensate the CB electron charges, with acetaldehyde as the two-electron two-proton oxidation product[10,11] according to the stoichiometry of eq 2.1.

$$ZnO + \tfrac{1}{2}\, CH_3CH_2OH \xrightarrow{h\nu} e^-_{CB}{:}ZnO\text{-}H^+ + \tfrac{1}{2}\, CH_3CHO \qquad \text{(Equation 2.1)}$$

In this system, multiple delocalized CB electrons per ZnO nanocrystal can be accumulated photochemically, with the average ($\langle n \rangle$) reaching as high as >100 in some cases.[6] Under rigorously anaerobic conditions, the CB electrons are stable after terminating the nanocrystal photoexcitation,[5] making these *n*-doped ZnO nanocrystals well suited for further spectroscopic or chemical investigations. The average maximum number of electrons per nanocrystal ($\langle n_{max} \rangle$) was found to be proportional to nanocrystal volume, such that the average maximum electron *density* is constant for all sizes at $\langle N_{max} \rangle$ = ~1.4×10^{20} cm^{-3} for ZnO photodoped using EtOH.[6] The microscopic origin of this maximum remains unidentified, and both kinetic and thermodynamic limitations to further electron accumulation can be postulated.[2,6] Photoluminescence measurements[12,13] and electron-transfer chemistries[14,15] provide strong evidence that the potentials of CB electrons in colloidal ZnO nanocrystals are subject to quantum confinement effects, but these measurements have only probed the limit of $\langle n \rangle = 1$. The ability

to accumulate tens to hundreds of excess CB electrons per nanocrystal *via* photodoping raises intriguing questions about how to describe the redox potentials and Fermi levels (E_F) of such heavily reduced ZnO nanocrystals, and the dependence of these parameters on the method of reduction.

Here, we report contactless *in situ* determination of the redox potentials of *n*-type colloidal ZnO nanocrystals using an optical redox indicator. The data show that E_F is subject to quantum confinement effects in the limit of one electron per nanocrystal, as anticipated from prior results. With further electron accumulation, however, E_F becomes independent of quantum confinement and depends only on electron density. E_F is shown to depend strongly on the identity of the charge-compensating cation, spanning a range of ~600 meV when only one electron per nanocrystal is present, consistent with previous reactivity studies.[16] $<N_{max}>$ and E_F^{max} are found to be determined by electron Fermi-level pinning, which occurs at the same potential for all nanocrystal sizes. Aldehyde hydrogenation, *i.e.*, the two-electron two-proton reaction that reverses the EtOH photooxidation, is proposed to be the microscopic origin of this Fermi-level pinning.

2.3 Experimental Details

ZnO nanocrystal synthesis. Colloidal ZnO nanocrystals were synthesized by base-initiated hydrolysis and condensation of Zn^{2+} as detailed previously.[17,18] In a typical synthesis, a solution of 22 mmol of TMAH in 40 mL of EtOH was added drop wise to a stirred solution of 13 mmol of $Zn(OAc)_2$ in 135 mL of DMSO at room temperature. Nanocrystals were grown for ~1 hr, after which the reaction was stopped by precipitation with 300 mL of ethyl acetate. Nanocrystals were collected via centrifugation and resuspended in EtOH, followed by precipitation with heptane. To suspend the nanocrystals in nonpolar solvents, the surface ligands were exchanged by suspending the nanocrystals in excess of dodecylamine (DDA) that had been heated above the melting point (29 °C), followed by precipitation with EtOH. Finally, the nanocrystals were heated in trioctylphosphine oxide (TOPO, 90%) at 130 °C for 30 min. The resulting TOPO-capped nanocrystals were then washed with 3:1 EtOH/toluene and resuspended in toluene. The largest ZnO nanocrystals were made in a similar manner but were heated under N_2 in DDA at 180 °C for ~24 h prior to TOPO capping to promote growth to various sizes.

Physical characterization. UV-Vis-NIR absorption spectra were collected in a 1 cm air-free quartz cuvette using a Cary 500 spectrometer, with typical nanocrystal concentrations of 5-20 μM. The radii of small nanocrystals ($r \leq 2.8$ nm) were determined from the empirical correlation between radii and absorption spectra.[13,19] The radii of larger nanocrystals (r = 3.7 nm) were determined by statistical analysis of transmission electron microscope (TEM) images collected using a FEI Tecnai G2 F20. ZnO nanocrystal concentrations were determined analytically. 200 μL of the nanocrystal suspension was dried and digested in 200 μL of ultrapure nitric acid (TraceSELECT, Fluka). The resulting solution was diluted with a known amount of ultrapure water (10.00 g, measured to two decimal places on a balance), and the Zn^{2+} concentration was measured using inductively coupled plasma atomic emission spectroscopy (Perkin-Elmer 8300). The nanocrystal concentration was then calculated using the known dilution factors and nanocrystal radii to convert from Zn^{2+} concentration to nanocrystal concentration.

Photodoping. ZnO nanocrystals were suspended in dry, anaerobic toluene/THF (1:14) solutions and prepared in a 1 cm air-free cuvette, then photodoped to their maximum level by prolonged exposure to UV irradiation from a 100 W Hg/Xe Oriel broad-band photolysis lamp (2 W/cm^2, 1.5 cm illumination diameter) in the presence of EtOH and $[Cp_2Co][PF_6]$ (0.233–0.633 mM). THF was used to aid the solubility of $[Cp_2Co][PF_6]$. The UV-Vis-NIR absorption was collected periodically during the photodoping process. When the NIR absorption did not change over 20 min of UV exposure, the nanocrystals were considered to have reached their maximum photodoping level. Maximum photodoping was typically achieved within 90 min of UV irradiation.

Electron counting by titration. The average number of photodoped electrons per ZnO nanocrystal (<n>) was determined by titration with $[FeCp^*_2][BAr_F]$ (Figure S1).[6,20,21] Aliquots of $[FeCp^*_2][BAr_F]$ in THF were added to the maximally photodoped nanocrystals and the reduction of the NIR absorption was monitored. After complete elimination of the NIR absorption, additional aliquots led to growth of $FeCp^*_2{}^+$ absorption centered at 700 nm. The data were then fit with a linear function and the maximum number of photodoped electrons was determined from the x-intercept of the fitted line.

Electron counting from NIR absorption. The average number of electrons per nanocrystal, <n>, was determined spectroscopically from the NIR absorption involving intraband transitions of the CB electrons. For this, molar extinction coefficients (ε) were determined for each ZnO

nanocrystal size at five different wavelengths (500, 778, 1000, 1300, and 1600 nm) and at various values of <*n*>, by [FeCp*$_2$][BAr$_F$] titration. These ε values were fit to a power function with the general form $\varepsilon_\lambda = Q_\lambda \times \langle n \rangle^p$ (Figure S1b), where Q (M^{-1} cm^{-1} $electron^{-1}$) and *p* (unitless) are constants. Substitution into the Beer's-law equation and rearranging for <*n*>, the expression becomes $\langle n \rangle = Abs_\lambda \times \exp(p) \times Q_\lambda^{-1} \times b^{-1} \times C^{-1}$, where b is the optical pathlength (cm) and C is the concentration (M). Values of <*n*> calculated from the absorption at 778, 1000, 1300, and 1600 nm were averaged together to obtain the reported values of <*n*>, with error bars reported as ±σ from the mean value of <*n*>. The <*n*> values reported here were measured without UV illumination. Under these conditions, <*n*> is constant.

Optical Fermi-level measurements. Fermi levels (E_F) were measured using Cp_2Co as an *in situ* optical redox indicator. Measurements of E_F were performed in the absence of UV photoexcitation. Under these conditions, <*n*> and E_F are stable. Cp_2Co concentrations were measured spectroscopically using the absorption feature at 500 nm (ε_{500} = 301 $M^{-1}cm^{-1}$),[22] accounting for overlapping ZnO intraband absorption. Cp_2Co concentrations were then determined using Beer's law, and E_F was calculated from the Nernst equation. The E_F values reported here are thus equilibrium values measured without UV illumination and are stable under rigorously anaerobic conditions.

2.4 Results and Analysis

Figure 2.1.A plots electronic absorption spectra of colloidal ZnO nanocrystals (*r* = 1.9 nm) collected at various stages of nanocrystal photodoping using EtOH as the hole quencher. In these measurements, [Cp_2Co][PF_6] (Cp_2Co^+ = cobaltocenium, PF_6^- = hexafluorophosphate) has been added to the reaction mixture for use as an optical redox indicator. As detailed previously, photodoping leads to bleaching of the ZnO band-edge absorption (inset) and growth of a comparably intense IR intra-band absorption feature, both indicating a growing population of delocalized CB electrons (e^-_{CB}).[1-3,5,6,14-16,23-26] The IR absorbance can be analyzed to provide the average number of electrons per ZnO nanocrystal (<*n*>) at each level of photodoping. In the present experiments, new absorption features at 390 and 500 nm are also observed upon photodoping, attributable to the LMCT and *d–d* transitions of cobaltocene (Cp_2Co), respectively.[22] The concentration of Cp_2Co is determined from the Cp_2Co absorbance at 500 nm and its extinction coefficient (ε_{500} = 301 $M^{-1}cm^{-1}$) using Beer's law. Using the Nernst equation

(eq 2.2) and the experimental Cp_2Co redox potential (E^o = −1.37 V vs Fc^+/Fc, see Appendix A), the solution potential (E_{cell}) may then be calculated. As measured by the quotient $[Cp_2Co]/[Cp_2Co^+]$, E_{cell} directly reports the electron Fermi level (E_F) of the ensemble of ZnO nanocrystals, which are in thermodynamic equilibrium with the Cp_2Co^+/Cp_2Co couple.[27,28] The solution potential therefore equals the ZnO electron Fermi level.

$$E_F(V) = E_{cell}(V) = E^o - 0.02568 \times ln\frac{[Cp_2Co]}{[Cp_2Co^+]} \qquad \text{(Equation 2.2)}$$

Figure 2.1b plots E_F vs $\langle n \rangle$ for the entire data set of Figure 2.1.A. Initially, mixing undoped ZnO nanocrystals with Cp_2Co^+ yields no detectable Cp_2Co, indicating that E_F of the undoped ZnO nanocrystals is far more positive than –1.37 V (the Cp_2Co^+/Cp_2Co redox couple). Upon UV photoexcitation of this mixture, E_F increases rapidly in concert with ZnO photodoping, growing from −1.28 to ~ −1.35 V, where its value levels off until $\langle n \rangle$ ~ 3.7, at which point E_F increases sharply to reach its maximum value of E_F^{max} ~ −1.37 V at $\langle n \rangle$ = 4.3. This value of $\langle n \rangle$ is the maximum number of electrons ($\langle n_{max} \rangle$) that can be introduced under these conditions.[6] Further UV irradition yields no change in $\langle n \rangle$ or E_F. The full range of E_F in these data is ~90 meV, smaller than the ~350 meV range measured in electrochemical ZnO nanocrystal reduction experiments.[29] This difference is in large part due to the absence of an E_F data point prior to photodoping, and it may also relate to the different counterions of the two measurements (*vide infra*).

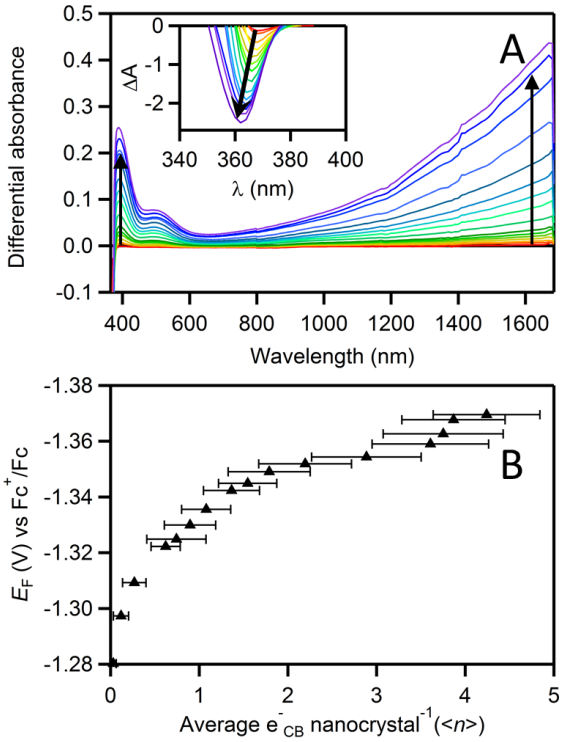

Figure 2.1. Electronic absorption of increasingly photodoped ZnO with Cp_2Co^+ as an optical redox indicator.

(A) Representative differential electronic absorption spectra collected at various illumination times between 0 and 1 hr during photochemical reduction of 9.45 μM colloidal ZnO (r = 1.9 nm) nanocrystals in the presence of 466 μM $[Cp_2Co][PF_6]$ in a 14:1:0.5 THF/toluene/ethanol mixture. The main panel shows the visible spectral range, and the inset shows the UV (ZnO interband) range. Note the different y-axis scaling. The arrows indicate the direction of increased photodoping. **(B)** Plot of electron Fermi level (E_F, black triangles) vs average number of CB electrons per nanocrystal (<n>), calculated from the Cp_2Co absorbance at λ = 500 nm (ε_{500} = 301 $M^{-1}cm^{-1}$) at each stage of photodoping. E_F values are referenced to the ferrocenium/ferrocene (Fc^+/Fc) redox couple. The error bars indicate ±σ from the mean value of <n>. The quotient $[Cp_2Co]/([Cp_2Co] + [Cp_2Co^+])$ is ~0.5 at <n_{max}> in these measurements.

Measurements under the same photodoping conditions but using different Cp_2Co^+ concentrations all yield the same values of E_F vs <n> (see Appendix A). Additionally, when the weaker oxidant decamethylcobaltocenium ($Cp^*_2Co^+$, E^o = −1.91V vs Fc/Fc^+ in MeCN[30]) is added instead of Cp_2Co^+, no formation of decamethylcobaltocene (Cp^*_2Co) is observed (see Appendix A).

Together, these results confirm that the Cp_2Co^+/Cp_2Co redox couple is indeed in equilibrium with the ZnO nanocrystals.

We have previously reported that $\langle n_{max} \rangle$ in photodoped ZnO nanocrystals scales with nanocrystal volume,[6] but the fundamental origins of this scaling have not been identified. It is possible that $\langle n \rangle$ is limited kinetically, for example by the lifetimes of photogenerated holes, but it is also possible that $\langle n \rangle$ is limited thermodynamically, for example by reductive metallization of the ZnO nanocrystals at high carrier densities.[6] To address this issue, we have used this redox-indicator method to measure changes in E_F with changes in $\langle n \rangle$ for ZnO nanocrystals of three different sizes, and the results are summarized in Figure 2.2. From Figure 2.2.A, the largest ZnO nanocrystals (r = 3.7 nm) show the least negative E_F value at $\langle n \rangle$ = 1, followed by the intermediate (r = 2.8 nm) and then the smallest (r = 1.9 nm) nanocrystals. From the optical bandgap energies of this series of nanocrystals (see Appendix A) and the optically deduced ratio of CB-to-bandgap shifts with quantum confinement,[12,15] the CB energy is predicted to shift negatively by ~76 meV going from r = 3.7 to 1.9 nm. In good agreement with this prediction, the data in Figure 2.2.A show a shift of ~60 meV at $\langle n \rangle$ = 1, the two values being indistinguishable within the uncertainty in $\langle n \rangle$ ($\sigma = \pm 0.2$ electrons at $\langle n \rangle$ = 1). The effect of quantum confinement on E_F in the one-electron limit is thus well understood from optical studies. Beyond $\langle n \rangle$ = 1, the plots of E_F vs $\langle n \rangle$ in Figure 2.2.A all show similar asymptotic curvature, and notably, each curve plateaus at a similar potential near −1.37 V. Figure 2.2.B plots the same E_F data *vs* average electron density ($\langle N \rangle$). Remarkably, all three curves are now superimposable within experimental uncertainty. E_F increases by < 25 meV going from $\langle N \rangle = 2 \times 10^{19}$ cm^{-3} to 5×10^{19} cm^{-3}, which agrees well with previously reported values for electron-electron repulsion in ZnO nanocrystals with H^+ counter ions.[31] Like $\langle N_{max} \rangle$, E_F^{max} is thus also independent of nanocrystal size for a given hole quencher. For all three nanocrystal sizes, E_F maximizes near −1.37 V at $\langle N_{max} \rangle = \sim 1.6 \pm 0.3 \times 10^{20}$ cm^{-3}. The data in Figure 2.2 provide a strong indication of Fermi-level pinning during nanocrystal photodoping. This result points to the conclusion that $\langle N_{max} \rangle$ in photodoped ZnO nanocrystals is determined specifically by the electron Fermi level, rather than by kinetic limitations.

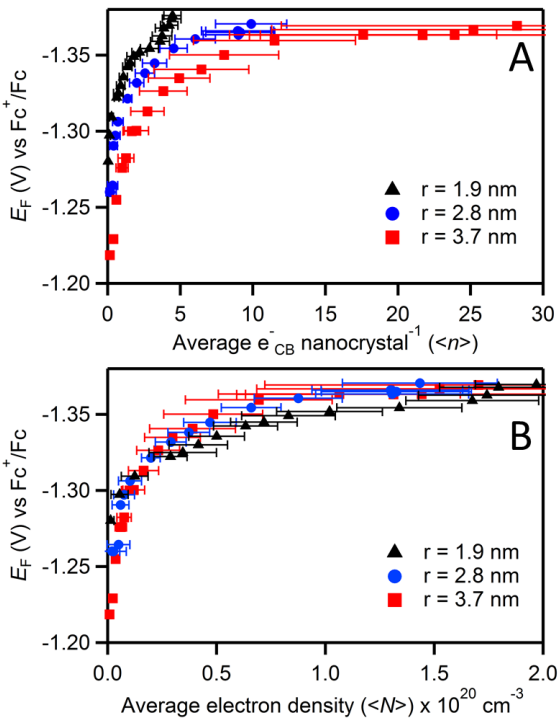

Figure 2.2. Size dependence of ZnO NC Fermi-levels with increasing <*n*> and <*N*>. **(A)** E_F values for r = 1.9 nm (5 μM, black triangles), 2.8 nm (8 μM, blue circles), and 3.7 nm (6 μM, red squares) ZnO nanocrystals photodoped with ethanol, plotted vs <*n*>. **(B)** The same E_F data plotted vs average electron density (<*N*>). E_F values are referenced to the ferrocenium/ferrocene (Fc^+/Fc) redox couple.

It is important to note that all values of <*N*> and E_F reported here have been measured in the absence of ZnO UV photoexcitation. Under these conditions, and when rigorously anaerobic, <*N*> and E_F (or $<N_{max}>$ and E_F^{max}) remain constant for very long times (*e.g.*, k_{decay} < ~0.01/week at 298 K).[5] Kinetic contributions to <*N*> and E_F are observed under continuous UV photoexcitation, of course, where their precise steady-state (photostationary) values depend on the ZnO photoexcitation rate. Under illumination, steady-state values of <*N*> can exceed $<N_{max}>$, and electron quasi-Fermi levels can exceed E_F^{max} (see Appendix A). Upon termination of the UV illumination, however, <*N*> and E_F both relax quickly in the dark to $<N_{max}>$ and E_F^{max}, at which point they are stable. Resuming the UV illumination again raises <*N*> and E_F to some steady-state values that depend on the UV irradiation parameters, but after terminating the UV illumination they again return to the same $<N_{max}>$ and E_F^{max} (see Appendix A). $<N_{max}>$ and E_F^{max}

are thus independent of the ZnO photoexcitation parameters. These observations strongly support the conclusion that $<N_{max}>$ and E_F^{max} are determined thermodynamically, not kinetically.

We propose that the limit to E_F^{max} arises from the existence of a side redox reaction that occurs spontaneously at more reducing values of E_F. Specifically, we propose that E_F^{max} (and hence $<N_{max}>$ and also $<n_{max}>$) under the present photodoping reaction conditions is pinned by the reversibility of the EtOH oxidation reaction, *i.e.*, by the spontaneous two-electron/two-proton transfer from heavily reduced ZnO nanocrystals to acetaldehyde. This back reaction should occur at the same potential regardless of the nanocrystal radius, consistent with the size-independent E_F^{max} observed in Figure 2.2. Experimentally, detection of EtOH formed from the proposed back reaction is not trivial, so to test the hypothesis of aldehyde hydrogenation by photoreduced ZnO nanocrystals, two sets of experiments were performed that indirectly probe the role of acetaldehyde. In the first, ZnO nanocrystals were photodoped to $<N_{max}>$ in the presence of different amounts of added acetaldehyde. Figure 2.3 reveals that $<N_{max}>$ decreases nearly linearly with added acetaldehyde, consistent with the hypothesized aldehyde hydrogenation chemistry.

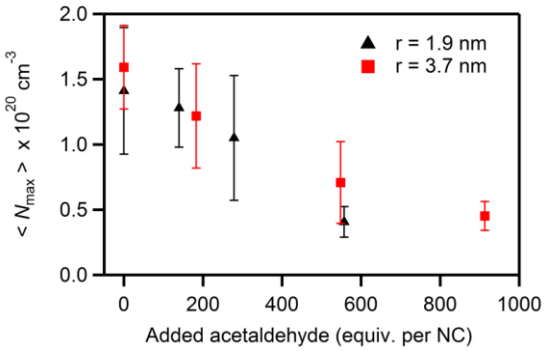

Figure 2.3. Maximum electron density dependence on the acetaldehyde concentration.

Maximum average electron densities ($<N_{max}>$) achievable in colloidal ZnO nanocrystals photoreduced using EtOH as the hole scavenger, measured in the presence of added acetaldehyde. Data for r = 1.9 nm (5 μM, black triangles) and 3.7 nm (6 μM, red squares) ZnO nanocrystals are plotted. The error bars indicate ±σ from $<N>$.

In the second, benzaldehyde was used as a surrogate for acetaldehyde. In these experiments, ZnO nanocrystals were photodoped using EtOH as described above, but now in the presence of added benzaldehyde (see Appendix A). Hydrogenation of benzaldehyde generates benzyl alcohol,

which can be identified by its characteristic ^{1}H NMR peak at 4.2 ppm (vs TMS) arising from its α-CH_2 protons. ^{1}H NMR spectroscopy thus offers a convenient and sensitive probe of this chemistry. Figure 2.4.A plots ^{1}H NMR data collected after various durations of UV illumination under the normal photodoping conditions, but now in the presence of added benzaldehyde. $\langle N_{max} \rangle$ is reached after ~45 min of UV excitation in these measurements (see Appendix A), but over longer illumination times the formation of benzyl alcohol becomes evident from the appearance and growth of the broad α-CH_2 signal at 4.22 ppm, accompanied by a concomitant decrease in the intensity of the α-CH signal of benzaldehyde at 9.63 ppm. The broadening of the 4.2 ppm signal relative to that of neat benzyl alcohol (see Appendix A) is likely due to association of the benzyl alcohol with the ZnO surface[32] or surface-capping ligands. Figure 2.4.B plots integrated benzaldehyde and benzyl alcohol NMR intensities as a function of UV illumination time, showing that the changes in the concentrations of these two species are inversely correlated. Benzyl alcohol formation was confirmed by GC-MS. Importantly, benzyl alcohol is not formed under the same conditions when benzaldehyde is irradiated by extensive UV illumination in the absence of the ZnO nanocrystals (see Appendix A). We thus conclude that photoreduced ZnO nanocrystals can indeed hydrogenate aldehydes to form alcohols. Combined with the data from Figure 2.3, these results provide strong support for the conclusion that acetaldehyde hydrogenation is responsible for Fermi-level pinning during ZnO photodoping when using EtOH as the hole quencher, explaining at a microscopic level one of the more striking features of this nanocrystal redox chemistry.

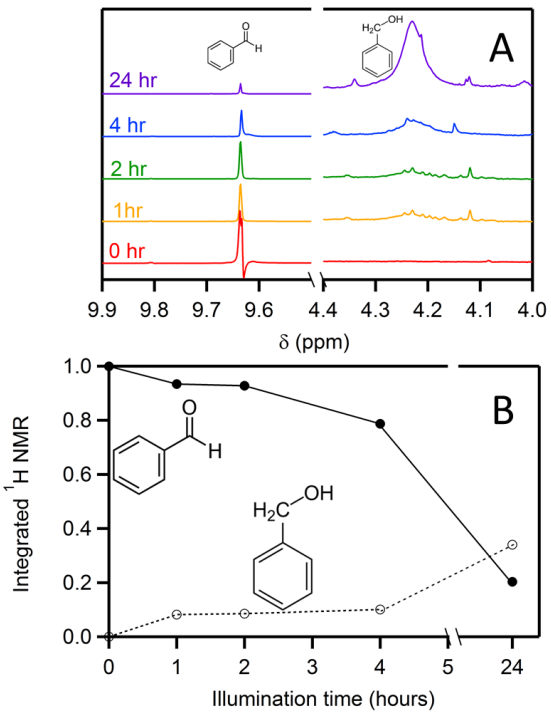

Figure 2.4. Hydrogenation of benzaldehyde with photodoped ZnO.

(A) ^{1}H NMR spectra (500 MHz) of TOPO-capped ZnO nanocrystals (r = 1.9 nm, 94 μM) in 1:3 toluene-d_8/benzene-d_6 spiked with ethanol and benzaldehyde in ~10^4x excess (per ZnO NC) at 0 hr (red), 1 hr (yellow), 2 hr (green), 4 hr (blue), and 24 hr (violet) of UV illumination. Control measurements show no benzyl alcohol formation under UV irradiation in the absence of the ZnO nanocrystals (see Appendix A). For clarity, the spectra are offset vertically and each side is normalized to the TOPO ligand signal at 2.5 ppm (not shown, see Appendix A). **(B)** Integrated intensities of the α-CH benzaldehyde (9.8 ppm) and α-CH_2 benzyl alcohol (4.3 ppm) ^{1}H NMR signals relative to the TOPO CH_2 signal (2.5 ppm). These data are normalized to the benzaldehyde integrated intensity at 0 hours. The presence of two α-CH_2 protons per benzyl alcohol was accounted for by halving the total normalized intensity for this signal. For reference, $\langle N_{max} \rangle$ is reached after ~45 min of UV excitation in these measurements.

Finally, we address the influence of charge-compensating cations on E_F. Charge-compensating cations play an integral role in the formation, stabilization, and reactivity of reduced ZnO nanocrystals.[6,16,31] In particular, protons greatly facilitate the reduction of ZnO NCs electrochemically[31] and by chemical reductants,[16] displaying exceptional effectiveness in

stabilizing reduced ZnO nanocrystals relative to bulkier cations. To quantify the effects of protons, E_F values were measured for colloidal r = 1.9 nm ZnO nanocrystals reduced either photochemically (using EtOH) or chemically (using Cp^*_2Co). Figure 2.5 summarizes these results. Strikingly, E_F is nearly 600 meV more negative for the chemically reduced nanocrystals than for the photodoped nanocrystals, and photodoping can introduce more than four times as many CB electrons as achieved by chemical reduction under these conditions. If E_F were determined solely by factors intrinsic to ZnO, such as the initial one-electron orbital energies or unscreened electron-electron repulsion, no difference in E_F would be observed with different reductants. The data in Figure 2.5 thus demonstrate and quantify the very large difference between CB electrons stabilized by H^+ and those stabilized by $Cp^*_2Co^+$.

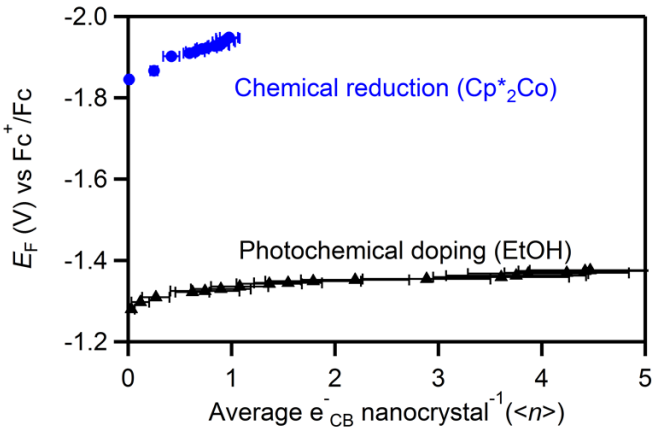

Figure 2.5. Comparison of charge compensating counter ion on ZnO E_F.
Comparison of E_F values measured for colloidal ZnO nanocrystals (r = 1.9 nm) reduced chemically using Cp^*_2Co (blue circles) and photochemically using EtOH (black triangles), both measured using the Cp_2Co^+/Cp_2Co couple as an optical redox indicator. The error bars indicate ±σ from the average value of <n>.

2.5 Discussion

Figure 2.5 summarizes the changes in ZnO nanocrystal Fermi level during progressive photodoping using EtOH as the hole quencher and relates them to the changes observed upon chemical reduction by electron transfer from Cp^*_2Co. For the same nanocrystals reduced photochemically and chemically, comparison of E_F values measured at <n> = 1 (Figure 2.5)

reveals that electrons compensated by H^+ are nearly 600 meV more stable than those compensated by $Cp^*_2Co^+$, a remarkably large difference. This difference could arise from more effective Coulombic stabilization (screening) of CB electrons by protons than by the bulky $Cp^*_2Co^+$ counter ions, especially if protons are able to diffuse into the internal volumes of the nanocrystals, but it likely also reflects the formation of a strong O–H bond upon nanocrystal reduction using EtOH. Formation of a strong ZnO-H bond stabilizes the reduced nanocrystal product, lowers the electron's chemical potential, and in turn allows greater maximum electron densities to be attained in the same ZnO nanocrystals via photodoping than via reduction by Cp^*_2Co.

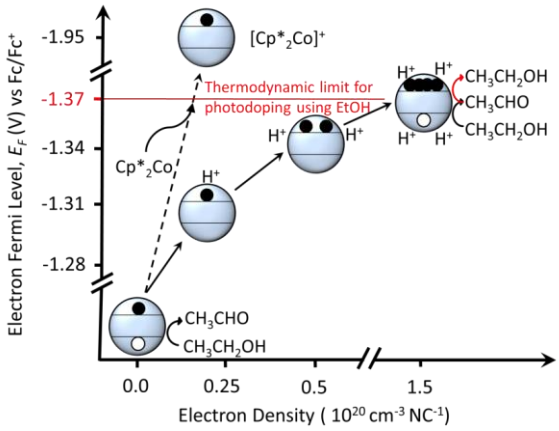

Figure 2.5. Schematic representation of increasingly negative E_F in photodoped ZnO.

With extended photodoping (eq 2.1), E_F becomes dominated by electron-electron repulsive interactions that scale with electron density, yielding a single relationship between E_F and $\langle N \rangle$ that holds for all nanocrystal sizes. Between $\langle N \rangle$ = 2 x 10^{19} cm^{-3} and 5 x 10^{19} cm^{-3}, E_F rises with a slope of ca. −130 meV/(10^{20} cm^{-3}), but subsequently shows asymptotic behavior indicative of Fermi-level pinning. The microscopic origin of the Fermi-level pinning has been identified as the acetaldehyde hydrogenation reaction, which at low electron densities is negligible but becomes more favorable as E_F increases. When E_F reaches ca. −1.37 V vs Fc^+/Fc (E_F^{max}), at $\langle N_{max} \rangle$ = ~1.6 x 10^{20} cm^{-3}, UV illumination yields no further stable electron accumulation within the ZnO nanocrystals. At this point, further EtOH photooxidation is followed by spontaneous (dark) aldehyde hydrogenation (eq 2.3). The E_F^{max} values reported here are thus dictated by the dark reverse reaction of eq 2.1.

$$e^-_{CB}:ZnO\text{-}H^+ + \tfrac{1}{2}\, CH_3CHO \longrightarrow ZnO + \tfrac{1}{2}\, CH_3CH_2OH \qquad \text{(Equation 2.3)}$$

It is possible that this reaction continues on an imperceptibly slow timescale (> days) after its apparent equilibration within seconds or minutes. Strictly speaking, these photodoped nanocrystals would then be kinetically stable but not at a true equilibrium. This scenario could arise from proton diffusion. For example, it is possible that the correct proton configurations at the nanocrystal surfaces do not exist in these reduced nanocrystals because of proton diffusion into the internal nanocrystal volumes, driven by the greater electron density within the nanocrystal cores and by proton-proton repulsion in these types of structures where two proximal protons are required for aldehyde hydrogenation. At this time, the details of this reaction remain poorly understood. Clarification of such details will be the focus of future studies with this system.

Heterogeneous catalytic hydrogenation of aldehydes by ZnO has been reported previously, but the reaction generally takes place at elevated temperature (~650 K) under continuous H_2 flow,[32,33] or requires a noble metal co-catalyst,[34] and it is not driven by photons. Here, aldehyde hydrogenation occurs as the result of a very negative E_F in ZnO achieved by extensive nanocrystal photoreduction. Although further analysis of this aldehyde hydrogenation reactivity is beyond the scope of the present study, this observation of multi-electron/multi-proton chemistry involving heavily reduced semiconductor nanocrystals generated photochemically could have interesting implications in the area of solar fuels.[35,36]

Finally, recent work has demonstrated analogous photodoping of colloidal In_2O_3 nanocrystals using EtOH as the hole quencher,[7] as well as photodoping of ZnO[6] and CdE (E = S, Se, Te)[8] nanocrystals with a variety of hydride hole quenchers (*e.g.*, $Li[Et_3BH]$). Although beyond the scope of the present study, it is interesting to consider the possibility that Fermi-level pinning might also be responsible for the maximum photodoping levels observed in these nanocrystals. In_2O_3 is most similar to ZnO. In_2O_3 nanocrystals can be photodoped using EtOH to comparable maximum electron densities as in ZnO nanocrystals, which would be consistent with a similar limiting mechanism, but the different surface chemistries of In_2O_3 and ZnO nanocrystals can reasonably be anticipated to lead to different hydrogenation catalysis and hence different limiting Fermi levels. In contrast with ZnO nanocrystals, CdE nanocrystals often have mid-gap surface electron traps that may impact photodoping, and these nanocrystals also do not

form strong bonds with protons, suggesting unrelated redox chemistries may instead dominate. Overall, while the specific redox processes described here for ZnO may not be central in these other photodoping chemistries, the concept of photodoping limited by competing redox reactions rather than by photophysical recombination kinetics may be general. Future studies on photodoping involving these other materials will address these interesting open questions.

2.6 Conclusion

A simple optical method employing a solvated redox indicator has been applied for *in situ* determination of reduced ZnO nanocrystal redox potentials. These measurements reveal that the Fermi levels of solutions of nanocrystals possessing an average of just one CB electron per nanocrystal can vary by over 600 meV depending upon the method of charge compensation, and also reveal electron quantum-confinement effects for a fixed charge-compensating cation (H^+) but different nanocrystal sizes. For ZnO nanocrystals photodoped using EtOH as the hole quencher, the Fermi level becomes independent of nanocrystal size at average electron densities of ~2×10^{19} cm^{-3}. The maximum carrier densities achievable via photodoping, ~2×10^{20} cm^{-3}, are found to be determined by electron Fermi-level pinning. Microscopically, this Fermi-level pinning is identified as arising from the spontaneous two-electron two-proton hydrogenation of acetaldehyde, which reverses the EtOH photooxidation reaction. This hydrogenation reaction, and hence the maximum nanocrystal photodoping level, occurs at the same potential for all nanocrystal sizes, explaining the microscopic basis for the maximum electron densities achievable via this photochemistry.

2.7 References

(1) Haase, M.; Weller, H.; Henglein, A.: Photochemistry and radiation chemistry of colloidal semiconductors. 23. Electron storage on zinc oxide particles and size quantization. *J. Phys. Chem.* **1988**, *92*, 482-487.

(2) Shim, M.; Guyot-Sionnest, P.: Organic-Capped ZnO Nanocrystals: Synthesis and n-Type Character. *J. Am. Chem. Soc.* **2001**, *123*, 11651-11654.

(3) Wood, A.; Giersig, M.; Mulvaney, P.: Fermi Level Equilibration in Quantum Dot−Metal Nanojunctions. *J. Phys. Chem. B* **2001**, *105*, 8810-8815.

(4) Germeau, A.; Roest, A. L.; Vanmaekelbergh, D.; Allan, G.; Delerue, C.; Meulenkamp, E. A.: Optical Transitions in Artificial Few-Electron Atoms Strongly Confined Inside ZnO Nanocrystals. *Phys. Rev. Lett.* **2003**, *90*, 097401.

(5) Liu, W. K.; Whitaker, K. M.; Kittilstved, K. R.; Gamelin, D. R.: Stable Photogenerated Carriers in Magnetic Semiconductor Nanocrystals. *J. Am. Chem. Soc.* **2006**, *128*, 3910-3911.

(6) Schimpf, A. M.; Gunthardt, C. E.; Rinehart, J. D.; Mayer, J. M.; Gamelin, D. R.: Controlling Carrier Densities in Photochemically Reduced Colloidal ZnO Nanocrystals: Size Dependence and Role of the Hole Quencher. *J. Am. Chem. Soc.* **2013**, *135*, 16569-16577.

(7) Schimpf, A. M.; Lounis, S. D.; Runnerstrom, E. L.; Milliron, D. J.; Gamelin, D. R.: Redox Chemistries and Plasmon Energies of Photodoped In2O3 and Sn-Doped In2O3 (ITO) Nanocrystals. *J. Am. Chem. Soc.* **2015**, *137*, 518−524.

(8) Rinehart, J. D.; Schimpf, A. M.; Weaver, A. L.; Cohn, A. W.; Gamelin, D. R.: Photochemical Electronic Doping of Colloidal CdSe Nanocrystals. *J. Am. Chem. Soc.* **2013**, *135*, 18782-18785.

(9) Cohn, A. W.; Janßen, N.; Mayer, J. M.; Gamelin, D. R.: Photocharging ZnO Nanocrystals: Picosecond Hole Capture, Electron Accumulation, and Auger Recombination. *J. Phys. Chem. C* **2012**, *116*, 20633-20642.

(10) Markham, M. C.; Hannan, M. C.; Paternostro, R. M.; Rose, C. B.: Oxidation of Alcohols Catalyzed by Zinc Oxide and Light. *J. Am. Chem. Soc.* **1958**, *80*, 5394-5397.

(11) Cunningham, J.; Hodnett, B. K.: Kinetic Studies of Secondary Alcohol Photo-oxidation on ZnO and TiO2 at 348 K Studied by Gas-chromatographic Analysis. *J. Chem. Soc., Faraday Trans. 1* **1981**, *77*, 2777-2801.

(12) van Dijken, A.; Meulenkamp, E. A.; Vanmaekelbergh, D.; Meijerink, A.: Identification of the transition responsible for the visible emission in ZnO using quantum size effects. *J. Lumin.* **2000**, *90*, 123-128.

(13) Wood, A.; Giersig, M.; Hilgendorff, M.; Vilas-Campos, A.; Liz-Marzán, L. M.; Mulvaney, P.: Size effects in ZnO: The cluster to quantum dot transition. *Aust. J. Chem.* **2003**, *56*, 1051-1057.

(14) Hayoun, R.; Whitaker, K. M.; Gamelin, D. R.; Mayer, J. M.: Electron Transfer Between Colloidal ZnO Nanocrystals. *J. Am. Chem. Soc.* **2011**, *133*, 4228-4231.

(15) Cohn, A. W.; Kittilstved, K. R.; Gamelin, D. R.: Tuning the Potentials of "Extra" Electrons in Colloidal n-Type ZnO Nanocrystals via Mg2+ Substitution. *J. Am. Chem. Soc.* **2012**, *134*, 7937-7943.

(16) Valdez, C. N.; Braten, M.; Soria, A.; Gamelin, D. R.; Mayer, J. M.: Effect of Protons on the Redox Chemistry of Colloidal Zinc Oxide Nanocrystals. *J. Am. Chem. Soc.* **2013**, *135*, 8492-8495.

(17) Schwartz, D. A.; Norberg, N. S.; Nguyen, Q. P.; Parker, J. M.; Gamelin, D. R.: Magnetic Quantum Dots: Synthesis, Spectroscopy, and Magnetism of Co2+- and Ni2+-Doped ZnO Nanocrystals. *J. Am. Chem. Soc.* **2003**, *125*, 13205-13218.

(18) Norberg, N. S.; Gamelin, D. R.: Influence of Surface Modification on the Luminescence of Colloidal ZnO Nanocrystals. *J. Phys. Chem. B* **2005**, *109*, 20810-20816.

(19) Meulenkamp, E. A.: Synthesis and Growth of ZnO Nanoparticles. *J. Phys. Chem. B* **1998**, *102*, 5566-5572.

(20) Schimpf, A. M.; Ochsenbein, S. T.; Buonsanti, R.; Milliron, D. J.; Gamelin, D. R.: Comparison of extra electrons in colloidal n-type Al3+-doped and photochemically reduced ZnO nanocrystals. *Chem. Commun.* **2012**, *48*, 9352-9354.

(21) Schrauben, J. N.; Hayoun, R.; Valdez, C. N.; Braten, M.; Fridley, L.; Mayer, J. M.: Titanium and Zinc Oxide Nanoparticles Are Proton-Coupled Electron Transfer Agents. *Science* **2012**, *336*, 1298-1301.

(22) Gordon, K. R.; Warren, K. D.: Spectroscopic and magnetic studies of the 3d metallocenes. *Inorg. Chem.* **1978**, *17*, 987-994.

(23) Liu, W. K.; Whitaker, K. M.; Smith, A. L.; Kittilstved, K. R.; Robinson, B. H.; Gamelin, D. R.: Room-Temperature Electron Spin Dynamics in Free-Standing ZnO Quantum Dots. *Phys. Rev. Lett.* **2007**, *98*, 186804.

(24) Schimpf, A. M.; Thakkar, N.; Gunthardt, C. E.; Masiello, D. J.; Gamelin, D. R.: Charge-Tunable Quantum Plasmons in Colloidal Semiconductor Nanocrystals. *ACS Nano* **2013**, *8*, 1065-1072.

(25) Shim, M.; Guyot-Sionnest, P.: n-type colloidal semiconductor nanocrystals. *Nature* **2000**, *407*, 981-983.

(26) Goings, J. J.; Schimpf, A. M.; May, J. W.; Johns, R. W.; Gamelin, D. R.; Li, X.: Theoretical Characterization of Conduction-Band Electrons in Photodoped and Aluminum-Doped Zinc Oxide (AZO) Quantum Dots. *J. Phys. Chem. C* **2014**, *118*, 26584-26590.

(27) Reiss, H.: The Fermi level and the redox potential. *J. Phys. Chem.* **1985**, *89*, 3783-3791.

(28) Khan, S. U. M.; Kainthla, R. C.; Bockris, J. O. M.: The redox potential and the Fermi level in solution. *J. Phys. Chem.* **1987**, *91*, 5974-5977.

(29) Roest, A. L.; Kelly, J. J.; Vanmaekelbergh, D.; Meulenkamp, E. A.: Staircase in the Electron Mobility of a ZnO Quantum Dot Assembly due to Shell Filling. *Phys. Rev. Lett.* **2002**, *89*, 036801.

(30) Connelly, N. G.; Geiger, W. E.: Chemical Redox Agents for Organometallic Chemistry. *Chem. Rev.* **1996**, *96*, 877-910.

(31) Roest, A. L.; Germeau, A.; Kelly, J. J.; Vanmaekelbergh, D.; Allan, G.; Meulenkamp, E. A.: Long-Range Transport in an Assembly of ZnO Quantum Dots: The Effects of Quantum Confinement, Coulomb Repulsion and Structural Disorder. *ChemPhysChem* **2003**, *4*, 959-966.

(32) Haffad, D.; Kameswari, U.; Bettahar, M. M.; Chambellan, A.; Lavalley, J. C.: Reduction of Benzaldehyde on Metal Oxides. *J. Catal.* **1997**, *172*, 85-92.

(33) Bowker, M.; Houghton, H.; Waugh, K. C.: Temperature-programmed reaction studies of the interaction of methyl formate and ethanol with polycrystalline zinc oxide. *J. Phys. Chem. Soc., Faraday Trans.* **1982**, *78*, 2573-2582.

(34) Mäki-Arvela, P.; Hájek, J.; Salmi, T.; Murzin, D. Y.: Chemoselective hydrogenation of carbonyl compounds over heterogeneous catalysts. *Appl. Catal. A* **2005**, *292*, 1-49.

(35) Smestad, G. P.; Steinfeld, A.: Review: Photochemical and Thermochemical Production of Solar Fuels from H2O and CO2 Using Metal Oxide Catalysts. *Indus. Eng. Chem. Res.* **2012**, *51*, 11828-11840.

(36) Rausch, B.; Symes, M. D.; Chisholm, G.; Cronin, L.: Decoupled catalytic hydrogen evolution from a molecular metal oxide redox mediator in water splitting. *Science* **2014**, *345*, 1326-1330.

Chapter 3. Potentiometric Measurements of Semiconductor Nanocrystal Redox Potentials

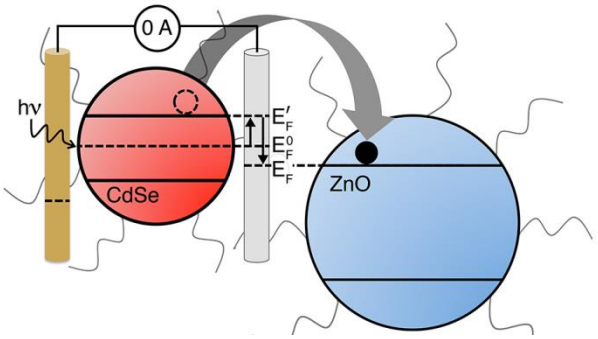

Adapted from: Carroll, G. M.; Brozek, C. K.; Hartstein, K. H.; Tsui, E.Y; and Gamelin, D. R. *JACS.* **2016**, *138*, 4310.

3.1 Overview

A potentiometric method for measuring redox potentials of colloidal semiconductor nanocrystals (NCs) is described. Fermi levels of colloidal ZnO NCs are measured *in situ* during photodoping, allowing correlation of NC redox potentials and reduction levels. Excellent agreement is found between electrochemical and optical redox-indicator methods. Potentiometry is also reported for colloidal CdSe NCs, which show more negative conduction-band-edge potentials than in ZnO. This difference is highlighted by spontaneous electron transfer from reduced CdSe NCs to ZnO NCs in solution, with potentiometry providing a direct measure of the inter-NC electron-transfer driving force. Future applications of NC potentiometry are briefly discussed.

3.2 Introduction

The redox potentials of colloidal semiconductor nanocrystals (NCs) play central roles in many current and envisioned technologies. For example, electron-transfer (ET) kinetics and reaction spontaneity for NC-sensitized solar photocatalysis are governed by the redox potentials of the NC photo-absorbers.[1-6] Likewise, relative potentials of band-like and surface-trapped electronic configurations dictate NC electronic doping,[7] which governs the utility of NCs for electronic and opto-electronic technologies such as photovoltaics.[8,9] Although critical for many target applications, *in situ* measurements of colloidal NC redox potentials have proven challenging.

Cyclic voltammetry (CV) is the most commonly employed electrochemical technique for measuring colloidal NC redox potentials.[10-12] Irreversibility of NC CV waves, low current-to-NC ratios, redox-active surface states, and surface-composition inhomogeneities have all been found to complicate solution-phase NC electrochemistry. CV measurements of NCs immobilized on electrode surfaces have been successful,[12-15] but NC redox potentials are very sensitive to their surface chemistry,[16,17] and the redox potentials of the same NCs as free-standing colloids may therefore differ substantially. As a consequence of these complications, it is common for driving forces of ET reactions involving colloidal semiconductor NCs to be discussed in terms of band-edge potentials estimated from vacuum ionization and electron-affinity measurements, often of the corresponding bulk material. Although this approach has powerful intuitive value, observations[16,18] that altering surface ligation alone can shift NC band edges by as much as 1 eV highlight the need for *in situ* redox measurements of colloidal NCs in their native form. Here, we report a potentiometric method for measuring colloidal NC redox potentials. Potentiometry has been a valuable tool in metal nanoparticle research.[19] By coupling potentiometry with optical detection of conduction-band (CB) electrons in colloidal semiconductor NCs generated *via* photodoping,[20,21] redox potentials associated with these electrons can be deduced. As a simple proof of concept, we show that our colloidal CdSe NCs have CB-edge potentials more negative than our ZnO NCs, leading to spontaneous inter-NC ET from photoreduced CdSe NCs to ZnO NCs in solution. Additional mechanistic details are revealed by the transient open-circuit potentials.

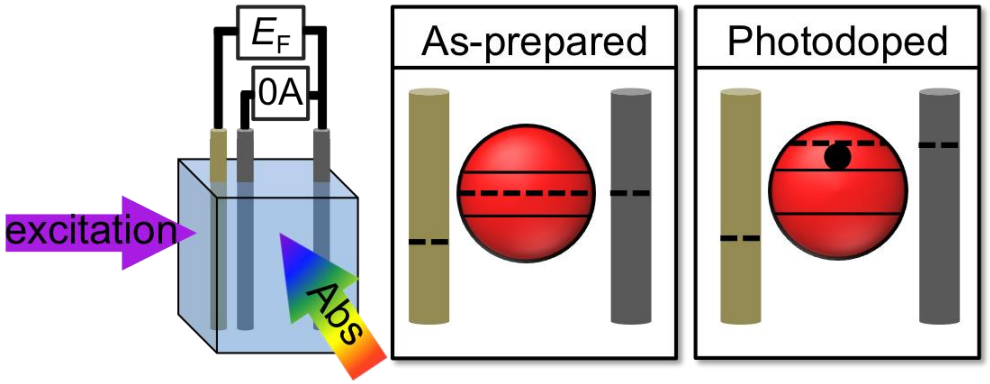

Figure 3.1. Schematic illustration of optical potentiometry.

Apparatus used to collect potentiometric and absorption data during colloidal NC photodoping (left). Set to 0 amps, the galvanostatic cell measures the solution potential during NC photodoping. NC absorption is measured simultaneously. The working electrode (grey) responds to changes in Fermi level upon NC photodoping.

Figure 3.1 illustrates the apparatus used to measure Fermi levels (E_F) during NC photodoping. In an air-tight optical cuvette, solutions of NCs under N_2 atmosphere are photoreduced using hole quenchers.[7] The average number of CB electrons per NC (<*n*>) is quantified during photodoping using absorption spectroscopy. Simultaneously, electrodes in the NC solution track changes in E_F under galvanostatic (I = 0 amps) control, *i.e.*, the potentiostat biases the working electrode in response to the photo-induced increase in E_F (Figure 3.1, right). The electrode and solution E_F remain equivalent at all times. Consequently, no depletion region at the electrode/electrolyte interface develops, and the recorded half-cell potential represents E_F of the NC suspension.[19] From these combined data, NC redox potentials at various electron densities can be determined. Accurate transient potentiometry requires a stable reference electrode. We use a leakless Ag/AgCl reference electrode, which avoids instabilities due to solution contamination, ionic activity, or electrode/electrolyte junction potentials (see Appendix B). To account for possible electrochemical drift, CVs of an internal standard (cobaltocenium hexafluorophosphate, $[Cp_2Co][PF_6]$) were collected before and after most experiments. Drift was generally very small (< ~10 mV). All data are referenced experimentally to the ferrocenium/ferrocene couple (Fc^+/Fc, see Appendix B).

3.3 Results and Analysis

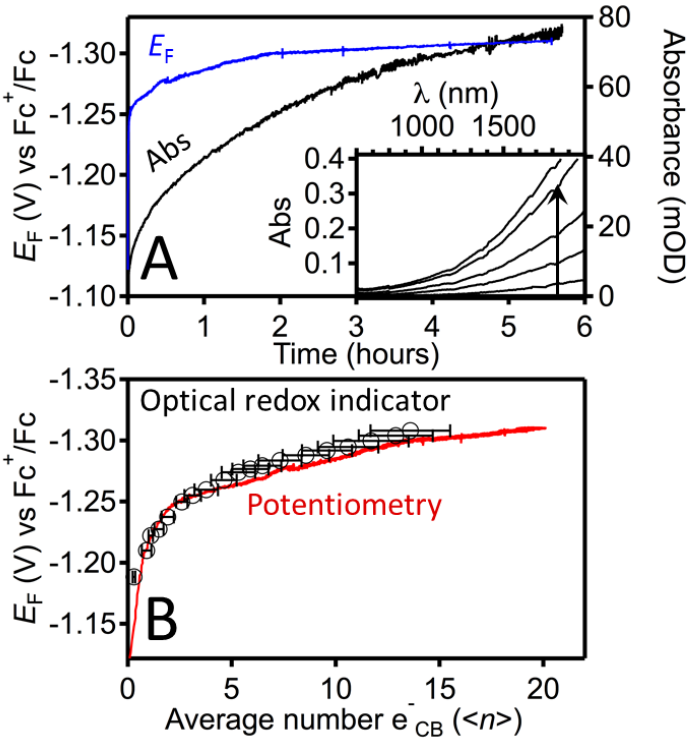

Figure 3.2. Comparison of optical potentiometry and optical-redox-indicator methods of photodoped ZnO

(A) Potentiometry (blue) and electronic absorption (black, λ = 1000 nm) data collected during photodoping of d = 6.8 nm ZnO NCs (2 μM) using EtOH as the hole quencher. A 14:1 THF/toluene solution of 0.1 M tetrabutylammonium hexafluorophosphate ([Bu-$_4$N][PF_6]), 660 μM [Cp_2Co][PF_6] was irradiated at 340 nm (12 mW) while stirring. The inset shows NIR absorption spectra of the same ZnO NCs growing with increasing <n>. **(B)** Plot of E_F *vs* <n> for photodoped ZnO NCs derived from potentiometric (curve) and ORI (circles) methods. <n> was determined spectroscopically (see Appendix B). The error bars represent ±σ from the mean. E_F is referenced to the Fc^+/Fc redox couple.

Figure 3.2.A plots E_F and the absorbance at λ = 1000 nm (A_{1000}) measured simultaneously during ZnO NC photodoping using ethanol as the hole quencher.[22,23] A_{1000} increases with ZnO photoexcitation, reflecting photodoping.[21,24-26] Concomitantly, E_F becomes more negative. From the per-electron extinction at λ = 1000 nm (ε_{1000} = 1097<n>$^{0.7}$ M^{-1} cm^{-1}, see Appendix B), <n> ≈

20 e^-_{CB}/NC at its maximum ($\langle n_{max} \rangle$), corresponding to an average electron density of $\langle N_{max} \rangle \approx 1.21 \times 10^{20}$ cm^{-3}, in agreement with previous reports.[7,21,23,26] Because E_F and A_{1000} were measured simultaneously, it is valuable to plot E_F against $\langle n \rangle$ as shown in Figure 3.2.B. E_F rises steeply at ~ –70 mV/$\langle n \rangle$ between $\langle n \rangle$ = 0 and 2, after which its rise decreases to ~ –4 mV/$\langle n \rangle$ until photodoping is complete.

It is instructive to compare these potentiometric data with those obtained using a solvated optical redox indicator (ORI),[1-3] an approach we applied recently to monitor ZnO NC photodoping.[27] Here, E_F is measured during photodoping using the optically detected equilibrium constant of a solvated redox couple that is also in equilibrium with the NCs. For the present comparison, ORI data were collected while photodoping the same ZnO NCs as probed electrochemically, under the same experimental conditions, and the ratio $[Cp_2Co^+]/[Cp_2Co]$ measured spectrophotometrically to determine E_F. These results are included in Figure 3.2.B. The two methods yield nearly indistinguishable results.

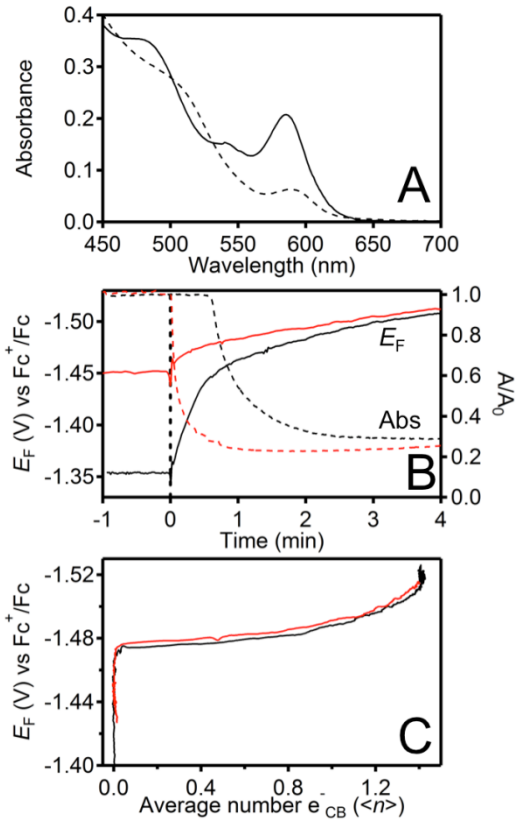

Figure 3.3. Potentiometric measurement of photodoping CdSe NCs

(A) Electronic absorption spectra of as-prepared (solid) and photodoped (dashed) d = 4.1 nm CdSe NCs. Experiments were performed using a 2:1 THF:toluene solution of NCs (0.9 μM), 0.05 M $[Bu_4N][PF_6]$, and 0.15 M trioctylphosphineoxide (TOPO). Photodoping used continuous 50 mW/cm^2 405 nm irradiation and $Na[Et_3BH]$ (200 μM) as the hole quencher. CB electrons are compensated by Na^+ and H^+.[21] **(B)** Transient potentiometric (E_F, solid) and excitonic absorption (A/A_0, dashed, λ = 590 nm) data collected simultaneously, using 0 (red) and 60 μM (black) $[Cp_2Co][PF_6]$, before (t < 0) and during ($t \geq 0$) 405 nm irradiation with constant stirring. E_F is referenced to the Fc^+/Fc couple. **(C)** Plot of E_F *vs* <n> from the data of panel B. <n> was calculated from <n> = 2 x (1 - A/A_0).

Despite yielding the same results, potentiometry offers an important advantage over the ORI method: Potentiometry circumvents the need for a transparent spectroscopic window in which to monitor the ORI (*e.g.*, for Cp_2Co, $\lambda_{probe} \approx 500$ nm). Because of this advantage, the redox potentials of narrower-gap NCs can be readily monitored potentiometrically, making this

the more general approach. As proof of concept, potentiometry and absorption were measured simultaneously during photodoping of CdSe NCs (with absorption overlapping that of Cp_2Co). Figure 3.3.A plots electronic absorption spectra of undoped and maximally photodoped d = 4.1 nm CdSe NCs, photoexcited at 405 nm in the presence of $Na[Et_3BH]$ (hole quencher[20]), $[Bu_4N][PF_6]$ (electrolyte), and TOPO (NC stabilizer). Photodoping causes the first NC excitonic transition to bleach to $A/A_0 \approx 0.3$ (A_0 = absorbance before photodoping) and redshift slightly, consistent with prior results.[20] From the established linear relationship between $\langle n \rangle$ and A/A_0,[20,29] these data imply $\langle n_{max} \rangle = 1.4$, again consistent with previous results.[20] Note that the CdSe NC photodoping experiment is considerably quicker than the ZnO NC photodoping experiment (Figure 3.2) because of ~5 times greater photoexcitation rates, greater conversion yields using $[Et_3BH]^-$ hole quenchers,[21] and smaller $\langle n_{max} \rangle$ in the CdSe NCs.

Figure 3.3.B plots E_F and A/A_0 data collected transiently during CdSe NC photodoping for two experiments, one performed with Cp_2Co^+ as an internal redox standard and the other without Cp_2Co^+. Prior to irradiation, E_F and A/A_0 are both constant, but E_F is ~100 mV more positive in the sample containing Cp_2Co^+. This difference reflects a small amount of Cp_2Co^+ reduction prior to deliberate CdSe irradiation. Upon irradiation of the sample without Cp_2Co^+, E_F immediately shifts more negative, reaching a value near –1.52 V vs Fc^+/Fc after 4 min. Similarly, A/A_0 decreases immediately, reaching a new value of ~0.3. Upon irradiation of the sample with Cp_2Co^+, E_F again immediately shifts more negative, reaching a similar value near –1.52 V *vs* Fc^+/Fc after 4 min. Interestingly, the onset of CdSe photodoping (as indicated by the inflection in A/A_0) is clearly delayed by ~40 s in the presence of Cp_2Co^+, even though E_F starts shifting more negative immediately upon photoexcitation. This delayed photodoping reflects electron equilibration between the CdSe NCs and Cp_2Co^+/Cp_2Co redox couple, which initially strongly favors Cp_2Co^+ reduction. Reduction of Cp_2Co^+ by photodoped CdSe NCs continues until the CdSe CB-edge potential is reached, at which point both Cp_2Co^+ reduction and CdSe NC electron accumulation proceed simultaneously with further photoexcitation. This observation is an example of the new insights that can be gained from potentiometry in the time domain.

Figure 3.3.C plots E_F *vs* $\langle n \rangle$ for both experiments of Figure 3.3.B. Although E_F is very different for the two samples prior to photodoping, the onset of CdSe NC reduction occurs at ~ –1.47 V (± 0.01 V) in both experiments. Once CB electrons begin to accumulate, the change in E_F between $\langle n \rangle = 0$ and $\langle n \rangle = 1$ is small, with a slope of ~ –10 mV/$\langle n \rangle$. The slope of E_F *vs* $\langle n \rangle$

increases as $\langle n_{max} \rangle$ is approached, and photodoping maximizes at $\langle n_{max} \rangle \sim 1.4$ and ~ –1.52 V (± 0.01 V) for both experiments. Plotted in this manner, the electrochemical data from these two experiments, which initially appeared markedly different (Figure 3.3.B), are now essentially superimposable. From this result we conclude that the CdSe CB-edge potential is independent of the presence of Cp_2Co^+ under these conditions.

Comparing E_F data (Figures 3.2.B and 3.3.C), we note that the CdSe NCs at $\langle n \rangle = 1$ are ~260 mV more reducing than the ZnO NCs at $\langle n \rangle = 1$ (–1.48 *vs* –1.22 eV, respectively). This difference is notably smaller than would be estimated from bulk data (~1.47 eV, see Appendix B), but it still indicates a driving force for inter-NC ET. To illustrate, a mixture of similar CdSe and ZnO NCs was prepared containing Li[Et_3BH] as the hole quencher, with all conditions similar to those of Figures 3.2 and 3.3. Figure 3.4 shows absorption spectra of this solution collected after selective CdSe photoexcitation for various durations. The broad NIR (< 2 eV) absorption characteristic of *n*-ZnO (Figure 3.2.A) grows with photoexcitation time. The CdSe excitonic absorption maximum redshifts by ~20 meV over the same time window, but there is no evident bleach, allowing attribution of this shift to a Stark effect tentatively associated with surface charge redistribution. Control experiments performed in the absence of CdSe NCs (see Appendix B) show no spectroscopic changes, ruling out direct ZnO photodoping under these conditions. The absence of CdSe excitonic absorption bleach and growth of ZnO NIR absorbance indicate that photodoped CdSe NCs indeed transfer their electrons to ZnO NCs under these conditions, as anticipated from the favorable ET driving force measured electrochemically.

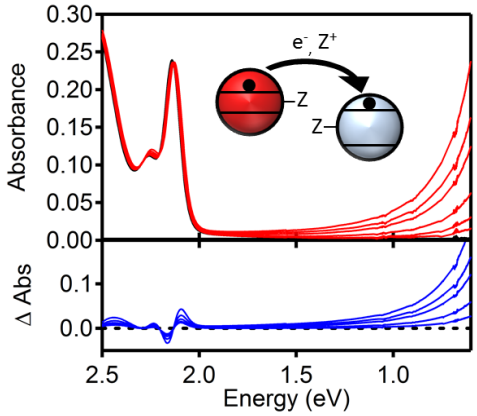

Figure 3.4. CdSe-ZnO inter particle electron transfer

Top: Electronic absorption spectra of a mixture of d = 3.8 nm CdSe NCs (1.25 μM), d = 9.6 nm ZnO NCs (2 μM), and Li[Et_3BH] (660 μM), collected after various durations of

selective CdSe NC photoexcitation (broad-band, $\lambda > 480$ nm). Bottom: Difference spectra ($A - A_0$). For clarity, the data are plotted against energy (eV).

During the course of these experiments, several interesting complexities were noted. First, as anticipated from prior observations,[16,18] CdSe NC redox potentials are found to be extraordinarily sensitive to sample preparation and measurement conditions, varying reproducibly by hundreds of mV depending on the specific details. Consequently, the redox potentials reported here reflect the particular reaction conditions employed, just as standard reduction potentials ($E°$) of molecular reagents correspond to a standard set of conditions. These observations will be described in detail in a subsequent report, but this preliminary observation already highlights the utility of this technique for identifying sample-specific redox potentials through *in situ* measurements. Additionally, we found it possible to measure the potentials of sub-CB electron traps in CdSe NCs by combining potentiometry with photoluminescence spectroscopy (PL, see Appendix B). Here, we observe PL brightening as E_F is raised, starting at least 120 mV below the CB edge, before the characteristic darkening that coincides with CB filling and the resulting Auger recombination.[20] NC PL brightening at sub-CB potentials is consistent with several recent observations[32-35] and indicates reductive passivation of surface electron traps. We note that in some cases CdSe NC surface-trap reduction appears to have exactly the opposite effect of quenching PL,[18,20,36] reflecting the complexity of these surface chemistries and highlighting the need for *in situ* electrochemical measurements.

3.4 Conclusion

Overall, the results presented here demonstrate potentiometry as a powerful and broadly applicable approach to semiconductor NC electrochemistry. With this approach, it is possible to quantify band-edge potentials *in situ*, without special apparatus or modification of NC surface chemistries. The impact of NC composition (isovalent or aliovalent impurities, *etc.*),[37-39] charge-compensating cations (H^+, Li^+, $[CoCp_2]^+$, *etc.*),[1,2,7,40] or NC surface ligands (with dipoles, conjugation, *etc.*)[16,18,41] should be readily quantified, and extension to other redox-active NC heterostructures[3,23] or non-photochemical reductants appears equally promising. The transient potentiometry described by Figures 2 and 3 further suggests interesting possibilities for probing

dynamical processes. NC potentiometry thus opens new opportunities for future fundamental and applied research involving redox-active colloidal semiconductor NCs.

3.5 References

(1) Duonghong, D.; Ramsden, J.; Grätzel, M.: Dynamics of Interfacial Electron-Transfer Processes in Colloidal Semiconductor Systems. *J. Am. Chem. Soc.* **1982**, *104*, 2977-2985.

(2) Nenadović, M. T.; Rajh, T.; Mićić, O. I.; Nozik, A. J.: Electron Transfer Reactions and Flat-Band Potentials of WO_3 Colloids. *J. Phys. Chem.* **1984**, *88*, 5827-5830.

(3) Jakob, M.; Levanon, H.; Kamat, P. V.: Charge Distribution between UV-Irradiated TiO_2 and Gold Nanoparticles: Determination of Shift in the Fermi Level. *Nano Letters* **2003**, *3*, 353-358.

(4) Huang, J.; Stockwell, D.; Huang, Z.; Mohler, D. L.; Lian, T.: Photoinduced Ultrafast Electron Transfer from CdSe Quantum Dots to Re-bipyridyl Complexes. *J. Am. Chem. Soc.* **2008**, *130*, 5632-5633.

(5) Han, Z.; Qiu, F.; Eisenberg, R.; Holland, P. L.; Krauss, T. D.: Robust Photogeneration of H2 in Water Using Semiconductor Nanocrystals and a Nickel Catalyst. *Science* **2012**, *338*, 1321-1324.

(6) Jensen, S. C.; Homan, S. B.; Weiss, E. A.: Photocatalytic Conversion of Nitrobenzene to Aniline through Sequential Proton-Coupled One-Electron Transfers from a Cadmium Sulfide Quantum Dot. *J. Am. Chem. Soc.* **2016**, in press (DOI:10.1021/jacs.5b11353).

(7) Schimpf, A. M.; Knowles, K. E.; Carroll, G. M.; Gamelin, D. R.: Electronic Doping and Redox-Potential Tuning in Colloidal Semiconductor Nanocrystals. *Accts. Chem. Res.* **2015**, *48*, 1929-1937.

(8) Ning, Z.; Voznyy, O.; Pan, J.; Hoogland, S.; Adinolfi, V.; Xu, J.; Li, M.; Kirmani, A. R.; Sun, J.-P.; Minor, J.; Kemp, K. W.; Dong, H.; Rollny, L.; Labelle, A.; Carey, G.; Sutherland, B.; Hill, I.; Amassian, A.; Liu, H.; Tang, J.; Bakr, O. M.; Sargent, E. H.: Air-stable n-type colloidal quantum dot solids. *Nat. Mater.* **2014**, *13*, 822-828.

(9) Chuang, C.-H. M.; Brown, P. R.; Bulović, V.; Bawendi, M. G.: Improved performance and stability in quantum dot solar cells through band alignment engineering. *Nat. Mater.* **2014**, *13*, 796-801.

(10) Haram, S. K.; Quinn, B. M.; Bard, A. J.: Electrochemistry of CdS Nanoparticles: A Correlation between Optical and Electrochemical Band Gaps. *J. Am. Chem. Soc.* **2001**, *123*, 8860-8861.

(11) Inamdar, S. N.; Ingole, P. P.; Haram, S. K.: Determination of Band Structure Parameters and the Quasi-Particle Gap of CdSe Quantum Dots by Cyclic Voltammetry. *ChemPhysChem* **2008**, *9*, 2574-2579.

(12) Amelia, M.; Lincheneau, C.; Silvi, S.; Credi, A.: Electrochemical properties of CdSe and CdTe quantum dots. *Chem. Soc. Rev.* **2012**, *41*, 5728-5743.

(13) Kucur, E.; Riegler, J.; Urban, G. A.; Nann, T.: Determination of quantum confinement in CdSe nanocrystals by cyclic voltammetry. *J. Chem. Phys.* **2003**, *119*, 2333-2337.

(14) Querner, C.; Reiss, P.; Sadki, S.; Zagorska, M.; Pron, A.: Size and ligand effects on the electrochemical and spectroelectrochemical responses of CdSe nanocrystals. *Phys. Chem. Chem. Phys.* **2005**, *7*, 3204-3209.

(15) Vanmaekelbergh, D.; Liljeroth, P.: Electron-conducting quantum dot solids: novel materials based on colloidal semiconductor nanocrystals. *Chem. Soc. Rev.* **2004**, *34*, 299-312.

(16) Brown, P. R.; Kim, D.; Lunt, R. R.; Zhao, N.; Bawendi, M. G.; Grossman, J. C.; Bulović, V.: Energy Level Modification in Lead Sulfide Quantum Dot Thin Films through Ligand Exchange. *ACS Nano* **2014**, *8*, 5863-5872.

(17) Jeong, K. S.; Deng, Z.; Keuleyan, S.; Liu, H.; Guyot-Sionnest, P.: Air-Stable n-Doped Colloidal HgS Quantum Dots. *J. Phys. Chem. Lett.* **2014**, *5*, 1139-1143.

(18) Wang, C.; Shim, M.; Guyot-Sionnest, P.: Electrochromic Nanocrystal Quantum Dots. *Science* **2001**, *291*, 2390-2392.

(19) Scanlon, M. D.; Peljo, P.; Mendez, M. A.; Smirnov, E.; Girault, H. H.: Charging and discharging at the nanoscale: Fermi level equilibration of metallic nanoparticles. *Chem. Sci.* **2015**, *6*, 2705-2720.

(20) Rinehart, J. D.; Schimpf, A. M.; Weaver, A. L.; Cohn, A. W.; Gamelin, D. R.: Photochemical Electronic Doping of Colloidal CdSe Nanocrystals. *J. Am. Chem. Soc.* **2013**, *135*, 18782-18785.

(21) Schimpf, A. M.; Gunthardt, C. E.; Rinehart, J. D.; Mayer, J. M.; Gamelin, D. R.: Controlling Carrier Densities in Photochemically Reduced Colloidal ZnO Nanocrystals: Size Dependence and Role of the Hole Quencher. *J. Am. Chem. Soc.* **2013**, *135*, 16569-16577.

(22) Haase, M.; Weller, H.; Henglein, A.: Photochemistry and radiation chemistry of colloidal semiconductors. 23. Electron storage on zinc oxide particles and size quantization. *J. Phys. Chem.* **1988**, *92*, 482-487.

(23) Wood, A.; Giersig, M.; Mulvaney, P.: Fermi Level Equilibration in Quantum Dot−Metal Nanojunctions. *J. Phys. Chem. B* **2001**, *105*, 8810-8815.

(24) Shim, M.; Guyot-Sionnest, P.: n-type colloidal semiconductor nanocrystals. *Nature* **2000**, *407*, 981-983.

(25) Shim, M.; Guyot-Sionnest, P.: Organic-Capped ZnO Nanocrystals: Synthesis and n-Type Character. *J. Am. Chem. Soc.* **2001**, *123*, 11651-11654.

(26) Liu, W. K.; Whitaker, K. M.; Smith, A. L.; Kittilstved, K. R.; Robinson, B. H.; Gamelin, D. R.: Room-Temperature Electron Spin Dynamics in Free-Standing ZnO Quantum Dots. *Phys. Rev. Lett.* **2007**, *98*, 186804.

(27) Carroll, G. M.; Schimpf, A. M.; Tsui, E. Y.; Gamelin, D. R.: Redox Potentials of Colloidal n-Type ZnO Nanocrystals: Effects of Confinement, Electron Density, and Fermi-Level Pinning by Aldehyde Hydrogenation. *J. Am. Chem. Soc.* **2015**, *137*, 11163-11169.

(28) Zong, X.; Wu, G.; Yan, H.; Ma, G.; Shi, J.; Wen, F.; Wang, L.; Li, C.: Photocatalytic H2 Evolution on MoS2/CdS Catalysts under Visible Light Irradiation. *J. Phys. Chem. C* **2010**, *114*, 1963-1968.

(29) Shim, M.; Wang, C.; Guyot-Sionnest, P.: Charge-Tunable Optical Properties in Colloidal Semiconductor Nanocrystals. *J. Phys. Chem. B* **2001**, *105*, 2369-2373.

(30) Licht, S.: Multiple Band Gap Semiconductor/Electrolyte Solar Energy Conversion. *J. Phys. Chem. B* **2001**, *105*, 6281-6294.

(31) Lenglet, M.; Jørgensen, C. K.: Reinvestigation of the optical properties of Co3O4. *Chem. Phys. Lett.* **1994**, *229*, 616-620.

(32) Jha, P. P.; Guyot-Sionnest, P.: Electrochemical Switching of the Photoluminescence of Single Quantum Dots. *J. Phys. Chem. C* **2010**, *114*, 21138-21141.

(33) Galland, C.; Ghosh, Y.; Steinbruck, A.; Sykora, M.; Hollingsworth, J. A.; Klimov, V. I.; Htoon, H.: Two types of luminescence blinking revealed by spectroelectrochemistry of single quantum dots. *Nature* **2011**, *479*, 203-207.

(34) Weaver, A. L.; Gamelin, D. R.: Photoluminescence Brightening via Electrochemical Trap Passivation in ZnSe and Mn^{2+}-Doped ZnSe Quantum Dots. *J. Am. Chem. Soc.* **2012**, *134*, 6819-6825.

(35) Rinehart, J. D.; Weaver, A. L.; Gamelin, D. R.: Redox Brightening of Colloidal Semiconductor Nanocrystals Using Molecular Reductants. *J. Am. Chem. Soc.* **2012**, *134*, 16175-16177.

(36) Gooding, A. K.; Gomez, D. E.; Mulvaney, P.: The Effects of Electron and Hole Injection on the Photoluminescence of CdSe/CdS/ZnS Nanocrystal Monolayers. *ACS Nano* **2008**, *2*, 669-676.

(37) Cohn, A. W.; Kittilstved, K. R.; Gamelin, D. R.: Tuning the Potentials of "Extra" Electrons in Colloidal n-Type ZnO Nanocrystals via Mg^{2+} Substitution. *J. Am. Chem. Soc.* **2012**, *134*, 7937-7943.

(38) Zhou, D.; Kittilstved, K. R.: Control over Fe^{3+} speciation in colloidal ZnO nanocrystals. *J. Mater. Chem. C* **2015**, *3*, 4352-4358.

(39) Schimpf, A. M.; Lounis, S. D.; Runnerstrom, E. L.; Milliron, D. J.; Gamelin, D. R.: Redox Chemistries and Plasmon Energies of Photodoped In_2O_3 and Sn-Doped In_2O_3 (ITO) Nanocrystals. *J. Am. Chem. Soc.* **2015**, *137*, 518-524.

(40) Valdez, C. N.; Braten, M.; Soria, A.; Gamelin, D. R.; Mayer, J. M.: Effect of Protons on the Redox Chemistry of Colloidal Zinc Oxide Nanocrystals. *J. Am. Chem. Soc.* **2013**, *135*, 8492-8495.

(41) Frederick, M. T.; Weiss, E. A.: Relaxation of Exciton Confinement in CdSe Quantum Dots by Modification with a Conjugated Dithiocarbamate Ligand. *ACS Nano* **2010**, *4*, 3195-3200.

Chapter 4. Spectroelectrochemical Measurement of Electrostatic Surface Dipole Contributions to Colloidal CdSe Nanocrystal Band-Edge Potentials.

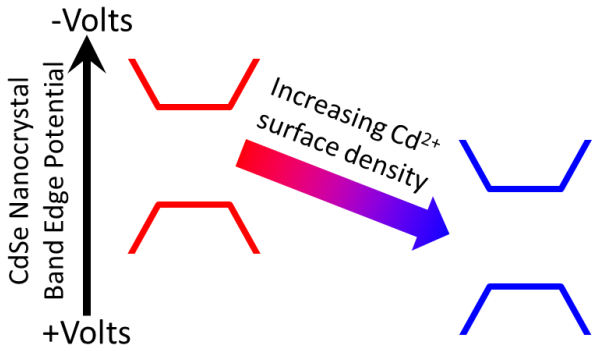

Adapted from: Carroll, G. M.; Tsui, E.Y; Brozek, C. K.; and Gamelin, D. R. *Submitted*

4.1 Overview

Understanding and controlling the redox properties of colloidal semiconductor nanocrystals is critical for application of this class of materials in many proposed technologies. Here, we use spectroelectrochemical potentiometry to analyze the redox potentials of free-standing colloidal *n*-type CdSe nanocrystals. We show that both the redox potentials and the maximum number of conduction-band electrons that can be accumulated through photodoping are strongly affected by the nanocrystal's surface stoichiometry, varying reproducibly by over 400 meV with changes in relative Cd^{2+}:Se^{2-} surface concentration. The data suggest that Se^{2-} binding induces surface dipoles that shift the CdSe nanocrystal band-edge potentials more negative, and that these dipoles are eliminated upon Cd^{2+} binding. These results demonstrate the importance of nanocrystal surface stoichiometry in applications involving tuned nanocrystal redox potentials, band-edge alignment, or electron-transfer driving forces.

4.2 Introduction

The band-edge potentials of semiconductor nanocrystals (NCs) are critical parameters in NC-based optoelectronic,[1,2] photovoltaic,[3-6] and photocatalytic[7-10] technologies. Although the effects of quantum confinement on NC band-edge potentials are well understood,[11-13] the roles of the surfaces are less clear. Photoelectron spectroscopy has revealed that surface ligands on PbS NCs can shift the NC band-edge potentials as much as 1 V, interpreted in terms of the magnitudes and directions of interfacial dipoles.[5] This unique tunability has been exploited to tailor the band-edge offsets in NC photovoltaic devices, enabling high power-conversion efficiencies for PbS NC-based PV.[3,4,14,15] Similarly, electronic doping of colloidal semiconductor NCs is also extremely sensitive to the NC surface chemistries.[16-20] Differences in charge-compensating counter ions (*e.g.*, Li^+, H^+, $[CoCp_2]^+$) can tune the band-edge potentials of free-standing colloidal ZnO NCs by as much as 0.5 V,[19] and surface Hg^{2+} or S^{2-} enrichment can shift the band-edge potentials of HgS NC films by over 300 mV.[18] These effects rival or exceed the magnitude of band-edge potential tuning accessible *via* quantum confinement. Quantifying the shifts in NC band-edge potentials is not trivial, however. Typical solution-based voltammetric techniques provide fair agreement between electrochemical and optical bandgap energies,[11,21-24] but complications from NC insolubility, inhomogeneity, redox irreversibility, and NC surface defects frequently lead to imprecise or irreproducible values of the band-edge potentials.[11] Voltammetric spectroelectrochemical measurements of NC films on electrodes provide a valuable measure of NC band-edge potentials,[25-28] but these measurements can be strongly influenced by parameters of the films, such as thickness or inter-particle void sizes,[25] and these measurements often require ligand exchange to improve carrier mobility or cross-link NCs, limiting the ability to probe the effects of the NC surfaces themselves.

Here, we describe the effects of surface-ion stoichiometry on the redox properties of free-standing colloidal CdSe NCs. CdSe NC photodoping[29] with borohydride reductants (*e.g.*, $Na[Et_3BH]$) is used as a contactless way to tune the NC Fermi level (E_F). *In situ* spectroelectrochemical potentiometry[29,30] is then used as a non-invasive probe of NC Fermi levels and average conduction-band (CB) electron occupancies ($\langle n \rangle$), allowing quantification of the effects of surface perturbations on the NC redox properties. Using this approach, we quantify the Fermi levels of free-standing colloidal CdSe NCs as their surface compositions are tuned

from Se^{2-}-enriched to Cd^{2+}-enriched. We find that the maximum E_F (E_F^{max}) and the maximum average number of CB electrons ($<n_{max}>$) achievable *via* photodoping are both strongly dependent on the surface densities of Se^{2-} and Cd^{2+} ions. We show that CdSe NC band-edge potentials can be shifted reproducibly by ~400 mV with changes in surface stoichiometry. By measuring E_F at different electrolyte concentrations, we show that this band-edge tuning is linked to interface dipoles. These results demonstrate facile tuning of CdSe NC band-edge potentials *via* NC surface stoichiometry, with broad implications for application of NCs as photo-redox or electron-transfer reagents.

4.3 Results and Analysis

Figure 4.1a plots the electronic absorption spectra of undoped and maximally photodoped d = 5.4 nm Se^{2-}-enriched (1.39:1 surface Se^{2-}:Cd^{2+}, see Appendix C) CdSe NCs. Prior to photoexcitation, the NCs are undoped, but upon illumination in the presence of the reductant $Na[Et_3BH]$, the first excitonic absorption band bleaches slightly to reach a new value of A/A_0 = 0.9 (A_0 = absorbance before photodoping) at maximum photodoping, indicating the introduction of delocalized CB electrons into the ensemble of CdSe NCs.[17,31,32] Repeating the same experiment on the same NCs but in the presence of excess $Cd(oleate)_2$ results in a much greater excitonic bleach, reaching A/A_0 = 0.2 at maximum photodoping. A small redshift of the exciton is observed with photodoping and tentatively attributed to a Stark shift (see Supporting Information).[29,30] Similar red shifts have been observed in the trion photoluminescence of transiently charged CdSe quantum dots.[33,34] From the linear relationship between the excitonic bleach and the average electron occupancy (average number of CB electrons per NC, $<n>$),[29,35] these values of A/A_0 reflect maximum electron occupancies of $<n_{max}>$ = 0.2 and 1.6 for the Se^{2-}-enriched and Cd^{2+}-enriched NCs, respectively.

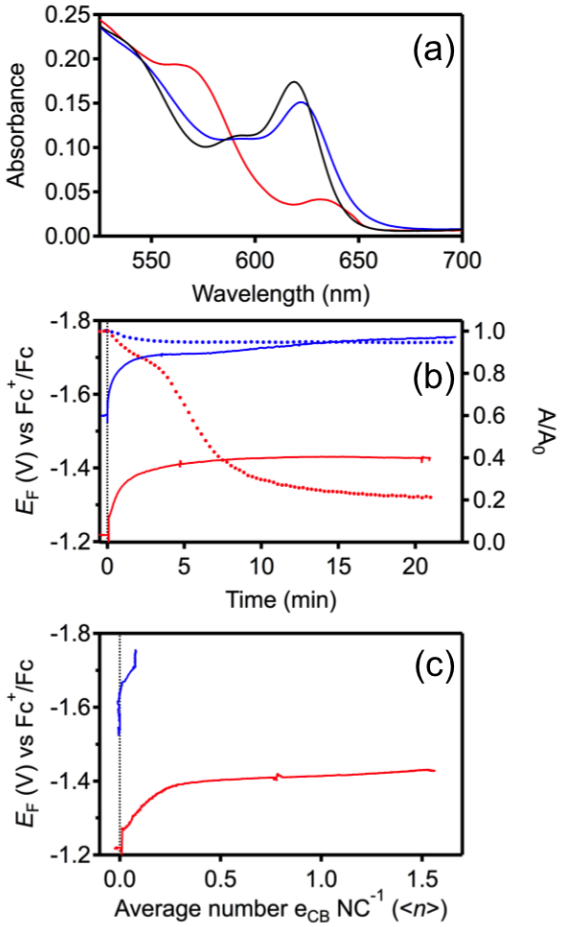

Figure 4.1. Surface stoichiometry dependence on *n*-type CdSe NCs

(a) Electronic absorption spectra of Se^{2-}-enriched d = 5.4 nm CdSe NCs (0.3 μM) before photodoping (black) and after maximum photodoping (blue). The red curve shows the absorption spectrum of the same NCs photodoped to the maximum extent in the presence of 1500 equiv. of $Cd(oleate)_2$ per NC. **(b)** Transient potentiometric (E_F, solid) and excitonic absorbance (A/A_0, dotted, λ = 620 nm) data measured before (t < 0) and during ($t \geq 0$) 405 nm photoexcitation of the same d = 5.4 nm CdSe NCs from panel (a). The blue curve describes the Se^{2-}-enriched NCs and the red curve describes the same NCs in the presence of 1500 equiv. of added $Cd(oleate)_2$. **(c)** Plot of E_F *vs* <n> from the data of panel (b). <n> was calculated as <n> = $2(1 - A/A_0)$. The NCs were suspended in 2:1 THF/toluene with 0.05 M $[Bu_4N][PF_6]$, 0.15 M trioctylphosphine oxide (TOPO), 30 μM $Na[Et_3BH]$ as the reductant, and 60 μM $[Cp_2Co][PF_6]$ as an internal electrochemical

standard. Experiments were performed under continuous stirring. E_F is referenced to the Fc^+/Fc couple.

Figure 4.1b plots E_F and A/A_0 data collected during photodoping for the same two CdSe NC samples as used for Figure 4.1a. Prior to photodoping ($t < 0$), E_F is ~300 mV more negative for the Se^{2-}-enriched NCs than for the Cd^{2+}-enriched NCs. This difference is attributed to a small amount of photodoping by exposure to room light; E_F of Se^{2-}-enriched CdSe NCs kept in the dark does not change when $Cd(oleate)_2$ is added (see Appendix C). Upon NC photoexcitation ($t \geq 0$), E_F becomes increasingly negative for both samples. E_F for the Se^{2-}-enriched CdSe NCs shifts by ~ -250 mV, from -1.52 to a maximum of E_F^{max} = -1.77 V, whereas E_F for the Cd^{2+}-enriched NCs shifts by only ~ -180 mV, from -1.22 V to E_F^{max} = -1.43 V. In agreement with Figure 4.1a, A/A_0 for the Se^{2-}-enriched CdSe NCs decreases steadily until it plateaus at ~0.95 ($<n_{max}> \approx 0.1$), and for the Cd^{2+}-enriched CdSe NCs it plateaus at ~0.2 ($<n_{max}> \approx 1.6$). These results show a striking dependence of the NC photodoping on surface stoichiometry.

To examine the difference between the photodoping of Se^{2-}- and Cd^{2+}-enriched CdSe NCs in more detail, Figure 4.1c plots E_F *vs* $<n>$ for each sample from the data in Figure 4.1b. From Figure 4.1c, photoexcitation of the Se^{2-}-enriched CdSe NCs initially raises E_F slightly without depositing any CB electrons. Then, at E_F ~ -1.68 V, electrons begin to appear in the CdSe NC CB, reaching $<n_{max}>$ ~ 0.1. Continued photoexcitation does not deposit more CB electrons, but E_F continues to shift increasingly more negative. We interpret this observation as reflecting surface electron trap formation upon Se^{2-} surface enrichment.[36] The shift of E_F with surface electron trapping is discussed below. For the Cd^{2+}-enriched CdSe NCs, photoexcitation again raises E_F slightly without depositing CB electrons, and then at E_F ~ -1.28 V, CB electrons begin to appear. The slope of E_F *vs* $<n>$ is relatively shallow (~40 mV/e^-_{CB}) between $<n>$ = 0.3 and 1.5, at which point the NCs reach their photodoping maximum.

Quantum confinement alone cannot account for the large differences in E_F and $<n_{max}>$ between the Se^{2-}- and Cd^{2+}-enriched CdSe NCs described in Figure 4.1. Increasing the NC diameter through Cd^{2+} adsorption should shift the CB band-edge potential more positive by relaxing quantum confinement, and larger CdSe NCs do indeed show larger values of $<n_{max}>$,[25,29] but the first excitonic absorption band shows only a relatively small decrease in energy upon addition of $Cd(oleate)_2$ (Figure 4.1a), and the estimated CB shift upon addition of

one Cd^{2+} monolayer to d = 5.4 nm CdSe NCs is < 20 meV,[12] well below the difference of ~350 mV in CB band-edge potentials observed in Figure 4.1c. Instead, the data in Figure 4.1 indicate that the CB band-edge potential is strongly dependent upon the NC surface stoichiometry.

To probe the effects of CdSe NC surface composition systematically, experiments were performed in which different amounts of Cd^{2+} were added to Se^{2-}-enriched CdSe NCs, and the photodoping examined by spectroelectrochemical potentiometry. Figure 4.2 summarizes data collected for NCs of two sizes. Figure 4.2a plots E_F^{max} (measured when E_F no longer changes from increased photoexcitation) for each NC sample as a function of added Cd^{2+}. Notably, the dependence of E_F^{max} on added Cd^{2+} is nearly identical for the two CdSe NC samples when the data are plotted normalized to NC surface area (or surface density of added Cd^{2+}), as shown here. For comparison, the same data plotted against the number of Cd^{2+} per NC are presented as Appendix C. Figure 4.2a shows that without any added Cd^{2+}, E_F^{max} reaches ~ -1.75 V *vs* Fc^+/Fc for both NC sizes. As Cd^{2+} is added, E_F^{max} becomes more positive with a slope of ~ -39 mV $Cd^{-1}nm^{-2}$, eventually plateauing at -1.4 V when the added Cd^{2+} concentration equals ~10 nm^{-2}. Above 10 nm^{-2}, addition of more Cd^{2+} results in no change to E_F^{max}. The relationship between E_F^{max} and surface density of added Cd^{2+} is discussed below.

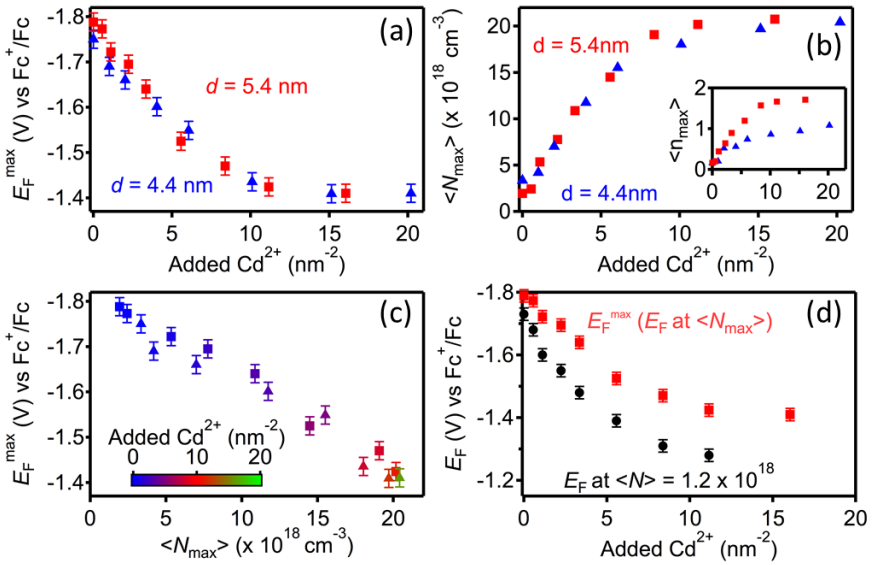

Figure 4.2. Cd^{2+} titration of photodoped Se^{2-}-enriched CdSe NCs

(a) Maximum Fermi level (E_F^{max}) measured potentiometrically during photodoping of d = 4.4 nm (blue, triangles) and d = 5.4 nm (red, squares) Se^{2-}-enriched CdSe NCs, plotted *vs* added $Cd(oleate)_2$ in units of added Cd^{2+} per NC surface area. The error bars indicate the uncertainty in the Cp_2Co^+/Cp_2Co half-wave potential. **(b)** Average maximum electron density ($<N_{max}>$) in photodoped d = 4.5 nm (blue, triangles) and 5.4 nm (red, squares) Se^{2-}-enriched CdSe NCs plotted *vs* added Cd^{2+} per NC surface area. The inset shows the same data plotted as $<n_{max}>$ *vs* added Cd^{2+} per NC surface area. **(c)** Plot of the E_F^{max} data from Figure 2a *vs* the $<N_{max}>$ data from Figure 2b. The colors of the markers relate to the scale bar shown in the inset and indicate added Cd^{2+} per NC surface area. **(d)** Plots of E_F *vs* added $Cd(oleate)_2$ Cd^{2+} per NC surface area for Se^{2-}-enriched d = 5.4 nm CdSe NCs, measured at $<N>$ = 1.2 x 10^{18} cm^{-3} ($<n>$ = 0.1) (black circles) and at $<N_{max}>$ (red squares). All experiments were carried out under continuous 405 nm photoexcitation in air-free 2:1 THF/toluene solutions with 0.03 μM CdSe NCs, 0.05 M $[Bu_4N][PF_6]$, 100 μM $[Cp_2Co][PF_6]$ as an internal electrochemical standard, 0.15 M trioctylphosphine oxide (TOPO) as a stabilizer, and 30 μM $Na[Et_3BH]$ as the reductant. E_F is referenced to the Fc^+/Fc redox couple.

Figure 4.2b plots the maximum average electron density ($<N_{max}>$) for the same NC samples from Figure 4.2a, measured as a function of added Cd^{2+} per NC surface area. Before

Cd^{2+} addition, $\langle N_{max} \rangle$ for both NC diameters is ~2 x 10^{18} cm^{-3}. Upon addition of Cd^{2+}, $\langle N_{max} \rangle$ increases steadily for both NC diameters, eventually plateauing at $\langle N_{max} \rangle$ = 2.2 x 10^{19} cm^{-3} above ~10 Cd^{2+} nm^{-2}. Plotting the same data as $\langle n_{max} \rangle$ *vs* added Cd^{2+} per NC surface area yields different maxima for the two NC diameters (Figure 4.2b, inset), consistent with our prior observations.[29] Volumetric scaling of $\langle n_{max} \rangle$ has also been reported for both photodoped and chemically reduced colloidal ZnO NCs,[19,37,38] but no analogous dependence on surface stoichiometry has been described. Figure 4.2 demonstrates that in these CdSe NCs, the surface stoichiometry appears to dictate both E_F^{max} and $\langle N_{max} \rangle$. Figure 4.2c plots the E_F^{max} data from Figure 4.2a against the $\langle N_{max} \rangle$ data from Figure 4.2b, with color coding to indicate Cd^{2+} enrichment level. This plot reveals a size-independent linear relationship between E_F^{max} and $\langle N_{max} \rangle$, with both properties dictated by the surface stoichiometry.

The (111) and (100) facet-averaged density of ions in stoichiometric zinc-blende CdSe corresponds to ~5.8 nm^{-2}, split evenly between cations and anions. From energy dispersive X-ray analysis (see Appendix C), the Se^{2-} surface densities of the Se^{2-}-enriched d = 5.4 and 4.4 nm CdSe NCs are 4.0 and 3.1 nm^{-2}, respectively, confirming Se^{2-} enrichment. As an independent confirmation, ^{1}H NMR measurements on d = 4.4 nm Se^{2-}-enriched CdSe NCs show a combined oleate and oleylamine surface ligand density of ~2.7 nm^{-2} (see Appendix C). These ligands are expected to bind exclusively to surface Cd^{2+} ions, and this result therefore suggests that the Se^{2-} surface density is between 3 and 4 nm^{-2}. Importantly, the surface Se^{2-} density represents an upper limit for additional $Cd(oleate)_2$ binding. Steric constraints and ligand crystallization limit the maximum total $Cd(oleate)_2$ surface density to ~3-4 nm^{-2},[39] which implies that only an additional ~1-2 $Cd(oleate)_2$ nm^{-2} can be added to the surfaces of our Se^{2-}-enriched NCs. The observation in Figure 4.2 that both E_F^{max} and $\langle N_{max} \rangle$ vary nearly linearly between an equivalent surface density of 0 and 10 Cd^{2+} nm^{-2} thus indicates that the binding efficiency of $Cd(oleate)_2$ is not unity. Neutral, two-electron L-type donor ligands such as oleylamine are known to remove Z-type metal-carboxylate units ($Cd(oleate)_2$) at the surfaces of CdSe NCs *via* the formation of soluble $L_nCd(oleate)_2$ species.[39,40] Competitive binding reactions between oleylamine, TOPO, and the added $Cd(oleate)_2$ are therefore expected. Given that E_F^{max} and $\langle N_{max} \rangle$ stop changing at an equivalent surface density only ~3-4 times greater than the theoretical maximum, the equilibrium binding constant for surface-bound $Cd(oleate)_2$ must be reasonably large.

For the same d = 5.4 nm CdSe NCs, Figure 4.2d plots E_F *vs* added Cd^{2+} measured (*i*) at $\langle N_{max} \rangle$, which is different for each Cd^{2+} addition, and (*ii*) at a fixed value of $\langle N \rangle$ ($\langle N \rangle$ = 1.2 x 10^{18} cm^{-3}), corresponding to $\langle n \rangle$ = 0.1. E_F at $\langle n \rangle$ = 0.1 is taken as a measure of the band-edge potential, E_{CB}. In both representations, E_F shows a dramatic positive shift as Cd^{2+} is added. The total shift in E_F at $\langle N_{max} \rangle$ is +380 mV, and in E_F at $\langle N \rangle$ = 1.2 x 10^{18} cm^{-3} is +440 mV. The raw data plotting E_F vs $\langle N \rangle$ for several Cd^{2+} additions are provided as Supporting Information in Appendix C.

Collectively, the data in Figure 4.2 demonstrate that NC surface composition plays an integral role in determining the band-edge potentials of colloidal CdSe NCs. Through the empirical relationship between CdSe NC diameter and the quantum confined band-edge potential, $E_{CB} = 2.97d^{-1.24} - 3.49$,[12] the calculated shift in E_{CB} between d = 4.4 and 5.4 nm CdSe NCs resulting from quantum confinement effects is ~110 meV, whereas the electrochemical range in E_{CB} for NCs of the same diameter but different surface stoichiometries is > 400 mV (Figure 4.2d). Moreover, E_F^{max} and $\langle N_{max} \rangle$ are indistinguishable for these two NC sizes when compared at any specific surface ion stoichiometry and under otherwise identical experimental conditions, indicating that surface stoichiometry overwhelmingly dominates the redox properties of these NCs.

Several factors could conceivably contribute to the positive shift in E_F with added $Cd(oleate)_2$. In bulk semiconductors, surface traps can pin Fermi levels near their own potentials.[41,42] Fermi-level pinning is not observed in bulk CdSe photoelectrodes at potentials < -1 V *vs* Fc^+/Fc when the surface is tuned from Cd^{2+}- to Se^{2-}-enriched,[43] however, arguing against this interpretation. Alternatively, ligands or NC surface stoichiometries are known to alter NC band-edge potentials through electrostatic surface dipoles.[5,12,15,18,44-46] The impact of surface dipoles on semiconductor band-edge potentials can be described using the Helmholtz relationship (eq. 4.1), where ΔV_n is the surface-potential change due to modification of the surface dipoles, μ describes the magnitude of the net dipole moment, N_{ss} is the dipole surface density (m^{-2}), $\cos\Theta$ accounts for dipole orientation relative to the surface, ε_0 is the permittivity of free space, and ε_d is the medium dielectric constant.[18,47,48]

$$\Delta E_F(\langle n \rangle) \approx \Delta V_n = \mu \times N_{ss} \times \cos\Theta / \varepsilon_0 \varepsilon_d \qquad (4.1)$$

The net dipole moment, μ, has contributions from interfacial dipoles formed between NC surface ions and bound ligands, intrinsic ligand dipole moments, and dipoles of other molecules interacting with the NC surfaces. In the present experiments, surface modification likely alters both the interfacial and intrinsic ligand dipole moments. As shown by photoelectron spectroscopy, electron affinities of d = 4.7 nm CdSe NCs ligated by primary amines can differ by ~200 meV from those of the same NCs ligated by oleates.[12] Although the NC ligand shell does indeed change from an amine/oleate mixture (Se^{2-}-enriched) to primarily oleates (Cd^{2+}-enriched) in these experiments, the magnitude of the shift observed here is even greater. We propose that NC surface-ion-induced electrostatic dipole moments are primarily responsible for the changes in E_F reported here. We hypothesize that surface Se^{2-} anions introduce dipoles pointing toward the CdSe NC center, destabilizing CB electrons and shifting E_F to more negative potentials. Upon Cd^{2+} binding, the Se^{2-}-induced dipole is reduced and E_F shifts positively.

To probe these electrostatic effects further, the dependence of E_F^{max} and $\langle n_{max} \rangle$ on electrolyte concentration was examined. Figure 4.3a plots E_F^{max} and $\langle n_{max} \rangle$ against the concentration of $[Bu_4N][PF_6]$, for the same photodoped d = 5.4 nm Se^{2-}- and Cd^{2+}-enriched CdSe NCs as in Figures 4.1 and 4.2 (11 Cd^{2+} nm^{-2}). In the dilute limit of $[Bu_4N][PF_6]$ (4 mM, $\log([Bu_4N][PF_6]\ NC^{-1}) = 4.3$), E_F^{max} for the Se^{2-}-enriched NCs is ~400 mV more negative than for the Cd^{2+}-enriched NCs, while $\langle n_{max} \rangle$ = 0.1 and 1.5 for the Se^{2-}- and Cd^{2+}-enriched NCs, respectively. As the concentration of $[Bu_4N][PF_6]$ is increased, E_F^{max} of the Se^{2-}-enriched NCs becomes more positive with an apparent logarithmic dependence of ~160 mV/decade. This slope is independent of the NC concentration (see Supporting Information). In stark contrast, for the Cd^{2+}-enriched NCs, increasing the $[Bu_4N][PF_6]$ concentration causes no change to E_F^{max} within experimental uncertainty. Because the NC ligation is largely unchanged in these experiments, changes in ligand-specific dipole moments can be ruled out as the cause of the shift in E_F^{max}. Moreover, the positive shift in E_F^{max} with increasing $[Bu_4N][PF_6]$ concentration observed for the Se^{2-}-enriched CdSe NCs is strong evidence for surface dipole moments associated with Se^{2-} surface ions. Increasing the electrolyte concentration stabilizes the CdSe NCs electrostatically and shifts E_F^{max} to more positive potentials, as illustrated schematically in Figure 4.3b. The electrolyte ions do not bind to the NC surfaces, and this effect can thus be interpreted as a manifestation of changes in the NC electrical double layer. For Cd^{2+}-enriched NCs, the observation that E_F^{max} does not change with increasing $[Bu_4N][PF_6]$ suggests not only that

surface dipoles are largely eliminated by addition of Cd^{2+}, but also that the CB electrons are well screened from the external environment in these Cd^{2+}-enriched NCs.

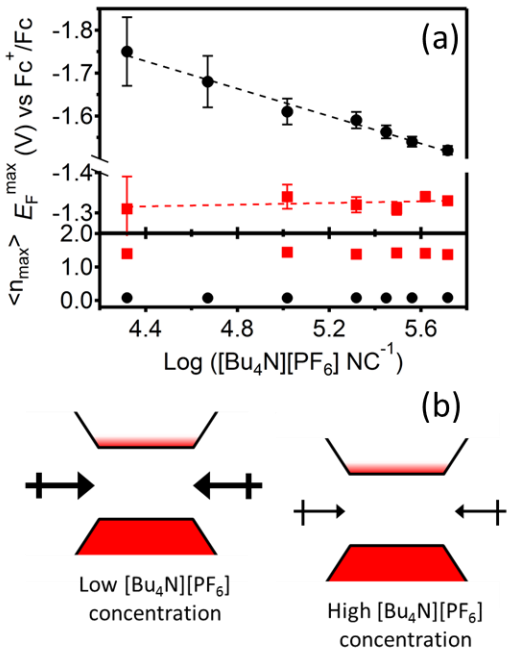

Figure 4.3. Electrolyte dependence variable surface *n*-type CdSe NCs

(a) Top: E_F^{max} values measured for photodoped Se^{2-}-enriched d = 5.4 nm CdSe NCs with (red, squares) and without (black, circles) the addition of excess $Cd(oleate)_2$ (11.2 nm^{-2}), plotted as a function of the ratio of the concentrations of electrolyte ([Bu_4N][PF_6]) and CdSe NCs. The dashed lines show linear best fits to the experimental data, and the error bars represent the uncertainty in the Cp_2Co^+/Cp_2Co half-wave potential. **Bottom:** $<n_{max}>$ for the same Se^{2-}-enriched d = 5.4 nm CdSe NCs with (red, squares) and without (black, circles) added $Cd(oleate)_2$, again plotted *vs* electrolyte concentration. All experiments were carried out in THF with 30 μM Na[Et_3BH] as the reductant. The CdSe NC concentration is 0.2 μM and the concentration of [Bu_4N][PF_6] ranges from 4 to 100 mM. [Fc*][PF_6] was added after the experiment as an internal electrochemical standard. E_F is referenced against the Fc^+/Fc redox couple. **(b)** Schematic illustration of the surface dipole reduction and concomitant band-edge shift observed for photodoped Se^{2-}-enriched CdSe NCs upon increasing the electrolyte concentration.

4.4 Discussion

Figure 4.4 summarizes the effect of surface stoichiometry on E_F and $<N>$ in colloidal CdSe NCs. When the CdSe NC surfaces are Se^{2-}-enriched, the electrons from the reductant occupy localized NC surface traps[36] rather than the NC CB. The reduced surface sites introduce electrostatic dipoles at the NC surfaces. From the Helmholtz equation, the change in potential should scale with the density of surface dipoles. When the NC surfaces are Cd^{2+}-enriched, the band-edge potentials shift more positive by ~400 mV. Despite a 20-fold increase in $<N_{max}>$ upon Cd^{2+} surface enrichment, E_F^{max} for the Cd^{2+}-enriched CdSe NCs is insensitive to the electrolyte concentration, indicating effective screening of the delocalized CB electrons from the NC environment in this limit.

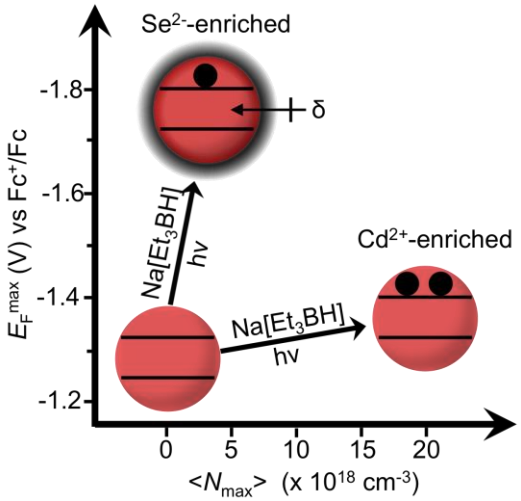

Figure 4.4. Schematic illustration of NC redox potential modulation from surface composition

The observation of widely tunable redox potentials in free-standing colloidal semiconductor NCs without corresponding changes in size or absorption spectra has important implications for understanding and controlling charge flow in photoinduced electron-transfer reactions, for example in quantum-dot-sensitized solar cells or solar H_2 generation.[10,49] In photochemical proton reduction to form H_2, the driving force for electron transfer between the NCs and protons reflects the potential difference between the CB edge and the proton reduction potential, and the results presented here thus suggest that this driving force may be tunable over

hundreds of meV through simple surface composition changes. It is reasonable to expect that other surface modifications will also affect such driving forces. For example, many recent descriptions of H^+ reduction with colloidal CdSe NCs involve surface-bound catalysts.[7,10,50] It is likely that catalyst attachment to the NC surface may itself alter the NC band-edge potentials and hence the driving force for proton reduction.

4.5 Conclusion

The redox potentials of colloidal *n*-type CdSe NCs have been measured *in situ* using potentiometry coupled with electronic absorption spectroscopy and NC photodoping. The CdSe NC band-edge potentials can be tuned by hundreds of meV through systematic alteration of the NC surface composition, corresponding to tunability of the maximum CB electron densities by over an order of magnitude under otherwise identical conditions. A linear relationship between E_F^{max} and $\langle N_{max} \rangle$ that is controlled by the ratio of surface Cd^{2+}:Se^{2-} ions has been identified. These changes in E_F are shown to originate from Se^{2-}-induced electrostatic dipoles at the NC surfaces.

4.6 References

(1) Talapin, D. V.; Lee, J.-S.; Kovalenko, M. V.; Shevchenko, E. V.: Prospects of Colloidal Nanocrystals for Electronic and Optoelectronic Applications. *Chem. Rev.* **2010**, *110*, 389-458.

(2) Kovalenko, M. V.; Manna, L.; Cabot, A.; Hens, Z.; Talapin, D. V.; Kagan, C. R.; Klimov, V. I.; Rogach, A. L.; Reiss, P.; Milliron, D. J.; Guyot-Sionnnest, P.; Konstantatos, G.; Parak, W. J.; Hyeon, T.; Korgel, B. A.; Murray, C. B.; Heiss, W.: Prospects of Nanoscience with Nanocrystals. *ACS Nano* **2015**, *9*, 1012-1057.

(3) Boles, M. A.; Ling, D.; Hyeon, T.; Talapin, D. V.: The surface science of nanocrystals. *Nat Mater* **2016**, *15*, 141-153.

(4) Ning, Z.; Voznyy, O.; Pan, J.; Hoogland, S.; Adinolfi, V.; Xu, J.; Li, M.; Kirmani, A. R.; Sun, J.-P.; Minor, J.; Kemp, K. W.; Dong, H.; Rollny, L.; Labelle, A.; Carey, G.; Sutherland, B.; Hill, I.; Amassian, A.; Liu, H.; Tang, J.; Bakr, O. M.; Sargent, E. H.: Air-stable n-type colloidal quantum dot solids. *Nat Mater* **2014**, *13*, 822-828.

(5) Brown, P. R.; Kim, D.; Lunt, R. R.; Zhao, N.; Bawendi, M. G.; Grossman, J. C.; Bulović, V.: Energy Level Modification in Lead Sulfide Quantum Dot Thin Films through Ligand Exchange. *ACS Nano* **2014**, *8*, 5863-5872.

(6) Carey, G. H.; Abdelhady, A. L.; Ning, Z.; Thon, S. M.; Bakr, O. M.; Sargent, E. H.: Colloidal Quantum Dot Solar Cells. *Chem. Rev.* **2015**, *115*, 12732-12763.

(7) Han, Z.; Qiu, F.; Eisenberg, R.; Holland, P. L.; Krauss, T. D.: Robust Photogeneration of H2 in Water Using Semiconductor Nanocrystals and a Nickel Catalyst. *Science* **2012**, *338*, 1321-1324.

(8) Wu, K.; Lian, T.: Quantum confined colloidal nanorod heterostructures for solar-to-fuel conversion. *Chem. Soc. Rev.* **2016**.

(9) Kalisman, P.; Nakibli, Y.; Amirav, L.: Perfect Photon-to-Hydrogen Conversion Efficiency. *Nano Lett.* **2016**, *16*, 1776-1781.

(10) Vaneski, A.; Schneider, J.; Susha, A. S.; Rogach, A. L.: Colloidal hybrid heterostructures based on II–VI semiconductor nanocrystals for photocatalytic hydrogen generation. *J. Photochem. Photobiol. C: Photochem. Rev.* **2014**, *19*, 52-61.

(11) Amelia, M.; Lincheneau, C.; Silvi, S.; Credi, A.: Electrochemical properties of CdSe and CdTe quantum dots. *Chem. Soc. Rev.* **2012**, *41*, 5728-5743.

(12) Jasieniak, J.; Califano, M.; Watkins, S. E.: Size-Dependent Valence and Conduction Band-Edge Energies of Semiconductor Nanocrystals. *ACS Nano* **2011**, *5*, 5888-5902.

(13) Brus, L. E.: A simple model for the ionization potential, electron affinity, and aqueous redox potentials of small semiconductor crystallites. *J. Chem. Phys.* **1983**, *79*, 5566-5571.

(14) Milliron, D. J.: Quantum dot solar cells: The surface plays a core role. *Nat Mater* **2014**, *13*, 772-773.

(15) Chuang, C.-H. M.; Brown, P. R.; Bulović, V.; Bawendi, M. G.: Improved performance and stability in quantum dot solar cells through band alignment engineering. *Nat Mater* **2014**, *13*, 796-801.

(16) Vanmaekelbergh, D.; Liljeroth, P.: Electron-conducting quantum dot solids: novel materials based on colloidal semiconductor nanocrystals. *Chem. Soc. Rev.* **2005**, *34*, 299-312.

(17) Schimpf, A. M.; Knowles, K. E.; Carroll, G. M.; Gamelin, D. R.: Electronic Doping and Redox-Potential Tuning in Colloidal Semiconductor Nanocrystals. *Acc. Chem. Res.* **2015**, *48*, 1929-1937.

(18) Jeong, K. S.; Deng, Z.; Keuleyan, S.; Liu, H.; Guyot-Sionnest, P.: Air-Stable n-Doped Colloidal HgS Quantum Dots. *J. Phys. Chem. Lett.* **2014**, *5*, 1139-1143.

(19) Carroll, G. M.; Schimpf, A. M.; Tsui, E. Y.; Gamelin, D. R.: Redox Potentials of Colloidal n-Type ZnO Nanocrystals: Effects of Confinement, Electron Density, and Fermi-Level Pinning by Aldehyde Hydrogenation. *J. Am. Chem. Soc.* **2015**, *137*, 11163-11169.

(20) Valdez, C. N.; Braten, M.; Soria, A.; Gamelin, D. R.; Mayer, J. M.: Effect of Protons on the Redox Chemistry of Colloidal Zinc Oxide Nanocrystals. *J. Am. Chem. Soc.* **2013**, *135*, 8492-8495.

(21) Inamdar, S. N.; Ingole, P. P.; Haram, S. K.: Determination of Band Structure Parameters and the Quasi-Particle Gap of CdSe Quantum Dots by Cyclic Voltammetry. *ChemPhysChem* **2008**, *9*, 2574-2579.

(22) Kucur, E.; Riegler, J.; Urban, G. A.; Nann, T.: Determination of quantum confinement in CdSe nanocrystals by cyclic voltammetry. *J. Chem. Phys.* **2003**, *119*, 2333-2337.

(23) Querner, C.; Reiss, P.; Sadki, S.; Zagorska, M.; Pron, A.: Size and ligand effects on the electrochemical and spectroelectrochemical responses of CdSe nanocrystals. *Phys Chem Chem Phys* **2005**, *7*, 3204-3209.

(24) Amelia, M.; Impellizzeri, S.; Monaco, S.; Yildiz, I.; Silvi, S.; Raymo, F. M.; Credi, A.: Structural and Size Effects on the Spectroscopic and Redox Properties of CdSe Nanocrystals in Solution: The Role of Defect States. *ChemPhysChem* **2011**, *12*, 2280-2288.

(25) Boehme, S. C.; Wang, H.; Siebbeles, L. D. A.; Vanmaekelbergh, D.; Houtepen, A. J.: Electrochemical Charging of CdSe Quantum Dot Films: Dependence on Void Size and Counterion Proximity. *ACS Nano* **2013**, *7*, 2500-2508.

(26) Guyot-Sionnest, P.: Charging colloidal quantum dots by electrochemistry. *Microchim. Acta* **2008**, *160*, 309-314.

(27) Yu, D.; Wang, C.; Guyot-Sionnest, P.: n-Type Conducting CdSe Nanocrystal Solids. *Science* **2003**, *300*, 1277-1280.

(28) Jha, P. P.; Guyot-Sionnest, P.: Electrochemical Switching of the Photoluminescence of Single Quantum Dots. *J. Phys. Chem. C* **2010**, *114*, 21138-21141.

(29) Rinehart, J. D.; Schimpf, A. M.; Weaver, A. L.; Cohn, A. W.; Gamelin, D. R.: Photochemical Electronic Doping of Colloidal CdSe Nanocrystals. *J. Am. Chem. Soc.* **2013**, *135*, 18782-18785.

(30) Carroll, G. M.; Brozek, C. K.; Hartstein, K. H.; Tsui, E. Y.; Gamelin, D. R.: Potentiometric Measurements of Semiconductor Nanocrystal Redox Potentials. *J. Am. Chem. Soc.* **2016**.

(31) Shim, M.; Guyot-Sionnest, P.: n-type colloidal semiconductor nanocrystals. *Nature* **2000**, *407*, 981-983.

(32) Wang, C.; Shim, M.; Guyot-Sionnest, P.: Electrochromic Nanocrystal Quantum Dots. *Science* **2001**, *291*, 2390-2392.

(33) Shimizu, K. T.; Woo, W. K.; Fisher, B. R.; Eisler, H. J.; Bawendi, M. G.: Surface-Enhanced Emission from Single Semiconductor Nanocrystals. *Phys. Rev. Lett.* **2002**, *89*, 117401.

(34) Patton, B.; Langbein, W.; Woggon, U.: Trion, biexciton, and exciton dynamics in single self-assembled CdSe quantum dots. *Physical Review B* **2003**, *68*, 125316.

(35) Shim, M.; Wang, C.; Guyot-Sionnest, P.: Charge-Tunable Optical Properties in Colloidal Semiconductor Nanocrystals. *The Journal of Physical Chemistry B* **2001**, *105*, 2369-2373.

(36) Tsui, E. Y.; Carroll, G. M.; Miller, B.; Marchioro, A.; Gamelin, D. R.: Distributed Spontaneous Electron-Trapping Kinetics in Photodoped *n*-type CdSe Nanocrystals. *Submitted*.

(37) Schimpf, A. M.; Gunthardt, C. E.; Rinehart, J. D.; Mayer, J. M.; Gamelin, D. R.: Controlling Carrier Densities in Photochemically Reduced Colloidal ZnO Nanocrystals: Size Dependence and Role of the Hole Quencher. *J. Am. Chem. Soc.* **2013**, *135*, 16569-16577.

(38) Valdez, C. N.; Schimpf, A. M.; Gamelin, D. R.; Mayer, J. M.: Proton-Controlled Reduction of ZnO Nanocrystals: Effects of Molecular Reductants, Cations, and Thermodynamic Limitations. *J. Am. Chem. Soc.* **2016**, *138*, 1377-1385.

(39) Anderson, N. C.; Hendricks, M. P.; Choi, J. J.; Owen, J. S.: Ligand Exchange and the Stoichiometry of Metal Chalcogenide Nanocrystals: Spectroscopic Observation of Facile Metal-Carboxylate Displacement and Binding. *J. Am. Chem. Soc.* **2013**, *135*, 18536-18548.

(40) Boles, M. A.; Ling, D.; Hyeon, T.; Talapin, D. V.: The surface science of nanocrystals. *Nat. Mater.* **2016**, *15*, 141-153.

(41) Bard, A. J.; Bocarsly, A. B.; Fan, F. R. F.; Walton, E. G.; Wrighton, M. S.: The concept of Fermi level pinning at semiconductor/liquid junctions. Consequences for energy

conversion efficiency and selection of useful solution redox couples in solar devices. *J. Am. Chem. Soc.* **1980**, *102*, 3671-3677.

(42) Tanaka, S.; Bruce, J. A.; Wrighton, M. S.: Deliberate modification of the behavior of n-type cadmium telluride/electrolyte interfaces by surface etching. Removal of Fermi level pinning. *J. Phys. Chem.* **1981**, *85*, 3778-3787.

(43) Aruchamy, A.; Bruce, J. A.; Tanaka, S.; Wrighton, M. S.: Characterization of the Interface Energetics for N-Type Cadmium Selenide/Nonaqueous Electrolyte Junctions. *J. Electrochem. Soc.* **1983**, *130*, 359-364.

(44) Yang, S.; Prendergast, D.; Neaton, J. B.: Tuning Semiconductor Band Edge Energies for Solar Photocatalysis via Surface Ligand Passivation. *Nano Lett.* **2012**, *12*, 383-388.

(45) Chuang, C.-H. M.; Brown, P. R.; Bulović, V.; Bawendi, M. G.: Improved performance and stability in quantum dot solar cells through band alignment engineering. *Nat. Mater.* **2014**, *13*, 796.

(46) Bloom, B. P.; Zhao, L.-B.; Wang, Y.; Waldeck, D. H.; Liu, R.; Zhang, P.; Beratan, D. N.: Ligand-Induced Changes in the Characteristic Size-Dependent Electronic Energies of CdSe Nanocrystals. *J. Phys. Chem. C* **2013**, *117*, 22401-22411.

(47) Mönch, W.: *Semiconductor surfaces and interfaces*; Springer Science & Business Media, 2013; Vol. 26.

(48) Cohen, R.; Ashkenasy, G.; Shanzer, A.; Cahen, D.: Grafting Molecular Properties onto Semiconductor Surfaces. *Encyclopedia of Electrochemistry* **2002**.

(49) Rühle, S.; Shalom, M.; Zaban, A.: Quantum-Dot-Sensitized Solar Cells. *ChemPhysChem* **2010**, *11*, 2290-2304.

(50) Wu, K.; Lian, T.: Quantum confined colloidal nanorod heterostructures for solar-to-fuel conversion. *Chemical Society Reviews* **2016**, *45*, 3781-3810.

Chapter 5. Mechanistic Insights into Solar Water Oxidation by Cobalt-Phosphate-Modified α-Fe_2O_3 Photoanodes

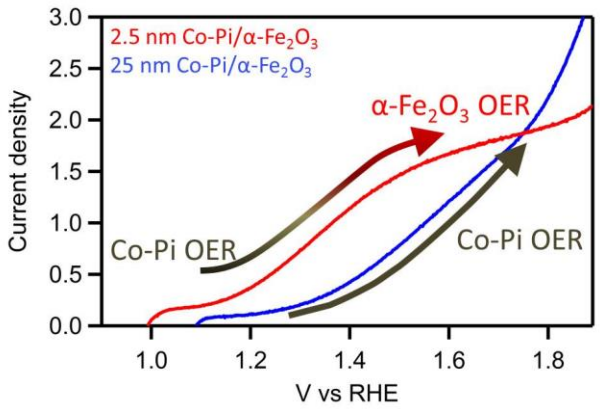

Adapted from: Carroll, G. M.; Zhong, D. K.; Gamelin, D. R. *Energy Environ. Sci.* **2015**, *8*, 577.

5.1 Overview

Interfacing α-Fe_2O_3 photoanodes with the water-oxidation electrocatalyst Co-Pi is known to enhance their photon-to-current conversion efficiencies by reducing electron-hole recombination near their surfaces, particularly at more negative potentials, but the mechanism by which Co-Pi modification achieves this enhancement remains poorly understood. Conflicting experimental observations have been recorded with respect to the role of Co-Pi thickness and even the participation of Co-Pi in catalysis, raising important general questions concerning the fundamental properties of catalyst-modified PEC water-oxidation photoanodes for solar energy conversion. In this chapter, results from electrochemical, spectroscopic, and microscopic measurements on mesostructured Co-Pi/α-Fe_2O_3 composite photoanodes are reported that reveal evolving pathways of water oxidation with increasing Co-Pi thickness. These results highlight major fundamental differences between structured and planar Co-Pi/α-Fe_2O_3 composite photoanodes and help to reconcile previously conflicting mechanistic interpretations.

5.2 Introduction

Photoelectrochemical (PEC) water splitting into hydrogen and oxygen is a promising strategy for capturing and storing the abundant solar energy incident upon the Earth's surface.[1-6] Photoelectrolysis of water poses significant technical challenges, however. The oxidation half reaction is a four-proton, four-electron process that typically requires a large overpotential.[1-6] Additionally, PEC photoelectrodes must be efficient, stable under operating conditions, able to absorb a large fraction of the visible spectrum, possess properly aligned band edges for thermodynamically favorable charge transfer, and be cost effective.[4,5,7] To date, no single material has demonstrated all of these characteristics.

With a band gap of 2.1 eV, stability under operating conditions, and a valence-band potential ~1.6 V more positive than the thermodynamic water-oxidation potential (+1.23 V vs RHE), hematite (α-Fe_2O_3) continues to attract attention as a model photoanode for PEC water oxidation.[7-11] Owing to poor charge mobility (10^{-2} to 10^{-1} $cm2s^{-1}V^{-1}$),[12] short hole-diffusion lengths (2-20 nm),[13,14] and slow charge-transfer kinetics (10^{-3} sec to 1 sec),[15-22] however, the solar-to-hydrogen efficiencies achieved with α-Fe_2O_3 photoelectrodes suffer greatly from electron-hole recombination, both within the bulk and at the semiconductor liquid junction (SCLJ).

Several strategies have been explored to reduce bulk electron-hole recombination in α-Fe_2O_3, including doping with Si, Ti, Al, Ge, Sn, and Nb[23-28] and nano-structuring.[9,23-26,29-33] Similarly, several groups have explored interfacing α-Fe_2O_3 with water-oxidation catalysts to reduce surface electron-hole recombination.[8,15,34-36] In particular, the earth-abundant, self-healing water-oxidation electrocatalyst known as cobalt phosphate (Co-Pi)[37,38] has received enormous attention since initial observations of water-oxidation onsets shifted to more negative potentials in Co-Pi/α-Fe_2O_3 composite photoanodes.[8,34,39] As a "self-healing" catalyst,[38] Co-Pi has practical advantages over other molecular or nanocrystalline catalysts, which may degrade or dissociate from the photoanode surface over time.

Since first reported,[34] numerous studies have addressed optimization and mechanistic probing of the Co-Pi/α-Fe_2O_3 interface.[8,15,39-42] Interestingly, these studies have generated seemingly incompatible models to explain the nature of the Co-Pi photocurrent enhancement on α-Fe_2O_3 photoanodes. For example, some of the most detailed insights into this interface have

come from studies of planar Co-Pi/α-Fe_2O_3 "model" systems[41] but the experimental results from these model systems haven't been in full agreement with those from PEC studies of high-surface-area Co-Pi/α-Fe_2O_3 composite photoanodes.[8,39] Specifically, photoelectrochemical measurements on mesostructured α-Fe_2O_3 photoanodes have indicated an optimal Co-Pi thickness of only <~10 nm, beyond which the PEC performance actually diminished because of a "kinetic bottleneck".[8,39] In contrast, analogous PEC measurements on planar α-Fe_2O_3 photoanodes have showed continued PEC improvement with increasing Co-Pi thickness up to as thick as 425 nm.[41] One hypothesis[41] to explain these contradictory observations is that the latter measurements involved backside illumination (i.e., through the substrate and α-Fe_2O_3, Figure 5.2a), whereas the former involved frontside illumination (i.e., through the Co-Pi); Frontside illumination is potentially subject to parasitic photon absorption by the Co-Pi itself,[43] introducing new absorption losses with increasing Co-Pi thickness. This hypothesis has never been tested, and the stark contrast between mesostructured and planar Co-Pi/α-Fe_2O_3 composite photoanodes thus remains unexplained. Additionally, transient absorption measurements on mesostructured Co-Pi/α-Fe_2O_3 composite photoanodes have revealed photogenerated holes with extended lifetimes apparently within the α-Fe_2O_3 itself, leading to the suggestion that Co-Pi does not directly participate in water-oxidation catalysis but instead plays an indirect role by inducing additional α-Fe_2O_3 band bending that reduces electron-hole recombination.[40,44] This suggestion appears incompatible with observations of an "adaptive junction" formed between α-Fe_2O_3 and Co-Pi or related catalysts,[42,45] and of capacitive hole storage within the Co-Pi layer.[41] These mechanistic contrasts also remain unresolved. Further mechanistic studies of PEC water oxidation by Co-Pi/α-Fe_2O_3 composite photoanodes are required to reconcile these divergent understandings of this important interface.

Here, we assess the influence of Co-Pi layer thickness on the PEC performance of mesostructured α-Fe_2O_3 photoanodes with the aim of consolidating the understanding of the role of Co-Pi in enhancing PEC water oxidation by α-Fe_2O_3 photoanodes. The results demonstrate the existence of an optimal Co-Pi thickness that is rather small (~2.5 nm, estimated from Coulometry) and independent of the illumination direction, confirming a non-trivial origin of the diminished PEC performance with thicker Co-Pi catalyst layers. This bottleneck with thick Co-Pi layers is proposed to stem from the texturing of these mesostructured α-Fe_2O_3 photoanodes, which enhances surface electron-hole recombination relative to planar α-Fe_2O_3 photoanodes.

Furthermore, mechanistic insights gained from measuring the pH dependence of this PEC activity as a function of Co-Pi thickness reveal that at large Co-Pi thicknesses, all water oxidation proceeds via Co-Pi, whereas at the optimal Co-Pi thickness, charge transfer to water occurs through Co-Pi-catalyzed water oxidation and by direct α-Fe_2O_3 water oxidation, the relative importance of each pathway changing with applied potential. These findings shed new light on the role Co-Pi plays in improving the performance of these and related solar water-splitting photoanodes, and highlight fundamentally important contrasts between planar and structured composite photoanodes.

5.3 Experimental Details

Mesostructured α-Fe_2O_3 photoanodes were fabricated on fluorine doped tin oxide (FTO) coated glass (TEC 15, Hartford Glass Co.) by an atmospheric pressure chemical vapor deposition (APCVD) method described previously.[8,33,39] The APCVD synthesis was modified to optimize α-Fe_2O_3 for backside illumination photocurrent densities by decreasing the deposition period to ~70% of the typical deposition time, and thus producing thinner α-Fe_2O_3 films. To fabricate the Co-Pi/α-Fe_2O_3 composite photoanodes, Co-Pi was deposited onto α-Fe_2O_3 photoanodes by photo-assisted electrodeposition under AM1.5 simulated solar irradiation from the back of the sample (through the FTO). All Co-Pi depositions were carried out at a constant current of 6 μA/cm^2 from a solution of 0.5 mM cobalt nitrate in 0.1 M potassium phosphate buffer at pH 8. The Co-Pi thickness was controlled by varying the amount charge passed, *i.e.*, the duration of deposition. Co-Pi thicknesses are reported as the average values estimated from the charges passed during deposition. Co-Pi dissolution was achieved by submerging Co-Pi/α-Fe_2O_3 composite photoanodes in fresh aqueous 0.1M KPi (pH 8) solutions for fixed times.

Photoelectrochemcial (PEC) and electrochemical (EC) measurements were conducted in a three-electrode configuration, with the photoanode as the working electrode, Ag/AgCl as the reference electrode, and Pt as the counter electrode. A Gamry Series G 300 potentiostat with a frequency response analyzer was used for all measurements. Unless otherwise stated, all PEC measurements were performed in 0.1M KPi (pH8) using backside illumination (through the FTO, Figure 2a) with calibrated 1 sun AM 1.5 simulated sunlight irradiation using an Oriel 96000 solar simulator equipped with a 150 W Xenon arc lamp and an Oriel AM 1.5 filter. Potentials vs the reversible hydrogen electrode (RHE) were calculated using the Nernst equation

as $E_{RHE} = E_{Ag/AgCl} + 0.0591(pH) + 0.1976$ V. All photocurrent-voltage and current-voltage data were collected at a scan rate of 10 mV/s. Masks with 6 mm diameter apertures were applied onto all working electrodes for defined active surface areas.

Galvanostatic pH-dependent PEC measurements were performed by titrating aqueous 0.5M KPi (pH 5) with aqueous 0.1M KOH. Incident photon-to-current conversion efficiency (IPCE) data were collected using a 250 W tungsten light source directed through an Oriel Cornerstone 74000 monochromator blazed at 350 nm. Spectral efficiency was calculated using the equation: IPCE(λ) = 1240*Current(A)/Power(W)*λ(nm). Light intensity was measured with a calibrated silicon detector with a maximum light output of ~6 mW/cm^2 at 540 nm. The steady-state dark current was collected prior to each IPCE measurement and was subtracted from the resulting spectrum. Scanning electron microscopy (SEM) images were collected using an FEI Sirion SEM at an accelerating voltage of 15 keV.

5.4 Results and Analysis

Figure 5.1 compares scanning electron microscopy (SEM) images of an α-Fe_2O_3 photoanode collected before and after photo-assisted electrochemical deposition of Co-Pi with backside illumination. Whereas photo-assisted electrochemical deposition of Co-Pi onto α-Fe_2O_3 mesostructures using frontside illumination has previously been shown to yield uniform catalyst coverage across the entire α-Fe_2O_3 surface,[8] Co-Pi deposition via backside illumination has not been explored. The bare α-Fe_2O_3 photoanode displays a highly structured surface with resolvable features on the order of ~10nm in diameter, typical for mesostructured α-Fe_2O_3 photoanodes prepared by APCVD.[33] Following Co-Pi deposition, the smallest resolvable features grow to ~30 nm. Assuming an average volume of ~125 Å^3 per CoO_6 subunit,[46] and an α-Fe_2O_3 surface roughness factor of 20,[33] an average Co-Pi thickness of ~25 nm can be estimated from the charge passed during deposition to make the composite photoanode in Figure 5.1b. Although it is difficult to extract the exact Co-Pi thickness from SEM, the loss of resolvable microstructure in Figure 5.1b is consistent with this estimated thickness.

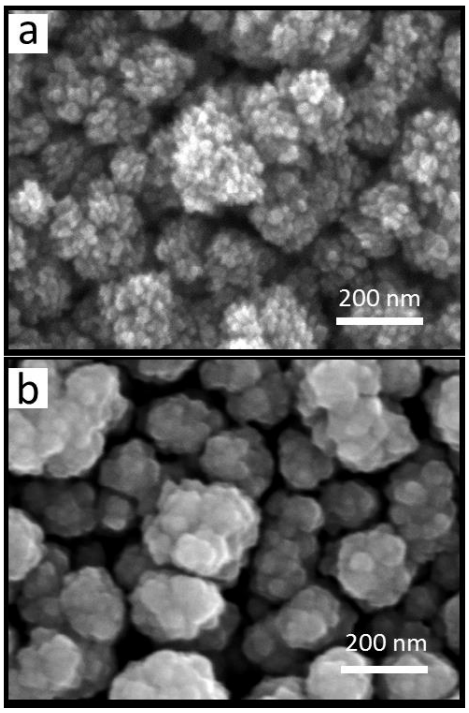

Figure 5.1. SEM of bare and Co-Pi coated mesostructured α-Fe_2O_3.
Scanning electron microscope images of **(a)** a bare mesostructured α-Fe_2O_3 photoanode, and **(b)** the same photoanode following deposition of a ~25 nm thick layer of Co-Pi via photo-assisted electrochemical deposition using backside illumination. The viewing angle is normal to the sample surface.

Figure 5.2b describes the photocurrent density–voltage (*J*-*V*) characteristics of an α-Fe_2O_3 photoanode whose surface has been modified by deposition of a thick (~25 nm) layer of Co-Pi, illuminated with 1 sun, AM1.5 simulated sunlight from the back side. Remarkably, the onset potential for PEC water oxidation is approximately the same with and without the thick Co-Pi layer. The photocurrent density measured at +1.8 V is greater for the Co-Pi/α-Fe_2O_3 photoanode than for the parent α-Fe_2O_3 photoanode, but close inspection reveals that this enhancement arises from direct electrocatalysis by Co-Pi (Fig. 5.2b, inset), instead of from enhanced photoelectrocatalysis as desired. Subtracting the steady state dark current yields a photocurrent density of only 1.2 mA/cm^2 at +1.8 V for the composite photoanode, well below that of the parent α-Fe_2O_3 photoanode (1.5 mA/cm^2 at +1.8 V). Interfacing with a ~25 nm Co-Pi layer thus actually diminishes the PEC performance of mesostructured α-Fe_2O_3 photoanodes

under backside illumination, confirming previous observations of a kinetic bottleneck in this regime.

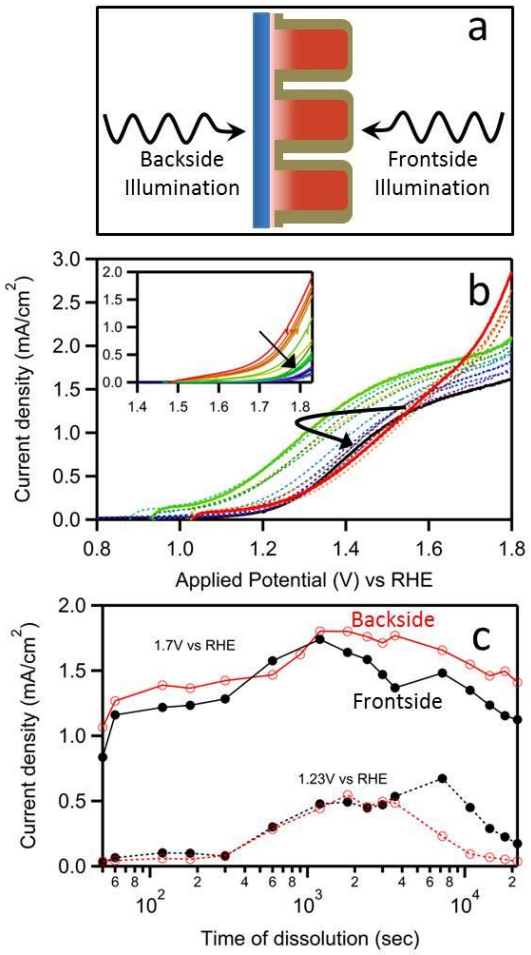

Figure 5.2. Dissolution of Co-Pi from α-Fe_2O_3.

(a) Schematic illustration of front- and backside illumination. **(b)** *J-V* scans under simulated 1 sun AM 1.5 backside illumination of a bare α-Fe_2O_3 electrode (black) and following Co-Pi deposition (red, ~25 nm thick). Intermediate colors from orange to blue show the *J-V* scans of the same electrode after 1|3|5|10|15|20|30|40|50|60|120|240|360|480|600 minutes of Co-Pi dissolution in fresh 0.1M KPi (pH 8) electrolyte solution. The solid lines correspond to minima (bare α-Fe_2O_3, and with ~25 nm-thick Co-Pi) and the maximum (after 30 min dissolution). Inset: Dark current response of the same anode at each of the same stages of Co-Pi dissolution. **(c)** Steady-state photocurrent densities (steady-state dark current subtracted) for front (black, closed circles) and backside (red, open circles) illumination measured at +1.7 V

(solid) and +1.23 V (dashed) vs RHE. All data were collected using 0.1M KPi (pH 8) buffer.

Co-Pi slowly disproportionates and dissolves in cobalt-free electrolyte under open-circuit conditions.[38] Here, we show that this dissolution can be used to optimize the Co-Pi thickness in Co-Pi/α-Fe_2O_3 composite photoanodes. To illustrate this optimization, a series of PEC measurements was performed on the same photoanode in cobalt-free electrolyte, with deliberate Co-Pi dissolution steps performed between each pair of *J-V* measurements. Specifically, the composite photoelectrode was transferred to a cobalt-free aqueous solution following each PEC measurement, where dissolution was allowed to proceed for a fixed time, and the photoelectrode was then transferred back into the PEC cell and its *J-V* response measured again. From the initial thickness of ~25 nm (red trace), Figure 5.2b shows that the onset potential shifts to more *negative* potentials with Co-Pi dissolution until a maximum shift is reached at ~30 min dissolution time (green trace). Further dissolution then shifts the onset potential to more positive potentials again, until eventually all of the Co-Pi has been removed and the *J-V* curve converges on that of the parent α-Fe_2O_3 photoanode, measured prior to any Co-Pi deposition. From the inset in Figure 5.2b, the dark current density does not follow the same trend; its onset potential only increases with Co-Pi dissolution. Figure 5.2c summarizes steady-state photocurrent density data (see Appendix D) measured with both front- and backside illumination at +1.7 V and +1.23 V as a function of Co-Pi dissolution time. Both the front- and backside PEC follow the same trend, proceeding through a maximum at ~30 min dissolution. This trend illustrates the "kinetic bottleneck" effect described previously,[39] but here is demonstrated with backside illumination. This result eliminates nonproductive photon absorption by Co-Pi as a viable hypothesis to explain the reduced PEC performance of composite Co-Pi/α-Fe_2O_3 photoanodes having thick Co-Pi layers.

Figure 5.3 shows incident-photon-to-current-conversion-efficiency (IPCE) curves measured for the same α-Fe_2O_3 photoanode with various Co-Pi thicknesses. The bare α-Fe_2O_3 photoanode shows a typical response, with its photocurrent onset at the α-Fe_2O_3 absorption edge ($\lambda \approx 600$ nm) and a maximum of 14% at $\lambda = 450$ nm. The decreasing IPCE at even shorter wavelengths is typical for backside illumination, and reflects bulk-recombination losses of photo-generated charge carriers created near the α-Fe_2O_3/FTO interface. Deposition of a thin Co-

Pi layer (~2.3 nm) onto this photoanode's surface increases the IPCE values at all wavelengths, yielding a maximum of ~19% at 445 nm. Addition of more Co-Pi (to ~9.7 nm thick) causes a decrease in IPCE throughout the entire spectral window, however, and the IPCE curve is almost indistinguishable from that of the bare photoanode. Even further Co-Pi addition (to ~25 nm) decreases the IPCE values yet further, yielding an IPCE maximum of only 7% at λ = 445 nm. The uniform decrease in IPCE with thick Co-Pi deposition differs from what would be expected if this large reduction in PEC performance came from photon absorption by Co-Pi (dotted curve, transmittance), further arguing against the hypothesis of substantial non-productive light absorption by the catalyst. Instead, the results presented here indicate that a more complex and fundamentally important limitation is encountered with thick Co-Pi layers.

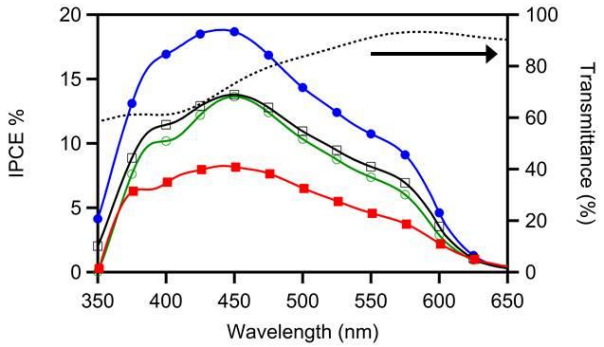

Figure 5.3. IPCE of variable thickness Co-Pi on mesostructured α-Fe_2O_3.
Incident photon to current conversion efficiency (IPCE) spectra for bare (black, open square), 2.3 nm (blue, closed circle), 9.7 nm (green, open circle) and 25 nm (red, closed square) thick Co-Pi on α-Fe_2O_3 in 0.1 M KPi at 1.7 V vs. RHE from backside illumination. For reference, the dashed line shows the transmittance spectrum of a ~25 nm thick Co-Pi layer deposited on FTO.

In our experiments, the optimized thicknesses of the APCVD α-Fe_2O_3 photoanodes themselves for front- and backside illumination are ~600 and ~450 nm, respectively. Figure 5.4 shows *J-V* curves measured for two Co-Pi/α-Fe_2O_3 composite photoelectrodes, with α-Fe_2O_3 growth optimized for either front (~600 nm thick) or backside (~450 nm thick) illumination. Figure 5.4a shows that the thicker α-Fe_2O_3 photoanode achieves a lower plateau current density (~1 mA/cm^2) than the thinner one (~2 mA/cm^2) under backside illumination. Upon deposition of ~25 nm (average) Co-Pi onto these two photoanodes, the photocurrent onset potential of the

thicker photoanode shifts to more *negative* potentials by ~200 mV, whereas that of the thinner photoanode actually shifts to more *positive* potentials. A close inspection of the SEM image of this Co-Pi/α-Fe_2O_3 photoelectrode (Figure 5.4a, inset) reveals that backside photo-assisted electrodeposition does not uniformly deposit Co-Pi onto the surface of the thicker α-Fe_2O_3 photoanode. The nodules still show their fine microstructure whereas the dark regions in the valleys now appear flat, suggesting that Co-Pi deposits preferentially in the valleys. This result implies that the PEC activity of the thicker α-Fe_2O_3 photoanode is restricted to these valleys when using backside illumination, and the high-surface-area nodules do not participate equally. This loss of active surface area causes the thicker α-Fe_2O_3 photoelectrodes to behave like planar α-Fe_2O_3 photoanodes when interfaced with Co-Pi, showing continued shifting to more negative potentials of the onset potential even with application of thick Co-Pi layers (Figure 5.4a).[41] In contrast, the thinner α-Fe_2O_3 photoanode shows evidence of substantial Co-Pi deposition onto the high-surface-area nodules (Figure 5.4b, inset) even with backside illumination, showing that the full surface area participates in water oxidation, as desired. In this limit, thick Co-Pi layers impair PEC performance (Figure 5.4b).

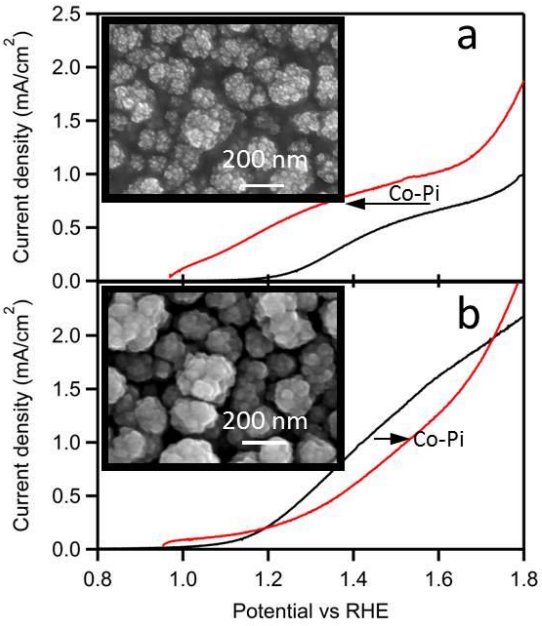

Figure 5.4. Variations in the photoactivity of mesostructured α-Fe_2O_3 surfaces.
J-V scans for bare (black) and ~25 nm Co-Pi-coated (red) α-Fe_2O_3 photoanodes measured in 0.1 M KPi (pH 8) with backside illumination. **(a)** Co-Pi/α-Fe_2O_3 optimized for frontside illumination (~600 nm thick α-Fe_2O_3). **(b)** Co-Pi/α-Fe_2O_3 optimized for

backside illumination (~450 nm thick α-Fe_2O_3). The insets show SEM images of the two Co-Pi/α-Fe_2O_3 photoelectrodes.

We now turn to the water oxidation catalysis itself. To probe this chemistry, galvanostatic pH titrations were conducted under illumination for four different Co-Pi thicknesses at two different current densities on the same 450 nm thick α-Fe_2O_3 photoanode (Fig. 5.5). As an electrocatalyst, Co-Pi is known to proceed through a proton-coupled electron-transfer step that precedes the rate-limiting O-O bond formation step.[46] This mechanism yields a Nernstian pH dependence of -59 mV/pH. A pH dependence of ~-59 mV/pH would therefore be expected for a Co-Pi/α-Fe_2O_3 composite photoanode if PEC water oxidation proceeds exclusively via the Co-Pi electrocatalyst. For reference, the bare α-Fe_2O_3 photoanode was measured and shows a pH dependence of -97 mV/pH under AM 1.5 illumination from the backside (at both 35 and 700 μA/cm^2, Figure 5.5). Addition of 0.6 nm Co-Pi onto the bare α-Fe_2O_3 photoanode changes the pH dependence from -97 to -82 mV/pH at 35 μA/cm^2, and -95 mV/pH at 700 μA/cm^2. These changes indicate that Co-Pi is modifying the mechanism of water oxidation in these composite photoanodes, but does so more at low potentials (low currents) than at high potentials (higher currents). Further addition of Co-Pi continues to decrease the pH dependence until, at a Co-Pi thickness of ~25 nm, the slopes of both the 35 and 700 μA/cm^2 data sets are both close to -59 mV/pH, *i.e.*, both resemble the inverse first order dependence on proton activity anticipated from water-oxidation catalysis by Co-Pi. Co-Pi/α-Fe_2O_3 composite photoanodes with thick Co-Pi catalyst layers thus appear to oxidize water solely via the Co-Pi electrocatalyst.

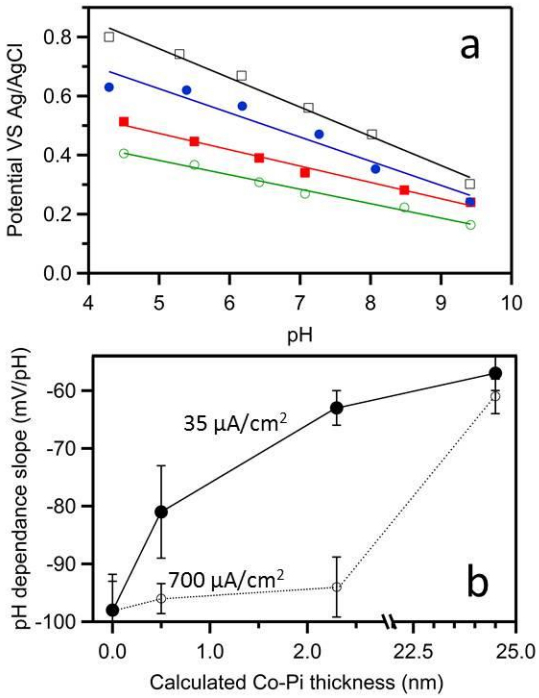

Figure 5.5. pH dependence of variable thickness Co-Pi on α-Fe_2O_3.
(a) Galvanostatic pH titration taken at 35 µA/cm^2 of bare α-Fe_2O_3 (black, open square), 0.62 nm Co-Pi/α-Fe_2O_3 (blue, closed circle), 2.3 nm Co-Pi/α-Fe_2O_3 (green, open circle) and ~25 nm Co-Pi/α-Fe_2O_3 (red, closed square) in 0.5 M KPi under AM1.5 illumination from the backside. All pH data were collected on the same 450 nm thick α-Fe_2O_3 sample. **(b)** The fitted slopes from the galvanostatic pH titrations at 35 µA/cm^2 (closed circles, solid line) and 700 µA/cm^2 (open circles, dotted line) plotted vs Co-Pi thickness. Error bars indicate the uncertainty associated with the linear fit to the pH data.

The above data show that Co-Pi/α-Fe_2O_3 composite photoanodes prepared with the optimized Co-Pi thickness (~2.3 nm) exhibit a pH dependence that is intermediate between those of the bare α-Fe_2O_3 and thick-composite photoelectrodes. This intermediate regime is interpreted as reflecting a superposition of two mechanisms (see Appendix D), one involving water oxidation directly at the α-Fe_2O_3 surface (-97 mV/pH) and the other water oxidation by Co-Pi (-59 mV/pH). The degree to which each mechanism participates varies with current density and hence with applied potential. At low potential (current), the majority of oxygen evolution occurs via Co-Pi, but at higher potentials (currents) the α-Fe_2O_3 surface mechanism dominates. The

optimized Co-Pi/α-Fe_2O_3 composite photoanodes thus rely on Co-Pi catalysis for activity at low potentials and on direct α-Fe_2O_3 water oxidation for activity at high potentials. To our knowledge, this result constitutes the first mechanistic evidence of water oxidation by Co-Pi in such composite photoanodes.

5.5 Discussion

Co-Pi can be described as forming an "adaptive Schottky junction"[42,45] with the surface of the underlying α-Fe_2O_3 photoelectrode, in which the open circuit voltage and quasi-Fermi level splitting increase upon oxidation of the ion permeable electrocatalyst, increasing the driving force for electron-hole separation and reducing surface recombination. From this description, it is expected that increasing the thickness of Co-Pi should only improve the *J-V* characteristics of the composite photoelectrode. Such behavior is indeed observed in planar Co-Pi/α-Fe_2O_3 photoanodes,[41] but it is not observed with mesostructured Co-Pi/α-Fe_2O_3 photoanodes.[8,39] Although mesostructured α-Fe_2O_3 photoanodes yield substantially higher photocurrent densities than planar α-Fe_2O_3 photoanodes, the PEC performance of mesostructured Co-Pi/α-Fe_2O_3 composite photoanodes maximizes at an intermediate Co-Pi thickness, implicating the existence of a new process that limits the overall performance.

We attribute this new limiting process (the "kinetic bottleneck"[39]) to increased interfacial recombination between conduction-band electrons and Co-Pi holes with increasing Co-Pi layer thickness in the mesostructures, ultimately arising from the inability to sweep electrons away from the SCLJ because of the α-Fe_2O_3 texturing. This interpretation is summarized in Figure 6a. Electron diffusion in a planar α-Fe_2O_3 photoanode is largely perpendicular to (away from) the SCLJ (Figure 5.6a, left). Increasing the surface area of an α-Fe_2O_3 photoanode increases the distance that photogenerated electrons must travel before they are no longer in proximity to this interface. Much of this added distance is actually parallel to the SCLJ (Figure 5.6a, right). The probability of electron recombination with holes stored within the Co-Pi layer increases in proportion to the time the electrons must reside near the SCLJ. This contrast results in the existence of the kinetic bottleneck only in highly structured Co-Pi/α-Fe_2O_3 composite photoanodes, and only when the entire high surface area participates in the photoelectrocatalysis (Figure 5.4).

The pH data presented here (Figure 5.5) indicate that water-oxidation catalysis proceeds exclusively *via* Co-Pi when the Co-Pi layer is thick. Under these conditions, however, many oxidizing equivalents are stored in the Co-Pi layer at steady state, and surface electron-hole recombination in mesostructured photoanodes becomes overwhelmingly problematic. For mesostructured Co-Pi/α-Fe_2O_3 composite photoanodes, PEC performance is therefore optimized when the Co-Pi layer is thin. Interestingly, in these optimized mesostructured Co-Pi/α-Fe_2O_3 composite photoanodes, water-oxidation catalysis proceeds *via* Co-Pi at low potentials but directly *via* the α-Fe_2O_3 surface at high potentials. In this way, Co-Pi improves the performance of mesostructured α-Fe_2O_3 photoanodes by catalyzing water oxidation at the lowest potentials, shifting their onset potentials more negative as desired for practical applications. These conclusions are summarized graphically in Figure 5.6b and highlight the important fundamental differences between mesostructured and planar PEC photoanodes for solar water oxidation. Importantly, these results shed new light onto the longstanding uncertainty about whether Co-Pi is an active catalyst or merely a spectator in such photoelectrochemistry.[47] Because of the marked contrasts observed between mesostructured and planar Co-Pi/α-Fe_2O_3 photoanodes, the results here motivate a more comprehensive mechanistic investigation into the kinetic processes *specific* to mesostructured Co-Pi/α-Fe_2O_3 interfaces, and such experiments are currently underway in our laboratories.

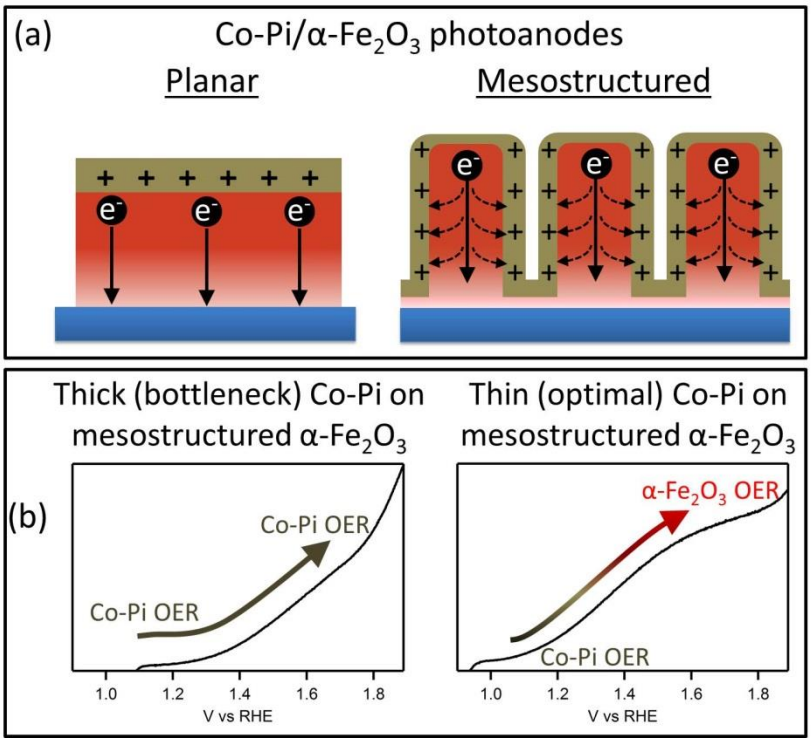

Figure 5.6. Summary of Co-Pi assisted α-Fe_2O_3 solar water oxidation.

(**a**) Schematic comparison of contrasting surface electron-hole recombination processes during photoelectrochemical water oxidation by mesostructured and planar Co-Pi/α-Fe_2O_3 photoanodes. In planar photoanodes, electrons travel away from the SCLJ, and hence away from accumulated holes in the Co-Pi catalyst layer. This configuration minimizes surface electron-hole recombination. In mesostructured photoanodes, electrons spend more time traveling parallel to the SCLJ. When the Co-Pi catalyst layer is thick, it stores many oxidizing equivalents, and thicker Co-Pi deposition results in increased surface electron-hole recombination. (**b**) In PEC water oxidation by mesostructured Co-Pi/α-Fe_2O_3 photoanodes, the water-oxidation mechanism depends on the catalyst thickness and the applied potential. For thick Co-Pi catalyst layers, water oxidation is always performed by Co-Pi. For thin (optimized) Co-Pi layers, water oxidation at low potentials is performed by Co-Pi, whereas water oxidation at high potentials and high currents is performed directly by the α-Fe_2O_3 surface.

5.6 Conclusion

Highly structured α-Fe_2O_3 photoanodes are susceptible to kinetic constraints when interfaced with thick Co-Pi catalyst layers. Optimization of the Co-Pi electrocatalyst thickness is necessary to achieve the maximum PEC efficiency at potentials <+1.6 V vs RHE. Attenuation of photocurrent with increasing Co-Pi thickness arises due to interfacial recombination between photogenerated conduction-band electrons and accumulated Co-Pi holes ("kinetic bottleneck"). The importance of such recombination depends on the texture of the underlying photoanode. For mesostructured α-Fe_2O_3 photoanodes, the overall PEC efficiency is optimized with rather thin Co-Pi layers (~2.5 nm) because of this recombination. At these optimal Co-Pi thicknesses, PEC water oxidation can occur from both the Co-Pi electrocatalyst, which dominates at low applied bias, and directly from the α-Fe_2O_3 surface, which dominates at high applied bias. For planar α-Fe_2O_3 photoanodes, this recombination channel is no longer dominant, and very thick Co-Pi layers do not limit PEC performance.[41] These results clarify the mechanistic role that Co-Pi plays in improving the PEC performance of composite Co-Pi/α-Fe_2O_3 photoanodes, and may have broad implications with respect to formation and optimization of related composite catalyst/photoelectrodes.

5.7 References

(1) Fujishima, A.; Honda, K.: Electrochemical Photolysis of Water at a Semiconductor Electrode. *Nature* **1972**, *238*, 37-38.

(2) Lewis, N. S.; Nocera, D. G.: Powering the planet: Chemical challenges in solar energy utilization. *PNAS* **2006**, *103*, 15729-15735.

(3) Nocera, D. G.: Personalized Energy: The Home as a Solar Power Station and Solar Gas Station. *ChemSusChem* **2009**, *2*, 387-390.

(4) Bard, A. J.; Fox, M. A.: Artificial Photosynthesis: Solar Splitting of Water to Hydrogen and Oxygen. *Acc. Chem. Res.* **1995**, *28*, 141-145.

(5) Moomow, W.; Yamba, F.; Kamimoto, M.; Maurice, L.; Nyboer, J.; Urama, K.; Weir, T.: Introduction. In *IPCC Special Report on Renewable Energy Sources and Climate change Mitigation*; Edenhofer, O., Pichs-Madruga, R., Sokona, Y., Seyboth, K., Matschoss, P., Kadner, S., Zwickel, T., Eickemeier, P., Hansen, G., Schlömer, S., von Stechow, C., Eds.; Cambridge University Press: United Kingdom and New York, NY, USA, 2011.

(6) Khaselev, O.; Turner, J. A.: A Monolithic Photovoltaic-Photoelectrochemical Device for Hydrogen Production via Water Splitting. *Science* **1998**, *280*, 425-427.

(7) Grätzel, M.: Photoelectrochemical cells. *Nature* **2001**, *414*, 338-344.

(8) Zhong, D. K.; Cornuz, M.; Sivula, K.; Gratzel, M.; Gamelin, D. R.: Photo-assisted electrodeposition of cobalt-phosphate (Co-Pi) catalyst on hematite photoanodes for solar water oxidation. *Energy Environ. Sci.* **2011**, *4*, 1759-1764.

(9) Duret, A.; Grätzel, M.: Visible Light-Induced Water Oxidation on Mesoscopic α-Fe_2O_3 Films Made by Ultrasonic Spray Pyrolysis. *J. Phys. Chem. B* **2005**, *109*, 17184-17191.

(10) Osterloh, F. E.: Inorganic Materials as Catalysts for Photochemical Splitting of Water. *Chem. Mater.* **2007**, *20*, 35-54.

(11) Osterloh, F. E.: Inorganic nanostructures for photoelectrochemical and photocatalytic water splitting. *Chem. Soc. Rev.* **2013**, *42*, 2294-2320.

(12) Gardner, R. F. G.; Sweett, F.; Tanner, D. W.: The electrical properties of alpha ferric oxide—I.: The impure oxide. *J. Phys. Chem. Solids* **1963**, *24*, 1175-1181.

(13) Kennedy, J. H.; Frese, K. W.: Photooxidation of Water at α-Fe_2O_3 Electrodes. *J. Electrochem. Soc.* **1978**, *125*, 709-714.

(14) Dare-Edwards, M. P.; Goodenough, J. B.; Hamnett, A.; Trevellick, P. R.: Electrochemistry and photoelectrochemistry of iron(III) oxide. *J. Chem. Soc. Faraday Trans.* **1983**, *79*, 2027-2041.

(15) Le Formal, F.; Sivula, K.; Grätzel, M.: The Transient Photocurrent and Photovoltage Behavior of a Hematite Photoanode under Working Conditions and the Influence of Surface Treatments. *J. Phys. Chem. C* **2012**, *116*, 26707-26720.

(16) Upul Wijayantha, K. G.; Saremi-Yarahmadi, S.; Peter, L. M.: Kinetics of oxygen evolution at α-Fe_2O_3 photoanodes: a study by photoelectrochemical impedance spectroscopy. *Phys. Chem. Chem. Phys.* **2011**, *13*, 5264-5270.

(17) Hamann, T. W.: Splitting water with rust: hematite photoelectrochemistry. *Dalton Trans.* **2012**, *41*, 7830-7834.

(18) Klahr, B.; Gimenez, S.; Fabregat-Santiago, F.; Bisquert, J.; Hamann, T. W.: Electrochemical and photoelectrochemical investigation of water oxidation with hematite electrodes. *Energy Environ. Sci.* **2012**, *5*, 7626-7636.

(19) Klahr, B. M.; Hamann, T. W.: Current and Voltage Limiting Processes in Thin Film Hematite Electrodes. *J. Phys. Chem. C* **2011**, *115*, 8393-8399.

(20) Barroso, M.; Mesa, C. A.; Pendlebury, S. R.; Cowan, A. J.; Hisatomi, T.; Sivula, K.; Grätzel, M.; Klug, D. R.; Durrant, J. R.: Dynamics of photogenerated holes in surface modified α-Fe_2O_3 photoanodes for solar water splitting. *PNAS* **2012**, *109*, 15640-15645.

(21) Barroso, M.; Pendlebury, S. R.; Cowan, A. J.; Durrant, J. R.: Charge carrier trapping, recombination and transfer in hematite (α-Fe_2O_3) water splitting photoanodes. *Chem. Sci.* **2013**, *4*, 2724-2734.

(22) Pendlebury, S. R.; Cowan, A. J.; Barroso, M.; Sivula, K.; Ye, J.; Gratzel, M.; Klug, D. R.; Tang, J.; Durrant, J. R.: Correlating long-lived photogenerated hole populations with photocurrent densities in hematite water oxidation photoanodes. *Energy Environ. Sci.* **2012**, *5*, 6304-6312.

(23) Chemelewski, W. D.; Hahn, N. T.; Mullins, C. B.: Effect of Si Doping and Porosity on Hematite's (α-Fe2O3) Photoelectrochemical Water Oxidation Performance. *J. Phys. Chem. C* **2012**, *116*, 5255-5261.

(24) Hahn, N. T.; Mullins, C. B.: Photoelectrochemical Performance of Nanostructured Ti- and Sn-Doped α-Fe2O3 Photoanodes. *Chem. Mater.* **2010**, *22*, 6474-6482.

(25) Tang, H.; Matin, M. A.; Wang, H.; Deutsch, T.; Al-Jassim, M.; Turner, J.; Yan, Y.: Synthesis and characterization of titanium-alloyed hematite thin films for photoelectrochemical water splitting. *J. Appl. Phys.* **2011**, *110*, 123511.

(26) Wang, G.; Ling, Y.; Wheeler, D. A.; George, K. E. N.; Horsley, K.; Heske, C.; Zhang, J. Z.; Li, Y.: Facile Synthesis of Highly Photoactive α-Fe2O3-Based Films for Water Oxidation. *Nano Lett.* **2011**, *11*, 3503-3509.

(27) He, J.; Parkinson, B. A.: Combinatorial Investigation of the Effects of the Incorporation of Ti, Si, and Al on the Performance of α-Fe2O3 Photoanodes. *ACS. Comb. Sci.* **2011**, *13*, 399-404.

(28) Zandi, O.; Klahr, B. M.; Hamann, T. W.: Highly photoactive Ti-doped [small alpha]-Fe2O3 thin film electrodes: resurrection of the dead layer. *Energy Environ. Sci.* **2013**, *6*, 634-642.

(29) Sivula, K.; Zboril, R.; Le Formal, F.; Robert, R.; Weidenkaff, A.; Tucek, J.; Frydrych, J.; Grätzel, M.: Photoelectrochemical Water Splitting with Mesoporous Hematite Prepared by a Solution-Based Colloidal Approach. *J. Am. Chem. Soc.* **2010**, *132*, 7436-7444.

(30) Hahn, N. T.; Ye, H.; Flaherty, D. W.; Bard, A. J.; Mullins, C. B.: Reactive Ballistic Deposition of α-Fe2O3 Thin Films for Photoelectrochemical Water Oxidation. *ACS Nano* **2010**, *4*, 1977-1986.

(31) Gonçalves, R. H.; Lima, B. H. R.; Leite, E. R.: Magnetite Colloidal Nanocrystals: A Facile Pathway To Prepare Mesoporous Hematite Thin Films for Photoelectrochemical Water Splitting. *J. Am. Chem. Soc.* **2011**, *133*, 6012-6019.

(32) Le Formal, F.; Grätzel, M.; Sivula, K.: Controlling Photoactivity in Ultrathin Hematite Films for Solar Water-Splitting. *Adv. Funct. Mater.* **2010**, *20*, 1099-1107.

(33) Kay, A.; Cesar, I.; Grätzel, M.: New Benchmark for Water Photooxidation by Nanostructured α-Fe_2O_3 Films. *J. Am. Chem. Soc.* **2006**, *128*, 15714-15721.

(34) Zhong, D. K.; Sun, J.; Inumaru, H.; Gamelin, D. R.: Solar Water Oxidation by Composite Catalyst/α-Fe_2O_3 Photoanodes. *J. Am. Chem. Soc.* **2009**, *131*, 6086-6087.

(35) Riha, S. C.; Klahr, B. M.; Tyo, E. C.; Seifert, S.; Vajda, S.; Pellin, M. J.; Hamann, T. W.; Martinson, A. B. F.: Atomic Layer Deposition of a Submonolayer Catalyst for the Enhanced Photoelectrochemical Performance of Water Oxidation with Hematite. *ACS Nano* **2013**, *7*, 2396-2405.

(36) Du, C.; Yang, X.; Mayer, M. T.; Hoyt, H.; Xie, J.; McMahon, G.; Bischoping, G.; Wang, D.: Hematite-Based Water Splitting with Low Turn-On Voltages. *Angew. Chem. Int. Ed.* **2013**, *52*, 12692-12695.

(37) Kanan, M. W.; Nocera, D. G.: In Situ Formation of an Oxygen-Evolving Catalyst in Neutral Water Containing Phosphate and Co^{2+}. *Science* **2008**, *321*, 1072-1075.

(38) Lutterman, D. A.; Surendranath, Y.; Nocera, D. G.: A Self-Healing Oxygen-Evolving Catalyst. *J. Am. Chem. Soc.* **2009**, *131*, 3838-3839.

(39) Zhong, D. K.; Gamelin, D. R.: Photoelectrochemical Water Oxidation by Cobalt Catalyst ("Co−Pi")/α-Fe_2O_3 Composite Photoanodes: Oxygen Evolution and Resolution of a Kinetic Bottleneck. *J. Am. Chem. Soc.* **2010**, *132*, 4202-4207.

(40) Barroso, M.; Cowan, A. J.; Pendlebury, S. R.; Grätzel, M.; Klug, D. R.; Durrant, J. R.: The Role of Cobalt Phosphate in Enhancing the Photocatalytic Activity of α-Fe_2O_3 toward Water Oxidation. *J. Am. Chem. Soc.* **2011**, *133*, 14868-14871.

(41) Klahr, B.; Giménez, S.; Fabregat-Santiago, F.; Bisquert, J.; Hamann, T. W.: Photoelectrochemical and Impedance Spectroscopic Investigation of Water Oxidation with "Co-Pi" coated Hematite Electrodes. *J. Am. Chem. Soc.* **2012**, *134*, 16693-16700.

(42) Lin, F.; Boettcher, S. W.: Adaptive semiconductor/electrocatalyst junctions in water-splitting photoanodes. *Nat. Mater.* **2014**, *13*, 81-86.

(43) Trotochaud, L.; Mills, T. J.; Boettcher, S. W.: An Optocatalytic Model for Semiconductor–Catalyst Water-Splitting Photoelectrodes Based on In Situ Optical Measurements on Operational Catalysts. *J. Phys. Chem. Lett.* **2013**, *4*, 931-935.

(44) Cowan, A. J.; Durrant, J. R.: Long-lived charge separated states in nanostructured semiconductor photoelectrodes for the production of solar fuels. *Chem. Soc. Rev.* **2013**, *42*, 2281-2293.

(45) Hamann, T. W.: Water splitting: An adaptive junction. *Nat Mater* **2014**, *13*, 3-4.

(46) McAlpin, J. G.; Surendranath, Y.; Dincă, M.; Stich, T. A.; Stoian, S. A.; Casey, W. H.; Nocera, D. G.; Britt, R. D.: EPR Evidence for Co(IV) Species Produced During Water Oxidation at Neutral pH. *J. Am. Chem. Soc.* **2010**, *132*, 6882-6883.

(47) Gamelin, D. R.: Water splitting: Catalyst or spectator? *Nat. Chem.* **2012**, *4*, 965-967.

Chapter 6. Kinetic Analysis of Photoelectrochemical Water Oxidation by Mesostructured Co-Pi/α-Fe_2O_3 Photoanodes

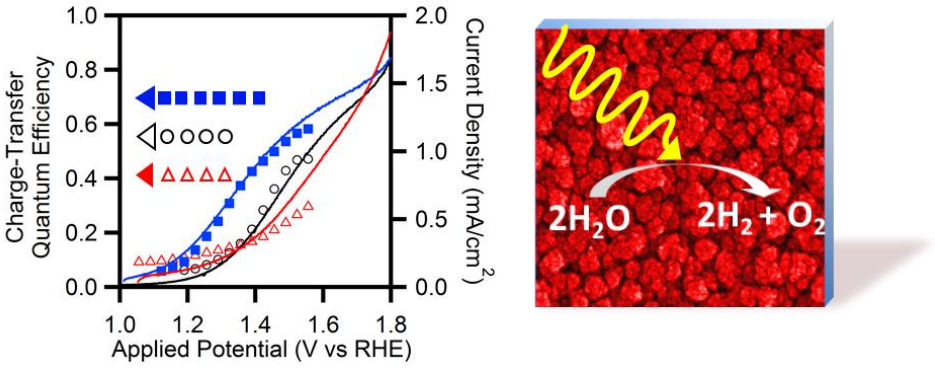

Adapted from: Carroll, G.M.; Gamelin, D.R. *J. Mat. Chem. A.* **2016**, *4*, 2986.

6.1 Overview

Solar water splitting using catalyst-modified semiconductor photoelectrodes is a promising approach to harvesting and storing solar energy. Prior studies have demonstrated that modification of α-Fe_2O_3 photoanodes with the water-oxidation electrocatalyst Co-Pi enhances photon-to-current conversion efficiencies, particularly at less positive potentials, but the mechanism underlying this enhancement remains poorly understood. Different experimental techniques have suggested very different interpretations of the microscopic origins of this improvement. Here, we report results from photoelectrochemical and impedance measurements aimed at understanding the Co-Pi/α-Fe_2O_3 interface of mesostructured composite photoanodes. Contrary to expectations, these measurements reveal that α-Fe_2O_3 water-oxidation kinetics actually slow upon deposition of Co-Pi, but electron-hole recombination slows even more, resulting in a net enhancement of water-oxidation quantum efficiency. The negative shift in the *J-V* curve caused by Co-Pi deposition is found to result from the introduction of an alternative pathway for water oxidation catalyzed by Co-Pi, which allows the composite photoanode to avoid positive charge accumulation at the α-Fe_2O_3 surface. We detail the role of Co-Pi thickness optimization in balancing the slower recombination against the slower water oxidation kinetics to

achieve the lowest water-oxidation onset potential. These results provide new insights into the microscopic properties of the catalyst/semiconductor interface in Co-Pi/α-Fe_2O_3 composite solar water-splitting photoanodes.

6.2 Introduction

Photoelectrochemical (PEC) water splitting has been proposed as a promising strategy for harvesting and storing solar energy.[1-6] Hematite (α-Fe_2O_3) has emerged as a model system for the water-oxidation half reaction in PEC water-splitting cells. With a band gap of 2.1 eV, stability under operating conditions, and a valence-band potential ~1.6 V more positive than the thermodynamic water-oxidation potential (+1.23 V), α-Fe_2O_3 balances many of the necessary criteria for PEC applications.[7-11] Owing to its poor electron mobility (10^{-2} to 10^{-1} $cm^2s^{-1}V^{-1}$),[12] short hole-diffusion lengths (2-20 nm),[13,14] and slow water-oxidation kinetics, however,[15-22] the solar-to-hydrogen efficiencies of α-Fe_2O_3 PEC cells are typically low, suffering greatly from electron-hole recombination within the bulk and at the semiconductor/liquid junction (SCLJ).

Recently, the strategy of interfacing α-Fe_2O_3 and related photoanodes with water-oxidation catalysts to improve their PEC performance has attracted tremendous attention.[23-26] Interfacing mesostructured α-Fe_2O_3 with the earth-abundant, self-healing, and ion-permeable amorphous water-oxidation electrocatalyst cobalt phosphate (Co-Pi)[27-30] shifts the water-oxidation onset potential in the negative direction by ~100-150 mV.[7,31,32] Optimization of the Co-Pi thickness is necessary because PEC water-oxidation onset potentials can actually increase when the Co-Pi layer is too thick, depending on the active surface area of the α-Fe_2O_3 photoelectrode.[33]

Despite advances in the development of Co-Pi/α-Fe_2O_3 and related composite photoanodes showing improved water-oxidation current densities at more negative potentials, it remains unclear *how* Co-Pi enhances water-oxidation rates at low potentials. Initial reports hypothesized that Co-Pi catalyzes water oxidation at the α-Fe_2O_3 surface.[7,31,32] An alternative hypothesis suggests that Co-Pi is instead a spectator in the water-oxidation catalysis, and its primary role is to increase α-Fe_2O_3 band bending near the SCLJ, resulting in reduced surface electron-hole recombination and a negatively shifted water-oxidation onset potential.[20,21,34,35] This hypothesis stems from transient absorption measurements on mesostructured α-Fe_2O_3 photoanodes showing that Co-Pi prolongs the lifetimes of photogenerated holes to timescales

(0.1 - 1.0 s) which resemble those of the bare α-Fe_2O_3 photoanodes under positive bias.[20,21,34,36] Charge transfer from α-Fe_2O_3 to Co-Pi is not invoked in this hypothesis. Similar conclusions were drawn in an independent study employing intensity-modulated photocurrent spectroscopy.[37] α-Fe_2O_3 surface passivation with non-catalytic layers does shift the PEC water-oxidation onset potential more negative,[15] confirming this general mechanism for α-Fe_2O_3,[38] but impedance and transient photocurrent spectroscopies have also demonstrated capacitive charging of the Co-Pi layer in planar Co-Pi/α-Fe_2O_3 photoanodes, confirming hole transfer to Co-Pi.[39] Similarly, dual-potentiostat measurements have shown that Co-Pi forms an 'adaptive junction' with hematite, which relies on ion permeability and capacitive hole storage in Co-Pi.[24,40] Measurements of the PEC water-oxidation pH dependence show a change in the microscopic mechanism with Co-Pi deposition, confirming water oxidation directly by Co-Pi in mesostructured Co-Pi/α-Fe_2O_3 photoanodes.[33] Lastly, the current-potential behavior with increasing Co-Pi thickness has been shown to depend strongly on the surface morphology of the underlying photoanode.[33] This observation undermines assumptions that planar and highly structured Co-Pi/α-Fe_2O_3 photoanodes behave in the same way.[18,35,38] Additional characterization of mesostructured Co-Pi/α-Fe_2O_3 photoanodes is therefore warranted. The role of Co-Pi thus appears more rich and complex than originally anticipated, and to date, no single model can account for all of the experimental observations made on Co-Pi/α-Fe_2O_3 composite water-oxidation photoanodes.

Here, we report the results of photoelectrochemical (PEC) and photoelectrochemical impedance spectroscopy (PEIS) measurements on mesostructured Co-Pi/α-Fe_2O_3 photoanodes aimed at understanding the impact of Co-Pi at this interface. The data suggest that the negative shift in onset potential with Co-Pi deposition is related to facile charge transfer to Co-Pi followed by Co-Pi-catalyzed water oxidation. At low potentials, the trap-state-mediated charge-transfer mechanism for water oxidation at the surface of α-Fe_2O_3 is bypassed upon Co-Pi addition, resulting in both an increase in band bending *and* a decrease in trap-centered surface recombination, confirming aspects of both hypotheses presented above. Contrary to expectations, the data show that the PEC water-oxidation kinetics actually *slow* upon addition of Co-Pi to the α-Fe_2O_3 surface, but the surface electron-hole recombination slows even more, such that the quantum efficiency for PEC water oxidation at low potentials increases. Finally, these measurements show that thick layers of Co-Pi inhibit catalytic turnover by allowing increased interfacial recombination between Co-Pi holes and α-Fe_2O_3 conduction-band electrons, a

behavior greatly exacerbated by the high surface areas of these mesostructured photoanodes. These results help tie together many of the disparate observations made in previous studies of Co-Pi/α-Fe_2O_3 composite water-oxidation photoanodes, improving the fundamental understanding of this complex interface.

6.3 Experimental Details

Synthesis. Mesostructured silicon-doped α-Fe_2O_3 photoanodes were fabricated on fluorine-doped tin oxide (FTO) coated glass (TEC 15, Hartford Glass Co.) by an atmospheric pressure chemical vapor deposition (APCVD) method described previously.[7,31,41] The APCVD synthesis was modified to yield α-Fe_2O_3 photoanodes optimized for backside illumination (through the FTO). This optimization was achieved by decreasing the deposition period to ~70% of the typical deposition time, thus producing thinner α-Fe_2O_3 films. To prepare the Co-Pi/α-Fe_2O_3 composite photoanodes, Co-Pi was deposited onto α-Fe_2O_3 photoanodes by photo-assisted electrodeposition under calibrated 1 sun simulated AM1.5 solar irradiation through the back side of the sample. All Co-Pi depositions were carried out at a constant current of 6 μA/cm^2 from a solution of 0.5 mM cobalt nitrate in 0.1 M potassium phosphate buffer at pH 8, where the Co-Pi thickness was controlled by varying the amount of charge passed, *i.e.*, the deposition duration as described previously.[33] Masks of black electrical tape with 6 mm apertures were applied onto all working electrodes for defined active surface areas.

Physical measurements. Photoelectrochemical (PEC), electrochemical (EC), and electrochemical impedance spectroscopy (PEIS) measurements were conducted in a three-electrode configuration with the photoanode as the working electrode, Ag/AgCl as the reference electrode, and Pt as the counter electrode. A Gamry Series G 300 potentiostat with a frequency response analyzer was used for all measurements. All PEC measurements were performed in 0.1M KPi pH8 under backside illumination with calibrated 1 sun simulated AM 1.5 irradiation using an Oriel 96000 solar simulator equipped with a 150 W Xenon arc lamp and an Oriel AM 1.5 filter. Steady state photocurrent densities were taken as the current density after 100 seconds under illumination at a given applied potential. Impedance data were gathered using a 10 mV amplitude perturbation at frequencies between 20,000 and 0.01 Hz, with a 100 sec conditioning period prior to each potential measured to achieve a steady-state current density. Data were fit using Gamry Echem Analyst fitting software package. Potentials vs the reversible hydrogen

electrode (RHE) were calculated using the Nernst equation, $V_{RHE} = V_{Ag/AgCl} + 0.0591(pH) + 0.1976$ V. All photocurrent-voltage and current-voltage data were collected at a scan rate of 10mV/s unless otherwise stated. Steady-state PEC current densities were collected after 60 sec.

6.4 Results and Analysis

Figure 6.1 plots three photocurrent-voltage (*J-V*) response curves measured for the same α-Fe_2O_3 photoanode after deposition of Co-Pi at three different thicknesses, each under the same backside-illumination conditions (see Experimental). Upon deposition of ~2.3 nm thick ("optimized"[33]) Co-Pi, the photocurrent onset potential shifts in the negative direction by ~200 mV relative to the bare α-Fe_2O_3. Increasing the Co-Pi thickness to ~24.6 nm ("bottlenecked"[31,33]) yields reduced PEC current densities at all potentials. The increased current density at ~1.8 V in the bottlenecked photoanode reflects the onset of dark current from Co-Pi-catalyzed water oxidation. Photoelectrodes with Co-Pi thicknesses in between these values show a progressive negative shift in onset potential as the Co-Pi thickness decreases from ~25nm (see Appendix E). These data are consistent with our previous observations.[31,33]

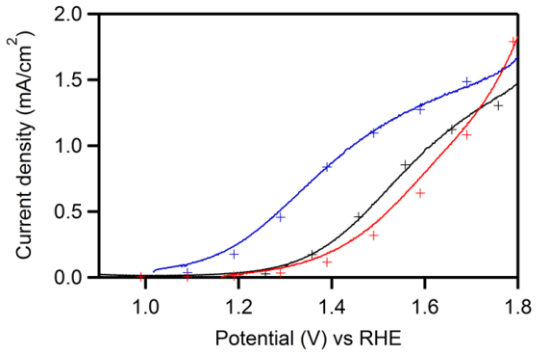

Figure 6.1. *J-V* curves of variable thickness Co-Pi on α-Fe_2O_3.
Photoelectrochemical current-voltage (*J-V*) curves measured for bare (black), optimized (~2.3 nm Co-Pi, blue), and bottlenecked (~24.6 nm Co-Pi, red) Co-Pi/α-Fe_2O_3 composite photoanodes in 0.1 M KPi buffer at pH 8. Measurements were performed using simulated AM 1.5 illumination of the photoanodes from the back side. The curves indicate data collected with a scan rate of 10mV/s. The + symbols indicate steady-state photocurrent densities after 100 seconds under illumination at the specified applied potential.

To probe the effects of Co-Pi thickness in more detail, photoelectrochemical impedance spectroscopy (PEIS) was performed on each of the three samples. Figure 6.2a shows Nyquist plots measured for the bare α-Fe_2O_3 and optimized Co-Pi/α-Fe_2O_3 photoanodes under backside illumination at +1.25 V. Two domains are clearly visible for each sample. For reference, the blue data show a typical Nyquist plot for Co-Pi on FTO measured in the dark at +1.8 V vs RHE. Here, only a single semicircle is observed, similar to Co-Pi/α-Fe_2O_3 photoanodes under dark conditions.

Figure 6.2b shows the simplified equivalent circuit (SEC) frequently used to model α-Fe_2O_3 electrochemical impedance data under illumination.[18,39,42,43] This SEC consists of series resistance (R_s), resistance from trapping of photogenerated conduction-band electrons (R_{trap}), and charge-transfer resistance from either α-Fe_2O_3 surface states or Co-Pi to water ($R_{CT\ SS,\ Co\text{-}Pi}$). The SEC also includes two capacitor elements: the capacitance of the bulk space-charge region and Helmholtz layer (C_{bulk}), and the minority (hole) capacitance of the surface states associated with α-Fe_2O_3 (C_{SS}) or Co-Pi ($C_{Co\text{-}Pi}$).

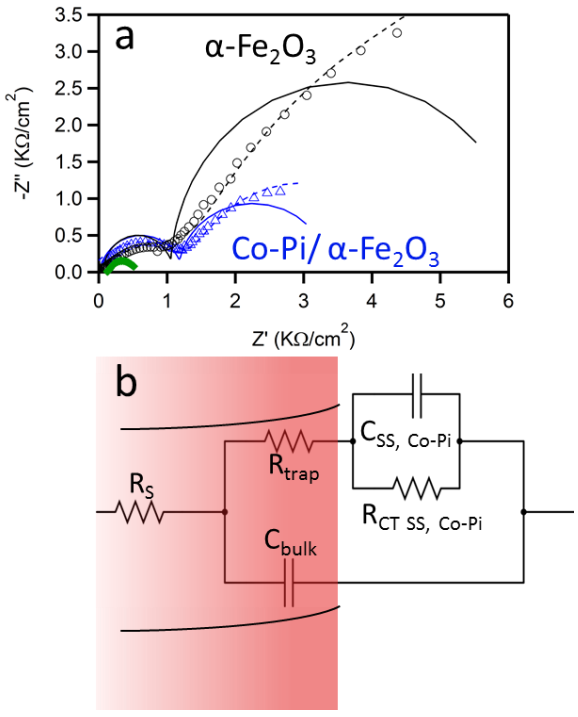

Figure 6.2. Nyquist plots of Co-Pi/α-Fe_2O_3 composite photoanodes.

Nyquist plots for bare α-Fe_2O_3 (black, open circles) and optimized (~2.3 nm Co-Pi, blue open triangles) Co-Pi/α-Fe_2O_3 photoanodes measured at +1.25 V vs RHE, and for an

FTO electrode with a ~490 nm-thick Co-Pi layer measured at +1.8 V vs RHE (green, open diamonds). The solid lines show fits to the data using a standard capacitor element, and the dashed lines shows fits using a CPE. (b) The equivalent circuit used to model the impedance spectra when two domains are visible. A simple Randles circuit was used for the Co-Pi/FTO electrochemical impedance data, where only one domain is visible.

The asymmetries of the Nyquist plots (relative to semicircles) are due to frequency dispersion detected in the impedance measurement.[44,45] Such dispersion is typical for rough surfaces with large populations of surface states. In light of this dispersion, the data were analyzed in two ways: (a) using a constant phase element (CPE), and (b) using a standard capacitor. The CPE analysis is often preferred for asymmetrical EIS data.[44,45] We find that the CPE and capacitor analyses yield similar results here, lending credence to the conclusions drawn from these analyses. Although the capacitor model underestimates the resistance for the charge-transfer semicircle slightly, it yields unique fits at low potentials (<+1.4 V) where the CPE analysis generally does not. In addition, modeling EIS data with a CPE contains an extra fitting parameter that damps –Z" relative to Z' in the Nyquist plot but has no physical significance (see Appendix E). For these reasons, the results presented here are those obtained using the standard capacitor analysis. For completeness, however, the analogous results obtained from the CPE analysis and statistical significance plots are provided as Supporting Information in Appendix E. For the Co-Pi/FTO sample, where only a single semicircle is visible in the Nyquist plot, a simple Randles circuit consisting of a series resistance (R_S) element followed by a parallel *RC* circuit (R_{CT}, C_{TOT}) was used.

Figure 6.3a plots $R_{CT\ SS}$, C_{SS}, and the *J-V* curve for the bare α-Fe_2O_3 photoanode measured under AM 1.5 backside illumination. Similar to planar α-Fe_2O_3 photoanodes,[17,18,42] C_{SS} maximizes and $R_{CT\ SS}$ drops at the onset potential for PEC water oxidation. The peak capacitance is ~1 mF/cm^2, which is consistent with values measured for planar films[18] after taking into account the surface roughness factor of ~20 in the present mesostructures.[41] On planar α-Fe_2O_3 photoanodes, PEIS measurements and spectroelectrochemical data have revealed that charge transfer from the semiconductor surface to the electrolyte proceeds through a series of surface-state-mediated steps involving high-oxidation-state iron species (Fe^{4+}, Fe^{5+}).[17,18,39,42] Surface states have also been observed on mesostructured α-Fe_2O_3.[15,20,21,37,46] From the similarities in

C_{SS}, $R_{CT\ SS}$, and the PEC *J-V* curves between planar and mesostructured α-Fe_2O_3, we conclude that charge transfer at the mesostructured α-Fe_2O_3 surface proceeds through a similar pathway as at the planar α-Fe_2O_3 surface.

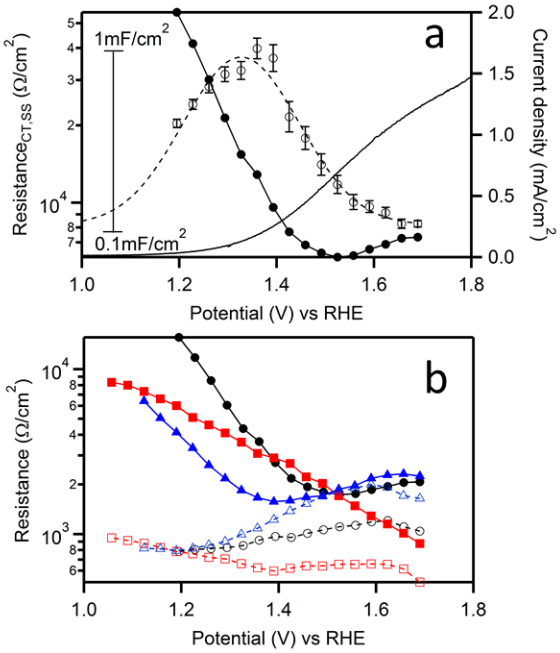

Figure 6.3. EIS parameters for α-Fe_2O_3 and resistances of composite photoelectrodes.

(a) Photoelectrochemical $R_{CT\ SS}$ (closed circles), C_{SS} (open circles), and *J-V* (solid line) data measured for a bare α-Fe_2O_3 photoanode, plotted vs applied potential. The inset scale bar refers to C_{SS}. The dashed line is a guide to the eye. The error bars represent uncertainties from the impedance fitting. **(b)** $R_{CT\ SS,\ Co\text{-}Pi}$ (solid symbols, solid lines) and R_{trap} (open symbols, dashed lines) of 0 (bare α-Fe_2O_3, black circles), ~2.3 (optimized Co-Pi/α-Fe_2O_3, blue triangles) and ~24.5 nm Co-Pi ("bottlenecked", red squares) on the same α-Fe_2O_3 photoanode, plotted vs applied potential.

Figure 6.3b plots $R_{CT\ SS,\ Co\text{-}Pi}$ and R_{trap} vs applied potential for the bare α-Fe_2O_3 photoanode as well as for the optimized and bottlenecked Co-Pi/α-Fe_2O_3 photoanodes. Apart from a -200 mV shift, $R_{CT\ Co\text{-}Pi}$ for the optimized composite photoanode closely resembles $R_{CT\ SS}$ for the bare α-Fe_2O_3 photoanode. In contrast, $R_{CT\ Co\text{-}Pi}$ for the bottlenecked photoanode exhibits behavior more characteristic of Co-Pi on FTO (see Appendix E). A similar evolution from α-

Fe_2O_3-like to Co-Pi-like kinetics with increasing Co-Pi thickness was also observed in the pH dependence of Co-Pi/α-Fe_2O_3 PEC measurements.[33]

For all Co-Pi thicknesses, R_{trap} behaves similarly at potentials more negative of ~+1.2 V, but as the potential is swept more positive, a clear dependence on Co-Pi thickness emerges. R_{trap} of the optimized Co-Pi/α-Fe_2O_3 photoanode increases relative to the bare photoanode to a maximum of 2000 Ω/cm^2 at +1.6 V, and R_{trap} for the bottlenecked photoanode decreases. Because R_{trap} probes conduction-band-electron trapping, changes in this parameter with the addition of Co-Pi suggest that Co-Pi influences surface electron-hole recombination (*vide infra).* As a cross check, the total resistance calculated from the PEIS analysis ($R_{TOT} = R_s + R_{trap} + R_{CT\ SS,\ Co\text{-}Pi}$) was plotted vs applied potential and compared with the differential resistance (dV/dI) obtained directly from the *J-V* data, plotted in the same way. These two independent data sets agree well (see Appendix E).

Figure 6.4 compares capacitance values measured for illuminated Co-Pi/α-Fe_2O_3 photoanodes with those of Co-Pi/FTO electrodes measured in the dark. Figure 6.4a plots $C_{Co\text{-}Pi}$ data overlaid with the *J-V* curves for optimized and bottlenecked Co-Pi thicknesses on the same α-Fe_2O_3 photoanode. As with the bare α-Fe_2O_3 photoanode, these data show maxima in $C_{Co\text{-}Pi}$ near the onset potentials for PEC water oxidation, where the maximum $C_{Co\text{-}Pi}$ scales with Co-Pi thickness. The increasing $C_{Co\text{-}Pi}$ with increasing Co-Pi thickness is interpreted as reflecting hole storage within Co-Pi. For example, if this increase in capacitance were the result of hole storage within α-Fe_2O_3 itself, then given an average unit cell volume of 34.8 nm^3, six Fe_2O_3 formula units per unit cell, and a surface area-to-volume ratio of 20,[41] every iron atom within ~3 nm of the surface must be formally oxidized to Fe^{4+} to accommodate this charge accumulation. Similar capacitance values have been measured on planar Co-Pi/α-Fe_2O_3 films in which the charge capacity is nearly equal to the total number of Fe^{3+} atoms in the film.[39] Such transformations would require a far greater applied potential, or the hematite surface would have to be permeable to electrolyte ions for charge compensation. Neither of these scenarios is considered probable given the close proximity and redox properties of Co-Pi. The increasing capacitance with increasing Co-Pi thickness is thus attributed to hole storage within Co-Pi, confirming hole transfer from α-Fe_2O_3 to Co-Pi.

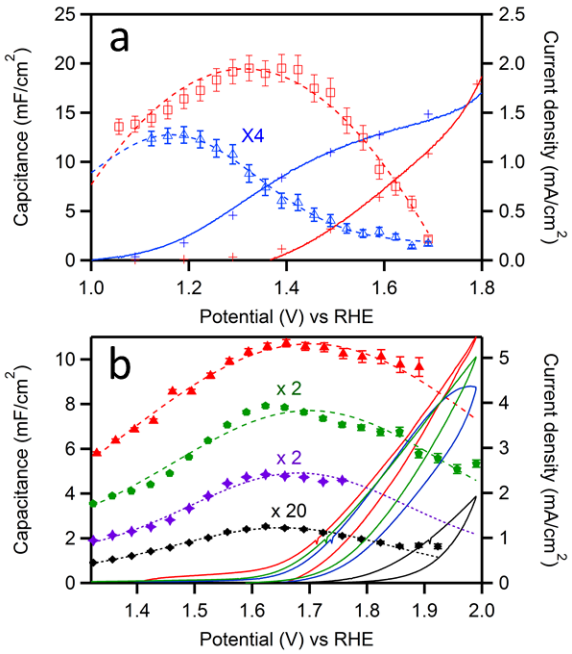

Figure 6.4. Comparison of capacitance values for composite photoanodes and Co-Pi thin films.

(a) $C_{SS\ Co\text{-}Pi}$ (open symbols) and *J-V* (hash marks) data measured for ~2.3 nm (blue triangles) and ~24.5 nm (red circles) Co-Pi thicknesses on the same α-Fe_2O_3 photoanode, plotted vs applied potential. Measurements used backside AM 1.5 illumination in 0.1 M KPi at pH 8. The symbols on the *J-V* curves represent steady-state current densities. **(b)** C_{TOT} (markers) and dark *J-V* (solid lines) data measured at 10 mV/s scan rate for ~1.2 (black closed diamonds), ~24.5 (purple closed stars), ~46.8 (green closed pentagons), and ~490 nm (red closed triangles) Co-Pi thicknesses on planar FTO, plotted vs applied potential. The dashed lines on the $C_{Co\text{-}Pi,\ TOT}$ data are guides to the eye.

The difference in potential between the two peak capacitances (~180 mV) is essentially the same as the difference in photocurrent onset potentials (~200 mV). Figure 6.4b shows the dark cyclic-voltammetry and EIS C_{TOT} data for four Co-Pi thicknesses on FTO. These *J-V* curves follow the trends reported previously for Co-Pi electrocatalysis.[27,28,30,47] For all Co-Pi thicknesses, electrocatalysis is preceded by a maximum in C_{TOT}. Importantly, C_{TOT} for the Co-Pi/FTO electrodes maximizes at nearly the same applied potential regardless of Co-Pi thickness. In contrast, the maximum in C_{TOT} shifts with Co-Pi thickness in the Co-Pi/α-Fe_2O_3 photoanodes (Fig. 6.4a). The shift in $C_{SS\ Co\text{-}Pi}$ between optimized and bottlenecked Co-Pi/α-Fe_2O_3 photoanodes

suggests that this PEC water oxidation is kinetically limited. Under thermodynamic control in the dark, the Fermi level of the electrocatalytic cell is dictated by the applied potential, and the peak capacitance therefore occurs at approximately the same potential regardless of Co-Pi thickness (Fig. 6.4b). Under AM 1.5 illumination in a thermodynamically limited regime, the driving force for catalytic turnover is determined by the potential of the holes entering the Co-Pi layer. In this case, the peak capacitance would also occur close to the same potential regardless of Co-Pi thickness. In a kinetically limited regime, however, the peak capacitance (and thus the current density) depends on the Co-Pi thickness. The positive shift in the peak $C_{\text{Co-Pi}}$ with increasing Co-Pi thickness observed in Fig. 6.4a thus implicates a Co-Pi-induced kinetic barrier in the bottlenecked Co-Pi/α-Fe_2O_3 photoanodes, *i.e.*, thick Co-Pi layers introduce kinetic limitations to the current densities achievable in mesostructured Co-Pi/α-Fe_2O_3 composite photoanodes.

Co-Pi shows first-order charge-transfer kinetics under electrochemical conditions, where a reversible proton-coupled electron transfer step is thought to precede the rate-determining O-O bond-formation step.[29,30] The rate-determining electron-transfer step for water-oxidation catalysis at the surface of α-Fe_2O_3 has also been described by a phenomenological charge-transfer rate constant (k_{CT}).[22,48] Likewise, recombination of photogenerated holes with conduction-band electrons can be parameterized phenomenologically by k_{rec}. Taking bulk recombination (>~5nm from the SCLJ) as independent of surface modification, PEC water oxidation is thus governed by the balance between k_{CT} and k_{rec}. k_{CT} can be obtained directly from PEIS data as the frequency at the maximum phase angle of the charge-transfer semicircle in the Nyquist plot (the RC time constant).

The resistance parameters measured by PEIS (R_{trap} and R_{CT}) and the rate constants k_{CT} and k_{rec} are related as described by equation 6.1,[16,49] where k_{trap} is the electron-trapping rate constant, n is the electron density (taken to be constant at constant illumination intensity), and $\gamma(V)$ is the probability of electron-trap occupation at a given trap energy and applied potential (V).

$$\frac{R_{trap}}{R_{CT}} = \frac{k_{CT}}{(nk_{trap}+k_{rec})} = \gamma(V)\frac{k_{CT}}{k_{rec}} \qquad \text{(Equation 6.1)}$$

$\gamma(V)$ has the functional form described by equation 6.2, where E_{F_0} is the Fermi level at equilibrium, E_T is the energy of the electron trap, q is the elementary charge, and k_B is the Boltzmann constant.

$$\gamma(V) = \left[1 + e^{\frac{E_{F_0} - E_T}{k_B T}} * e^{\frac{-qV}{k_b T}}\right]^{-1} \qquad \text{(Equation 6.2)}$$

Electron traps at α-Fe_2O_3 surfaces lie within a few hundred meV of the conduction-band edge (< 300 meV),[21,36] and consequently $\gamma(V)$ is essentially unity at the potentials of interest (>+1.2 V vs RHE, see Appendix E for details), simplifying eq 6.1.

Figure 6.5 summarizes the PEIS results and analysis. From Fig. 6.5a, k_{CT} for the bare electrode is constant at ~1 s^{-1} at potentials below +1.3 V vs RHE. When the potential is swept more positive, k_{CT} increases to ~6.6 s^{-1} at +1.56 V vs RHE. At the ideal SCLJ, k_{CT} would be independent of voltage. This change in k_{CT} thus implicates a potential drop across the Helmholtz layer, likely because of Fermi-level pinning. By changing the electronic environment within the Helmholtz region, the transition-state energy is lowered and k_{CT} increases.[16] Fermi-level pinning in aqueous electrolyte has been observed with α-Fe_2O_3 photoelectrodes and is proposed to be a primary cause for the overpotentials required to drive PEC water oxidation.[16,18-21,39] For the optimized composite photoelectrode, a similar increase with potential is seen, but k_{CT} is smaller than in the bare electrode at all potentials. k_{CT} decreases even further when a thick Co-Pi layer is deposited. This decrease in k_{CT} with increasing Co-Pi thickness is surprising given that Co-Pi is a competent water-oxidation electrocatalyst[27,28,30] and that at low applied potentials (> +1.3 V) PEC OER catalysis proceeds primarily through Co-Pi in mesostructured Co-Pi/α-Fe_2O_3 composite photoanodes.[33]

The recombination rate constants (k_{rec}) for bare, optimized, and bottlenecked Co-Pi/α-Fe_2O_3 photoanodes deduced from the PEIS analysis are plotted in Fig. 6.5b. Consistent with previous reports,[15,16,18,37] k_{rec} of the bare α-Fe_2O_3 photoanode at +1.2 V vs RHE is one order of magnitude larger than k_{CT} at the same potential (11 vs 1 s^{-1}). This slow charge transfer relative to recombination prevents Faradaic current flow, as reflected in the very small PEC currents observed at these potentials (Fig. 6.1). As expected, k_{rec} decreases with increasing positive bias, and at +1.56V it is approximately equal to k_{CT}. Meaningful values for k_{rec} at more positive potentials were not attainable. Interestingly, upon addition of Co-Pi at its optimized thickness,

k_{rec} is reduced by a factor of ~2 to 5 throughout the entire potential window. The bottlenecked photoelectrode shows an even greater decrease in k_{rec}, by a factor of ~10 to 50 relative to α-Fe_2O_3. For both Co-Pi thicknesses, k_{rec} is largely independent of the applied bias. In the absence of Co-Pi, all recombination must occur either within the bulk or at the α-Fe_2O_3 surface, and k_{rec} is expected to decrease as potential is increased and the depletion region is expanded.[37] When k_{rec} is independent of applied bias, however, the limiting recombination involves charges that are electronically decoupled from the semiconductor (*e.g.*, stored within the Co-Pi). Electronic decoupling is expected of materials that form a so-called 'adaptive junction'.[24,50] Therefore, we assign k_{rec} to recombination at the Co-Pi/α-Fe_2O_3 interface that is limited by the flux of Co-Pi holes to the α-Fe_2O_3 surface.

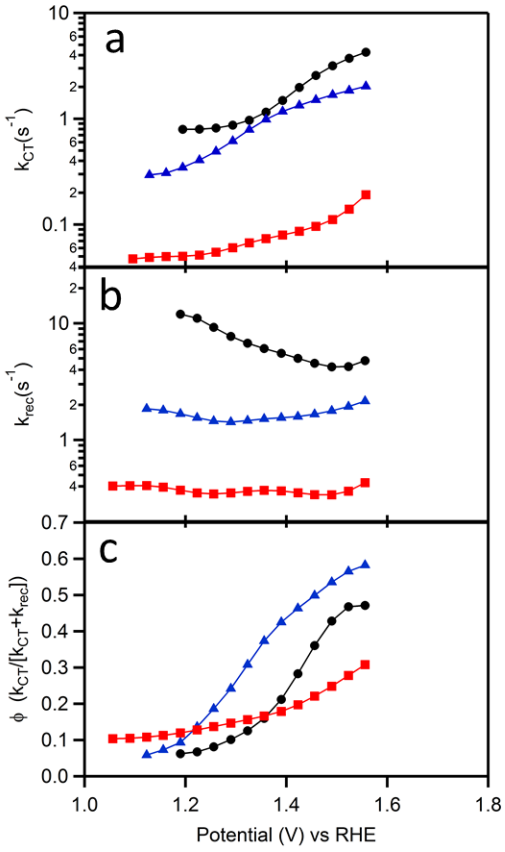

Figure 6.5. Charge transfer and recombination rate constants for Co-Pi/α-Fe_2O_3. **(a)** Charge-transfer rate constants (k_{CT}), **(b)** recombination rate constants (k_{rec}), and **(c)** water-oxidation quantum efficiencies for bare α-Fe_2O_3 (black circles), 2.3 nm Co-Pi/α-

Fe_2O_3 (blue triangles), and 24.5 nm Co-Pi/α-Fe_2O_3 (red squares) photoanodes determined from the analysis of PEIS data, all plotted vs applied potential.

The PEIS parameters detailed above now allow the water-oxidation quantum efficiency to be calculated as the charge-transfer branching ratio, as described by equation 6.3.

$$\varphi = \frac{k_{CT}}{k_{CT}+k_{rec}} \qquad \text{(Equation 6.3)}$$

Figure 6.5c plots this quantum efficiency vs potential. These quantum-efficiency plots, deduced entirely from analysis of PEIS data, agree remarkably well with the *J-V* data for the same samples presented in Fig. 6.1. This agreement illustrates that the shapes of the PEC *J-V* curves with and without Co-Pi are determined by the competition between charge-transfer and recombination processes at the α-Fe_2O_3 surface. Analysis of the individual rate constants used to generate these curves thus provides valuable new insight into the microscopic effects of Co-Pi on α-Fe_2O_3 PEC water oxidation.

Consistent with previous reports,[15,16,18,37] this analysis shows that the bare α-Fe_2O_3 photoanode is limited by fast recombination (large k_{rec}) despite its relatively favorable charge-transfer kinetics. Little photocurrent occurs at potentials where band bending is insufficient to slow this recombination. In contrast, the bottlenecked Co-Pi/α-Fe_2O_3 photoanode is limited by slow charge transfer (small k_{CT}), in spite of a k_{rec} that has been substantially reduced relative to α-Fe_2O_3. The optimized Co-Pi/α-Fe_2O_3 photoanode balances this *decrease* in k_{CT} against the concomitant *decrease* in k_{rec} to yield a net *increase* in photocurrent density at low potentials. The same conclusion is drawn when the EIS data are modeled using a constant phase element (CPE) instead of a capacitor (see Appendix E).

6.5 Discussion

The primary function of the Co-Pi electrocatalyst when deposited on the surface of α-Fe_2O_3 can now be understood. α-Fe_2O_3 is a self-limiting photoanode in which positive surface charge accumulation inhibits band bending through quasi-Fermi-level pinning, leading to rapid electron-hole recombination at low applied bias (Fig. 6.6). We propose that the primary role of Co-Pi is to provide an alternative pathway for water oxidation that avoids positive charge accumulation at the α-Fe_2O_3 surface. With thin Co-Pi layers, photogenerated holes can either be

transferred to Co-Pi or trapped at the α-Fe_2O_3 surface. Holes collected by Co-Pi reduce the surface hole concentration, relieving to a degree the pinned quasi-Fermi level, which in turn expands the depletion region and reduces surface electron-hole recombination at less positive potentials. Thicker Co-Pi layers almost completely eliminate the native surface-state charge-transfer water-oxidation pathway, allowing the semiconductor to behave in a more ideal fashion, where VB holes are only transferred to Co-Pi. The slower water oxidation by Co-Pi relative to α-Fe_2O_3 promotes interfacial recombination between photogenerated α-Fe_2O_3 conduction-band electrons and Co-Pi holes, however, leading to the "kinetic bottleneck" phenomenon observed in mesostructured Co-Pi/α-Fe_2O_3 photoanodes.[7,31,33]

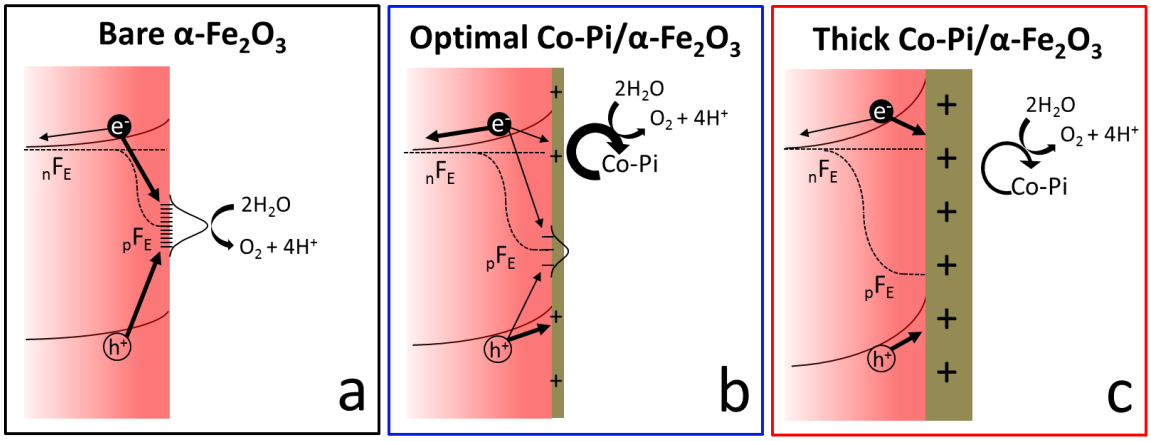

Figure 6.6. Schematic illustration of the relevant kinetic processes in Co-Pi/α-Fe_2O_3. Schematic illustration of the recombination and charge-transfer pathways of α-Fe_2O_3 photoanodes with **(a)** no, **(b)** a thin (optimized), and **(c)** a thick (bottleneck) Co-Pi layer on their surfaces, each under illumination at potentials negative of +1.5 V vs RHE. For bare α-Fe_2O_3, charge transfer proceeds through a surface-state-mediated pathway that pins the hole quasi-Fermi level ($_pF_E$), resulting in fast recombination and little Faradaic current. For the same α-Fe_2O_3 photoanode with an optimized Co-Pi layer, an alternative water-oxidation pathway exists that decreases the surface charge, partially unpins the hole quasi-Fermi level, and promotes charge transfer from both α-Fe_2O_3 and Co-Pi to water. For the same α-Fe_2O_3 photoanode with a thick Co-Pi layer, the direct α-Fe_2O_3 surface-mediated charge-transfer pathway is eliminated, completely unpinning the hole quasi-Fermi level, and all water oxidation proceeds through Co-Pi. From (b) to (c), the increased capacitive accumulation of Co-Pi oxidizing equivalents (Co^{4+}) leads to

increased interfacial recombination with photogenerated α-Fe_2O_3 conduction-band electrons, limiting Faradaic current flow in (c) relative to (b).

Although it is not clear exactly why k_{CT} decreases with increasing Co-Pi thickness, one hypothesis is that this decrease stems from a decrease in the Co-Pi hole density as the Co-Pi thickness (volume) is increased, which reduces the turnover frequency per cobalt and elongates the hole residence time. These changes create greater opportunity for interfacial recombination. Another possibility is that Co^{4+} intermediates are stabilized in thick Co-Pi layers, increasing the barrier to O-O bond formation and hence again elongating the hole residence time. Long lived Co^{4+} intermediates in thick Co-Pi films have been observed by EPR and X-ray spectroscopies.[29,51] In any case, it appears that Co-Pi thickness tunes the balance between surface recombination and charge-transfer kinetics, and in mesostructured α-Fe_2O_3 photoanodes the optimal balance occurs at small Co-Pi thicknesses. At this optimal thickness, water oxidation is catalyzed by Co-Pi at the onset potential and is catalyzed directly at the α-Fe_2O_3 surface at greater applied potentials.[29,33] The picture that emerges from these studies thus contains elements from both leading hypotheses about the mechanism by which Co-Pi enhances the PEC performance of α-Fe_2O_3 photoanodes, and helps to reconcile the results from transient absorption and photoelectrochemical measurements within a unified interpretation.

6.6 Conclusion

The primary function of Co-Pi when interfaced with α-Fe_2O_3 photoanodes is to provide a water-oxidation pathway that does not involve α-Fe_2O_3 surface hole traps. Bypassing these traps unpins the hole quasi-Fermi level and allows the semiconductor to behave more ideally at less positive potentials. At optimal Co-Pi thicknesses, water oxidation is competitive against surface-state-mediated electron-hole recombination and oxygen evolution catalysis occurs. With thick Co-Pi layers, recombination between α-Fe_2O_3 electrons and Co-Pi holes attenuates photocurrents at low potentials because of slow Co-Pi reaction kinetics. Although the results presented here were obtained using mesostructured α-Fe_2O_3 photoanodes prepared by APCVD, these insights should apply to other catalyst-modified photoanodes investigated for solar-driven photoelectrochemical water oxidation.

6.7 References

(1) Fujishima, A.; Honda, K.: Electrochemical Photolysis of Water at a Semiconductor Electrode. *Nature* 1972, *238*, 37-38.

(2) Lewis, N. S.; Nocera, D. G.: Powering the planet: Chemical challenges in solar energy utilization. *PNAS* 2006, *103*, 15729-15735.

(3) Nocera, D. G.: Personalized Energy: The Home as a Solar Power Station and Solar Gas Station. *ChemSusChem* 2009, *2*, 387-390.

(4) Bard, A. J.; Fox, M. A.: Artificial Photosynthesis: Solar Splitting of Water to Hydrogen and Oxygen. *Acc. Chem. Res.* 1995, *28*, 141-145.

(5) Moomow, W.; Yamba, F.; Kamimoto, M.; Maurice, L.; Nyboer, J.; Urama, K.; Weir, T.: Introduction. In *IPCC Special Report on Renewable Energy Sources and Climate change Mitigation*; Edenhofer, O., Pichs-Madruga, R., Sokona, Y., Seyboth, K., Matschoss, P., Kadner, S., Zwickel, T., Eickemeier, P., Hansen, G., Schlömer, S., von Stechow, C., Eds.; Cambridge University Press: United Kingdom and New York, NY, USA, 2011.

(6) Khaselev, O.; Turner, J. A.: A Monolithic Photovoltaic-Photoelectrochemical Device for Hydrogen Production via Water Splitting. *Science* 1998, *280*, 425-427.

(7) Zhong, D. K.; Cornuz, M.; Sivula, K.; Gratzel, M.; Gamelin, D. R.: Photo-assisted electrodeposition of cobalt-phosphate (Co-Pi) catalyst on hematite photoanodes for solar water oxidation. *Energy Environ. Sci.* 2011, *4*, 1759-1764.

(8) Grätzel, M.: Photoelectrochemical cells. *Nature* 2001, *414*, 338-344.

(9) Duret, A.; Grätzel, M.: Visible Light-Induced Water Oxidation on Mesoscopic α-Fe_2O_3 Films Made by Ultrasonic Spray Pyrolysis. *J. Phys. Chem. B* 2005, *109*, 17184-17191.

(10) Osterloh, F. E.: Inorganic Materials as Catalysts for Photochemical Splitting of Water. *Chem. Mater.* 2007, *20*, 35-54.

(11) Osterloh, F. E.: Inorganic nanostructures for photoelectrochemical and photocatalytic water splitting. *Chem. Soc. Rev.* 2013, *42*, 2294-2320.

(12) Gardner, R. F. G.; Sweett, F.; Tanner, D. W.: The electrical properties of alpha ferric oxide—I.: The impure oxide. *J. Phys. Chem. Solids* 1963, *24*, 1175-1181.

(13) Kennedy, J. H.; Frese, K. W.: Photooxidation of Water at α-Fe_2O_3 Electrodes. *J. Electrochem. Soc.* 1978, *125*, 709-714.

(14) Dare-Edwards, M. P.; Goodenough, J. B.; Hamnett, A.; Trevellick, P. R.: Electrochemistry and photoelectrochemistry of iron(III) oxide. *J. Chem. Soc. Faraday Trans.* 1983, *79*, 2027-2041.

(15) Le Formal, F.; Sivula, K.; Grätzel, M.: The Transient Photocurrent and Photovoltage Behavior of a Hematite Photoanode under Working Conditions and the Influence of Surface Treatments. *J. Phys. Chem. C* 2012, *116*, 26707-26720.

(16) Upul Wijayantha, K. G.; Saremi-Yarahmadi, S.; Peter, L. M.: Kinetics of oxygen evolution at α-Fe_2O_3 photoanodes: a study by photoelectrochemical impedance spectroscopy. *Phys. Chem. Chem. Phys.* 2011, *13*, 5264-5270.

(17) Hamann, T. W.: Splitting water with rust: hematite photoelectrochemistry. *Dalton Trans.* 2012, *41*, 7830-7834.

(18) Klahr, B.; Gimenez, S.; Fabregat-Santiago, F.; Bisquert, J.; Hamann, T. W.: Electrochemical and photoelectrochemical investigation of water oxidation with hematite electrodes. *Energy Environ. Sci.* 2012, *5*, 7626-7636.

(19) Klahr, B. M.; Hamann, T. W.: Current and Voltage Limiting Processes in Thin Film Hematite Electrodes. *J. Phys. Chem. C* 2011, *115*, 8393-8399.

(20) Barroso, M.; Mesa, C. A.; Pendlebury, S. R.; Cowan, A. J.; Hisatomi, T.; Sivula, K.; Grätzel, M.; Klug, D. R.; Durrant, J. R.: Dynamics of photogenerated holes in surface modified α-Fe_2O_3 photoanodes for solar water splitting. *PNAS* 2012, *109*, 15640-15645.

(21) Barroso, M.; Pendlebury, S. R.; Cowan, A. J.; Durrant, J. R.: Charge carrier trapping, recombination and transfer in hematite (α-Fe_2O_3) water splitting photoanodes. *Chem. Sci.* 2013, *4*, 2724-2734.

(22) Pendlebury, S. R.; Cowan, A. J.; Barroso, M.; Sivula, K.; Ye, J.; Gratzel, M.; Klug, D. R.; Tang, J.; Durrant, J. R.: Correlating long-lived photogenerated hole populations with photocurrent densities in hematite water oxidation photoanodes. *Energy Environ. Sci.* 2012, *5*, 6304-6312.

(23) Iandolo, B.; Wickman, B.; Zoric, I.; Hellman, A.: The rise of hematite: origin and strategies to reduce the high onset potential for the oxygen evolution reaction. *J. Mat. Chem. A* 2015, *3*, 16896-16912.

(24) Lin, F.; Boettcher, S. W.: Adaptive semiconductor/electrocatalyst junctions in water-splitting photoanodes. *Nat. Mater.* 2014, *13*, 81-86.

(25) Nocera, D. G.: The Artificial Leaf. *Acc. Chem. Res.* 2012, *45*, 767-776.

(26) Moniz, S. J. A.; Shevlin, S. A.; Martin, D. J.; Guo, Z.-X.; Tang, J.: Visible-light driven heterojunction photocatalysts for water splitting - a critical review. *Energy Environ. Sci.* 2015, *8*, 731-759.

(27) Kanan, M. W.; Nocera, D. G.: In Situ Formation of an Oxygen-Evolving Catalyst in Neutral Water Containing Phosphate and Co^{2+}. *Science* 2008, *321*, 1072-1075.

(28) Kanan, M. W.; Surendranath, Y.; Nocera, D. G.: Cobalt-phosphate oxygen-evolving compound. *Chem. Soc. Rev.* 2009, *38*, 109-114.

(29) Kanan, M. W.; Yano, J.; Surendranath, Y.; Dincă, M.; Yachandra, V. K.; Nocera, D. G.: Structure and Valency of a Cobalt−Phosphate Water Oxidation Catalyst Determined by in Situ X-ray Spectroscopy. *J. Am. Chem. Soc.* 2010, *132*, 13692-13701.

(30) Surendranath, Y.; Kanan, M. W.; Nocera, D. G.: Mechanistic Studies of the Oxygen Evolution Reaction by a Cobalt-Phosphate Catalyst at Neutral pH. *J. Am. Chem. Soc.* 2010, *132*, 16501-16509.

(31) Zhong, D. K.; Gamelin, D. R.: Photoelectrochemical Water Oxidation by Cobalt Catalyst ("Co−Pi")/α-Fe_2O_3 Composite Photoanodes: Oxygen Evolution and Resolution of a Kinetic Bottleneck. *J. Am. Chem. Soc.* 2010, *132*, 4202-4207.

(32) Zhong, D. K.; Sun, J.; Inumaru, H.; Gamelin, D. R.: Solar Water Oxidation by Composite Catalyst/α-Fe_2O_3 Photoanodes. *J. Am. Chem. Soc.* 2009, *131*, 6086-6087.

(33) Carroll, G. M.; Zhong, D. K.; Gamelin, D. R.: Mechanistic insights into solar water oxidation by cobalt-phosphate-modified α-Fe_2O_3photoanodes. *Energy Environ. Sci.* 2015, *8*, 577-584.

(34) Barroso, M.; Cowan, A. J.; Pendlebury, S. R.; Grätzel, M.; Klug, D. R.; Durrant, J. R.: The Role of Cobalt Phosphate in Enhancing the Photocatalytic Activity of α-Fe_2O_3 toward Water Oxidation. *J. Am. Chem. Soc.* 2011, *133*, 14868-14871.

(35) Gamelin, D. R.: Water splitting: Catalyst or spectator? *Nat. Chem.* 2012, *4*, 965-967.

(36) Cowan, A. J.; Durrant, J. R.: Long-lived charge separated states in nanostructured semiconductor photoelectrodes for the production of solar fuels. *Chem. Soc. Rev.* 2013, *42*, 2281-2293.

(37) Cummings, C. Y.; Marken, F.; Peter, L. M.; Tahir, A. A.; Wijayantha, K. G. U.: Kinetics and mechanism of light-driven oxygen evolution at thin film α-Fe_2O_3 electrodes. *Chem. Comm.* 2012, *48*, 2027-2029.

(38) Liu, R.; Zheng, Z.; Spurgeon, J.; Yang, X.: Enhanced photoelectrochemical water-splitting performance of semiconductors by surface passivation layers. *Energy Environ. Sci.* 2014, *7*, 2504-2517.

(39) Klahr, B.; Giménez, S.; Fabregat-Santiago, F.; Bisquert, J.; Hamann, T. W.: Photoelectrochemical and Impedance Spectroscopic Investigation of Water Oxidation with "Co-Pi" coated Hematite Electrodes. *J. Am. Chem. Soc.* 2012, *134*, 16693-16700.

(40) Hamann, T. W.: Water splitting: An adaptive junction. *Nat. Mater.* 2014, *13*, 3-4.

(41) Kay, A.; Cesar, I.; Grätzel, M.: New Benchmark for Water Photooxidation by Nanostructured α-Fe_2O_3 Films. *J. Am. Chem. Soc.* 2006, *128*, 15714-15721.

(42) Klahr, B.; Hamann, T.: Water Oxidation on Hematite Photoelectrodes: Insight into the Nature of Surface States through In Situ Spectroelectrochemistry. *J. Phys. Chem. C* 2014, *118*, 10393-10399.

(43) Le Formal, F.; Pendlebury, S. R.; Cornuz, M.; Tilley, S. D.; Grätzel, M.; Durrant, J. R.: Back Electron–Hole Recombination in Hematite Photoanodes for Water Splitting. *J. Am. Chem. Soc.* 2014, *136*, 2564-2574.

(44) Salvarezza, R. C.; Arvia, A. J.: A Modern Approach to Surface Roughness Applied to Electrochemical Systems. In *Modern Aspects of Electrochemistry*; Conway, B. E., Bockris, J. O. M., White, R., Eds.; Springer US, 1996; Vol. 28; pp 289-373.

(45) Lasia, A.: Electrochemical Impedance Spectroscopy and its Applications. In *Modern Aspects of Electrochemistry*; Conway, B. E., Bockris, J. O. M., White, R., Eds.; Springer US, 2002; Vol. 32; pp 143-248.

(46) Sivula, K.: Metal Oxide Photoelectrodes for Solar Fuel Production, Surface Traps, and Catalysis. *J. Phys. Chem. Lett.* 2013, *4*, 1624-1633.

(47) Surendranath, Y.; Dincă, M.; Nocera, D. G.: Electrolyte-Dependent Electrosynthesis and Activity of Cobalt-Based Water Oxidation Catalysts. *J. Am. Chem. Soc.* 2009, *131*, 2615-2620.

(48) Cowan, A. J.; Barnett, C. J.; Pendlebury, S. R.; Barroso, M.; Sivula, K.; Grätzel, M.; Durrant, J. R.; Klug, D. R.: Activation Energies for the Rate-Limiting Step in Water Photooxidation by Nanostructured α-Fe_2O_3 and TiO_2. *J. Am. Chem. Soc.* 2011, *133*, 10134-10140.

(49) Bertoluzzi, L.; Bisquert, J.: Equivalent Circuit of Electrons and Holes in Thin Semiconductor Films for Photoelectrochemical Water Splitting Applications. *J. Phys. Chem. Lett.* 2012, *3*, 2517-2522.

(50) Mills, T. J.; Lin, F.; Boettcher, S. W.: Theory and Simulations of Electrocatalyst-Coated Semiconductor Electrodes for Solar Water Splitting. *Phys. Rev. Lett.* 2014, *112*, 148304.

(51) McAlpin, J. G.; Surendranath, Y.; Dincă, M.; Stich, T. A.; Stoian, S. A.; Casey, W. H.; Nocera, D. G.; Britt, R. D.: EPR Evidence for Co(IV) Species Produced During Water Oxidation at Neutral pH. *J. Am. Chem. Soc.* 2010, *132*, 6882-6883.

Appendix A

Supporting Information for:

Chapter 2: Redox Potentials of Colloidal *n*-Type ZnO Nanocrystals: Effects of Confinement, Electron Density, and Fermi-Level Pinning by Aldehyde Hydrogenation

Adapted from: Carroll, G. M.; Schimpf, A. M.; Tsui, E. Y.; Gamelin, D. R. *J. Am. Chem. Soc.* **2015**, *137*, 11163.

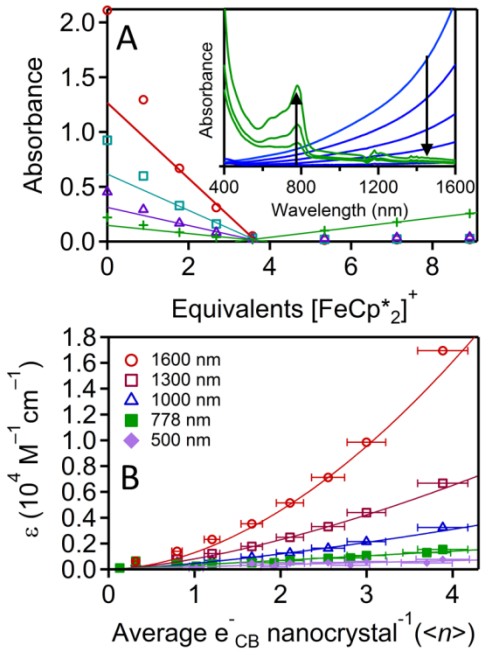

Figure A.1. Experimental determination of e^-_{CB}:ZnO extinction coefficients

(a) Absorbance values of maximally photodoped ZnO nanocrystals (r = 1.9 nm) at 1600 nm (red, open circles), 1300 nm (teal, open squares), 1000 nm (violet, open triangles), and 778 nm (green, hash marks), measured after addition of a known amount of $[Cp^*_2Fe][BAr_F]$. The solid lines are linear regression fits to the absorbance data nearest the intercept. The inset shows absorption spectra of the photodoped ZnO nanocrystals as $[Cp^*_2Fe][BAr_F]$ is titrated in. **(b)** Nanocrystal molar extinction coefficients measured at 1600 nm (red, open circles), 1300 nm (maroon, open squares), 1000 nm (blue, open

triangles), 778 nm (green, closed squares), and 500 nm (pink, closed diamonds) plotted as a function of <*n*>. The solid lines show best fits to the data with the power function $\varepsilon_\lambda = Q_\lambda \times \langle n \rangle^p$, where Q_λ and p are floating values (Table A.1).

Table A.1. 3.7 nm ZnO extinction coefficient parameters.

Fitting parameters used in Figure A.1.B.

Q_{1600nm}	Q_{1300nm}	Q_{1000nm}	Q_{778nm}	p_{1600nm}	p_{1300nm}	p_{1000nm}	p_{778nm}
1297	808	460	337	1.8	1.5	1.4	1.0

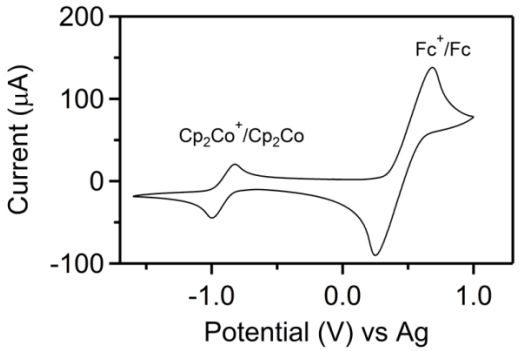

Figure A.2. Experimental determination of the Cp_2Co^+/Cp_2Co redox potential.

Cyclic voltammogram of Cp_2Co^+/Cp_2Co and Fc^+/Fc couples dissolved in a solution of deaerated, dried THF/toluene (14:1) with 0.1M $TBAPF_6$ as the supporting electrolyte and measured in a N_2 glovebox. The CV was measured using a three-electrode cell with Pt wire working and counter electrodes and an Ag wire pseudo-reference. The scan rate was 100 mV/s. From this measurement, ΔE^o = -1.37 V ($E_{1/2}(Cp_2Co^+/Cp_2Co) - E_{1/2}(Fc^+/Fc)$).

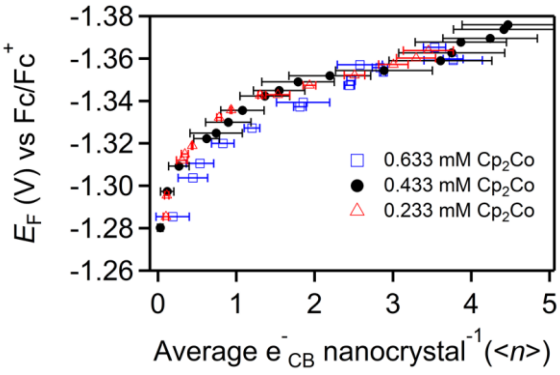

Figure A.3. Cp_2Co^+ concentration dependence on measured e^-_{CB}:ZnO E_F.

E_F values determined from optical redox indicator measurements using three different concentrations of $[Cp_2Co][PF_6]$, plotted at increasing photodoping levels of ZnO nanocrystals using EtOH as the hole quencher. E_F values are referenced to ferrocene, and the error bars represent ±σ from <*n*>.

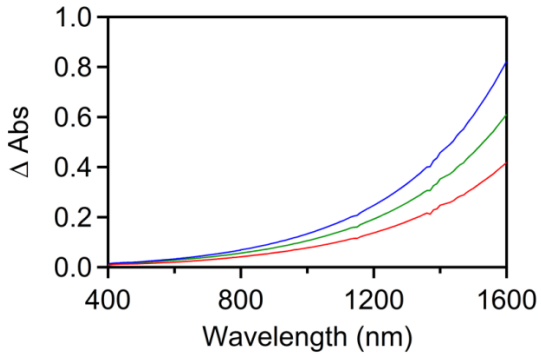

Figure A.4. Photodoping ZnO with Cp_2Co^* as the redox indicator.

Differential electronic absorption spectra of photochemically doped colloidal ZnO (*r* = 1.9 nm) nanocrystals with $[Cp^*_2Co][PF_6]$ (E^o = - 1.91 V vs Fc^+/Fc) in 14:1:0.5 THF:toluene:EtOH mixture after 10 min (red), 20 min (green), and 1 hr (blue) of UV irradiation.

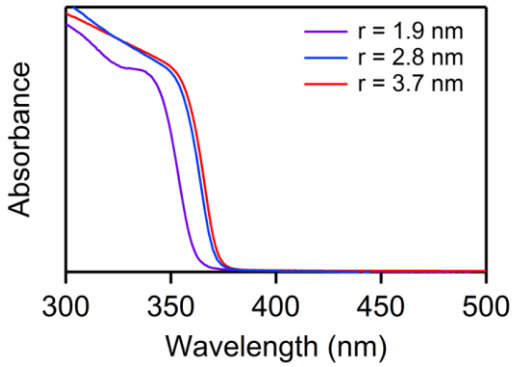

Figure A.5. Excitonic absorption spectra for 1.9, 2.8, and 3.7nm ZnO.

Excitonic absorption spectra of the three different sizes of TOPO-capped colloidal ZnO nanocrystals in 14:1:0.5 THF:toluene:ethanol mixture. The average radii of the smaller nanocrystals ($r \leq 2.8$ nm) were determined from empirical correlations between radii and absorption spectra.[1,2] The average radii of the larger nanocrystals (*r* = 3.7 nm) was

determined by powder X-ray diffraction and by analysis of transmission electron microscope images.

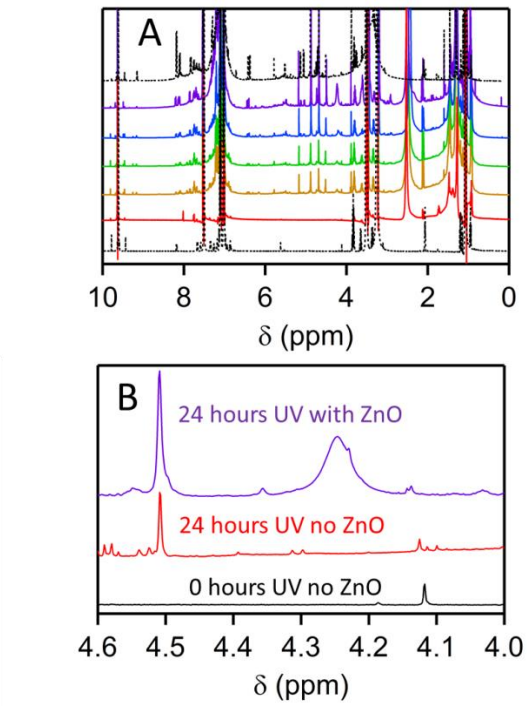

Figure A.6. Formation of benzyl alcohol from benzaldehyde with and without ZnO. ^{1}H NMR spectra (500 MHz) of **(A)**TOPO-capped ZnO nanocrystals (r = 1.9 nm) in 1:3 toluene-d_8/benzene-d_6 spiked with ethanol and benzaldehyde at 0 hr (red), 1 hr (yellow), 2 hr (green), 4 hr (blue), and 24 hr (violet) of UV irradiation. The black dashed lines show an identical solution without ZnO nanocrystals at 0 hr (bottom) and 24 hr (top) of UV irradiation. **(B)** The same control data without ZnO from panel A with a 20 x magnification and zoomed in on the benzyl alcohol region of the NMR spectrum.

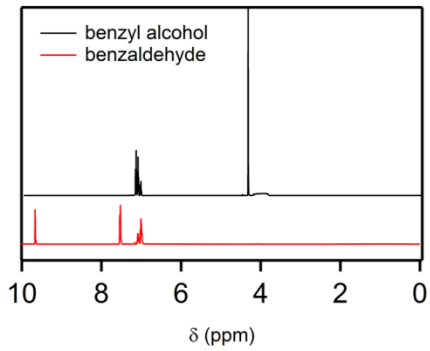

Figure A.7. ^{1}H NMR spectra of benzaldehyde and benzyl alcohol standards.

^{1}H NMR spectra (500 MHz) of benzaldehyde and benzyl alcohol standards in benzene-d_6.

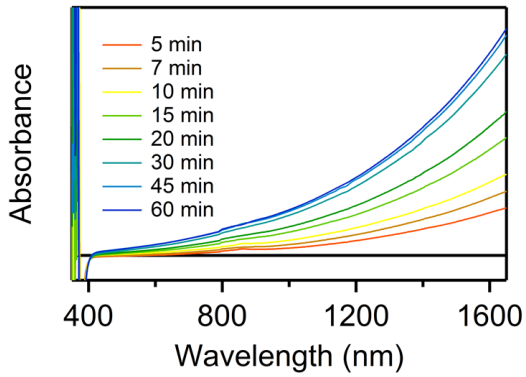

Figure A.8. Absorption spectra of photodoping ZnO in the presence of benzaldehyde.

Differential electronic absorption spectra of photochemically doped colloidal ZnO nanocrystals (r = 1.9 nm, 94 μM) in 14:1:0.5:0.5 THF:toluene:EtOH:benzaldehyde mixture at various UV irradiation times. The increasing IR absorbance shows that the ZnO nanocrystals are being photodoped in the presence of benzaldehyde. The maximum photodoping level was reached after ~45 min.

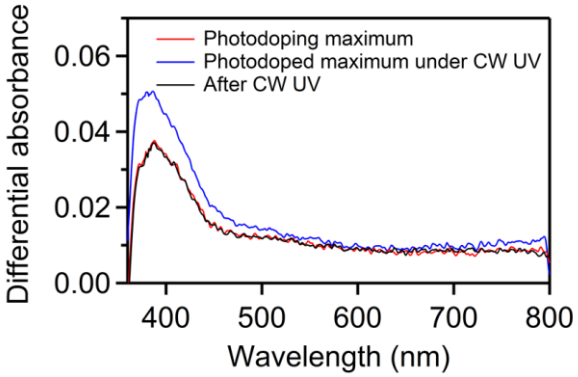

Figure A.9. Photostationary state exceeding N_{max} and E_F^{max} in doped ZnO.

Differential absorption spectra of (red) maximally photodoped ZnO NCs (r = 1.9 nm, 5.2 μM in 14:1:0.5 THF:toluene:EtOH solvent mixture) collected without UV illumination, (blue) the same sample while subsequently held under continuous UV illumination, and (black) the same sample after termination of the continuous UV illumination, all measured in the presence of Cp_2Co^+ (0.145 mM). The quantity of Cp_2Co reflected in the red curve corresponds to the values of E_F^{max} and $<N_{max}>$ reported in the main text. Growth of both Cp_2Co (390 and 500 nm) and ZnO (>700nm) absorption while under UV illumination indicates establishment of a photostationary state in which additional electrons occupy the ZnO NCs, yielding a more negative photostationary cell potential (E'_F). The return of the absorption spectrum to overlay the red spectrum when the UV irradiation is terminated (black) reflects spontaneous relaxation of this photostationary state back to the same equilibrium E_F^{max} and $<N_{max}>$ found for the red curve.

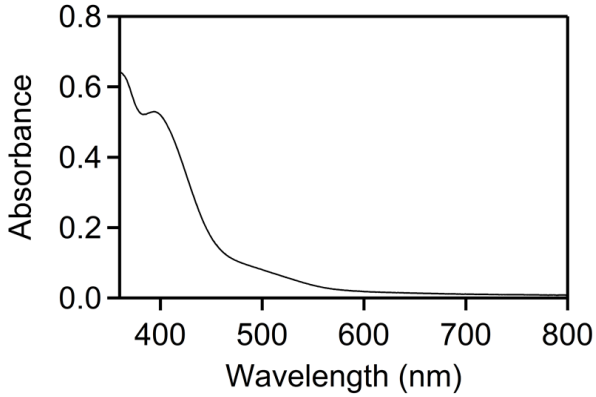

Figure A.10. Electronic absorption spectrum of cobaltocene.

Electronic absorption spectrum of cobaltocene in THF (6.4 x 10^{-4} M).

References

(1) Meulenkamp, E. A.: Synthesis and Growth of ZnO Nanoparticles. *J. Phys. Chem. B* **1998**, *102*, 5566-5572.

(2) Wood, A.; Giersig, M.; Hilgendorff, M.; Vilas-Campos, A.; Liz-Marzán, L. M.; Mulvaney, P.: Size effects in ZnO: The cluster to quantum dot transition. *Aust. J. Chem.* **2003**, *56*, 1051-1057.

Appendix B

Supporting Information for:

Chapter 3: Redox Potentials of Colloidal *n*-Type ZnO Nanocrystals: Effects of Confinement, Electron Density, and Fermi-Level Pinning by Aldehyde Hydrogenation

Adapted from: Carroll, G. M.; Brozek, C. K.; Hartstein, K. H.; Tsui, E.Y; and Gamelin, D. R. *JACS.* **2016**, *138*, 4310.

Experimental Methods

CdSe nanocrystal synthesis. CdSe nanocrystals of various diameters were prepared by an adaptation of a previously reported "heat-up" synthesis method.[1] Briefly, CdO (0.195 g, 1.52 mmol), oleic acid (1.6 mL, 5 mmol), and octadecene (36 g) were combined in a three-necked round bottom flask equipped with a stir bar and condenser and degassed under vacuum at 115 °C for 30 min. Under nitrogen, the mixture was heated to 300 °C until it became optically clear and colorless. The mixture was cooled to 115 °C, and SeO_2 (0.170 g, 1.53 mmol) was added under nitrogen flow. The mixture was then heated to 240 °C for 10 min, becoming an orange solution. This reaction mixture was cooled to room temperature, and the nanocrystals were precipitated using ethanol and then washed *via* repetitive dispersion/precipitation using toluene/ethanol. Nanocrystal sizes and concentrations were determined from UV/vis absorption spectra.

ZnO nanocrystal synthesis. Colloidal ZnO nanocrystals were synthesized by base-initiated hydrolysis and condensation of Zn^{2+} as detailed previously.[2,3] A solution of 22 mmol of tetramethylammonium hydroxide (TMAH) in 40 mL of EtOH was added drop wise to a stirred solution of 13 mmol of $Zn(OAc)_2 \bullet 2H_2O$ in 135 mL of dimethyl sulfoxide (DMSO) at room temperature. The reaction was stopped by precipitation with ethyl acetate. Nanocrystals were collected *via* centrifugation and resuspended in EtOH, followed by precipitation with hexanes. To suspend the nanocrystals in nonpolar solvents, the surface ligands were exchanged by suspending the nanocrystals in excess dodecylamine (DDA) that had been heated above the melting point (~29 °C), followed by precipitation with EtOH. Finally, the nanocrystals were

heated in trioctylphosphine oxide (TOPO, 90%). The resulting TOPO-capped nanocrystals were then washed with 3:1 EtOH/toluene and resuspended in toluene. Nanocrystal sizes were determined from Scherrer analysis of X-ray diffraction patterns and UV/vis absorption spectra, and concentrations were determined by ICP-OES analysis.

Nanocrystal photodoping. ZnO and CdSe nanocrystals were photodoped according to previously reported methods.[4,5] **(CdSe)** CdSe nanocrystals were photodoped using Na[Et_3BH] as the hole quencher, as detailed previously.[5] CdSe nanocrystals (~1 μM) were suspended in anaerobic 2:1 THF:toluene solvent with Na[Et_3BH] (~100 Na[Et_3BH]/nanocrystal), tetrabutylammonium hexafluorophosphate, and trioctylphosphineoxide (TOPO). The nanocrystals were illuminated with a 405 nm photodiode (50 mW/cm^2). Note that the specific maximum number of electrons per nanocrystal ($<n_{max}>$) that is achieved in a given experiment depends on the concentration of Na[Et_3BH], and too much Na[Et_3BH] causes nanocrystal etching and precipitation. The ratio of ~100-200 Na[Et_3BH]/nanocrystal used here was found to give stable CdSe NCs and approximately the largest values of $<n_{max}>$. **(ZnO)** ZnO nanocrystals (~2 μM) were photodoped using ethanol as the hole quenching reagent, as detailed previously.[4] ZnO nanocrystals were suspended in anaerobic mixtures of ethanol, tetrabutylammonium hexafluorophosphate, and 14:1 THF:toluene. The nanocrystals were then photodoped by illuminating them with a 340 nm photodiode (12 mW/cm^2) or a 2 W broad band Xe-arc photolysis lamp.

The proposed overall chemical reactions are shown in eqs B.1 and B.2.[4,5] From these reactions, the charges of the nanocrystal conduction-band electrons are compensated by the H^+ and Z^+ cations (Z^+ = Li^+, Na^+, K^+, *etc.*) also liberated photochemically.

$$e^-, h^+\text{:CdSe} + Z[Et_3BH] \rightarrow 2e^-\text{:CdSe} + Et_3B + H^+ + Z^+ \qquad \text{eq B.1}$$

$$e^-, h^+\text{:ZnO} + CH_3CHOH \rightarrow 2e^-\text{:ZnO} + 2H^+ + CH_3CHO \qquad \text{eq B.2}$$

ZnO electron counting by redox titration. The average number of electrons per photodoped ZnO nanocrystal (<n>) was determined by titration using [FeCp*2][BArF] as detailed previously.4,6,7 Aliquots of [FeCp*2][BArF] in THF were added to photodoped ZnO nanocrystals and the reduction of the NIR absorption was monitored with each equivalent addition. After complete elimination of the NIR absorption, additional aliquots led to growth of FeCp*2+ absorption centered at ~700 nm. The number of ZnO conduction-band electrons

introduced via photodoping was determined from the x-intercept of these data and converted to <n> using the analytical ZnO nanocrystal concentration.

Electron counting by absorption spectroscopy. (ZnO) The average number of electrons per nanocrystal (<*n*>) was determined from the near-IR absorption spectra of ZnO nanocrystals as detailed previously.[8] Briefly, molar extinction coefficients (ε) were determined for each ZnO nanocrystal sample at five different probe wavelengths (850, 900, 1000, 1500, and 2100 nm) and at various values of <*n*>, using $[FeCp^*_2][BAr_F]$ titration. These ε values were then fit to a power function: $\varepsilon_\lambda = Q_\lambda \times \langle n \rangle^p$ (Figure S1),[8] where Q (M^{-1} cm^{-1} $electron^{-1}$) and p (unitless) are constants. Substitution into Beer's law and rearrangement yields $\langle n \rangle = A_\lambda \times \exp(p) \times Q_\lambda^{-1} \times b^{-1} \times C^{-1}$, where b is the optical path length (cm) and C is the concentration (M). <*n*> values determined from the data at these 5 wavelengths were averaged to obtain the reported values of <*n*>, with error bars representing ±σ from the mean. **(CdSe)** <*n*> was determined spectroscopically through the linear relationship: $\langle n \rangle = 2 \times (1 - A/A_0)$, where A is the peak absorbance at the first exciton for the photodoped nanocrystals and A_0 is the peak absorbance at the first exciton for the undoped nanocrystals. Full absorption spectra were also fit with multiple gaussians to quantify A/A_0 (Figure S4), yielding similar results.

ZnO optical-redox-indicator (ORI) measurements. Fermi levels (E_F) were measured using the Cp_2Co^+/Cp_2Co redox couple as an *in situ* optical redox indicator as described previously.[8] ZnO NCs were photodoped in the presence of $[Cp_2Co][PF_6]$. Reduction of Cp_2Co^+ to Cp_2Co occurs in equilibrium with ZnO photodoping. Cp_2Co concentrations were measured spectroscopically using the absorption feature at 500 nm (ε_{500} = 301 $M^{-1}cm^{-1}$),[9] after accounting for overlapping ZnO intra-band absorption. Then, using Beer's law, E_F was calculated from the Nernst equation: $E_{\text{half-cell}}$ (T = 298 K, <*n*> = 1) = $E°´ - 0.0257 \times \ln([Cp_2Co]/[Cp_2Co^+])$, where formal potential, $E°´$ = –1.33 V *vs* Fc^+/Fc (figure S2).

Transient photo-potentiometric measurements. An air-free septum-capped quartz cuvette was modified by inserting two platinum wires (working and counter electrodes) and a 1 mm leakless (edaq) Ag/AgCl reference electrode through the septum cap to make a standard three-electrode electrochemical cell. Typically, Ag/AgCl reference electrodes are unsuitable for electrochemistry in organic media due to the high junction potentials associated with an aqueous/organic interface and the lack of electrolyte equilibrium. These problems are alleviated

by using leakless Ag/AgCl reference electrodes, where the junctions are non-porous but electronically conductive.

Solutions of 2:1 THF:toluene for CdSe, or 14:1 THF:toluene for ZnO, with tetrabutylammonium hexafluorophosphate ($[Bu_4N][PF_6]$) as the electrolyte, cobaltocenium hexafluorophosphate ($[Cp_2Co][PF_6]$) as the internal standard, and the respective hole quenchers ($Na[Et_3BH]$ for CdSe and EtOH for ZnO) were prepared in the cuvette in an N_2 glovebox. The samples were then irradiated with supra-band-gap light (λ = 405 nm, 50 mW for CdSe and λ = 340 nm, 12 mW for ZnO). The solution Fermi level (E_F) was recorded under galvanostatic control at I = 0 amps during illumination with a computer-controlled Eco Chemie Autolab II potentiostat. At the same time, the transmittance was measured using a 250 W tungsten halogen lamp directed through an Oriel Cornerstone 74000 monochromator at a specific wavelength (590 nm for CdSe, and 1000 nm with a 600 nm long-pass cutoff filter for ZnO) and passed through the sample perpendicular to the photodoping excitation source. The transmitted probe light was detected with a Thorlabs PDA 55 Si diode and converted into absorbance through the equation $A = -\log(T/T_0)$, where T is the transmittance through the sample and T_0 is the transmittance absent the sample. T_0 was collected prior to the experiment. A constant baseline measured independently was subtracted from this absorbance, and the resulting absorbance values were then used to calculate $\langle n \rangle$. The solution was stirred continuously with a magnetic stir bar throughout the measurements.

Inter-nanocrystal electron transfer. A THF solution of 0.1 M $[Bu_4N][PF_6]$, 2 μM ZnO nanocrystals (d = 9.4 nm), 1.25 μM CdSe nanocrystals (d = 3.8 nm), and 0.66 mM $Li[Et_3BH]$ was prepared under inert atmosphere and sealed in a quartz cuvette for optical measurement. Samples were irradiated with a 100 W Hg/Xe Oriel broadband photolysis lamp equipped with a 480 nm long-pass filter to selectively excite the CdSe nanocrystals. Absorption spectra were collected at room temperature on a Cary 500 (Varian) spectrometer. A control sample without CdSe was prepared and irradiated in the same manner, and showed no ZnO conduction-band electrons. We note that the colloidal stability of the nanocrystal suspension improved with the addition of $[Bu_4N][PF_6]$.

Estimation of NC band-edge potentials from bulk band potentials. Chapter 3 argues that real nanocrystal redox potentials cannot be estimated from bulk band-edge potentials, but must be measured *in situ* on the actual nanocrystals in question. To illustrate this argument, the CB-edge potentials of CdSe and ZnO NCs can be estimated from previously determined bulk

band-edge potentials.[10] At pH = 0 in aqueous media, the CB-edge potential of bulk CdSe = ~ -1 V *vs* Fc^+/Fc and of bulk ZnO = ~ -0.1 V *vs* Fc^+/Fc.[10] For the NCs used here, only the CdSe NCs are expected to exhibit significant perturbation of the CB-edge potential due to quantum confinement; For the ZnO NCs of Figure 2, d = 6.8 nm whereas the electron Bohr radius is < 2.5 nm.[11] The bulk band gap of CdSe is 1.75 eV, and an optical band gap of 2.10 eV was measured for the d = 4.1 nm CdSe NCs of Figure 3. The ratio of the change in band-edge energies due to quantum confinement has been measured experimentally by ultraviolet photoelectron spectroscopy[12] and is $\Delta E_{CB}/\Delta E_{VB}$ = ~5. Further, the direct coulomb stabilization energy from the electron-hole interaction is estimated at ~175meV for d = 4.1nm CdSe.[12] These numbers lead to an estimate of the d = 4.1 nm CdSe NC CB-edge potential of ~ -1.47 V *vs* Fc^+/Fc, yielding an electron-transfer driving force from these CdSe NCs to the d = 6.8 nm ZnO NCs of ~1.19 eV. The experimental potentiometry data in Figures 3.2 and 3.3 show that this estimated electron-transfer driving force is far greater than the actual driving force (~0.25 eV). The calculation of electron-transfer driving forces from bulk band-edge potentials is inadequate for many reasons. For example, the band-edge potentials used for this calculation are derived from aqueous electrolyte at pH = 0, but the actual bulk band-edge potentials in organic media may vary significantly. ZnO band edges are known to shift with a Nernstian dependence of -59 mV/pH, while those of CdSe generally do not. In organic media, the proton activities are not well defined, so a pH appropriate for the real experimental conditions cannot be assumed. Moreover, surface perturbations (*e.g.*, ion or ligand binding) are known to shift band-edge potentials of both bulk and nanoscale semiconductors significantly. This comparison illustrates the importance of *in situ* electrochemical measurement of nanocrystal redox potentials for understanding electron-transfer driving forces in real systems.

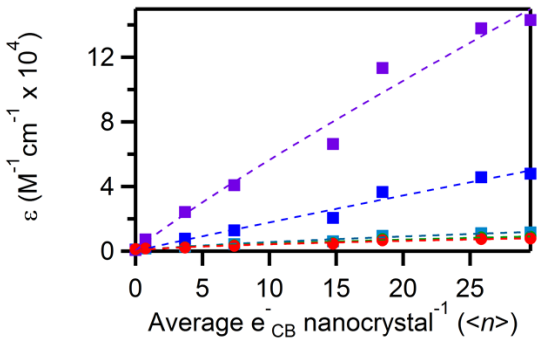

Figure B.1. Experimental absorption coefficients for ZnO NCs.

ZnO nanocrystal (d = 6.8 nm) molar extinction coefficients measured at 2100 (purple), 1500 (dark blue), 1000 (light blue), 900 (green), and 850 nm (red) plotted as a function of <n>. <n> was determined by titration with [FeCp*$_2$][BA$_{rF}$].[4,8] The solid lines show best fits of the data to the function $\varepsilon(\lambda) = Q_\lambda \times \langle n \rangle^p$, where Q_λ and p are floating parameters (Table B.1).

Table B.1. List of absorption coefficients for ZnO NCs.

Fitted parameters describing the near-IR extinction by d = 6.8 nm ZnO nanocrystal conduction-band electrons (see methods text and Figure S1).

Q_{850}	Q_{900}	Q_{1000}	Q_{1500}	Q_{2100}	P_{850}	P_{900}	P_{1000}	P_{1500}	P_{2100}
1107	1080	1097	1976	7060	0.58	0.62	0.70	0.95	0.91

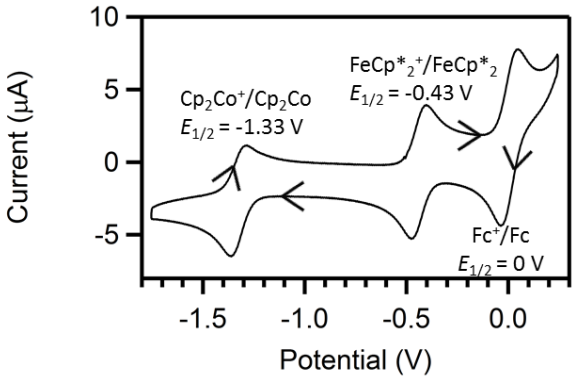

Figure B.2. Cyclic voltammogram of the internal standards.

Cyclic voltammogram of a mixture of $[Cp_2Co][PF_6]$, decamethyl ferrocene ($FeCp_2^*$), and ferrocene (Fc) in an air-free THF solution with 0.1 M $[Bu_4N][PF_6]$ as the supporting electrolyte. The trace has been shifted such that the half-wave potential of ferrocene = 0 V. The scan rate was 100 mV/s. These data were collect with Pt wires as the working and counter electrodes and a Ag/AgCl reference. The arrows indicate the direction of the scan.

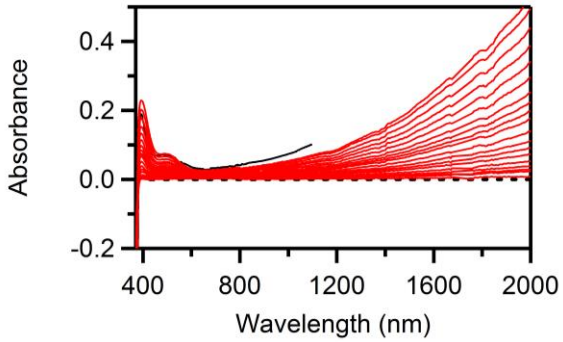

Figure B.3. Absorption spectra of photodoped ZnO NCs.

Electronic absorption spectra (red traces) of progressively photodoped d = 6.8 nm ZnO nanocrystals (using EtOH hole quencher) in a 1:3 toluene:THF solution of 0.1 M $[Bu_4N][PF_6]$, 266 μM $[Cp_2Co][PF_6]$ illuminated by a 2 W broad-band Xe-arc photolysis lamp. These spectra were used to generate the optical-redox-indicator (ORI) data presented in Figure 3.2. The black trace shows the absorption spectrum of maximally photodoped ZnO nanocrystals from the potentiometry measurement described in Figure 3.2.

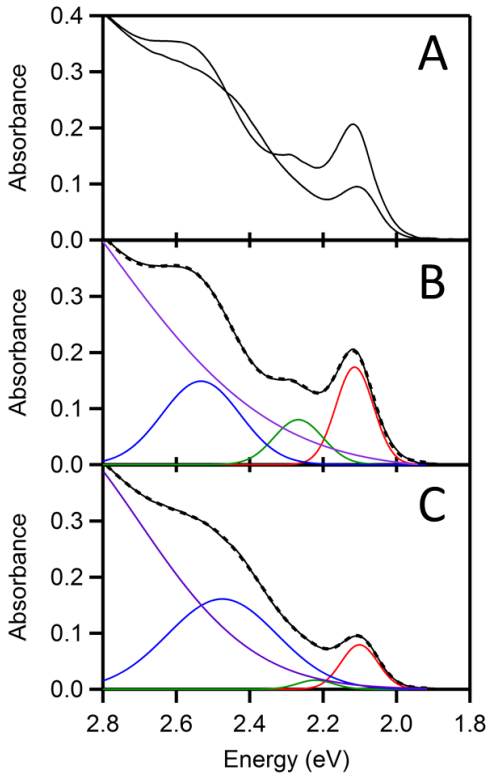

Figure B.4. Gaussian deconvolution of CdSe NC absorption spectra.

(a) Absorption spectra of d = 4.1 nm CdSe nanocrystals before photodoping and at $\langle n_{max} \rangle$. Multi-gaussian fits (thick black dashed) of the absorption spectra (thin black) before photodoping **(b)** and at $\langle n_{max} \rangle$ **(c)**. The magnitudes, positions, and widths of all of the peaks were allowed to float during fitting, but only the absorbance of the first excitonic feature is evaluated quantitatively. Integrating the first absorption band in these spectra yields a value of A/A_0 = 0.66, corresponding to $\langle n_{max} \rangle$ = 1.32. For comparison, the value obtained by the method described in chapter 3 (Figure 3.3) is $\langle n_{max} \rangle$ = 1.4, the difference attributed to experimental uncertainty.

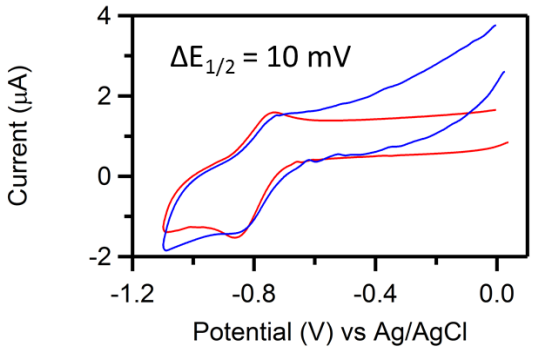

Figure B.5. Cyclic voltammogram of Cp_2Co during NC photodoping.

Cyclic voltammogram of Cp_2Co^+/Cp_2Co before (red) and during (blue) 405 nm photolysis of a solution of d = 4.1 nm CdSe nanocrystals (0.9 μM), $[Bu_4N][PF_6]$ (0.05 M), TOPO (0.15 M), and $Na[Et_3BH]$ (200 μM). The difference in the half-wave potential ($E_{1/2}$) between the solution before and during photodoping is 10 mV. The scan rate was 100 mV/s.

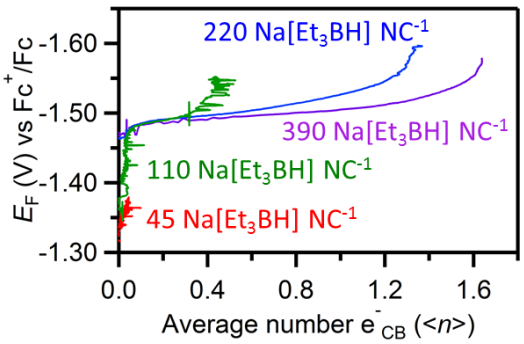

Figure B.6. $Na[Et_3BH]$ concentration dependence of CdSe NC photodoping.

Plot of E_F *vs* <*n*> for d = 4.1 nm CdSe NCs (0.9μM) with $Na[Et_3BH]$ concentrations of 40 μM (red), 100 μM (green), 200 μM (blue), and 350 μM (purple). Experiments were performed using a 2:1 THF:toluene solution 0.05 M $[Bu_4N][PF_6]$, and 0.15 M trioctylphosphineoxide (TOPO). <*n*> was calculated from the relationship <*n*> = 2 x (1 - A/A_0), where the absorbance (A) was monitored at λ = 590 nm and A_0 was collected prior to the experiment. E_F is referenced to the ferrocenium/ferrocene (Fc^+/Fc) redox couple. Photodoping was performed using continuous 50 mW/cm^2 405 nm irradiation.

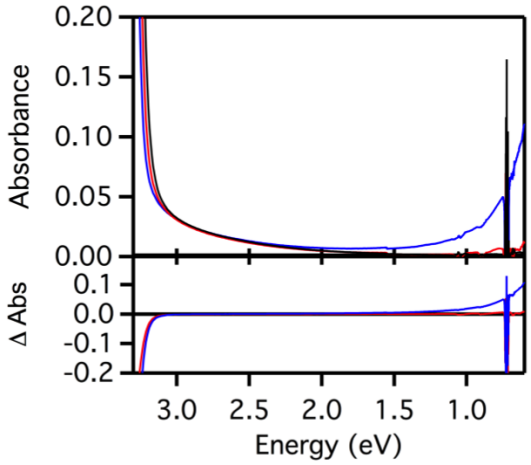

Figure B.7. Control experiment for CdSe-ZnO NC ET.

Electronic absorption spectra of d = 9.6 nm ZnO (2 μM) in a THF solution of 0.1M $[Bu_4N][PF_6]$, and 660 μM $Li[Et_3BH]$. Spectra were taken before irradiation (black trace), after 3 h of broad-band irradiation with a 480 nm long-pass filter (red trace), and after 1 min UV irradiation (blue trace). The bottom panel shows difference spectra to highlight changes observed upon photoexcitation. No NIR absorption (no photodoping) is observed when using the 480 nm long-pass filter (red), indicating no direct ZnO nanocrystal photodoping with this excitation. Rapid photodoping is observed with direct UV irradiation (blue).

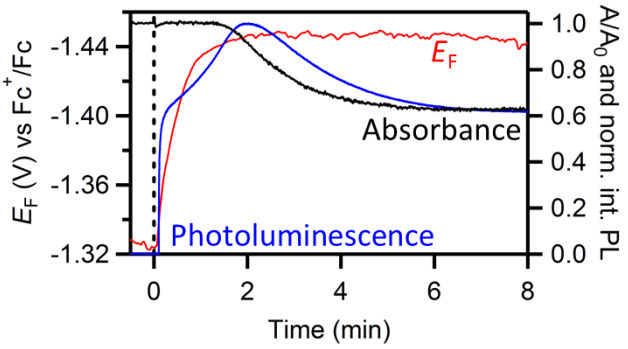

Figure B.8. Potentiometric measurement of surface states on CdSe NCs.

Transient E_F (red), A/A_0 (black), and integrated excitonic photoluminescence (blue) data collected during photodoping of d = 3.4 nm CdSe nanocrystals (18 μM) using $Na[Et_3BH]$ (200 μM) as the hole quencher. The nanocrystals were in a 1:2 toluene:THF solution of 0.05 M $[Bu_4N][PF_6]$, 0.15 M TOPO, and 30 μM $[Cp_2Co][PF_6]$. Nanocrystal absorption was monitored at the peak of the first excitonic maximum (λ = 565 nm).

References

(1) Chen, O.; Chen, X.; Yang, Y.; Lynch, J.; Wu, H.; Zhuang, J.; Cao, Y. C.: Synthesis of Metal–Selenide Nanocrystals Using Selenium Dioxide as the Selenium Precursor. *Angew. Chem. Int. Ed.* **2008**, *47*, 8638-8641.

(2) Schwartz, D. A.; Norberg, N. S.; Nguyen, Q. P.; Parker, J. M.; Gamelin, D. R.: Magnetic Quantum Dots: Synthesis, Spectroscopy, and Magnetism of Co2+- and Ni2+-Doped ZnO Nanocrystals. *J. Am. Chem. Soc.* **2003**, *125*, 13205-13218.

(3) Norberg, N. S.; Gamelin, D. R.: Influence of Surface Modification on the Luminescence of Colloidal ZnO Nanocrystals. *J. Phys. Chem. B* **2005**, *109*, 20810-20816.

(4) Schimpf, A. M.; Gunthardt, C. E.; Rinehart, J. D.; Mayer, J. M.; Gamelin, D. R.: Controlling Carrier Densities in Photochemically Reduced Colloidal ZnO Nanocrystals: Size Dependence and Role of the Hole Quencher. *J. Am. Chem. Soc.* **2013**, *135*, 16569-16577.

(5) Rinehart, J. D.; Schimpf, A. M.; Weaver, A. L.; Cohn, A. W.; Gamelin, D. R.: Photochemical Electronic Doping of Colloidal CdSe Nanocrystals. *J. Am. Chem. Soc.* **2013**, *135*, 18782-18785.

(6) Schimpf, A. M.; Ochsenbein, S. T.; Buonsanti, R.; Milliron, D. J.; Gamelin, D. R.: Comparison of extra electrons in colloidal n-type Al3+-doped and photochemically reduced ZnO nanocrystals. *Chem. Commun.* **2012**, *48*, 9352-9354.

(7) Schrauben, J. N.; Hayoun, R.; Valdez, C. N.; Braten, M.; Fridley, L.; Mayer, J. M.: Titanium and Zinc Oxide Nanoparticles Are Proton-Coupled Electron Transfer Agents. *Science* **2012**, *336*, 1298-1301.

(8) Carroll, G. M.; Schimpf, A. M.; Tsui, E. Y.; Gamelin, D. R.: Redox Potentials of Colloidal n-Type ZnO Nanocrystals: Effects of Confinement, Electron Density, and Fermi-Level Pinning by Aldehyde Hydrogenation. *J. Am. Chem. Soc.* **2015**, *137*, 11163-11169.

(9) Gordon, K. R.; Warren, K. D.: Spectroscopic and magnetic studies of the 3d metallocenes. *Inorg. Chem.* **1978**, *17*, 987-994.

(10) Chen, S.; Wang, L.-W.: Thermodynamic Oxidation and Reduction Potentials of Photocatalytic Semiconductors in Aqueous Solution. *Chem. Mater.* **2012**, *24*, 3659-3666.

(11) Senger, R. T.; Bajaj, K. K.: Optical properties of confined polaronic excitons in spherical ionic quantum dots. *Physical Review B* **2003**, *68*, 045313.

(12) Jasieniak, J.; Califano, M.; Watkins, S. E.: Size-Dependent Valence and Conduction Band-Edge Energies of Semiconductor Nanocrystals. *ACS Nano* **2011**, *5*, 5888-5902.

Appendix C

Supporting Information for:

Chapter 4: Electrochemical Measurement of Surface Composition Effects on Colloidal CdSe Nanocrystal Redox Potentials

Experimental Methods

CdSe NC synthesis. Zinc blende CdSe nanocrystals of various diameters were prepared by an adaptation of a previously reported heat-up synthesis method.[1] As an example: CdO (0.195 g, 1.52 mmol), oleic acid (1.6 mL, 5 mmol), and octadecene (36 g) were combined in a three-necked round bottom flask equipped with a stir bar and condenser and degassed under vacuum at 115 °C for 30 min. Under nitrogen, the mixture was heated to 300 °C until it became optically clear and colorless. The mixture was cooled to 115 °C, and SeO_2 (0.170 g, 1.53 mmol) was added under nitrogen flow, and the mixture was heated to 240 °C for 10 min., becoming an orange solution. The reaction mixture was cooled to room temperature, and the nanocrystals were precipitated using ethanol and then washed via redispersion/precipitation with toluene/ethanol.

Selenium surface enrichment. The ratios of Cd and Se were changed by an adaptation of the method published by Peng and co-workers.[2] A toluene solution of CdSe NCs prepared as described above was added to a three-necked round-bottom flask equipped with a stir bar and condenser and charged with octadecene (8 mL) and oleylamine (2 mL). The mixture was degassed under vacuum at 100 °C for 30 min., then heated to 140 °C under nitrogen. A dispersion of Se (0.1 mL, ca. 0.1 M in ODE) was added via syringe, and the mixture stirred at 140 °C for 10 min. This Se treatment was repeated three times. The mixture was precipitated with ethanol and resuspended in toluene three times.

$Cd(oleate)_2$ Synthesis. A 50ml methanolic solution containing 1.41g oleaic acid, and 0.2g sodium hydroxide was sonicated and heated to 60 C° while stirring. To this solution, a solution of 3.08g cadmium nitrate tetrahydrate dissolved in 8ml of methanol was added drop wise (1 drop s^{-1}). Following total addition of the $Cd(NO_3)_2$ solution, the final solution was cooled in an ice

bath. The white precipitate was vacuum filtered, washed with cold methanol and dried under vacuum overnight. The powder was then dissolved in THF in an N_2 glove box. $Zn(oleate)_2$ was synthesized in the same way, only substituting $Zn(NO_3)_2 \cdot 6H_2O$ for $Cd(NO_3)_2 \cdot 4H_2O$.

CdSe Photodoping Suspension. Se-enriched CdSe nanocrystals were photodoped using $Na[Et_3BH]$ as the hole quencher, as detailed previously.[3,4] CdSe nanocrystals (~ 0.2 μM) were suspended in an anaerobic 2:1 THF:toluene solvent with $Na[Et_3BH]$ (~100 $Na[Et_3BH]$/nanocrystal), tetrabutylammonium hexafluorophosphate ($[Et_4N][PF_6]$ as the supporting electrolyte), trioctylphosphineoxide (TOPO, as a NC stabilizer), and cobaltocenium hexafluorophosphate (as an internal standard). Predetermined amounts of $Cd(oleate)_2$ were added to the photodoping mixture prior to photodoping.

Transient potentiometric and A/A_0 measurements. Transient potentiometric and A/A_0 measurements were carried out as previously detailed.[4] An air-free septum-capped quartz cuvette was modified by inserting two platinum wires (working and counter electrodes) and a 1 mm leakless (edaq) Ag/AgCl reference electrode through the septum cap to make a standard three-electrode electrochemical cell which was screwed onto a 1 cm optical cuvette with 4 polished sides containing the NC photodoping mixture. The photodoping mixture was prepared in an N_2 filled glovebox. The solution Fermi level (E_F) was recorded under galvanostatic control at $I = 0$ amps during 405 nm illumination with a computer-controlled Eco Chemie Autolab II potentiostat. The optical transmittance (T) at the peak of the first excitonic transition was measured using a 250 W tungsten halogen lamp directed through an Oriel Cornerstone 74000 monochromator and passed through the sample perpendicular to the photodoping excitation source. The transmitted probe light was detected with a Thorlabs PDA 55 Si diode and converted into absorbance through the equation $A = -\log(T/T_0)$, where T_0 is the transmittance absent the sample. T_0 was collected prior to the experiment. A constant baseline measured independently was subtracted from this absorbance, and the resulting absorbance values were then used to calculate $\langle n \rangle$ through the equation $\langle n \rangle = 2*(1-A/A_0)$. The solution was stirred continuously with a magnetic stir bar throughout the measurements. Dark potentiometric experiments were carried out in the same way as photodoping experiments except that the NC suspensions were prepared in an electrochemical cell, which had been covered in black electrical tape to prevent room light exposure.

Elemental analysis of CdSe NCs. Energy Dispersive X-ray Spectroscopy (EDS) measurements were performed on both 5.4nm and 4.4nm Se^{2-} -enriched CdSe NCs, as well as 4.4 nm as-prepared CdSe NCs with an FEI Sirion XL30 microscope and an attached Oxford EDS detector. The nanocrystals were washed via precipitation/redispersion with ethanol/toluene three times prior to the measurement. For EDS measurements, the accelerating voltage was 20 kV, with 0.6 nA of current. The elemental excess of Se^{2-} was assumed to be surface-bound Se^{2-}, while the core was assumed to be a 1:1 composition of Se^{2-}:Cd^{2+}.

Sample Identification	EDS ratio (Se^{2-}/Cd^{2+})	Calculated Se^{2-} surface coverage (%)
5.4 nm Se^{2-} -enriched CdSe	0.525	67%
4.4 nm Se^{2-} -enriched CdSe	0.506	55%
4.4 nm as-prepared CdSe	0.480	42%

Table C.1. Relative surface stoichiometry for CdSe NCs

NMR Spectroscopy. ^{1}H NMR spectra were recorded on Bruker AV300 or Bruker AV500 instruments. Samples in C_6D_6 (10−20 μM) were referenced to the solvent residual peak (7.16 ppm). A 15 s relaxation delay was used. Ferrocene (0.15−0.35 mM) was included as an internal standard to quantify the ligand concentrations.

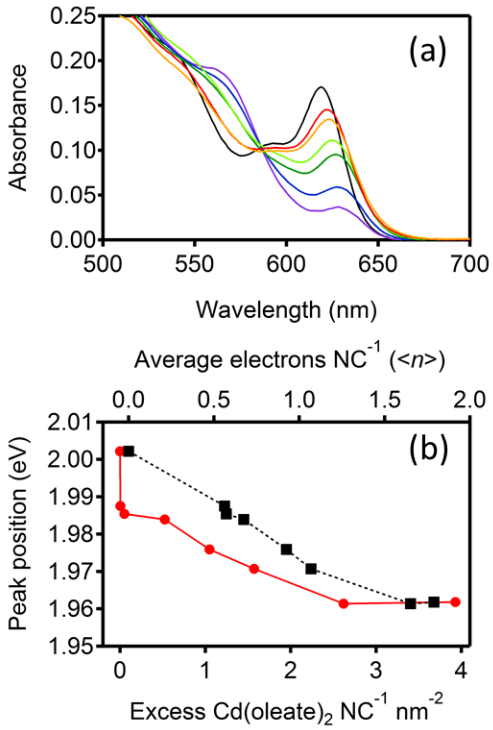

Figure C.1. Excitonic redshift for photodoped CdSe with increasing Cd(oleate)$_2$

(a) Electronic absorption spectra of maximally photodoped d = 5.4 nm Se-enriched CdSe NCs with increasing Cd(oleate)$_2$ up to an equivalent 12 Cd(oleate)$_2$ nm^{-2}. **(b)** Plot of the peak of the first exciton as a function of the added Cd(oleate)$_2$ (red, circles) and <n_{max}> (black, squares).

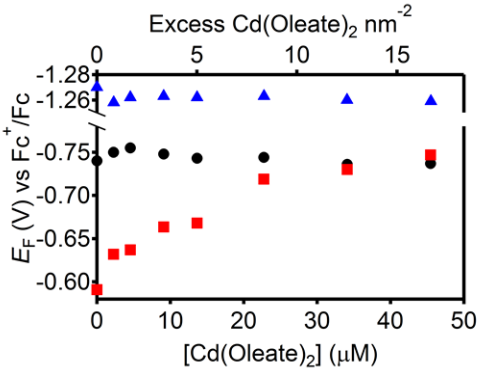

Figure C.2. Dark potentiometric titration Se^{2-}-enriched CdSe with Cd(oleate)$_2$

Dark potentiometric titration of a blank solution (red, squares), 0.3 μM 5.4 nm Se-enriched CdSe (black, circles), and a Se-enriched CdSe/30 μM Na[Et$_3$BH] mixture (blue, triangles) with a 1mM solution of Cd(oleate)$_2$ in THF. All titrations were carried out in a 2:1 THF:toluene solution with 0.05 M [Bu$_4$N][PF$_6$], 0.15 M trioctylphosphineoxide

(TOPO), and $[Cp_2Co][PF_6]$ as an internal standard. The solution was kept in a rigorously dark environment to avoid light contamination. E_F is referenced to the ferrocinium/ferrocene redox couple.

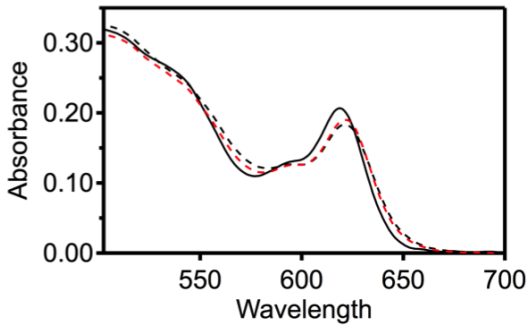

Figure C.3. Absorption of photodoping CdSe with excess Zn(oleate)$_2$

Excitonic absorption spectrum of undoped (black, solid line), and maximally photodoped (black, dashed line) Se-enriched CdSe. The red dashed line shows the maximally photodoped Se-enriched CdSe in the presence of $Zn(oleate)_2$ at an equivalent 10 $Zn(oleate)_2$ NC^{-1} nm^{-2}. All experiments were carried out under continuous 405nm photoexcitation in an air-free 2:1 THF:toluene solution with 0.05 M $[Bu_4N][PF_6]$, 100 μM $[Cp_2Co][PF_6]$ as an internal standard, 0.15 M trioctylphosphineoxide (TOPO) as a stabilizer, and 30 μM $Na[Et_3BH]$ as the hole quencher. E_F is referenced to the ferrocinium/ferrocene redox couple.

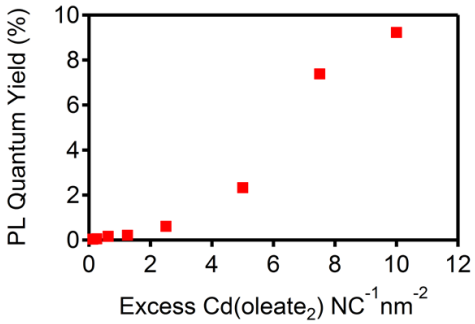

Figure C.4. PL increase with Cd(oleate)$_2$ addition

Integrated photoluminescence quantum yield of d = 5.4 nm Se^{2-}enriched CdSe NCs (0.3μM) in a 2:1 THF:toluene solution with 0.05 M $[Bu_4N][PF_6]$, 0.15 M trioctylphosphineoxide (TOPO) plotted as a function of the excess $Cd(oleate)_2$. The NCs

were first photodoped to their maximum and then opened to air to remove all excess conduction band electrons.

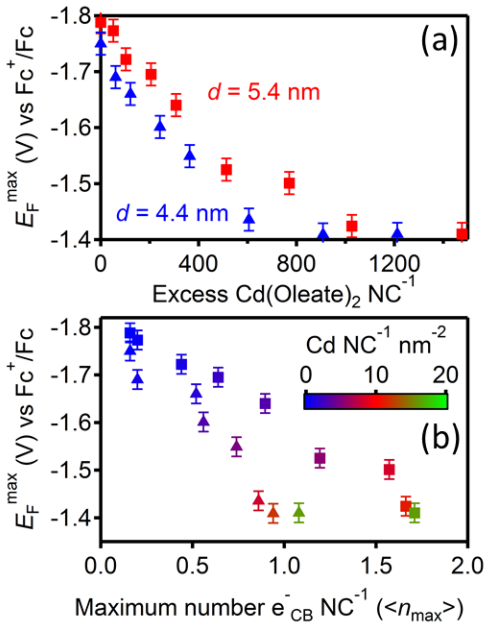

Figure C.5. E_F^{max} of Cd(oleate)$_2$ titration plotted against Cd NC^{-1}

(a) Plot of the maximum Fermi-level (E_F^{max}) for photodoping d = 4.4 nm (blue, triangles) and d = 5.4 nm (red, squares) Se-enriched CdSe NCs against the added Cd(oleate)$_2$ NC^{-1}. The error bars indicate the uncertainty in the Cp_2Co^+/Cp_2Co half wave potential. **(c)** E_F^{max} data in figure 2a plotted against $\langle n_{max} \rangle$ for d = 5.4 nm CdSe (squares) and d =4.4nm (circles). The color of the markers correspond to the scale bar which indicate the excess Cd(oleate)$_2$ NC^{-1} nm^{-2}. All experiments were carried out under continuous 405nm photoexcitation in an air-free 2:1 THF:toluene solution with 0.05 M $[Bu_4N][PF_6]$, 100 μM $[Cp_2Co][PF_6]$ as an internal standard, 0.15 M trioctylphosphineoxide (TOPO) as a stabilizer, and 30 μM $Na[Et_3BH]$ as the hole quencher. E_F is referenced to the ferrocinium/ferrocene redox couple.

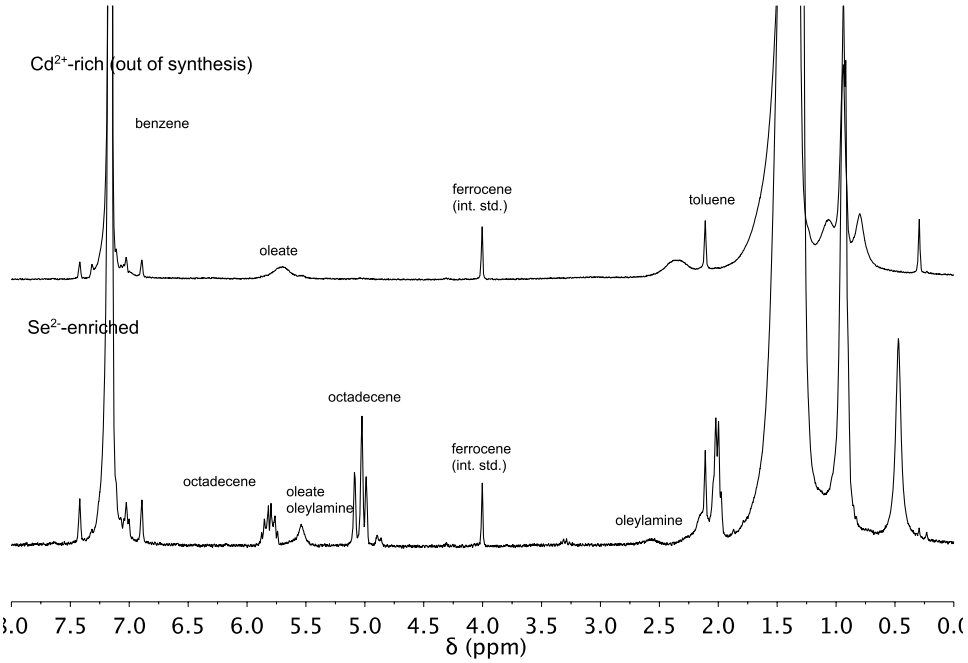

Figure C.6. ^{1}H NMR spectra of Se^{2-} and Cd^{2+}-enriched CdSe NCs

^{1}H NMR spectra in C_6D_6 of CdSe NCs out of synthesis (Cd^{2+}-rich, top) and after Se^{2-} enrichment (bottom).

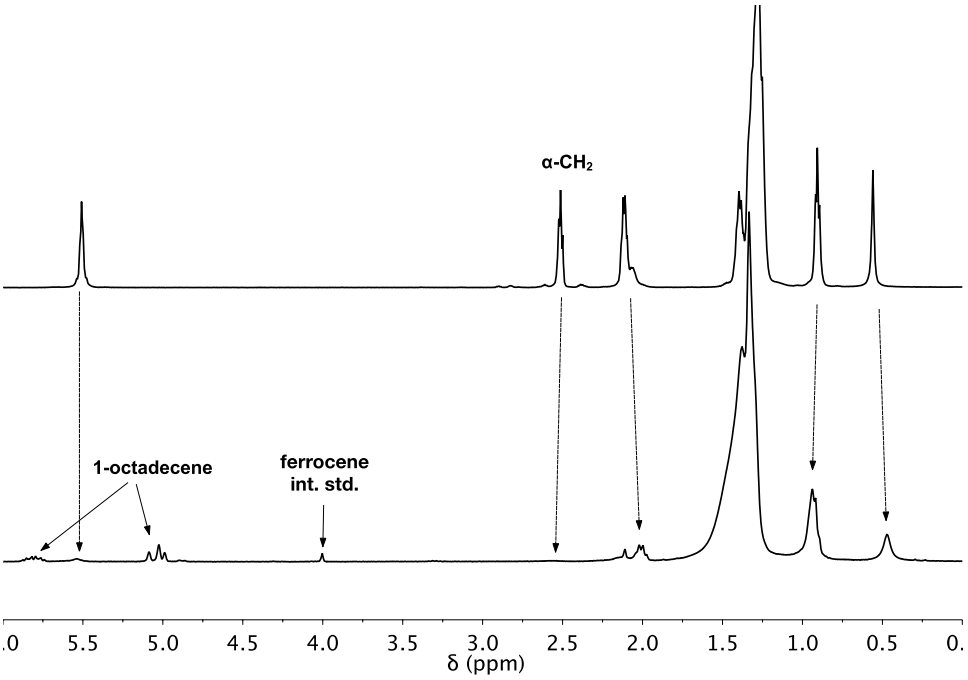

Figure C.7. ^{1}H NMR spectra in C_6D_6 of oleylamine and Se^{2-}-enriched CdSe NCs.

^{1}H NMR spectra in C_6D_6 of oleylamine (top) and Se^{2-}-enriched CdSe NCs. The CdSe NC sample contains some residual 1-octadecene (590 equiv/NC) that was not removed after 2 cycles of ethanol-precipitation/toluene-redispersion.

^{1}H NMR spectroscopy of CdSe NC samples (d ~ 4.4 nm, 10−20 μM in C_6D_6) with ferrocene as an internal standard was used to estimate the ligand coverage before and after surface selenide enrichment and nanocrystal purification. CdSe NCs out of synthesis were coordinated solely by oleate ligands (320 oleate ligands/NC, 5 carboxylates/nm^2). After Se^{2-} enrichment and purification by two cycles of ethanol-precipitation/toluene-redispersion, ligand coverage decreased (~70 oleate ligands/NC, 1.2 carboxylates/nm^2 and 90 oleylamine ligands/NC, 1.5 oleylamines/nm^2). Ligand coverages vary between batches and is purification-dependent. As an example, a separate sample of Se^{2-}-enriched CdSe NCs (d ~ 3.9 nm) that was purified by three cycles of ethanol-precipitation/toluene-redispersion was coordinated only by oleate ligands (~12 oleates/NC, 0.3 carboxylates/nm^2), with no oleylamine ligands.

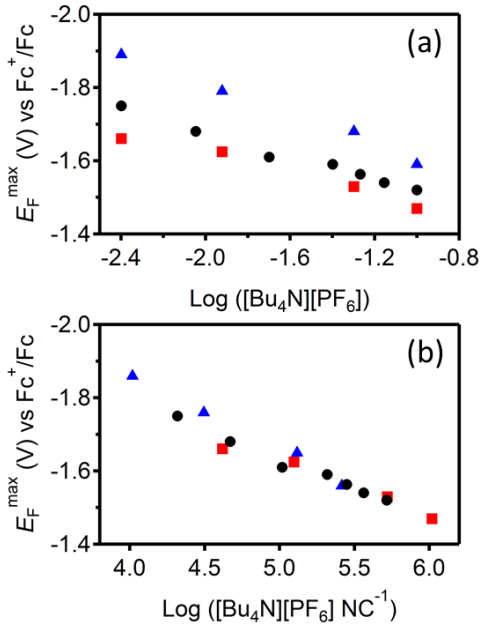

Figure C.8. Ratiometric dependence of NC E_F^{max} on [Bu_4N][PF_6]

(a) Plot of E_F^{max} for photodoping 0.1 (red, square), 0.2 (black, circles), and 0.4 μM (blue, triangles) 5.4 nm Se-enriched CdSe NCs as a function of the [Bu_4N][PF_6] concentration.

(b) Plot of the same data in panel (a), but now plotted against the ratio of $[Bu_4N][PF_6]$:CdSe. Fitted to line, the slopes of all three NC concentrations are within 20mV of the 160mV/decade slope reported in the main text. All experiments were carried out in THF with 30 μM $Na[Et_3BH]$ as the hole quencher. The CdSe concentration is 0.2μM and the $[Bu_4N][PF_6]$ ranges from 4mM to 100mM. $[Fc^*][PF_6]$ was added after the experiment as an internal standard. E_F is referenced against the ferrociunium/ferrocene redox couple.

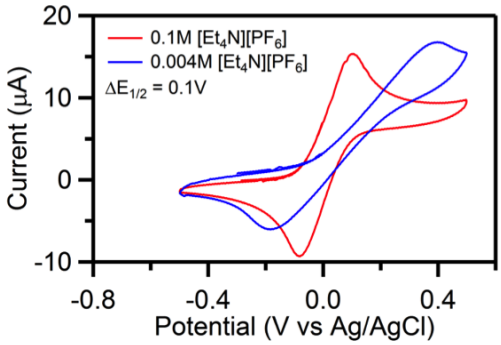

Figure C.9. CV of Fc^+/Fc at different electrolyte concentrations

Cyclic voltammogram of decamethylferrocene/decamethylferrocinium redox couple in 0.1M (red) and 0.004M (blue) $[Bu_4N][PF_6]$ in THF. The half wave potential ($E_{1/2}$) was used as the reference for placing E_F^{max} of photodoped CdSe in figure 3 of the main text. The change in the half wave potential ($\Delta E_{1/2}$) for the two different electrolyte concentrations is 100mV, which corresponds to the error bars in fig 3 of the main text. The broadening of the redox waves with decreasing $[Bu_4N][PF_6]$ is due to an increasing solution resistance.

References

(1) Chen, O.; Chen, X.; Yang, Y.; Lynch, J.; Wu, H.; Zhuang, J.; Cao, Y. C. Synthesis of Metal–Selenide Nanocrystals Using Selenium Dioxide as the Selenium Precursor. *Angew. Chem. Int. Ed.* **2008**, *47*, 8638-8641.

(2) Gao, Y.; Peng, X. Photogenerated Excitons in Plain Core CdSe Nanocrystals with Unity Radiative Decay in Single Channel: The Effects of Surface and Ligands. *Journal of the American Chemical Society* **2015**, *137*, 4230-4235.

(3) Rinehart, J. D.; Schimpf, A. M.; Weaver, A. L.; Cohn, A. W.; Gamelin, D. R. Photochemical Electronic Doping of Colloidal CdSe Nanocrystals. *J. Am. Chem. Soc.* **2013**, *135*, 18782-18785.

(4) Carroll, G. M.; Brozek, C. K.; Hartstein, K. H.; Tsui, E. Y.; Gamelin, D. R. Potentiometric Measurements of Semiconductor Nanocrystal Redox Potentials. *Journal of the American Chemical Society* **2016**.

Appendix D

Supporting Information for:

Chapter 5: Mechanistic Insights into Solar Water Oxidation by Cobalt-Phosphate-Modified α-Fe_2O_3 Photoanodes

Adapted from: Carroll, G. M.; Zhong, D. K.; Gamelin, D. R. *Energy Environ. Sci.* **2015**, *8*, 577.

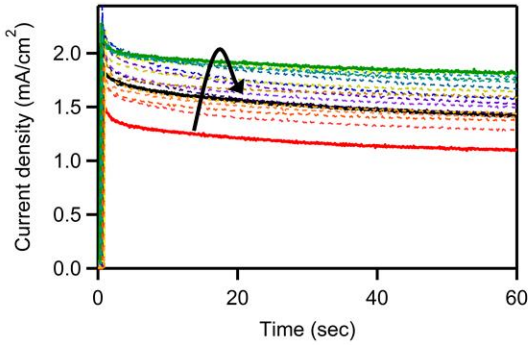

Figure D.1. Steady state photocurrent for variable thickness Co-Pi on α-Fe_2O_3.
Steady state photocurrent density under simulated 1 sun AM 1.5 back-side illumination of a bare hematite electrode (black) and following Co-Pi deposition (red, 24.5 nm thick) at 1.7V vs RHE. Intermediate colors from orange to blue show the *J-V* scans of the same electrode after |1|3|5|10|15|20|30|40|50|60|120|240|360|480|600 minutes of Co-Pi dissolution in fresh 0.1M KPi pH 8 electrolyte solution. Steady state dark current has been subtracted from the data.

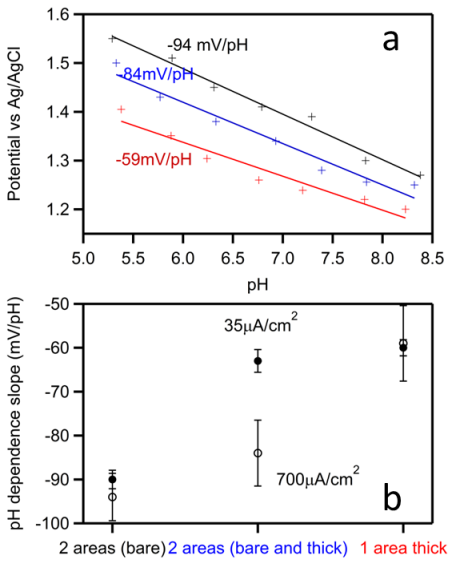

Figure D.2. Double spot pH dependence for Co-Pi modified and bare α-Fe_2O

(a) Galvanostatic titration of double spot experiment at 700μA/cm2 showing two bare spots (black), only the Co-Pi covered spot (red) and both the bare and Co-Pi coated spots measured simultaneously (blue). **(b)** Plot of the slopes from the linear regression of the pH dependence data for: 700 μA/cm2 (open circle), and 35 μA/cm2 (closed circle). The error bars indicate the error to the fits.

Figure D2 shows the results from a double spot experiment in which two areas on the same photoanode were masked separately. By partitioning the sample into two spots, Co-Pi could be selectively deposited onto one and not the other, and the pH dependence of both spots measured separately or simultaneously. From Figure D2b, when both spots are bare, the pH dependence is consistent with that of the data presented in Figure 4.5 (main text). When Co-Pi is deposited onto the surface of only one of the spots, the pH dependence for the current density 30μA/cm^2 increase from -90mV/pH to -62mV/pH, and for a current density of 700μA/cm^2 the slope changes from -94mV/pH to -85mV/pH. When only the spot with Co-Pi is measured, the slopes for 30 and 700μA/cm^2 are -60 and -59mV/pH, respectively. Following the pH measurements, the region with no deposited Co-Pi was investigated with EDX measurements, and no cobalt was detected. This result indicates that an intermediate pH dependence slope is consistent with two simultaneous water oxidation mechanisms.

Appendix E

Supporting Information for:

Chapter 5: Mechanistic Insights into Solar Water Oxidation by Cobalt-Phosphate-Modified α-Fe_2O_3 Photoanodes.

Adapted from: Carroll, G. M.; Gamelin, D. R. *J. Mat. Chem. A* **2016.**

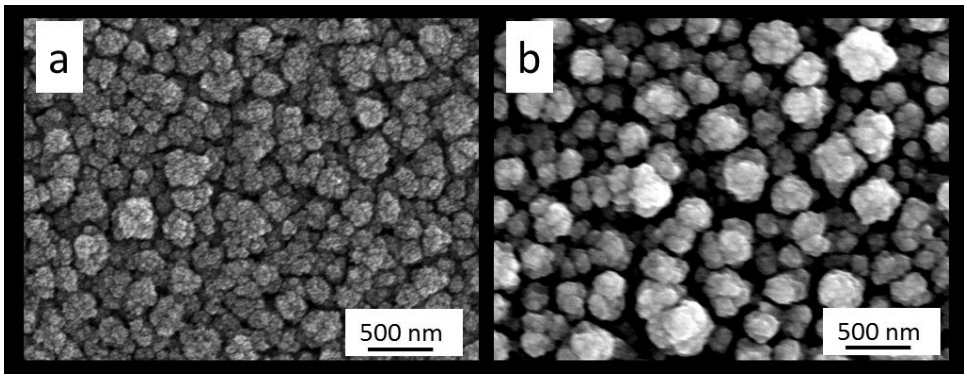

Figure E.1. SEM of representative photoelectrodes.

SEM images of (a) bare α-Fe_2O_3 and (b) 24.6nm thick Co-Pi coated α-Fe_2O_3

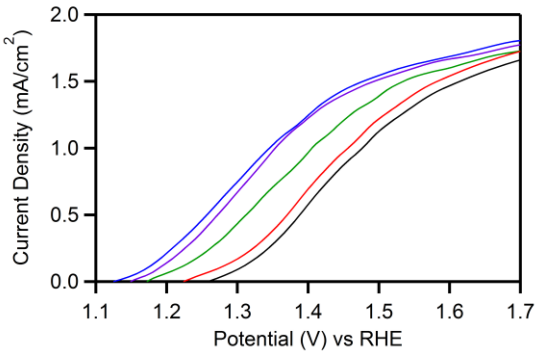

Figure E.2. *J-V* curves of α-Fe_2O_3 at various Co-Pi thicknesses.

J-V curves for an α-Fe_2O_3 photoanode measured before (black) and after (red) photo-assisted electrodeposition of a thick (~25nm) layer of Co-Pi. Additional curves were

measured after 1 (green), 2 (blue) and 3 (purple) hours of dissociative dissolution of Co-Pi in aqueous electrolyte at open circuit in the dark. Data courtesy of Diane K. Zhong (UW 2012)

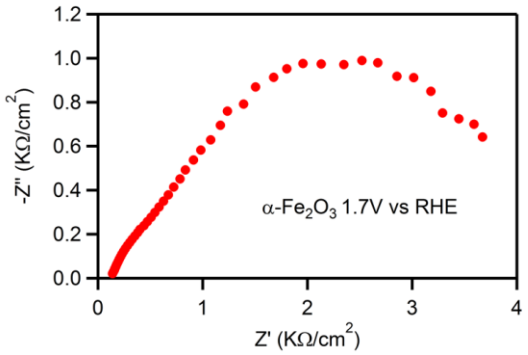

Figure E.3. Nyquist plot of α-Fe_2O_3 at high potentials.

Nyquist plot of the highest potential measured in the impedance analysis of a bare α-Fe_2O_3 photoanode.

In planar α-Fe_2O_3 films, the capacitive feature of the low-frequency semicircle disappears at potentials more positive than +1.5 V vs RHE, attributable to fast (non-rate-limiting) hole transfer from surface states.[1-4] Here, the capacitive feature at low frequencies is visible up to ~+1.7 V vs RHE, suggesting that hole transfer to water remains rate limiting throughout the voltammetric window of interest.

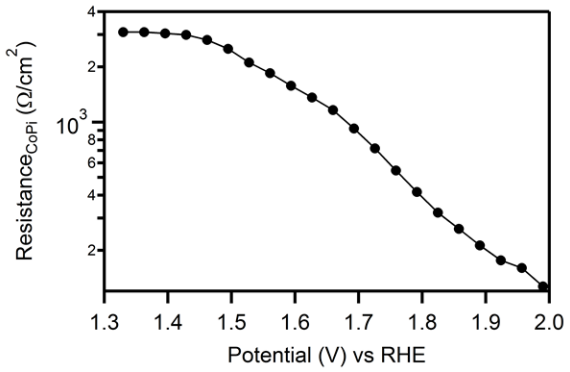

Figure E.4. $R_{Co\text{-}Pi}$/FTO electrodes.

Charge-transfer resistance ($R_{Co\text{-}Pi}$) values of Co-Pi/FTO anodes, measured in 0.1M KPi, pH 8. The solid line is a guide to the eye.

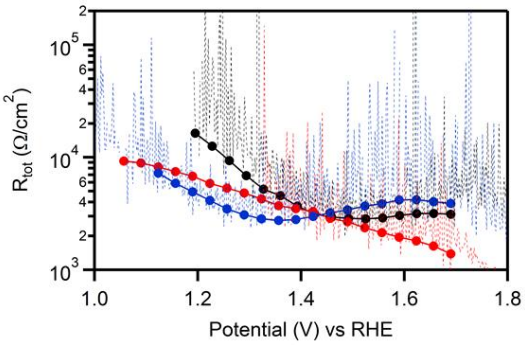

Figure E.5. Differential resistance plots for Co-Pi/α-Fe_2O_3 photoelectrodes.

Differential-resistance (d*V*/d*I*) data (dashed lines) and R_{TOT} data (closed circles) for bare α-Fe_2O_3 (black), ~2.3 nm Co-Pi/α-Fe_2O_3 (blue), and ~24.6 nm Co-Pi/α-Fe_2O_3 (red) photoanodes, plotted vs applied potential. Experimental details are described in the main text of Chapter 6.

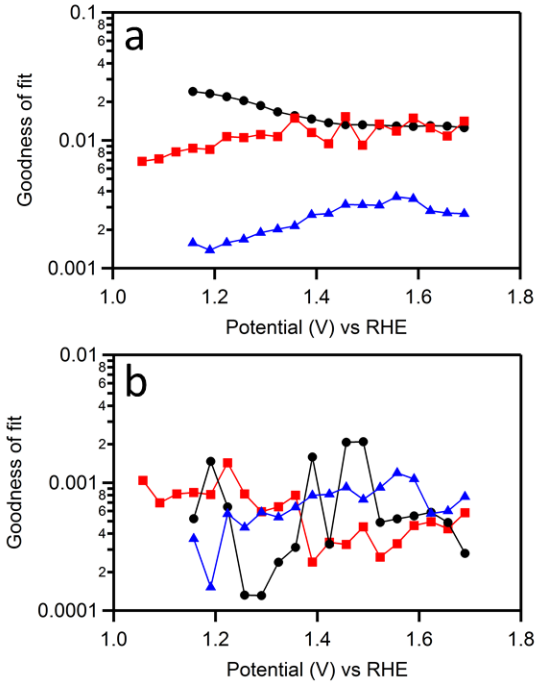

Figure E.6. Goodness-of-fit plots for EIS modeling of Co-Pi/α-Fe_2O_3.

Goodness-of-fit values between the experimental EIS data and the model for bare α-Fe_2O_3 (black circles), optimized Co-Pi/α-Fe_2O_3 (blue triangles), and bottlenecked Co-Pi/α-Fe_2O_3 (red squares) photoanodes. (a) Values obtained from modeling with a standard capacitor model. (b) Values obtained from a constant phase element model. Values

between 0.001 and 0.01 correspond to between ~3 and 10% difference between the data and the fit.

Capacitance values from models containing a constant phase element (CPE) were obtained using equation S1, where α is an empirical value obtained from the EIS fit and ω_{max} is the frequency at the maximum phase angle.

$$Capacitance = CPE \times (\omega_{\max})^{\alpha-1} \qquad \text{(Equation E1)}$$

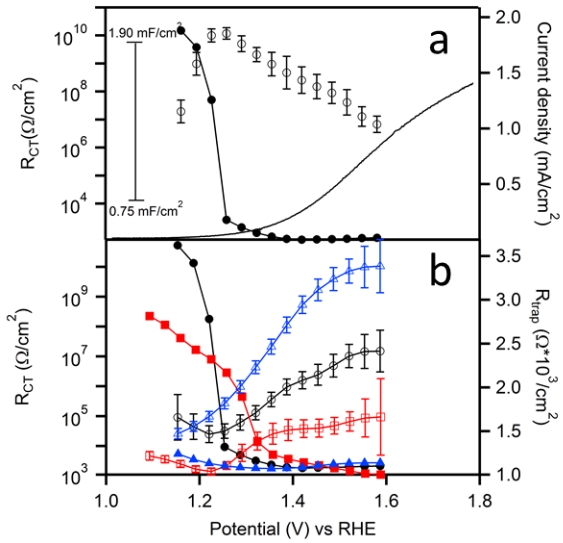

Figure E.7. EIS parameters for α-Fe_2O_3 and resistances of composite photoelectrodes modeled with a CPE.

(a) $R_{CT\ SS}$ (closed circles), C_{SS} (open circles), and *J-V* (solid line) data obtained for a bare α-Fe_2O_3 photoanode. These $R_{CT\ SS}$ and C_{SS} data were obtained from the PEIS data by fitting using a constant phase element. The linear inset scale bar refers to the C_{SS} data. Error bars correspond to uncertainties from the impedance fitting. **(b)** R_{CT} (closed shapes) and R_{trap} (open shapes) data for the same α-Fe_2O_3 photoanode measured with 0 (black circles), ~2.3 (blue triangles), and ~24.5 nm Co-Pi (red squares) surface coverage. These data are presented for comparison with the data in Figure 3 of the main text.

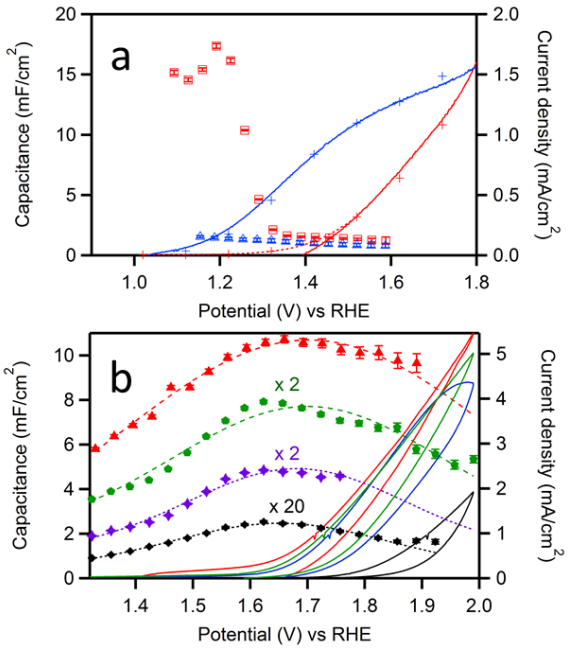

Figure E.8. Comparison of capacitance values for composite photoanodes and Co-Pi thin films modeled with a CPE.

(a) $C_{SS\ Co\text{-}Pi}$ (open shape) and *J-V* (solid line) data measured for the same α-Fe_2O_3 photoanode with ~2.3 nm (blue triangle) and ~24.5 nm (red square) thick Co-Pi on its surface. Measurements were collected under AM 1.5 illumination from the back side in 0.1 M KPi at pH 8 and fit using a constant phase element. The hash mark symbols on the *J-V* curves show steady-state current densities. **(b)** C_{TOT} (closed shapes), and *J-V* (solid lines) data measured at 10 mV/s scan rate for the same FTO anode with ~1.2 nm (black diamond), ~24.5 nm (purple star), ~46.8 nm (green pentagon), and ~490 nm (red triangle) Co-Pi thickness on the surface. The dashed lines are guides to the eye.

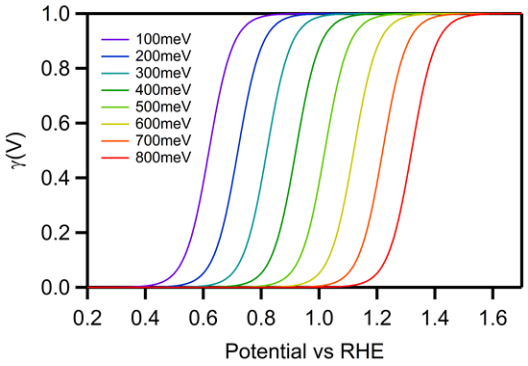

Figure E.9. Potential dependent electron-trap occupation at different trap depths.

Calculated values of $\gamma(V)$ as a function of applied potential. Electron trap energies between 100 and 800 meV more negative than the equilibrium Fermi level of the electrode are shown.

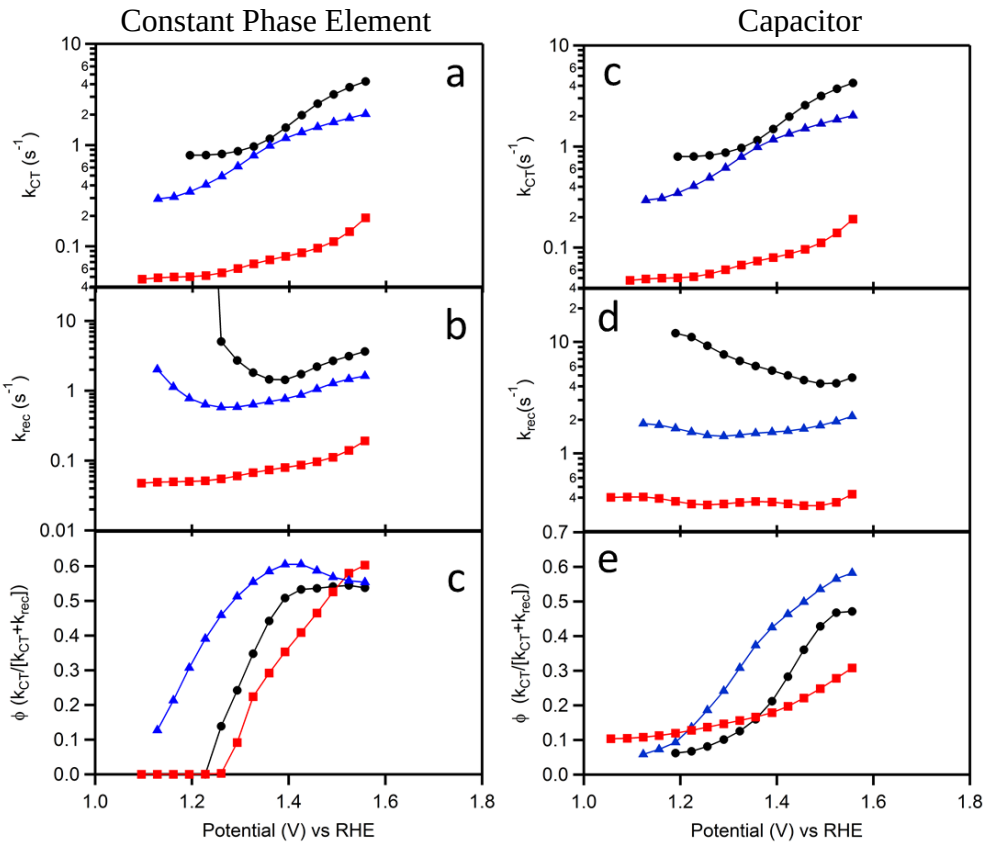

Figure E.10. Comparison of rate constants from capacitor and CPE analysis.

(a,c) Charge-transfer rate constants, **(b,d)** recombination rate constants, and **(c,e)** water-oxidation quantum efficiency plotted vs applied potential for bare α-Fe_2O_3 (black circles), 2.3 nm Co-Pi/α-Fe_2O_3 (blue triangles), and 24.5 nm Co-Pi/α-Fe_2O_3 (red squares) photoanodes. Panels **a**, **b**, and **c** plot values obtained from fitting impedance data with a constant phase element for comparison with panels **d**, **e**, and **f**, which plot the results from Figure 5 in the main text.

References

(1) Klahr, B.; Gimenez, S.; Fabregat-Santiago, F.; Bisquert, J.; Hamann, T. W.: Electrochemical and photoelectrochemical investigation of water oxidation with hematite electrodes. *Energy Environ. Sci.* **2012**, *5*, 7626-7636.

(2) Klahr, B.; Hamann, T.: Water Oxidation on Hematite Photoelectrodes: Insight into the Nature of Surface States through In Situ Spectroelectrochemistry. *J. Phys. Chem. C* **2014**, *118*, 10393-10399.

(3) Klahr, B. M.; Hamann, T. W.: Current and Voltage Limiting Processes in Thin Film Hematite Electrodes. *J. Phys. Chem. C* **2011**, *115*, 8393-8399.

(4) Bertoluzzi, L.; Bisquert, J.: Equivalent Circuit of Electrons and Holes in Thin Semiconductor Films for Photoelectrochemical Water Splitting Applications. *J. Phys. Chem. Lett.* **2012**, *3*, 2517-2522.

Bibliography

Amelia, M.; Impellizzeri, S.; Monaco, S.; Yildiz, I.; Silvi, S.; Raymo, F. M.; Credi, A. Structural and Size Effects on the Spectroscopic and Redox Properties of CdSe Nanocrystals in Solution: The Role of Defect States. *ChemPhysChem* **2011**, *12*, 2280-2288.

Amelia, M.; Lincheneau, C.; Silvi, S.; Credi, A. Electrochemical properties of CdSe and CdTe quantum dots. *Chem. Soc. Rev.* **2012**, *41*, 5728-5743.

Anderson, N. C.; Hendricks, M. P.; Choi, J. J.; Owen, J. S. Ligand Exchange and the Stoichiometry of Metal Chalcogenide Nanocrystals: Spectroscopic Observation of Facile Metal-Carboxylate Displacement and Binding. *J. Am. Chem. Soc.* **2013**, *135*, 18536-18548.

André, A.; Zherebetskyy, D.; Hanifi, D.; He, B.; Samadi Khoshkhoo, M.; Jankowski, M.; Chassé, T.; Wang, L.-W.; Schreiber, F.; Salleo, A.; Liu, Y.; Scheele, M. Toward Conductive Mesocrystalline Assemblies: PbS Nanocrystals Cross-Linked with Tetrathiafulvalene Dicarboxylate. *Chem. Mater.* **2015**, *27*, 8105-8115.

Araci, Z. O.; Shallcross, C. R.; Armstrong, N. R.; Saavedra, S. S. Potential-Modulated Attenuated Total Reflectance Characterization of Charge Injection Processes in Monolayer-Tethered CdSe Nanocrystals. *J. Phys. Chem. Lett.* **2010**, *1*, 1900-1905.

Aruchamy, A.; Bruce, J. A.; Tanaka, S.; Wrighton, M. S. Characterization of the Interface Energetics for N-Type Cadmium Selenide/Nonaqueous Electrolyte Junctions. *J. Electrchem. Soc.* **1983**, *130*, 359-364.

Bae, Y.; Myung, N.; Bard, A. J. Electrochemistry and Electrogenerated Chemiluminescence of CdTe Nanoparticles. *Nano Lett.* **2004**, *4*, 1153-1161.

Bard, A. J.; Bocarsly, A. B.; Fan, F. R. F.; Walton, E. G.; Wrighton, M. S. The concept of Fermi level pinning at semiconductor/liquid junctions. Consequences for energy conversion efficiency and selection of useful solution redox couples in solar devices. *J. Am. Chem. Soc.* **1980**, *102*, 3671-3677.

Bard, A. J.; Fox, M. A. Artificial Photosynthesis: Solar Splitting of Water to Hydrogen and Oxygen. *Accts. Chem. Res.* **1995**, *28*, 141-145.

Barroso, M.; Cowan, A. J.; Pendlebury, S. R.; Grätzel, M.; Klug, D. R.; Durrant, J. R. The Role of Cobalt Phosphate in Enhancing the Photocatalytic Activity of α-Fe2O3 toward Water Oxidation. *J. Am. Chem. Soc.* **2011**, *133*, 14868-14871.

Barroso, M.; Mesa, C. A.; Pendlebury, S. R.; Cowan, A. J.; Hisatomi, T.; Sivula, K.;

Grätzel, M.; Klug, D. R.; Durrant, J. R. Dynamics of photogenerated holes in surface modified α-Fe2O3 photoanodes for solar water splitting. *Proc. Natl. Acad. Sci.* **2012**.

Barroso, M.; Pendlebury, S. R.; Cowan, A. J.; Durrant, J. R. Charge carrier trapping, recombination and transfer in hematite (α-Fe_2O_3) water splitting photoanodes. *Chem. Sci.* **2013**, *4*, 2724-2734.

Bertoluzzi, L.; Bisquert, J. Equivalent Circuit of Electrons and Holes in Thin Semiconductor Films for Photoelectrochemical Water Splitting Applications. *J. Phys. Chem. Lett.* **2012**, *3*, 2517-2522.

Bloom, B. P.; Zhao, L.-B.; Wang, Y.; Waldeck, D. H.; Liu, R.; Zhang, P.; Beratan, D. N. Ligand-Induced Changes in the Characteristic Size-Dependent Electronic Energies of CdSe Nanocrystals. *J. Phys. Chem. C* **2013**, *117*, 22401-22411.

Boehme, S. C.; Azpiroz, J. M.; Aulin, Y. V.; Grozema, F. C.; Vanmaekelbergh, D.; Siebbeles, L. D. A.; Infante, I.; Houtepen, A. J. Density of Trap States and Auger-mediated Electron Trapping in CdTe Quantum-Dot Solids. *Nano Lett.* **2015**, *15*, 3056-3066.

Boehme, S. C.; Vanmaekelbergh, D.; Evers, W. H.; Siebbeles, L. D. A.; Houtepen, A. J. In Situ Spectroelectrochemical Determination of Energy Levels and Energy Level Offsets in Quantum-Dot Heterojunctions. *J. Phys. Chem. C* **2016**, *120*, 5164-5173.

Boehme, S. C.; Walvis, T. A.; Infante, I.; Grozema, F. C.; Vanmaekelbergh, D.; Siebbeles, L. D. A.; Houtepen, A. J. Electrochemical Control over Photoinduced Electron Transfer and Trapping in CdSe-CdTe Quantum-Dot Solids. *ACS Nano* **2014**, *8*, 7067-7077.

Boehme, S. C.; Wang, H.; Siebbeles, L. D. A.; Vanmaekelbergh, D.; Houtepen, A. J. Electrochemical Charging of CdSe Quantum Dot Films: Dependence on Void Size and Counterion Proximity. *ACS Nano* **2013**, *7*, 2500-2508.

Boles, M. A.; Ling, D.; Hyeon, T.; Talapin, D. V. The surface science of nanocrystals. *Nat Mater* **2016**, *15*, 141-153.

Bowker, M.; Houghton, H.; Waugh, K. C. Temperature-programmed reaction studies of the interaction of methyl formate and ethanol with polycrystalline zinc oxide. *J. Phys. Chem. Soc., Faraday Trans.* **1982**, *78*, 2573-2582.

Brovelli, S.; Galland, C.; Viswanatha, R.; Klimov, V. I. Tuning Radiative Recombination in Cu-Doped Nanocrystals via Electrochemical Control of Surface Trapping. *Nano Lett.* **2012**, *12*, 4372-4379.

Brown, K. A.; Harris, D. F.; Wilker, M. B.; Rasmussen, A.; Khadka, N.; Hamby, H.; Keable, S.; Dukovic, G.; Peters, J. W.; Seefeldt, L. C.; King, P. W. Light-driven

dinitrogen reduction catalyzed by a CdS:nitrogenase MoFe protein biohybrid. *Science* **2016**, *352*, 448-450.

Brown, P. R.; Kim, D.; Lunt, R. R.; Zhao, N.; Bawendi, M. G.; Grossman, J. C.; Bulović, V. Energy Level Modification in Lead Sulfide Quantum Dot Thin Films through Ligand Exchange. *ACS Nano* **2014**, *8*, 5863-5872.

Brus, L. E. A simple model for the ionization potential, electron affinity, and aqueous redox potentials of small semiconductor crystallites. *J. Chem. Phys.* **1983**, *79*, 5566-5571.

Carey, G. H.; Abdelhady, A. L.; Ning, Z.; Thon, S. M.; Bakr, O. M.; Sargent, E. H. Colloidal Quantum Dot Solar Cells. *Chem. Rev.* **2015**, *115*, 12732-12763.

Carroll, G. M.; Brozek, C. K.; Hartstein, K. H.; Tsui, E. Y.; Gamelin, D. R. Potentiometric Measurements of Semiconductor Nanocrystal Redox Potentials. *J. Am. Chem. Soc.* **2016**.

Carroll, G. M.; Schimpf, A. M.; Tsui, E. Y.; Gamelin, D. R. Redox Potentials of Colloidal n-Type ZnO Nanocrystals: Effects of Confinement, Electron Density, and Fermi-Level Pinning by Aldehyde Hydrogenation. *J. Am. Chem. Soc.* **2015**, *137*, 11163-11169.

Carroll, G. M.; Zhong, D. K.; Gamelin, D. R. Mechanistic insights into solar water oxidation by cobalt-phosphate-modified α-Fe_2O_3photoanodes. *Energy Environ. Sci.* **2015**, *8*, 577-584.

Chemelewski, W. D.; Hahn, N. T.; Mullins, C. B. Effect of Si Doping and Porosity on Hematite's (α-Fe2O3) Photoelectrochemical Water Oxidation Performance. *J. Phys. Chem. C* **2012**, *116*, 5255-5261.

Chen, O.; Chen, X.; Yang, Y.; Lynch, J.; Wu, H.; Zhuang, J.; Cao, Y. C. Synthesis of Metal–Selenide Nanocrystals Using Selenium Dioxide as the Selenium Precursor. *Angew. Chem. Int. Ed.* **2008**, *47*, 8638-8641.

Chen, S.; Wang, L.-W. Thermodynamic Oxidation and Reduction Potentials of Photocatalytic Semiconductors in Aqueous Solution. *Chem. Mater.* **2012**, *24*, 3659-3666.

Chuang, C.-H. M.; Brown, P. R.; Bulović, V.; Bawendi, M. G. Improved performance and stability in quantum dot solar cells through band alignment engineering. *Nat. Mater.* **2014**, *13*, 796-801.

Cohen, R.; Ashkenasy, G.; Shanzer, A.; Cahen, D. Grafting Molecular Properties onto Semiconductor Surfaces. *Encyclopedia of Electrochemistry* **2002**.

Cohn, A. W.; Janßen, N.; Mayer, J. M.; Gamelin, D. R. Photocharging ZnO Nanocrystals: Picosecond Hole Capture, Electron Accumulation, and Auger Recombination. *J. Phys. Chem. C* **2012**, *116*, 20633-20642.

Cohn, A. W.; Kittilstved, K. R.; Gamelin, D. R. Tuning the Potentials of "Extra" Electrons in Colloidal n-Type ZnO Nanocrystals via Mg^{2+} Substitution. *J. Am. Chem. Soc.* **2012**, *134*, 7937-7943.

Cohn, A. W.; Rinehart, J. D.; Schimpf, A. M.; Weaver, A. L.; Gamelin, D. R. Size Dependence of Negative Trion Auger Recombination in Photodoped CdSe Nanocrystals. *Nano Lett.* **2014**, *14*, 353-358.

Connelly, N. G.; Geiger, W. E. Chemical Redox Agents for Organometallic Chemistry. *Chem. Rev.* **1996**, *96*, 877-910.

Cowan, A. J.; Barnett, C. J.; Pendlebury, S. R.; Barroso, M.; Sivula, K.; Grätzel, M.; Durrant, J. R.; Klug, D. R. Activation Energies for the Rate-Limiting Step in Water Photooxidation by Nanostructured α-Fe2O3 and TiO2. *J. Am. Chem. Soc.* **2011**, *133*, 10134-10140.

Cowan, A. J.; Durrant, J. R. Long-lived charge separated states in nanostructured semiconductor photoelectrodes for the production of solar fuels. *Chem. Soc. Rev.* **2013**, *42*, 2281-2293.

Cummings, C. Y.; Marken, F.; Peter, L. M.; Tahir, A. A.; Wijayantha, K. G. U. Kinetics and mechanism of light-driven oxygen evolution at thin film α-Fe_2O_3 electrodes. *Chem. Comm.* **2012**, *48*, 2027-2029.

Cunningham, J.; Hodnett, B. K. Kinetic Studies of Secondary Alcohol Photo-oxidation on ZnO and TiO2 at 348 K Studied by Gas-chromatographic Analysis. *J. Chem. Soc., Faraday Trans. 1* **1981**, *77*, 2777-2801.

Dare-Edwards, M. P.; Goodenough, J. B.; Hamnett, A.; Trevellick, P. R. Electrochemistry and photoelectrochemistry of iron(III) oxide. *J. Chem. Soc., Faraday Trans. 1: Phys. Chem. Condensed Phases* **1983**, *79*, 2027-2041.

De Trizio, L.; Buonsanti, R.; Schimpf, A. M.; Llordes, A.; Gamelin, D. R.; Simonutti, R.; Milliron, D. J. Nb-Doped Colloidal TiO2 Nanocrystals with Tunable Infrared Absorption. *Chem. Mater.* **2013**, *25*, 3383-3390.

Ding, Z.; Quinn, B. M.; Haram, S. K.; Pell, L. E.; Korgel, B. A.; Bard, A. J. Electrochemistry and Electrogenerated Chemiluminescence from Silicon Nanocrystal Quantum Dots. *Science* **2002**, *296*, 1293-1297.

Du, C.; Yang, X.; Mayer, M. T.; Hoyt, H.; Xie, J.; McMahon, G.; Bischoping, G.; Wang, D. Hematite-Based Water Splitting with Low Turn-On Voltages. *Angew. Chem.*

Int. Ed. **2013**, *52*, 12692-12695.

Duonghong, D.; Ramsden, J.; Grätzel, M. Dynamics of Interfacial Electron-Transfer Processes in Colloidal Semiconductor Systems. *J. Am. Chem. Soc.* **1982**, *104*, 2977-2985.

Duret, A.; Grätzel, M. Visible Light-Induced Water Oxidation on Mesoscopic α-Fe2O3 Films Made by Ultrasonic Spray Pyrolysis. *J. Phys. Chem. B* **2005**, *109*, 17184-17191.

Ehamparam, R.; Pavlopoulos, N. G.; Liao, M. W.; Hill, L. J.; Armstrong, N. R.; Pyun, J.; Saavedra, S. S. Band Edge Energetics of Heterostructured Nanorods: Photoemission Spectroscopy and Waveguide Spectroelectrochemistry of Au-Tipped CdSe Nanorod Monolayers. *ACS Nano* **2015**, *9*, 8786-8800.

Ekimov, A. I.; Hache, F.; Schanne-Klein, M. C.; Ricard, D.; Flytzanis, C.; Kudryavtsev, I. A.; Yazeva, T. V.; Rodina, A. V.; Efros, A. L. Absorption and intensity-dependent photoluminescence measurements on CdSe quantum dots: assignment of the first electronic transitions. *J. Opt. Soc. Am. B* **1993**, *10*, 100-107.

Emin, S.; Singh, S. P.; Han, L.; Satoh, N.; Islam, A. Colloidal quantum dot solar cells. *Solar Energy* **2011**, *85*, 1264-1282.

Frederick, M. T.; Weiss, E. A. Relaxation of Exciton Confinement in CdSe Quantum Dots by Modification with a Conjugated Dithiocarbamate Ligand. *ACS Nano* **2010**, *4*, 3195-3200.

Fujishima, A.; Honda, K. Electrochemical Photolysis of Water at a Semiconductor Electrode. *Nature* **1972**, *238*, 37-38.

Galland, C.; Ghosh, Y.; Steinbruck, A.; Sykora, M.; Hollingsworth, J. A.; Klimov, V. I.; Htoon, H. Two types of luminescence blinking revealed by spectroelectrochemistry of single quantum dots. *Nature* **2011**, *479*, 203-207.

Gamelin, D. R. Water splitting: Catalyst or spectator? *Nat. Chem.* **2012**, *4*, 965-967.

Gao, Y.; Peng, X. Photogenerated Excitons in Plain Core CdSe Nanocrystals with Unity Radiative Decay in Single Channel: The Effects of Surface and Ligands. *J. Am. Chem. Soc.* **2015**, *137*, 4230-4235.

Garcia, G.; Buonsanti, R.; Llordes, A.; Runnerstrom, E. L.; Bergerud, A.; Milliron, D. J. Near-Infrared Spectrally Selective Plasmonic Electrochromic Thin Films. *Adv. Opt. Mat.* **2013**, *1*, 215-220.

Garcia, G.; Buonsanti, R.; Runnerstrom, E. L.; Mendelsberg, R. J.; Llordes, A.; Anders, A.; Richardson, T. J.; Milliron, D. J. Dynamically Modulating the Surface Plasmon Resonance of Doped Semiconductor Nanocrystals. *Nano Lett.* **2011**, *11*, 4415-4420.

Gardner, R. F. G.; Sweett, F.; Tanner, D. W. The electrical properties of alpha ferric oxide—I.: The impure oxide. *J. Phys. Chem. Sol.* **1963**, *24*, 1175-1181.

Germeau, A.; Roest, A. L.; Vanmaekelbergh, D.; Allan, G.; Delerue, C.; Meulenkamp, E. A. Optical Transitions in Artificial Few-Electron Atoms Strongly Confined Inside ZnO Nanocrystals. *Phys. Rev. Lett.* **2003**, *90*, 097401.

Goings, J. J.; Schimpf, A. M.; May, J. W.; Johns, R. W.; Gamelin, D. R.; Li, X. Theoretical Characterization of Conduction-Band Electrons in Photodoped and Aluminum-Doped Zinc Oxide (AZO) Quantum Dots. *J. Phys. Chem. C* **2014**, *118*, 26584-26590.

Gonçalves, R. H.; Lima, B. H. R.; Leite, E. R. Magnetite Colloidal Nanocrystals: A Facile Pathway To Prepare Mesoporous Hematite Thin Films for Photoelectrochemical Water Splitting. *J. Am. Chem. Soc.* **2011**, *133*, 6012-6019.

Gooding, A. K.; Gómez, D. E.; Mulvaney, P. The Effects of Electron and Hole Injection on the Photoluminescence of CdSe/CdS/ZnS Nanocrystal Monolayers. *ACS Nano* **2008**, *2*, 669-676.

Gordon, K. R.; Warren, K. D. Spectroscopic and magnetic studies of the 3d metallocenes. *Inorg. Chem.* **1978**, *17*, 987-994.

Grätzel, M. Photoelectrochemical cells. *Nature* **2001**, *414*, 338-344.

Guyot-Sionnest, P. Charging colloidal quantum dots by electrochemistry. *Microchimica Acta* **2008**, *160*, 309-314.

Guyot-Sionnest, P.; Wang, C. Fast Voltammetric and Electrochromic Response of Semiconductor Nanocrystal Thin Films. *J. Phys. Chem. B* **2003**, *107*, 7355-7359.

Haase, M.; Weller, H.; Henglein, A. Photochemistry and radiation chemistry of colloidal semiconductors. 23. Electron storage on zinc oxide particles and size quantization. *J. Phys. Chem.* **1988**, *92*, 482-487.

Haffad, D.; Kameswari, U.; Bettahar, M. M.; Chambellan, A.; Lavalley, J. C. Reduction of Benzaldehyde on Metal Oxides. *J. Catal.* **1997**, *172*, 85-92.

Hahn, N. T.; Mullins, C. B. Photoelectrochemical Performance of Nanostructured Ti- and Sn-Doped α-Fe2O3 Photoanodes. *Chem. Mat.* **2010**, *22*, 6474-6482.

Hahn, N. T.; Ye, H.; Flaherty, D. W.; Bard, A. J.; Mullins, C. B. Reactive Ballistic Deposition of α-Fe2O3 Thin Films for Photoelectrochemical Water Oxidation. *ACS Nano* **2010**, *4*, 1977-1986.

Hamann, T. W. Splitting water with rust: hematite photoelectrochemistry. *Dalton Trans.* **2012**, *41*, 7830-7834.

Hamann, T. W. Water splitting: An adaptive junction. *Nat. Mater.* **2014**, *13*, 3-4.

Han, Z.; Eisenberg, R. Fuel from Water: The Photochemical Generation of Hydrogen from Water. *Accts. Chem. Res.* **2014**, *47*, 2537-2544.

Han, Z.; Qiu, F.; Eisenberg, R.; Holland, P. L.; Krauss, T. D. Robust Photogeneration of H2 in Water Using Semiconductor Nanocrystals and a Nickel Catalyst. *Science* **2012**, *338*, 1321-1324.

Haram, S. K.; Quinn, B. M.; Bard, A. J. Electrochemistry of CdS Nanoparticles: A Correlation between Optical and Electrochemical Band Gaps. *J. Am. Chem. Soc.* **2001**, *123*, 8860-8861.

Hayoun, R.; Whitaker, K. M.; Gamelin, D. R.; Mayer, J. M. Electron Transfer Between Colloidal ZnO Nanocrystals. *J. Am. Chem. Soc.* **2011**, *133*, 4228-4231.

He, J.; Parkinson, B. A. Combinatorial Investigation of the Effects of the Incorporation of Ti, Si, and Al on the Performance of α-Fe2O3 Photoanodes. *ACS Comb. Sci.* **2011**, *13*, 399-404.

Henglein, A. Small-particle research: physicochemical properties of extremely small colloidal metal and semiconductor particles. *Chem. Rev.* **1989**, *89*, 1861-1873.

Hetsch, F.; Zhao, N.; Kershaw, S. V.; Rogach, A. L. Quantum dot field effect transistors. *Materials Today* **2013**, *16*, 312-325.

Hillhouse, H. W.; Beard, M. C. Solar cells from colloidal nanocrystals: Fundamentals, materials, devices, and economics. *Current Opinion in Colloid & Interface Science* **2009**, *14*, 245-259.

Hines, M. A.; Guyot-Sionnest, P. Synthesis and Characterization of Strongly Luminescing ZnS-Capped CdSe Nanocrystals. *J. Phys. Chem.* **1996**, *100*, 468-471.

Houtepen, A. J.; Vanmaekelbergh, D. Orbital Occupation in Electron-Charged CdSe Quantum-Dot Solids. *J. Phys. Chem. B* **2005**, *109*, 19634-19642.

Hoyer, P.; Weller, H. Potential-Dependent Electron Injection in Nanoporous Colloidal ZnO Films. *J. Phys. Chem.***1995**, *99*, 14096-14100.

Huang, J.; Stockwell, D.; Huang, Z.; Mohler, D. L.; Lian, T. Photoinduced Ultrafast Electron Transfer from CdSe Quantum Dots to Re-bipyridyl Complexes. *J. Am. Chem. Soc.* **2008**, *130*, 5632-5633.

Iandolo, B.; Wickman, B.; Zoric, I.; Hellman, A. The rise of hematite: origin and strategies to reduce the high onset potential for the oxygen evolution reaction. *J. Mat. Chem. A* **2015**, *3*, 16896-16912.

Impellizzeri, S.; Monaco, S.; Yildiz, I.; Amelia, M.; Credi, A.; Raymo, F. M. Structural Implications on the Electrochemical and Spectroscopic Signature of CdSe-ZnS Core−Shell Quantum Dots. *J. Phys. Chem. C* **2010**, *114*, 7007-7013.

Inamdar, S. N.; Ingole, P. P.; Haram, S. K. Determination of Band Structure Parameters and the Quasi-Particle Gap of CdSe Quantum Dots by Cyclic Voltammetry. *ChemPhysChem* **2008**, *9*, 2574-2579.

Jakob, M.; Levanon, H.; Kamat, P. V. Charge Distribution between UV-Irradiated TiO_2 and Gold Nanoparticles: Determination of Shift in the Fermi Level. *Nano Lett.* **2003**, *3*, 353-358.

Jarosz, M. V.; Porter, V. J.; Fisher, B. R.; Kastner, M. A.; Bawendi, M. G. Photoconductivity studies of treated CdSe quantum dot films exhibiting increased exciton ionization efficiency. *Phys. Rev. B* **2004**, *70*, 195327.

Jasieniak, J.; Califano, M.; Watkins, S. E. Size-Dependent Valence and Conduction Band-Edge Energies of Semiconductor Nanocrystals. *ACS Nano* **2011**, *5*, 5888-5902.

Jensen, S. C.; Homan, S. B.; Weiss, E. A. Photocatalytic Conversion of Nitrobenzene to Aniline through Sequential Proton-Coupled One-Electron Transfers from a Cadmium Sulfide Quantum Dot. *J. Am. Chem. Soc.* **2016**, in press (DOI:10.1021/jacs.1025b11353).

Jeong, K. S.; Deng, Z.; Keuleyan, S.; Liu, H.; Guyot-Sionnest, P. Air-Stable n-Doped Colloidal HgS Quantum Dots. *J. Phys. Chem. Lett.* **2014**, *5*, 1139-1143.

Jeong, K. S.; Deng, Z.; Keuleyan, S.; Liu, H.; Guyot-Sionnest, P. Air-Stable n-Doped Colloidal HgS Quantum Dots. *J. Phys. Chem. Lett.* **2014**, *5*, 1139-1143.

Jha, P. P.; Guyot-Sionnest, P. Electrochemical Switching of the Photoluminescence of Single Quantum Dots. *J. Phys. Chem. C* **2010**, *114*, 21138-21141.

Jha, P. P.; Guyot-Sionnest, P. Trion Decay in Colloidal Quantum Dots. *ACS Nano* **2009**, *3*, 1011-1015.

Jin, L.; Shang, L.; Zhai, J.; Li, J.; Dong, S. Fluorescence Spectroelectrochemistry of Multilayer Film Assembled CdTe Quantum Dots Controlled by Applied Potential in Aqueous Solution. *J. Phys. Chem. C* **2010**, *114*, 803-807.

Kalisman, P.; Nakibli, Y.; Amirav, L. Perfect Photon-to-Hydrogen Conversion Efficiency. *Nano Lett.* **2016**, *16*, 1776-1781.

Kamat, P. V. Quantum Dot Solar Cells. Semiconductor Nanocrystals as Light Harvesters. *J. Phys. Chem. C* **2008**, *112*, 18737-18753.

Kamat, P. V.; Tvrdy, K.; Baker, D. R.; Radich, J. G. Beyond Photovoltaics: Semiconductor Nanoarchitectures for Liquid-Junction Solar Cells. *Chem. Rev.* **2010**, *110*, 6664-6688.

Kanan, M. W.; Nocera, D. G. In Situ Formation of an Oxygen-Evolving Catalyst in Neutral Water Containing Phosphate and Co^{2+}. *Science* **2008**, *321*, 1072-1075.

Kanan, M. W.; Surendranath, Y.; Nocera, D. G. Cobalt-phosphate oxygen-evolving compound. *Chem. Soc. Rev.* **2009**, *38*, 109-114.

Kanan, M. W.; Yano, J.; Surendranath, Y.; Dincă, M.; Yachandra, V. K.; Nocera, D. G. Structure and Valency of a Cobalt−Phosphate Water Oxidation Catalyst Determined by in Situ X-ray Spectroscopy. *J. Am. Chem. Soc.* **2010**, *132*, 13692-13701.

Kay, A.; Cesar, I.; Grätzel, M. New Benchmark for Water Photooxidation by Nanostructured α-Fe2O3 Films. *J. Am. Chem. Soc.* **2006**, *128*, 15714-15721.

Kennedy, J. H.; Frese, K. W. Photooxidation of Water at α-Fe_2O_3 Electrodes. *J. Electrochem. Soc.* **1978**, *125*, 709-714.

Khan, S. U. M.; Kainthla, R. C.; Bockris, J. O. M. The redox potential and the Fermi level in solution. *J. Phys. Chem.* **1987**, *91*, 5974-5977.

Khaselev, O.; Turner, J. A. A Monolithic Photovoltaic-Photoelectrochemical Device for Hydrogen Production via Water Splitting. *Science* **1998**, *280*, 425-427.

Klahr, B. M.; Hamann, T. W. Current and Voltage Limiting Processes in Thin Film Hematite Electrodes. *J. Phys. Chem. C* **2011**, *115*, 8393-8399.

Klahr, B.; Gimenez, S.; Fabregat-Santiago, F.; Bisquert, J.; Hamann, T. W. Electrochemical and photoelectrochemical investigation of water oxidation with hematite electrodes. *Energy Environ. Sci.* **2012**, *5*, 7626-7636.

Klahr, B.; Giménez, S.; Fabregat-Santiago, F.; Bisquert, J.; Hamann, T. W. Photoelectrochemical and Impedance Spectroscopic Investigation of Water Oxidation with "Co-Pi" coated Hematite Electrodes. *J. Am. Chem. Soc.* **2012**.

Klahr, B.; Hamann, T. Water Oxidation on Hematite Photoelectrodes: Insight into the Nature of Surface States through In Situ Spectroelectrochemistry. *J. Phys. Chem. C* **2014**, *118*, 10393-10399.

Klimov, V. I.; Mikhailovsky, A. A.; McBranch, D. W.; Leatherdale, C. A.; Bawendi,

M. G. Quantization of Multiparticle Auger Rates in Semiconductor Quantum Dots. *Science* **2000**, *287*, 1011-1013.

Koh, W.-k.; Koposov, A. Y.; Stewart, J. T.; Pal, B. N.; Robel, I.; Pietryga, J. M.; Klimov, V. I. Heavily doped n-type PbSe and PbS nanocrystals using ground-state charge transfer from cobaltocene. *Scientific Reports* **2013**, *3*, 2004.

Kovalenko, M. V.; Manna, L.; Cabot, A.; Hens, Z.; Talapin, D. V.; Kagan, C. R.; Klimov, V. I.; Rogach, A. L.; Reiss, P.; Milliron, D. J.; Guyot-Sionnnest, P.; Konstantatos, G.; Parak, W. J.; Hyeon, T.; Korgel, B. A.; Murray, C. B.; Heiss, W. Prospects of Nanoscience with Nanocrystals. *ACS Nano* **2015**, *9*, 1012-1057.

Krishnan, R.: Fundamentals of Semiconductor Electrochemistry and Photoelectrochemistry. In *Encyclopedia of Electrochemistry*; Wiley-VCH Verlag GmbH & Co. KGaA, 2007.

Kucur, E.; Riegler, J.; Urban, G. A.; Nann, T. Determination of quantum confinement in CdSe nanocrystals by cyclic voltammetry. *J. Chem. Phys.* **2003**, *119*, 2333-2337.

Kucur, E.; Riegler, J.; Urban, G. A.; Nann, T. Determination of quantum confinement in CdSe nanocrystals by cyclic voltammetry. *J. Chem. Phys.* **2003**, *119*, 2333-2337.

Lasia, A.: Electrochemical Impedance Spectroscopy and its Applications. In *Modern Aspects of Electrochemistry*; Conway, B. E., Bockris, J. O. M., White, R., Eds.; Modern Aspects of Electrochemistry; Springer US, 2002; Vol. 32; pp 143-248.

Le Formal, F.; Grätzel, M.; Sivula, K. Controlling Photoactivity in Ultrathin Hematite Films for Solar Water-Splitting. *Adv. Func. Mat.* **2010**, *20*, 1099-1107.

Le Formal, F.; Pendlebury, S. R.; Cornuz, M.; Tilley, S. D.; Grätzel, M.; Durrant, J. R. Back Electron–Hole Recombination in Hematite Photoanodes for Water Splitting. *J. Am. Chem. Soc.* **2014**, *136*, 2564-2574.

Le Formal, F.; Sivula, K.; Grätzel, M. The Transient Photocurrent and Photovoltage Behavior of a Hematite Photoanode under Working Conditions and the Influence of Surface Treatments. *J. Phys. Chem. C* **2012**, *116*, 26707-26720.

Lenglet, M.; Jørgensen, C. K. Reinvestigation of the optical properties of Co_3O_4. *Chem. Phys. Lett.* **1994**, *229*, 616-620.

Lewis, N. S.; Nocera, D. G. Powering the planet: Chemical challenges in solar energy utilization. *Proc. Natl. Acad. Sci.* **2006**, *103*, 15729-15735.

Licht, S. Multiple Band Gap Semiconductor/Electrolyte Solar Energy Conversion. *J. Phys. Chem. B* **2001**, *105*, 6281-6294.

Lin, F.; Boettcher, S. W. Adaptive semiconductor/electrocatalyst junctions in water-splitting photoanodes. *Nat. Mater.* **2014**, *13*, 81-86.

Liu, R.; Zheng, Z.; Spurgeon, J.; Yang, X. Enhanced photoelectrochemical water-splitting performance of semiconductors by surface passivation layers. *Energy Environ. Sci.* **2014**, *7*, 2504-2517.

Liu, W. K.; Whitaker, K. M.; Kittilstved, K. R.; Gamelin, D. R. Stable Photogenerated Carriers in Magnetic Semiconductor Nanocrystals. *J. Am. Chem. Soc.* **2006**, *128*, 3910-3911.

Liu, W. K.; Whitaker, K. M.; Smith, A. L.; Kittilstved, K. R.; Robinson, B. H.; Gamelin, D. R. Room-Temperature Electron Spin Dynamics in Free-Standing ZnO Quantum Dots. *Phys. Rev. Lett.* **2007**, *98*, 186804.

Luther, J. M.; Law, M.; Song, Q.; Perkins, C. L.; Beard, M. C.; Nozik, A. J. Structural, optical, and electrical properties of self-assembled films of PbSe nanocrystals treated with 1, 2-ethanedithiol. *ACS nano* **2008**, *2*, 271-280.

Lutterman, D. A.; Surendranath, Y.; Nocera, D. G. A Self-Healing Oxygen-Evolving Catalyst. *J. Am. Chem. Soc.* **2009**, *131*, 3838-3839.

Mäki-Arvela, P.; Hájek, J.; Salmi, T.; Murzin, D. Y. Chemoselective hydrogenation of carbonyl compounds over heterogeneous catalysts. *Appl. Catal. A* **2005**, *292*, 1-49.

Markham, M. C.; Hannan, M. C.; Paternostro, R. M.; Rose, C. B. Oxidation of Alcohols Catalyzed by Zinc Oxide and Light. *J. Am. Chem. Soc.* **1958**, *80*, 5394-5397.

Mattox, T. M.; Bergerud, A.; Agrawal, A.; Milliron, D. J. Influence of Shape on the Surface Plasmon Resonance of Tungsten Bronze Nanocrystals. *Chem. Mater.* **2014**, *26*, 1779-1784.

McAlpin, J. G.; Surendranath, Y.; Dincă, M.; Stich, T. A.; Stoian, S. A.; Casey, W. H.; Nocera, D. G.; Britt, R. D. EPR Evidence for Co(IV) Species Produced During Water Oxidation at Neutral pH. *J. Am. Chem. Soc.* **2010**, *132*, 6882-6883.

Meulenkamp, E. A. Synthesis and Growth of ZnO Nanoparticles. *J. Phys. Chem. B* **1998**, *102*, 5566-5572.

Milliron, D. J. Quantum dot solar cells: The surface plays a core role. *Nat Mater* **2014**, *13*, 772-773.

Mills, T. J.; Lin, F.; Boettcher, S. W. Theory and Simulations of Electrocatalyst-Coated Semiconductor Electrodes for Solar Water Splitting. *Phys. Rev. Lett.* **2014**, *112*, 148304.

Mirri, A. M.; Corbelli, G.; Forti, P. Stark Effect and Electric Dipole Moment of D2Se. *J. Chem. Phys.* **1969**, *50*, 4118-4118.

Mönch, W.: *Semiconductor surfaces and interfaces*; Springer Science & Business Media, 2013; Vol. 26.

Moniz, S. J. A.; Shevlin, S. A.; Martin, D. J.; Guo, Z.-X.; Tang, J. Visible-light driven heterojunction photocatalysts for water splitting - a critical review. *Energy Environ. Sci.* **2015**, *8*, 731-759.

Moomow, W.; Yamba, F.; Kamimoto, M.; Maurice, L.; Nyboer, J.; Urama, K.; Weir, T.: Introduction. In *IPCC Special Report on Renewable Energy Sources and Climate change Mitigation*; Edenhofer, O., Pichs-Madruga, R., Sokona, Y., Seyboth, K., Matschoss, P., Kadner, S., Zwickel, T., Eickemeier, P., Hansen, G., Schlömer, S., von Stechow, C., Eds.; Cambridge University Press: United Kingdom and New York, NY, USA, 2011.

Munro, A. M.; Zacher, B.; Graham, A.; Armstrong, N. R. Photoemission Spectroscopy of Tethered CdSe Nanocrystals: Shifts in Ionization Potential and Local Vacuum Level As a Function of Nanocrystal Capping Ligand. *ACS Appl. Mater. Interfaces* **2010**, *2*, 863-869.

Murray, C. B.; Kagan, C. R.; Bawendi, M. G. Self-Organization of CdSe Nanocrystallites into Three-Dimensional Quantum Dot Superlattices. *Science* **1995**, *270*, 1335-1338.

Murray, C. B.; Norris, D. J.; Bawendi, M. G. Synthesis and characterization of nearly monodisperse CdE (E = sulfur, selenium, tellurium) semiconductor nanocrystallites. *J. Am. Chem. Soc.* **1993**, *115*, 8706-8715.

Myung, N.; Bae, Y.; Bard, A. J. Effect of Surface Passivation on the Electrogenerated Chemiluminescence of CdSe/ZnSe Nanocrystals. *Nano Lett.* **2003**, *3*, 1053-1055.

Myung, N.; Ding, Z.; Bard, A. J. Electrogenerated Chemiluminescence of CdSe Nanocrystals. *Nano Lett.* **2002**, *2*, 1315-1319.

Nenadović, M. T.; Rajh, T.; Mićić, O. I.; Nozik, A. J. Electron Transfer Reactions and Flat-Band Potentials of WO_3 Colloids. *J. Phys. Chem.* **1984**, *88*, 5827-5830.

Ning, Z.; Voznyy, O.; Pan, J.; Hoogland, S.; Adinolfi, V.; Xu, J.; Li, M.; Kirmani, A. R.; Sun, J.-P.; Minor, J.; Kemp, K. W.; Dong, H.; Rollny, L.; Labelle, A.; Carey, G.; Sutherland, B.; Hill, I.; Amassian, A.; Liu, H.; Tang, J.; Bakr, O. M.; Sargent, E. H. Air-stable n-type colloidal quantum dot solids. *Nat Mater* **2014**, *13*, 822-828.

Ning, Z.; Voznyy, O.; Pan, J.; Hoogland, S.; Adinolfi, V.; Xu, J.; Li, M.; Kirmani, A. R.; Sun, J.-P.; Minor, J.; Kemp, K. W.; Dong, H.; Rollny, L.; Labelle, A.; Carey, G.;

Sutherland, B.; Hill, I.; Amassian, A.; Liu, H.; Tang, J.; Bakr, O. M.; Sargent, E. H. Air-stable n-type colloidal quantum dot solids. *Nat. Mater.* **2014**, *13*, 822-828.

Nocera, D. G. Personalized Energy: The Home as a Solar Power Station and Solar Gas Station. *ChemSusChem* **2009**, *2*, 387-390.

Nocera, D. G. The Artificial Leaf. *Acc. Chem. Res.* **2012**, *45*, 767-776.

Norberg, N. S.; Gamelin, D. R. Influence of Surface Modification on the Luminescence of Colloidal ZnO Nanocrystals. *J. Phys. Chem. B* **2005**, *109*, 20810-20816.

Osterloh, F. E. Inorganic Materials as Catalysts for Photochemical Splitting of Water. *Chem. Mat.* **2007**, *20*, 35-54.

Osterloh, F. E. Inorganic nanostructures for photoelectrochemical and photocatalytic water splitting. *Chem. Soc. Rev.* **2013**, *42*, 2294-2320.

Oszajca, M. F.; Bodnarchuk, M. I.; Kovalenko, M. V. Precisely Engineered Colloidal Nanoparticles and Nanocrystals for Li-Ion and Na-Ion Batteries: Model Systems or Practical Solutions? *Chem. Mat.* **2014**, *26*, 5422-5432.

Patton, B.; Langbein, W.; Woggon, U. Trion, biexciton, and exciton dynamics in single self-assembled CdSe quantum dots. *Phys. Rev. B* **2003**, *68*, 125316.

Pendlebury, S. R.; Cowan, A. J.; Barroso, M.; Sivula, K.; Ye, J.; Gratzel, M.; Klug, D. R.; Tang, J.; Durrant, J. R. Correlating long-lived photogenerated hole populations with photocurrent densities in hematite water oxidation photoanodes. *Energy Environ. Sci.* **2012**, *5*, 6304-6312.

Peng, Z. A.; Peng, X. Formation of High-Quality CdTe, CdSe, and CdS Nanocrystals Using CdO as Precursor. *J. Am. Chem. Soc.* **2001**, *123*, 183-184.

Peter, L. M. Dye-sensitized nanocrystalline solar cells. *Phys. Chem. Chem. Phys.* **2007**, *9*, 2630-2642.

Qin, W.; Liu, H.; Guyot-Sionnest, P. Small Bright Charged Colloidal Quantum Dots. *ACS Nano* **2014**, *8*, 283-291.

Querner, C.; Reiss, P.; Sadki, S.; Zagorska, M.; Pron, A. Size and ligand effects on the electrochemical and spectroelectrochemical responses of CdSe nanocrystals. *Phys. Chem. Chem. Phys.* **2005**, *7*, 3204-3209.

Rausch, B.; Symes, M. D.; Chisholm, G.; Cronin, L. Decoupled catalytic hydrogen evolution from a molecular metal oxide redox mediator in water splitting. *Science* **2014**, *345*, 1326-1330.

Reiss, H. The Fermi level and the redox potential. *J. Phys. Chem.* **1985**, *89*, 3783-3791.

Riha, S. C.; Klahr, B. M.; Tyo, E. C.; Seifert, S.; Vajda, S.; Pellin, M. J.; Hamann, T. W.; Martinson, A. B. F. Atomic Layer Deposition of a Submonolayer Catalyst for the Enhanced Photoelectrochemical Performance of Water Oxidation with Hematite. *ACS Nano* **2013**, *7*, 2396-2405.

Rinehart, J. D.; Schimpf, A. M.; Weaver, A. L.; Cohn, A. W.; Gamelin, D. R. Photochemical Electronic Doping of Colloidal CdSe Nanocrystals. *J. Am. Chem. Soc.* **2013**, *135*, 18782-18785.

Rinehart, J. D.; Weaver, A. L.; Gamelin, D. R. Redox Brightening of Colloidal Semiconductor Nanocrystals Using Molecular Reductants. *J. Am. Chem. Soc.* **2012**, *134*, 16175-16177.

Roest, A. L.; Germeau, A.; Kelly, J. J.; Vanmaekelbergh, D.; Allan, G.; Meulenkamp, E. A. Long-Range Transport in an Assembly of ZnO Quantum Dots: The Effects of Quantum Confinement, Coulomb Repulsion and Structural Disorder. *ChemPhysChem* **2003**, *4*, 959-966.

Roest, A. L.; Houtepen, A. J.; Kelly, J. J.; Vanmaekelbergh, D. Electron-conducting quantum-dot solids with ionic charge compensation. *Faraday Discussions* **2004**, *125*, 55-62.

Roest, A. L.; Kelly, J. J.; Vanmaekelbergh, D. Coulomb blockade of electron transport in a ZnO quantum-dot solid. *App. Phys. Lett.* **2003**, *83*, 5530-5532.

Roest, A. L.; Kelly, J. J.; Vanmaekelbergh, D.; Meulenkamp, E. A. Staircase in the Electron Mobility of a ZnO Quantum Dot Assembly due to Shell Filling. *Phys. Rev. Lett.* **2002**, *89*, 036801.

Rühle, S.; Shalom, M.; Zaban, A. Quantum-Dot-Sensitized Solar Cells. *ChemPhysChem* **2010**, *11*, 2290-2304.

Runnerstrom, E. L.; Llordes, A.; Lounis, S. D.; Milliron, D. J. Nanostructured electrochromic smart windows: traditional materials and NIR-selective plasmonic nanocrystals. *Chem. Comm.* **2014**, *50*, 10555-10572.

Salvarezza, R. C.; Arvia, A. J.: A Modern Approach to Surface Roughness Applied to Electrochemical Systems. In *Modern Aspects of Electrochemistry*; Conway, B. E., Bockris, J. O. M., White, R., Eds.; Modern Aspects of Electrochemistry; Springer US, 1996; Vol. 28; pp 289-373.

Scanlon, M. D.; Peljo, P.; Mendez, M. A.; Smirnov, E.; Girault, H. H. Charging and discharging at the nanoscale: Fermi level equilibration of metallic nanoparticles. *Chem. Sci.* **2015**, *6*, 2705-2720.

Scheele, M.; Brutting, W.; Schreiber, F. Coupled organic-inorganic nanostructures (COIN). *Phys. Chem. Chem. Phys.* **2015**, *17*, 97-111.

Schimpf, A. M.; Gunthardt, C. E.; Rinehart, J. D.; Mayer, J. M.; Gamelin, D. R. Controlling Carrier Densities in Photochemically Reduced Colloidal ZnO Nanocrystals: Size Dependence and Role of the Hole Quencher. *J. Am. Chem. Soc.* **2013**, *135*, 16569-16577.

Schimpf, A. M.; Knowles, K. E.; Carroll, G. M.; Gamelin, D. R. Electronic Doping and Redox-Potential Tuning in Colloidal Semiconductor Nanocrystals. *Accts. Chem. Res.* **2015**, *48*, 1929-1937.

Schimpf, A. M.; Lounis, S. D.; Runnerstrom, E. L.; Milliron, D. J.; Gamelin, D. R. Redox Chemistries and Plasmon Energies of Photodoped In2O3 and Sn-Doped In2O3 (ITO) Nanocrystals. *J. Am. Chem. Soc.* **2015**, *137*, 518−524.

Schimpf, A. M.; Ochsenbein, S. T.; Buonsanti, R.; Milliron, D. J.; Gamelin, D. R. Comparison of extra electrons in colloidal n-type Al3+-doped and photochemically reduced ZnO nanocrystals. *Chem. Commun.* **2012**, *48*, 9352-9354.

Schimpf, A. M.; Thakkar, N.; Gunthardt, C. E.; Masiello, D. J.; Gamelin, D. R. Charge-Tunable Quantum Plasmons in Colloidal Semiconductor Nanocrystals. *ACS Nano* **2014**, *8*, 1065-1072.

Schrauben, J. N.; Hayoun, R.; Valdez, C. N.; Braten, M.; Fridley, L.; Mayer, J. M. Titanium and Zinc Oxide Nanoparticles Are Proton-Coupled Electron Transfer Agents. *Science* **2012**, *336*, 1298-1301.

Schwartz, D. A.; Norberg, N. S.; Nguyen, Q. P.; Parker, J. M.; Gamelin, D. R. Magnetic Quantum Dots: Synthesis, Spectroscopy, and Magnetism of Co2+- and Ni2+-Doped ZnO Nanocrystals. *J. Am. Chem. Soc.* **2003**, *125*, 13205-13218.

Senger, R. T.; Bajaj, K. K. Optical properties of confined polaronic excitons in spherical ionic quantum dots. *Phys. Rev. B* **2003**, *68*, 045313.

Shim, M.; Guyot-Sionnest, P. Comment on ``Staircase in the Electron Mobility of a ZnO Quantum Dot Assembly due to Shell Filling" and ``Optical Transitions in Artificial Few-Electron Atoms Strongly Confined inside ZnO Nanocrystals". *Phys. Rev. Lett.* **2003**, *91*, 169703.

Shim, M.; Guyot-Sionnest, P. n-type colloidal semiconductor nanocrystals. *Nature* **2000**, *407*, 981-983.

Shim, M.; Guyot-Sionnest, P. Organic-Capped ZnO Nanocrystals: Synthesis and n-

Type Character. *J. Am. Chem. Soc.* **2001**, *123*, 11651-11654.

Shim, M.; Wang, C.; Guyot-Sionnest, P. Charge-Tunable Optical Properties in Colloidal Semiconductor Nanocrystals. *J. Phys. Chem. B* **2001**, *105*, 2369-2373.

Shimizu, K. T.; Woo, W. K.; Fisher, B. R.; Eisler, H. J.; Bawendi, M. G. Surface-Enhanced Emission from Single Semiconductor Nanocrystals. *Phys. Rev. Lett.* **2002**, *89*, 117401.

Shirasaki, Y.; Supran, G. J.; Bawendi, M. G.; Bulovic, V. Emergence of colloidal quantum-dot light-emitting technologies. *Nat Photon* **2013**, *7*, 13-23.

Sivula, K. Metal Oxide Photoelectrodes for Solar Fuel Production, Surface Traps, and Catalysis. *J. Phys. Chem. Lett.* **2013**, *4*, 1624-1633.

Sivula, K.; Zboril, R.; Le Formal, F.; Robert, R.; Weidenkaff, A.; Tucek, J.; Frydrych, J.; Grätzel, M. Photoelectrochemical Water Splitting with Mesoporous Hematite Prepared by a Solution-Based Colloidal Approach. *J. Am. Chem. Soc.* **2010**, *132*, 7436-7444.

Smestad, G. P.; Steinfeld, A. Review: Photochemical and Thermochemical Production of Solar Fuels from H2O and CO2 Using Metal Oxide Catalysts. *Indus. Eng. Chem. Res.* **2012**, *51*, 11828-11840.

Snyder, G. J.; Toberer, E. S. Complex thermoelectric materials. *Nat Mater* **2008**, *7*, 105-114.

Surendranath, Y.; Dincă, M.; Nocera, D. G. Electrolyte-Dependent Electrosynthesis and Activity of Cobalt-Based Water Oxidation Catalysts. *J. Am. Chem. Soc.* **2009**, *131*, 2615-2620.

Surendranath, Y.; Kanan, M. W.; Nocera, D. G. Mechanistic Studies of the Oxygen Evolution Reaction by a Cobalt-Phosphate Catalyst at Neutral pH. *J. Am. Chem. Soc.* **2010**, *132*, 16501-16509.

Swart, I.; Liljeroth, P.; Vanmaekelbergh, D. Scanning probe microscopy and spectroscopy of colloidal semiconductor nanocrystals and assembled structures. *Chem. Rev.* **2016**.

Talapin, D. V.; Lee, J.-S.; Kovalenko, M. V.; Shevchenko, E. V. Prospects of Colloidal Nanocrystals for Electronic and Optoelectronic Applications. *Chem. Rev.* **2010**, *110*, 389-458.

Talgorn, E.; Moysidou, E.; Abellon, R. D.; Savenije, T. J.; Goossens, A.; Houtepen, A. J.; Siebbeles, L. D. A. Highly Photoconductive CdSe Quantum-Dot Films: Influence of Capping Molecules and Film Preparation Procedure. *J. Phys. Chem. C* **2010**, *114*,

3441-3447.

Tanaka, S.; Bruce, J. A.; Wrighton, M. S. Deliberate modification of the behavior of n-type cadmium telluride/electrolyte interfaces by surface etching. Removal of Fermi level pinning. *J. Phys. Chem.***1981**, *85*, 3778-3787.

Tang, H.; Matin, M. A.; Wang, H.; Deutsch, T.; Al-Jassim, M.; Turner, J.; Yan, Y. Synthesis and characterization of titanium-alloyed hematite thin films for photoelectrochemical water splitting. *J. Appl. Phys.* **2011**, *110*, 123511.

Trotochaud, L.; Mills, T. J.; Boettcher, S. W. An Optocatalytic Model for Semiconductor–Catalyst Water-Splitting Photoelectrodes Based on In Situ Optical Measurements on Operational Catalysts. *J. Phys. Chem. Lett.* **2013**, *4*, 931-935.

Upul Wijayantha, K. G.; Saremi-Yarahmadi, S.; Peter, L. M. Kinetics of oxygen evolution at α-Fe_2O_3 photoanodes: a study by photoelectrochemical impedance spectroscopy. *Phys. Chem. Chem. Phys.* **2011**, *13*, 5264-5270.

Valdez, C. N.; Braten, M.; Soria, A.; Gamelin, D. R.; Mayer, J. M. Effect of Protons on the Redox Chemistry of Colloidal Zinc Oxide Nanocrystals. *J. Am. Chem. Soc.* **2013**, *135*, 8492-8495.

Valdez, C. N.; Schimpf, A. M.; Gamelin, D. R.; Mayer, J. M. Proton-Controlled Reduction of ZnO Nanocrystals: Effects of Molecular Reductants, Cations, and Thermodynamic Limitations. *J. Am. Chem. Soc.* **2016**, *138*, 1377-1385.

van Dijken, A.; Meulenkamp, E. A.; Vanmaekelbergh, D.; Meijerink, A. Identification of the transition responsible for the visible emission in ZnO using quantum size effects. *J. Lumin.* **2000**, *90*, 123-128.

Vaneski, A.; Schneider, J.; Susha, A. S.; Rogach, A. L. Colloidal hybrid heterostructures based on II–VI semiconductor nanocrystals for photocatalytic hydrogen generation. *J. Photochem. Photobio. C: Photochem. Rev.* **2014**, *19*, 52-61.

Vanmaekelbergh, D. Self-assembly of colloidal nanocrystals as route to novel classes of nanostructured materials. *Nano Today* **2011**, *6*, 419-437.

Vanmaekelbergh, D.; Houtepen, A. J.; Kelly, J. J. Electrochemical gating: A method to tune and monitor the (opto)electronic properties of functional materials. *Electrochimica Acta* **2007**, *53*, 1140-1149.

Vanmaekelbergh, D.; Liljeroth, P. Electron-conducting quantum dot solids: novel materials based on colloidal semiconductor nanocrystals. *Chem. Soc. Rev.* **2005**, *34*, 299-312.

Vanmaekelbergh, D.; Roest, A. L.; Germeau, A.; Kelly, J. J.; Meulenkamp, E. A.;

Allan, G.; Delerue, C. Vanmaekelbergh Reply. *Phys. Rev. Lett.* **2003**, *91*, 169704.

Wang, C.; Shim, M.; Guyot-Sionnest, P. Electrochromic Nanocrystal Quantum Dots. *Science* **2001**, *291*, 2390-2392.

Wang, C.; Shim, M.; Guyot-Sionnest, P. Electrochromic semiconductor nanocrystal films. *App. Phys. Lett.* **2002**, *80*, 4-6.

Wang, G.; Ling, Y.; Wheeler, D. A.; George, K. E. N.; Horsley, K.; Heske, C.; Zhang, J. Z.; Li, Y. Facile Synthesis of Highly Photoactive α-Fe2O3-Based Films for Water Oxidation. *Nano Lett.* **2011**, *11*, 3503-3509.

Weaver, A. L.; Gamelin, D. R. Photoluminescence Brightening via Electrochemical Trap Passivation in ZnSe and Mn^{2+}-Doped ZnSe Quantum Dots. *J. Am. Chem. Soc.* **2012**, *134*, 6819-6825.

Wehrenberg, B. L.; Guyot-Sionnest, P. Electron and Hole Injection in PbSe Quantum Dot Films. *J. Am. Chem. Soc.* **2003**, *125*, 7806-7807.

Wehrenberg, B. L.; Yu, D.; Ma, J.; Guyot-Sionnest, P. Conduction in Charged PbSe Nanocrystal Films. *J. Phys. Chem. B* **2005**, *109*, 20192-20199.

Wood, A.; Giersig, M.; Hilgendorff, M.; Vilas-Campos, A.; Liz-Marzán, L. M.; Mulvaney, P. Size effects in ZnO: The cluster to quantum dot transition. *Aust. J. Chem.* **2003**, *56*, 1051-1057.

Wood, A.; Giersig, M.; Mulvaney, P. Fermi Level Equilibration in Quantum Dot−Metal Nanojunctions. *J. Phys. Chem. B* **2001**, *105*, 8810-8815.

Wu, K.; Lian, T. Quantum confined colloidal nanorod heterostructures for solar-to-fuel conversion. *Chem. Soc. Rev.* **2016**.

Yang, S.; Prendergast, D.; Neaton, J. B. Tuning Semiconductor Band Edge Energies for Solar Photocatalysis via Surface Ligand Passivation. *Nano Lett.* **2012**, *12*, 383-388.

Yu, D.; Wang, C.; Guyot-Sionnest, P. n-Type Conducting CdSe Nanocrystal Solids. *Science* **2003**, *300*, 1277-1280.

Zandi, O.; Klahr, B. M.; Hamann, T. W. Highly photoactive Ti-doped [small alpha]-Fe2O3 thin film electrodes: resurrection of the dead layer. *Energy Environ. Sci.* **2013**, *6*, 634-642.

Zhao, W.-W.; Wang, J.; Zhu, Y.-C.; Xu, J.-J.; Chen, H.-Y. Quantum Dots: Electrochemiluminescent and Photoelectrochemical Bioanalysis. *Anal. Chem.* **2015**, *87*, 9520-9531.

Zhong, D. K.; Cornuz, M.; Sivula, K.; Gratzel, M.; Gamelin, D. R. Photo-assisted electrodeposition of cobalt-phosphate (Co-Pi) catalyst on hematite photoanodes for solar water oxidation. *Energy Environ. Sci.* **2011**, *4*, 1759-1764.

Zhong, D. K.; Gamelin, D. R. Photoelectrochemical Water Oxidation by Cobalt Catalyst ("Co−Pi")/α-Fe2O3 Composite Photoanodes: Oxygen Evolution and Resolution of a Kinetic Bottleneck. *J. Am. Chem. Soc.* **2010**, *132*, 4202-4207.

Zhong, D. K.; Sun, J.; Inumaru, H.; Gamelin, D. R. Solar Water Oxidation by Composite Catalyst/α-Fe2O3 Photoanodes. *J. Am. Chem. Soc.* **2009**, *131*, 6086-6087.

Zhou, D.; Kittilstved, K. R. Control over Fe^{3+} speciation in colloidal ZnO nanocrystals. *J. Mater. Chem. C* **2015**, *3*, 4352-4358.

Zong, X.; Wu, G.; Yan, H.; Ma, G.; Shi, J.; Wen, F.; Wang, L.; Li, C. Photocatalytic H2 Evolution on MoS2/CdS Catalysts under Visible Light Irradiation. *J. Phys. Chem. C* **2010**, *114*, 1963-1968.